Thermoresponsive Core-Shell Microgels as Model System for Soft Colloids in Crowded Environments: Insights into the Phase Behavior via Small-Angle X-ray Scattering and Optical Spectroscopy

Inaugural-Dissertation

zur Erlangung des Doktorgrades
der Mathematisch-Naturwissenschaftlichen Fakultät
der Heinrich-Heine-Universität Düsseldorf

vorgelegt von

Marco Hildebrandt

aus Düsseldorf

Düsseldorf, Oktober 2023

aus dem Institut für Physikalische Chemie I, Kolloide und Nanooptik
der Heinrich-Heine-Universität Düsseldorf

Gedruckt mit der Genehmigung der
Mathematisch-Naturwissenschaftlichen Fakultät der

Heinrich-Heine-Universität Düsseldorf

Berichterstatter:

1. Prof. Dr. Matthias Karg

2. Prof. Dr. Peter R. Lang

Tag der mündlichen Prüfung: 25.01.2024

Eidesstattliche Erklärung

Ich, Marco Hildebrandt, versichere an Eides statt, dass die Dissertation von mir selbständig und ohne unzulässige fremde Hilfe unter Beachtung der ”Grundsätze zur Sicherung guter wissenschaftlicher Praxis an der Heinrich-Heine-Universität Düsseldorf“ erstellt worden ist. Alle verwendeten Quellen und Hilfsmittel sind als solche gekennzeichnet und im Literaturverzeichnis aufgelistet.

Die vorliegende Dissertation wurde ausschließlich an der Mathematisch-Naturwissenschaftlichen Fakultät der Heinrich-Heine-Universität Düsseldorf vorgelegt. Es wurden keine früheren Promotionsversuche unternommen.

Ort, Datum	Unterschrift

Table of Contents

Danksagung

An dieser Stelle, bevor der Leser sich der folgenden Arbeit zuwendet, möchte ich die Gelegenheit ergreifen, die volle Aufmerksamkeit auf die Menschen zu lenken, die dies erst möglich gemacht haben. Es war ein langer Weg mit einigen Herausforderungen, vielen schönen Erlebnissen und prägenden Erfahrungen.

Beginnen wir klassisch mit dem Doktorvater: Matthias Karg. Danke, dass ich meine Doktorarbeit mit diesem farbenfrohen und spannenden Thema in deiner Arbeitsgruppe anfertigen durfte. Auch für die vielen gebotenen Möglichkeiten, wie zahlreiche Konferenzbesuche und das Arbeiten an Projekten abseits der Chemie möchte ich mich wirklich bedanken. Nach mehr als sechs Jahren in dieser Gruppe möchte ich mich für deine Unterstützung und Anleitung in zahlreichen Gesprächen bedanken. Hier habe ich gelernt, was wissenschaftliches Arbeiten bedeutet.

Eine Person in diesem Arbeitsbereich sticht noch besonders hervor: Lieber Marius, seit der zweiten Matheübung im ersten Semester stehen wir das Ganze hier zusammen durch. Bachelor-, Master-Studium und schlussendlich auch die Doktorarbeit. Ich habe mir oft gedacht, dass ich das hier ohne Dich nicht schaffen würde und bin wirklich froh, diesen Weg mit einem so guten Freund beschreiten zu dürfen.

Damit kommen wir auch gleich zum Büro 27, mit Marius Otten, Déborah Feller und im Herzen auch Jonathan Garthe: Danke für die gute Atmosphäre über all die Jahre und dafür, dass wir hier alle, mit all unseren Ecken und Kanten, wir selbst sein konnten. Dankbar bin ich auch für die Kollegen im Arbeitskreis, die sich zu großartigen Freunden entwickelt haben. Déborah Feller, Casper Croonenbrock, Jonathan Garthe und Philipp Hammers ihr seid/wart ein Gewinn für die Gruppe und ich bin froh, euch hier kennengelernt zu haben.

Dass die Lehre auch ein Teil der Promotion ist, ist für die meisten eher ein negativer Punkt, doch gerade die Betreuung von Praktika und vor allem Abschlussarbeiten und Forschungspraktika fand ich sehr bereichernd. Hierbei möchte ich mich vor allem bei Sunny (Duong Pham Thuy) und auch bei Anna Domgans bedanken. Eure Arbeit hat mich maßgeblich unterstützt.

Für die unkomplizierte und offene Zusammenarbeit mit der Feinmechanik (Chemie/Pharmazie), möchte ich mich ganz herzlich bei Sonja Schiller und Corell Spöringer bedanken.

Dem ganzen Institut der PCI möchte ich für die größtenteils entspannte und konstruktive Zusammenarbeit danken. Insbesondere unserer guten Seele und Sekretärin Andrea, sowie Matze, der immer offen für einen Kaffee oder eine kurze Pause auf dem Balkon war.

Vielen Dank noch allen Kooperationspartnern, vor allem Janne-Mieke Meijer (TU Eindhoven) Sylvain Prevost (ILL Grenoble) und Andrea Scotti (RWTH Aachen), welche diese Arbeit zum Teil erst möglich gemacht haben.

An dieser Stelle gilt mein Dank auch Peter Lang vom Forschungszentrum Jülich für die Co-Begutachtung dieser Arbeit. Über den Spruch: „Traue niemals Daten, die nicht mindestens einmal im reziproken Raum waren!“ (P. Lang, Zsiqmondy Kolloqium 2020) musste ich in den folgenden Jahren noch mehrmals schmunzeln.

Ein ganz besonderer Dank gilt meiner Freundin Melissa: Ich glaube ich kann dir gar nicht genug danken für deine ganze Unterstützung während dieser Zeit und einfach dafür, dass du immer für mich da bist. Auch ein großer Dank an meine Eltern: Von euch kam nie Druck und auch keine leeren Floskeln als Durchhalteparolen, während es hier mal wieder schwieriger wurde, sondern Unterstützung und Verständnis.

List of Publications

1. Déborah Feller, Marius Otten, **Marco Hildebrandt**, Marcel Krüsmann, Garry Bryant and Matthias Karg

   Translational and rotational diffusion coefficients of gold nanorods functionalized with a high molecular weight, thermoresponsive ligand: a depolarized dynamic light scattering study.

   Published in *Soft Matter*, **2021**, 17, (15), 4019–4026.
   https://doi.org/10.1039/d1sm00077b

2. Ekaterina Ponomareva, Ben Tadgell, **Marco Hildebrandt**, Marcel Krüsmann, Sylvain Prévost, Paul Mulvaney and Matthias Karg

   The fuzzy sphere morphology is responsible for the increase in light scattering during the shrinkage of thermoresponsive microgels.

   Published in *Soft Matter*, **2022**, 18, (4), 807–825.
   https://doi.org/10.1039/d1sm01473k

3. **Marco Hildebrandt**, Sergey Lazarev, Javier Pérez, Ivan A. Vartanyants, Janne-Mieke Meijer and Matthias Karg

   SAXS Investigation of Core–Shell Microgels with High Scattering Contrast Cores: Access to Structure Factor and Volume Fraction.

   Published in *Macromolecules*, **2022**, 55, (7), 2959–2969.
   https://doi.org/10.1021/acs.macromol.2c00100

4. Marius Otten, **Marco Hildebrandt**, Ralf Kühnemuth and Matthias Karg

   Pyrolysis and Solvothermal Synthesis for Carbon Dots: Role of Purification and Molecular Fluorophores.

   Published in *Langmuir*, **2022**, 38, (19), 6148–6157.
   https://doi.org/10.1021/acs.langmuir.2c00508

5. **Marco Hildebrandt**, Duong Pham Thuy, Julian Kippenberger, Tillmann L. Wigger, Judith E. Houston, Andrea Scotti and Matthias Karg

   Fluid-solid transitions in photonic crystals of soft, thermoresponsive microgels

   Published in *Soft Matter*, **2023**, 19, (37), 7122-7135.
   https://doi.org/10.1039/D3SM01062G

6. **Marco Hildebrandt**, Duong Pham Thuy, Anna Domgans, Andrea Scotti, Sylvain Prévost and Matthias Karg

   Temperature-dependent phase diagrams of weakly charged, thermoresponsive microgels under charged and charge-screened conditions

   Manuscript in preparation for submission

7. Marius Otten, **Marco Hildebrandt**, Ben Pfeffing, Victoria Voigt, Thomas Hellweg and Matthias Karg

   Following the volume phase transition of thermoresponsive microgels by dynamic light scattering and turbidity: Correlations depend on microgel homogeneity

   Manuscript in preparation for submission.

8. Marius Otten, Diana Hildebrandt, Saskia Mölders, **Marco Hildebrandt** and Matthias Karg

   PNIPAM-based copolymer microgels as nanoreactors for the in situ synthesis of gold nanoparticles

   Manuscript in preparation for submission.

Presentations at Scientific Conferences

1. **Marco Hildebrandt**, Marius Otten and Matthias Karg

   Poster Presentation:

   Synthesis and Characterization of Colortunable Carbon Nanodots

   17th European Student Colloid Conference (**2019**), Varna, Bulgaria

2. **Marco Hildebrandt**, Janne-Mieke Meijer and Matthias Karg

   Poster Presentation:

   Characterization of temperature switchable photonic crystals via small angle X-ray scattering

   33rd Conference of the European Colloid and Interface Society (**2019**), Leuven, Belgium

3. **Marco Hildebrandt**, Duong Pham Thuy and Matthias Karg

   Oral Presentation:

   Role of Annealing for Soft-Colloidal Crystals

   2021 Virtual Symposium on Microgels (**2021**), Online, hosted in Aachen, Germany

4. **Marco Hildebrandt** and Matthias Karg

   Poster Presentation:

   Temperature dependent behavior of Soft-Colloidal Crystals

   35th Conference of the European Colloid and Interface Society (**2021**), Online, hosted in Athens, Greece

5. **Marco Hildebrandt** and Matthias Karg

Oral Presentation:

Core-shell microgels as soft model colloids to study phase behavior in dense packings via small angle X-ray scattering

36th Conference of the European Colloid and Interface Society (**2022**), Chania, Crete/Greece

6. **Marco Hildebrandt** and Matthias Karg

Poster Presentation:

Core-shell microgels as soft model colloids to study phase behavior in dense packings via small angle X-ray scattering

51st General assembly of the German Colloid Society (**2022**), Berlin, Germany

List of Abbreviations and Symbols

°C	Degree Celsius
A	Decay constant (form factor model)
Å	Angström
a	Lattice constant
a. u.	Arbitrary units
APS	Ammonium persulfate
Au	Gold
B	Baseline of the autocorrelation function
bcc	Body centered cubic
BIS	*N*,*N'*-methylenebisacrylamide
CS	Core-shell
d	Interparticle spacing
$d_{c\text{-}c}$	Center-to-center distance
DESY	Deutsches Elektronen Synchrotron
d_{hkl}	Crystal plane defined by miller indices
DLS	Dynamic light scattering
dSTORM	Direct stochastic optical reconstruction microscopy
d_{SC}	Distance between scattering centers
D_T	Translational diffusion constant
El. mobility	Electrophoretic mobility
eV	Electron volt
exp	Exponential function
ExpS-model	Exponential shell model
fcc	Face centered cubic
FS-model	Fuzzy sphere model
$G(\Gamma)$	Mean autocorrelation function
$g_{(1)}$	Field-time autocorrelation
$g_{(2)}$	Intensity-time autocorrelation
$g_{rad/azi}$	Radial and azimuthal strain
$HAuCL_4 \cdot 3H_2O$	Gold(III) chloride trihydrate hydrochloride
hcp	Hexagonally closed packed
$I(q)$	Scattering intensity
$I(t)$	Scattering intensity at respective time
I_0	Scattering intensity at infinitely small scattering angle
IB	Background intensity
$I_{conc.}$	Scattering intensity from concentrated state
$I_{dil.}$	Scattering intensity from dilute state

ILL	Institut Laue-Langevin
$I_{scatter}$	Scattering intensity
K	Kelvin
k_B	Boltzmann constant
KCl	Potassium chloride
$\vec{k}_{in}$	Wave vector of incoming light
$\vec{k}_{out}$	Wave vector of scattered light
LCST	Lower critical solution temperature
$L_{rad/azi}$	Radial and azimuthal coherently scattering domain size
LSPR	Localized surface plasmon resonance
M	Molar mass
m	Mass
mol%	Mol percent
MPS	3-(trimethoxysilyl)propyl methacrylate
N	Particle number concentration
n	Refractive Index
N_A	Avogadro's number
NaCl	Sodium chloride
NIR	Near infrared
NIST	National Institute of Standards and Technology (US)
NPs	Nanoparticles
$P(q)$	Form factor
PMMA	Polymethylmethacrylate
PNIPAM	Poly-*N*-isopropylacrylamide
PNIPMAM	Poly-*N*-isopropylmethacrylamide
PNNPAM	Poly-*N*-n-propylacrylamide
PPS	Potassium persulfate
PY	Percus-Yevick
q	Magnitude of the scattering vector
q^*	Position of the first structure factor maximum
q_{max}	Structure factor maximum
R	Radius
R_c	Radius of the core
rcf	Relative centrifugal forces
R_g	Radius of gyration
R_h	Hydrodynamic radius
R_{HC}	Hard-core radius
rhcp	Random hexagonally closed packed
R_{HS}	Hard sphere radius
$R_{P(q)}$	Form factor radius

$S(q)$	Structure factor
$S(q)_{max}$	Structure factor maximum
SALS	Small-angle light scattering
SANS	Small-angle neutron scattering
SAS	Small-angle scattering
SAXS	Small-angle X-ray scattering
SDS	Sodium dodecyl sulfate
SiO_2	Silicon dioxide
SLD	Scattering length density
SLR	Surface lattice resonance
SLS	Static light scattering
T	Temperature
t	Time
TEM	Transmission electron microscopy
TEOS	Tetraethyl orthosilicate
TOC	Table of contents
UCST	Upper critical solution temperature
USAXS	Ultra-small-angle X-ray scattering
UV	Ultraviolet
V	Volume
Vis	Visible
vol%	Volume percent
VPT	Volume phase transition
VPTT	Volume phase transition temperature
$w_{rad/azi}$	Radial and azimuthal full width half maximum of the Bragg peaks
wt%	Mass percent
β	Intercept of the autocorrelation function
Γ	Decay constant (DLS)
ΔSLD	Difference in scattering length density
Δt_{shell}	Shell thickness
ζ	Generalized volume fraction
$\zeta_{transition}$	Generalized volume fraction at phase transition
η	Dynamic viscosity
θ	Scattering angle
λ	Wavelength
λ_{Bragg}	Wavelength of the Bragg peak
λ_{diff}	Wavelength of the diffraction (Bragg) peak
μ_x	Respective cumulant
ξ_{OZ}	Correlation length

ρ	Density
σ	Polydispersity
τ	Delay time
ϕ	Volume fraction
$\phi_{\text{Bragg peak}}$	Volume fraction based on the Bragg peak
ϕ_{CS}	Volume fraction of core-shell microgels
ϕ_{HS}	Hard sphere volume fraction
ϕ_{polymer}	Polymer volume fraction

Abstract

Microgels are three-dimensional, crosslinked polymer networks with high internal solvent contents. In fundamental science, microgels are often considered as model for soft colloids. For life science microgels are of particular intertest due to their comparability to cells or viruses in terms of length scale and general soft behavior. Furthermore, microgels can exhibit responses towards external stimuli like mechanical force or ionic strength, which is comparable to biological systems. Here, microgels can be used as less complex systems, leading to a better understanding of fundamental processes, for example on the response of soft particles towards crowded environments. Therefore, the aim of this thesis was to establish a model system of core-shell microgels, for the investigation of soft colloids in dense packings via small-angle X-ray scattering (SAXS). The core-shell microgels consist of an inorganic core made from gold or silica and a thermoresponsive poly-*N*-isopropylacrylamide hydrogel shell, providing *in situ* control over the volume fraction of the system. Via the scattering intensity of the cores in SAXS, particle number concentrations became accessible, which is otherwise hard to achieve for soft and deformable systems like microgels. Core-shell microgels in the dilute state were characterized in great detail by electron microscopy and various scattering techniques like temperature-dependent dynamic light scattering and small-angle X-ray or neutron scattering. Dispersions of core-shell microgels in dense packings, forming crystalline structures, were investigated by synchrotron SAXS in order to receive information about the morphology, size and the structure of the self-assembled microgels in crowded environments. The photonic properties of the colloidal crystals were used to follow the phase transition of the core-shell microgels between the crystalline and fluid phase by temperature-dependent optical spectroscopy. In addition, the influence of electrostatics on the phase behavior of the core-shell microgels could be studied by the screening of charges, exhibited by the microgels, due to an alteration in the ionic strength of the dispersion.

1. Introduction

Scattering methods are powerful techniques, providing access to structural information from the atomic to colloidal length scale. Early examples are the Rutherford experiment[1] or crystal structure analysis via X-rays established by Bragg in 1913.[2] Scattering based techniques, are also widely applied as analysis methods in colloid science, focusing on elastic scattering processes between photons or neutrons with condensed matter. Starting with the work of Tyndall who reported on the influence of disperse media like smoke on visible light, scattering methods like dynamic or static light scattering became fundamental tools in modern colloid science. In addition, radiation sources for highly brilliant and coherent neutrons or X-rays allow for even more complex experiments like small-angle scattering, to study colloids on different length scales and various contrast situations.

In the past years microgels became a prominent class of materials in colloid science, being topic of numerous publications and are often considered as model systems for soft colloidal particles.[3-11] Microgels consist of a crosslinked polymer network, swollen by large amounts of solvent.[7, 8, 11] Due to their size, high internal solvent contents and overall polymeric nature, microgels exhibit characteristics attributed to colloids, surfactants and macromolecules. [10, 12-16] Depending on their composition, microgels are also prominent for their responsive behavior towards external stimuli like pH, ionic strength or temperature.[17-23] Since introduced by Pelton and Chibante in 1986,[24] microgels based on poly-*N*-isopropylacrylamide (PNIPAM) are a prominent example of responsive hydrogels, featuring the characteristic volume phase transition (VPT),[25-27] around the respective polymers lower critical solution temperature at 32 °C.[28] Microgels based on PNIPAM are usually synthesized by a precipitation polymerization in aqueous environment, above the VPT temperature (VPTT) and in presence of the crosslinker *N*,*N'*-methylenebisacrylamide (BIS). Due to the slightly faster consumption of the crosslinker during the synthesis, the microgels exhibit certain inhomogeneities in their internal network structure, accompanied by a gradient in crosslinking- and polymer density. [25, 29-31] **Figure 1.1** shows a schematic illustration of a microgel below and above the VPTT. In the swollen state (T < VPTT) the microgel exhibits a higher polymer density in the center which decreases towards the outer periphery where the loosely crosslinked chains nearly resemble free polymer.[30] In the collapsed state (T > VPPT) the microgel is decreased in size and possess a rather homogenous polymer density.[32]

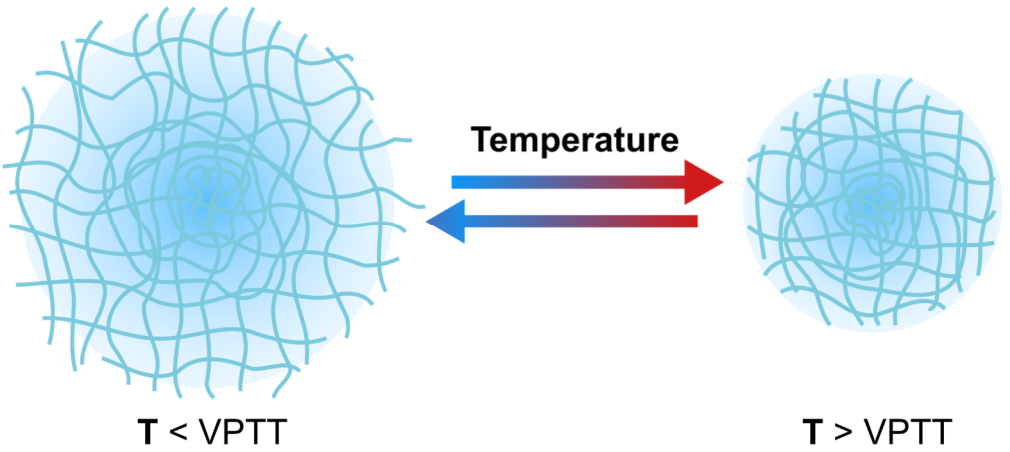

Figure 1.1 Schematic illustration of a thermoresponsive microgel. Below the VPTT, the microgel is in a swollen state (left), while it is in collapsed state above the VPTT (right).

In general, microgels are of great interest in science as they are highly versatile in terms of preparation or post-synthetic modifications and therefore can be used as simplified model systems to investigate soft particle interactions[33-36] or to mimic or interact with biological systems.[37-40] Application driven investigation of microgels focus on topics like viscosity modifiers, [41, 42] color changing systems[43-45] and printing.[46] Beyond modifications in terms of the polymer composition, microgels are also suitable for the fabrication of hybrid systems, for example hosting inorganic particles or even enzymatic units in their polymer network. Therefore, microgels can exhibit even more functionalities like for example optical or plasmonic properties as shown by Karg et al.[47-50] Furthermore, the group of Ballauff proposed hybrid microgel systems with catalytic activity, possessing immobilized enzymes or metal nanoparticles, as nanoreactor for chemical reactions.[51-54]

Due to their colloidal characteristics, microgels show assembly phenomena comparable to hard spheres in 2D at liquid-interfaces or in 3D in the bulk phase. Here, the microgels exhibit more complex interactions, compared to hard spheres, due to their soft and deformable character.[35, 55] When the interaction potential between two hard spheres is given as function of center-to-center distance, the potential is low until both spheres are in direct contact and the potential drastically increases. As microgels are soft objects, the interaction potential slightly increases when the objects come into contact and further increases when the center-to-center distance is decreased.[35] This is characteristic for the interaction between soft particles.

The investigation of the 2D phase behavior of microgels is often performed in the dried state, with microgels being transferred from the liquid-liquid or liquid-air interface onto a solid substrate. These samples are investigated *ex situ* by microscopy techniques like atomic force microscopy[56, 57] scanning electron microscopy[58, 59] or optical microscopy.[34] During the compression of microgel monolayers at the interface, an isostructural phase transition was observed *ex situ* in the dried state. Meaning that at a certain compression, interparticle distances are drastically reduced and microgels seem to collapse.[57-60] A recent study performed by Kuk et al. investigated the phase behavior of microgels at the liquid-air interphase during the compression of the monolayer *in situ*, by small-angle light scattering.[61] Here, the isostructural phase transition was not observed at the liquid-air interface and the origin of this process might be related to the transfer of the microgel monolayer from the interface to the substrate and the consequent drying of the sample. In addition to the mostly hexagonally ordered structures achieved by fluid interface assisted self-assembly of microgels, even more complex structures like honeycomb structures or Moiré lattices can be achieved by for example the deposition of a second layer of microgels.[62-64]

Microgels can undergo spontaneous self-assembly in 3D. For that, the microgels need to occupy a certain volume in the dispersion[22, 65-67] or exhibit long ranged interparticle interaction, often induced by the presence of charges.[65, 68] The structures formed by the microgels express crystalline characteristics and can be described as analogues to common crystals, based on atoms, but on a colloidal length scale. Crystal structures found for such monomodal systems are body centered cubic (bcc),[69, 70] face centered cubic (fcc),[66, 71] hexagonally closed packed (hcp) or random hexagonally closed packed (rhcp) structures.[71] The hcp and fcc structure exhibit the highest possible packing efficiency for spherical systems. With microgel dimensions comparable to the wavelength of visible light, the colloidal crystals can exhibit photonic properties, as light gets reflected on crystalline planes comparable to Bragg reflections in crystal structure analysis. In optical spectroscopy, the photonic properties of the colloidal crystals manifest as Bragg peaks in the recorded spectrum.[43, 47, 72, 73]

When studying microgels in dense packings, whether studies are focused on structural properties or on the response of the microgels towards crowded environments, the analysis can become challenging. **Figure 1.2** shows a simulated scattering profile of hard spherical particles, where the scattering intensity is given as function of the magnitude of the scattering vector *q*.

The form factor (P(q)) provides information about the size, shape and morphology of the investigated particle. Information about the spatial correlation of the particle ensemble and interparticle distances are provided by the structure factor S(q). The structure factor maximum ($S(q)_{max}$) and the first form factor minimum ($P(q)_{min}$) are indicated by black arrows. As shown in **Figure 1.2**, the structure factor and the form factor are usually superimposed as both occur on similar length scales.

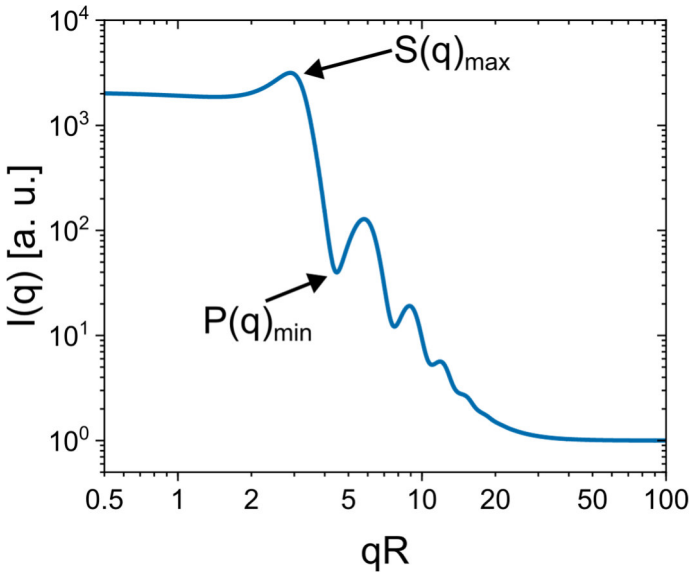

Figure 1.2 Simulated scattering profile from a sample of polydisperse hard spheres consisting of a structure factor S(q) and form factor P(q) contribution. Structure factor maximum ($S(q)_{max}$) and the first form factor minimum ($P(q)_{min}$) are indicated by black arrows.

In contrast to hard sphere like systems, microgels are soft and deformable objects which can also undergo deswelling and interpenetration processes in dense packing.[74-76] Therefore, the form factor of the microgels can be influenced by the packing density, which complicates the accurate extraction of the structure or form factor from the recorded scattering data. This extraction needs to be performed to get insights about the structure or morphology of the microgels. Even in microscopy, the interpenetration and deformation of microgels can hamper the spatial separation of individual microgels and the analysis of the recorded data becomes challenging. An additional challenge for the investigation of microgels in dense packings is the determination of particle number concentration and, correspondingly, the volume fraction. This task is rather difficult due to their inhomogeneous density and high internal solvent contents.

In microscopy, the challenge of deformation and interpenetration processes were addressed by the application of high-resolution optical microscopy techniques like fluorescent confocal laser scanning microscopy or direct stochastic optical reconstruction microscopy (dSTORM). [76, 77] **Figure 1.3** shows two color dSTORM images of microgels with different concentrations (mass contents / wt %).[76] The individual microgels as well as their response towards the crowded environment are presented in real space images with high spatial resolution. At low concentrations (10.8 %) the microgels are of nearly spherical shape and begin to interpenetrate as the concentration increases. At the concentration of 18.7 wt %, the packing density is high enough to force the microgels to undergo deformation.

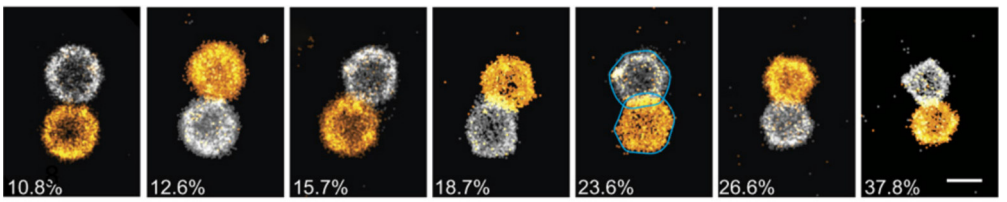

Figure 1.3 Two color super resolution microscopy images (dSTORM) of densely packed microgel pairs. Blue contour lines for the 23.6 wt % sample indicate the overlap of both microgels. The length of the scale bar is 500 nm. From G. M. Conley et al., Jamming and overpacking fuzzy microgels: Deformation, interpenetration, and compression. *Sci. Adv.* 3, (10), **2017**, e1700969.[76] Reprinted with permission from AAAS.

In scattering experiments, the challenge of interpenetration and deformation of microgels in dense packings with the consequent influence on the form factor can be addressed by the use of small-angle neutron scattering (SANS). The groups of Schurtenberger and Richtering made use of the special contrast situation provided by SANS, probing dispersions consisting of deuterated and hydrogenated microgels with similar sizes. In the group of Schurtenberger a zero average contrast approach was applied to investigate single-particle properties in SANS. [78, 79] Here it was shown that weakly charged microgels with low cross linker density exhibit interpenetration processes at high packing densities. In contrast, ionic microgels tend to show deswelling and do not undergo deformations. Richtering and Scotti made use of microgel dispersions consisting of a majority of deuterated particles in D_2O, creating a crowded environment for the microgels, while the recorded signal in SANS is related to the spatially separated, hydrogenated microgels.[74, 80]

Therefore, the form factor of the microgels is only related to the hydrogenated microgels, providing information about microgel size and shape in dense packings. These studies revealed that the microgel morphology and stiffness, which is related to the crosslinker content, influences whether the particles exhibit deswelling or deformation. Small-angle scattering also provides structural insights into assemblies of microgels, especially for crystalline samples, where the high spatial correlation of particles results in pronounced structure factors, giving access to interparticle spacing and the crystal structure.[66, 73, 81, 82]

An important aspect for the investigation of microgels in dense packings is the influence of electrostatics. Here, one can distinguish between two classes of microgels. Microgels being only weakly charged or even considered as neutral, when charges are introduced by the initiator, and ionic microgels. Ionic microgels usually consist of a main monomer or an additional comonomer which features ionic groups like carboxylic acids, introducing the respective functionalities into the polymer network during the microgel synthesis.[21, 79, 83] These particles often feature pronounced responses towards external stimuli like ionic strength or pH, as well as a prominent ionic contribution in the interaction potential.[35] Regarding weakly charged and ionic microgels, Bergman et al. presented a system, consisting of PNIPAM-based microgels copolymerized with pH responsive acrylic acid.[83] Due to the carboxylic acid, the microgels are only weakly charged at low pH, where the acidic groups are protonated and charges are only associated to the initiator. For an increase in pH, the carboxylic acid groups are deprotonated and the microgels change into an ionic state with much higher charge density. It was found that the ionic strength of the dispersion has distinct influences on the morphology and size of the microgels in their respective ionic and only weakly charged state. In a recent study, Petrunin et al. investigated the influence of charges on the response of microgels towards crowded environments.[21] Similar to Bergman et al., the microgels' ionic character could be adjusted by pH. In the weakly charged state, the microgels' response towards the dense packing was moderate deswelling followed by faceting, while in the ionic state, the microgels show pronounced isotropic deswelling without getting into direct contact. Bocanegra-Flores et al. presented microgel dispersions, exhibiting crystalline structures at very low volume fractions and temperatures above the VPT, attributed to electrostatic interactions.[68] The microgels used in this study can be considered as only weakly charged, as ionic functionalities are only introduced by the initiator.

These studies show that microgel properties related to the presence of charges need to be considered when investigating their phase behavior.

In his work “Pathways and challenges towards a complete characterization of microgels” Scheffold stated that one of the challenges in the field of microgels is their characterization in dense packings.[11] The author explained that scattering methods exhibit limitations in respect to the characterization, especially for hybrid microgels and densely packed systems. These restrictions are mostly related to anisotropy, potential deformations of microgels and the challenge of a sufficient extraction of the form and structure factor contributions from scattering profiles recorded in dense packings.

The aim of this thesis was to actually make use of hybrid microgels in scattering experiments, creating special contrast situations in synchrotron small-angle X-ray scattering (SAXS), in order to investigate densely packed dispersions of microgels. These core-shell microgels are schematically shown in **Figure 1.4** and consist of a PNIPAM hydrogel shell and an inorganic gold or silica core.

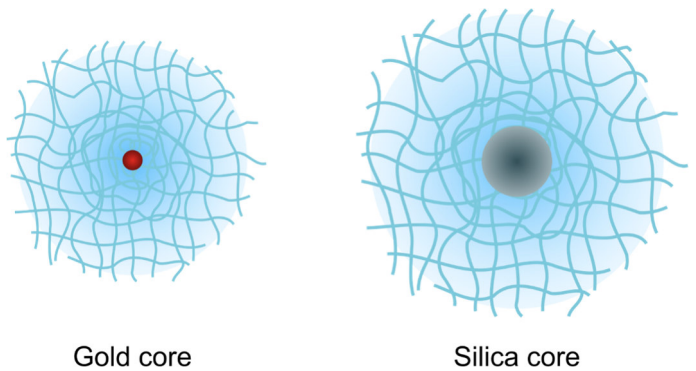

Figure 1.4 Schematic illustration of the core-shell microgels consisting of a PNIPAM shell and a gold (left) or silica core (right).

At dense packings, the core-shell microgels should self-assemble into colloidal crystals and express pronounced structure factors in SAXS. For the gold core-shell microgels the scattering of the gold core enhances the overall scattering intensity of the microgel. In addition, the form factor contribution of the gold core to the respective scattering profile dominates the form factor of the core-shell microgel and oscillations related to the shell are less pronounced.

Due to the less significant contribution of the microgel shell to the final scattering profile, the extraction of the structure factor recorded from core-shell microgels in dense packings is simplified, providing access to information about the particle assembly. One challenge for the investigation of microgels is the extraction of particle number concentrations and consequently accurate volume fractions. For the microgel system used in this work, the number of cores is accessible by the scattering intensity of the cores in SAXS. The microgels possess only a single core and therefore the number of cores in the dispersion equals the number of core-shell microgels. As a result, the particle number concentration of microgels becomes accessible, which is a quantity otherwise not easy to determine for microgels.

A similar system of core-shell microgels with cores consisting of silica instead of gold was also employed to study microgels in dense packings. Changing the core material from gold to silica maintained access to particle number concentrations via SAXS. Additionally, the larger shell size provided a more pronounced form factor contribution of the microgel shell to the scattering profile. The core-shell microgels formed colloidal crystals exhibiting multiple diffraction orders of Bragg peaks in SAXS. This indicates a high spatial correlation between the microgels which is typically found for crystalline structures. In this work, the high number of diffraction orders in the recorded scattering data, in combination with the narrow width of the Bragg peaks, even enabled the determination of the crystal structure and the domain sizes. For the silica core-shell microgels the form factor contribution of the polymer shell to the SAXS profile is much more pronounced than for the gold core-shell microgels. This is related to the larger size of the microgel shell and the lower contrast of the core material. The combination of narrow Bragg peaks and the low polydispersity of the core-shell microgels resulted in the presence of pronounced form factor oscillations. These are related to the microgel shell and even enabled form factor analysis of the core-shell microgels in dense packings. Due to the accurately modeled form factors, it became also possible to extract the structure factor from the scattering profiles.

The thermoresponsive properties of the core-shell microgels provide control over their volume fraction in the dispersion. In combination with the photonic properties of the crystalline samples, this enabled the investigation of the phase transition of the microgels between the crystalline and fluid phase, by temperature dependent absorbance spectroscopy.

These phase transitions can be induced by temperature, as the microgel shell collapses upon heating and thereby melting or crystallization processes can be induced. This is schematically shown by the core-shell microgels in **Figure 1.5**. At low temperatures and high-volume fractions, the microgels are in dense packings and form a crystalline phase while they undergo a transition into a fluid phase when temperatures are increased. The temperature dependent generalized volume fraction (ζ) of the core-shell microgels is shown in **Figure 1.5** and normalized to its value at 20 °C.

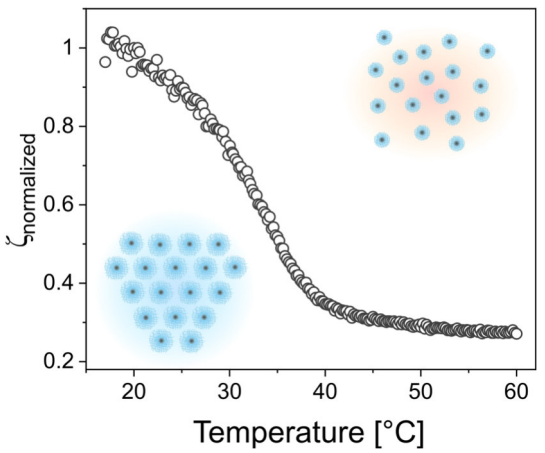

Figure 1.5 Normalized, generalized volume fraction (ζ) of the silica core-shell microgels as function of temperature. Schematic core-shell microgels in crystalline and fluid state are indicated at low and high temperatures, respectively.

Optical spectroscopy can be used as complementary method to SAXS for the investigation of colloidal crystals with photonic properties. The results of both methods can be compared quite well as they probe rather large sample volumes and provide insights into the phase behavior of the microgels. The investigation of the same samples via SAXS and optical spectroscopy even provides a direct relation between the domain sizes and spatial correlation of the crystalline samples and their optical properties. During the investigation of the phase transition of the core-shell microgels and their fluid phase, a certain electrostatic contribution to their phase behavior was found. The influence of electrostatics on the core-shell microgels was studied by comparing their phase behavior in absence and presence of salt.

Here, the ions introduced into the dispersion through the addition of salt are screening the charges of the microgels and reduce electrostatic interactions. Nevertheless, the core-shell microgels maintained colloidal stability above and below the VPT.

The influence of charge screening on the size and morphology of the microgels was studied by various scattering methods like SAXS, SANS and temperature-dependent DLS. Furthermore, temperature-dependent measurements of the electrophoretic mobility were conducted to investigate the electrostatic properties of the microgels. Concentrated dispersion with screened and unscreened charges in the crystalline (low temperature, swollen) and fluid (high temperature, collapsed) phase were studied by SAXS. Finally, due to the photonic properties of the samples, the influence of screening on the phase behavior of the core-shell microgels could be investigated by temperature-dependent optical spectroscopy. These measurements even enabled the preparation of a temperature-dependent phase diagram of the microgels. The phase diagrams reveal the significant influence of charge screening on the phase behavior of the microgels in dense packings. Due to the accessibility of the particle number concentration, the phase behavior could be presented as function of the generalized volume fraction. This might be a feasible base for theoretical and simulation based works in the future, which study the phase behavior of microgels.

2. Theoretical Background

2.1 Microgels

Microgels are a specific category of polymer-based materials, consisting of a three-dimensional, crosslinked polymer network exhibiting high internal solvent contents. The term microgels was first introduced by Baker in 1949, working on synthetic rubber, where he observed solvent swellable polybutadiene particles.[84] Microgels are discrete particles with average diameters between 20 nm and 50 µm consisting of various materials.[85] Currently, research mostly focuses on aqueous systems which are called hydrogels.[85] Furthermore, in comparison to polymers which get solvated under good solvent conditions, microgels form dispersions and swell to a certain extent, incorporating high amounts of solvent.[85] Due to their soft, polymeric nature, with high internal solvent contents and total dimensions up to several microns, microgels feature characteristics attributed to colloids, macromolecules and surfactants.[10, 12-16] Despite the most prominent example being crosslinked poly-*N*-isopropylacrylamide (PNIPAM) microgels, the variety of monomers and crosslinkers, even different types of crosslinking, provide great variability and a high degree of flexibility towards designing microgels for potential applications. Commonly, crosslinking of polymer-chains is achieved by two potential processes. Physical crosslinking, where the polymer-network is made of loops and entanglements between the polymer-chains. Ionic crosslinking which is a subsection of physical crosslinking. Here the polymers feature a certain polyelectrolyte-character and act as macroions, in which case oppositely charged ions or respective bifunctional molecules act as linkers between the polymer chains. The final type is covalent crosslinking, where polymer-chains are connected by covalent bonds. In microgel synthesis these bonds are often introduced by comonomers, described as crosslinkers, which exhibit two or more polymerizable units like vinyl, methacrylic and acrylamide groups. Microgel properties can be further tailored by adding additional comonomers during synthesis[37, 86-88] and even the initiator used to start the polymerization can influence the final properties of the particles.[89] With their high internal solvent content, leading to a generally soft behavior, microgels are often referred to as model colloids, to investigate soft particle interactions.[9, 35] This made microgels a prominent topic in interdisciplinary and fundamental research in the fields of polymer chemistry, colloid physics, material science and simulation focused computer science.[8, 11, 35, 90, 91]

2.1.1 Influence of Temperature on the Morphology of Thermoresponsive Microgels

Thermoresponsive polymers typically possess a lower or upper critical solution temperature (LCST/UCST). Critical solution temperatures describe how two substances can form a continuous phase and separate into two phases depending on the temperature and composition of the system. **Figure 2.1** shows a graphical illustration of the LCST- and UCST behavior based on a schematic phase diagram. The solid black lines indicate the miscibility gaps of the system. Here, the green and blue circles indicate the UCST and LCST, respectively. In the 1 phase state, both substances are miscible and form a solution. When the miscibility gaps are crossed due to changes in temperature or composition the solution undergoes a phase separation (2 phase state). The LCST or UCST marks the lowest or highest temperature where the phase separation can occur.[92]

PNIPAM is a LCST-type polymer, possessing a LCST at around 32 °C.[28] When the polymer is dispersed in water and the dispersion is heated above 32 °C, it undergoes a phase separation. The phase separation takes place on a microscopic level and is expressed by an increase in turbidity of the sample, rather than a separation in two continuous phases. This is often monitored by turbidity measurements and characterized by the cloud point.[93, 94]

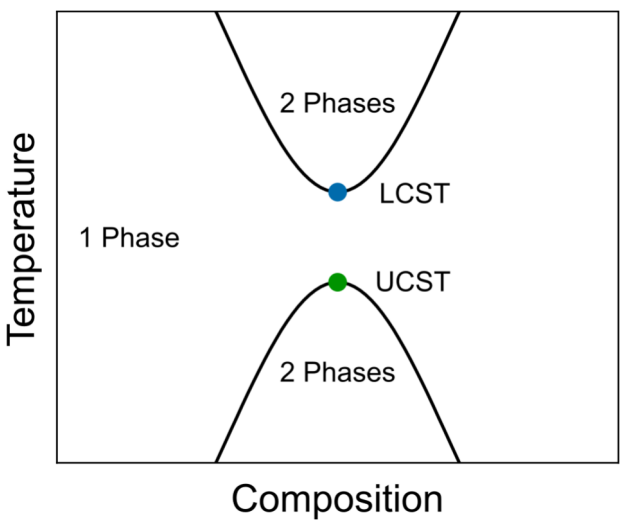

Figure 2.1 Schematic phase diagram illustrating LCST and UCST behavior as result of a miscibility gap.

For PNIPAM based microgels the thermoresponsive properties are usually characterized by the volume phase transition temperature (VPTT). The VPTT is defined by the temperature-dependent evolution of the microgels size. At low temperatures the microgels are in the swollen state with high internal solvent contents. Upon an increase in temperature and reaching the VPTT the microgels expel solvent and decrease in size. The temperature at which the microgel size reduction is most pronounced is defined as the VPTT. Therefore, by definition, the VPTT of a microgel differs from the LCST of a thermoresponsive polymer.

The reason for PNIPAM possessing a LCST in aqueous solution is related to its composition. With hydrophilic domains associated to the amide-groups and hydrophobic domains being the isopropyl group and the polymer backbone, PNIPAM exhibits an amphiphilic character. At low temperatures, water molecules hydrate the hydrophobic domains, lowering the entropy of the water molecules, while the system gains in enthalpy due to the formation of stable hydrogen bonds between the solvent molecules. This is called hydrophobic hydration. With the now “hydrated” hydrophobic domains, water molecules which do not participate in the hydration process possess high entropy inside the polymer network and microgels are able to incorporate large amounts of solvent.[95] When the temperature of the dispersion is increased above the LCST of 32 °C, the degree of hydration regarding the isopropyl groups is decreased. In contrast to the former dominating polymer-water interactions, polymer-polymer interactions are now favored. With the decrease in hydration, the entropy of the “free” water molecules inside the polymer network is decreased, forcing them to leave the system. This is accompanied by gains in enthalpy and the formation of polymer globule or regarding microgels, deswelling and collapsing. The water content of collapsed PNIPAM based gels is still around 50% and the system cannot be described as completely hydrophobic.[96] Therefore, PNIPAM does not undergo a transition from a hydrophilic to a hydrophobic material when heated above the LCST but rather becomes less hydrophilic compared to its behavior below the LCST/VPTT. In conclusion, the whole process is driven by a complex interplay between entropic and enthalpic processes, still not resolved to one hundred percent.

Alongside to PNIPAM based microgels, there are additional polymers exhibiting a LCST behavior in water, which are used for synthesizing microgels. Some of these polymers share similar molecular structures to PNIPAM. Examples being microgels consisting of poly-*N*-n-propylacrylamide (PNNPAM) with a VPTT around 21 °C[97] and poly-*N*-isopropylmethacrylamide (PNIPMAM) exhibiting a VPTT at approximately 44 °C.[97, 98] When the chemical structures of these polymers are compared to PNIPAM, the VPTT of the microgels shifts towards higher temperatures when the hydrophobicity of the microgels increases. The same trend can be observed for PNIPAM microgels with an increasing crosslinker content, shown in **Figure 2.2a**. Here, the normalized volume of a microgel is given as function of the temperature for nominal crosslinker ratios of 1 mol% (blue), 5 mol% (green) and 16 mol% (red) with regard to the monomer content. For an increase in temperature, the volume decreases and reaches a nearly constant value at high temperatures. The VPTT shifts from 32 °C to 35 °C, indicated by the dashed lines. This is a result of the increased crosslinker content of *N*,*N'*-methylenebisacrylamide (BIS), which increases the hydrophobicity of the microgel. An increase in the crosslinker content is also accompanied by a less defined VPT, as the decrease in volume is performed in a broader temperature section. It is also shown that the crosslinker content has a pronounced influence on the swelling capacity of the microgels. The particle volume is normalized to its value at 20 °C and upon heating a relative decrease of 92 % in volume is exhibited by the lowest crosslinker ratio of 1 mol%, while the microgels with a crosslinker ratio of 16 mol% only exhibit a decrease of 71 % in volume. A first theoretical approach to describe the swelling behavior of microgels is based on the classical binary Florey-Rehner theory.[99, 100] But even with modifications, when describing the swelling behavior of microgels, the model can suffer from difficulties in the interpretation of physical parameters.[101, 102] This is amplified by the versatility of microgels in terms of the composition with different comonomers, making the prediction of their behavior towards temperature even more challenging.

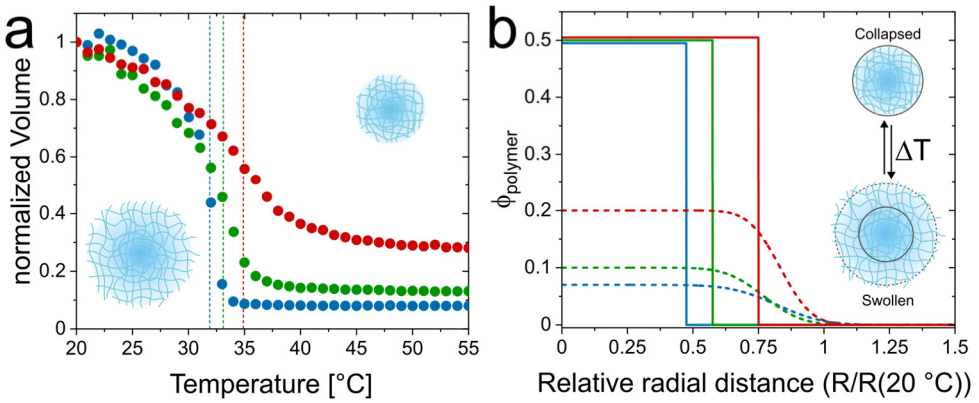

Figure 2.2 Influence of temperature on microgels. (**a**) Normalized volume as function of temperature for microgels with nominal crosslinker contents of 1 mol% (blue), 5 mol% (green) and 16 mol% (red). Volumes are based on temperature dependent dynamic light scattering measurements. Dashed lines indicate the respective VPTTs and normalization was performed with respect to the volume at 20 °C. Data was provided by Ben Pfeffing and Marius Otten. (**b**) Schematic radial density profile of the polymer volume fraction of microgels with different nominal crosslinker content in the swollen state (mixed dashed and solid lines, 20 °C) and the collapsed state (solid lines, 50 °C, assuming 50 % internal solvent content). Solid lines indicate the homogeneous center of the microgel and dashed lines are related to the inhomogeneous outer part possessing a pronounced decay in polymer density. Solid and dashed circles on the schematic microgels indicate the same section of the particle with respect to the given profiles. Profiles are based on the fuzzy sphere model.[9, 30]

When PNIPAM based microgels undergo the VPT, their morphology changes. In the swollen state, the center part of the microgel possesses a drastically higher polymer density than the outer part. This is a result of the faster consumption of the crosslinker (BIS), compared to the main monomer, during the precipitation polymerization.[25] Therefore, the microgels exhibit a gradient in crosslinking density towards the periphery of the particle.[25, 29-31] When heated above the VPTT, the microgel collapses and decreases in size, as solvent molecules leave the polymer network and a nearly homogeneous particle, in terms of its polymer density is formed. **Figure 2.2b** provides schematic density profiles where the polymer volume fraction ($\phi_{Polymer}$) is given in dependence of the radius, for microgels with increasing crosslinker content from low (blue) over medium (green) to high content (red) in the swollen (20 °C) and collapsed state (50 °C). The profiles were calculated based on the fuzzy sphere model[9, 30] and the values of $\phi_{Polymer}$ were approximated based on literature.[43]

Profiles referring to the swollen state consist of a solid and a dashed line section. The solid section is related to the more homogenous inner part of the microgel, while the dashed section indicates the decrease in $\phi_{Polymer}$ related to a decrease in crosslinker density. Schematic microgels in their swollen and collapsed state are shown in **Figure 2.2b** where the dashed and solid circles, indicate the respective section in the profiles. In the swollen state, some outer parts of the polymer chains are located outside of the dashed circle referring to dangling ends which nearly act as linear polymers. The density profiles referring to the collapsed state consist of a solid line and exhibit a clearly defined decay in polymer density at the respective radius of the collapsed microgel. Here, the microgels possess no gradient in polymer density and the dangling ends are collapsed on the surface of the particle. In conclusion, the microgel exhibits a gradient in polymer density in the swollen state and a rather homogenous structure in its collapsed state where it can be described as a homogenous sphere.[9, 103]

2.1.2 Core-Shell Microgels

Core-shell microgels usually consist of an inorganic or organic core and a microgel shell. The implementation of a core can provide further functionalities and provides possibilities to tailor the system. For example, microgels with a core and shell consisting of two different responsive polymers can be used to obtain an even more adjustable core-shell microgel. For example when both polymers are responsive towards temperature, but exhibit differences in their VPTT, the microgels can exhibit a unique two-step decay in their size as response to temperature.[104-106] Polymeric cores of non-water swellable or responsive materials, such as polystyrene are also encapsulated in microgels, being widely used in literature as model colloids to investigate particle assembly or rheological properties of dispersions.[67, 107] Inorganic core materials, like silica, iron-oxide, gold or silver can be introduced into core-shell microgels to provide magnetic, optical, plasmonic or catalytic properties.[48, 108-111] Silica particles provide cost-efficient and well established synthesis routes yielding monodisperse particles with good size control.[112-114] Encapsulation of a silica core in a microgel shell followed by dissolving the core yields hollow microgels with voids in the center of the particle.[115, 116] Due to their morphology, it is interesting to study the microgels response towards crowded environments, as they possess an increased potential for performing deswelling and deformation processes.[75, 117, 118]

For the investigation of microgels in crowded environments, core-shell microgels can also provide specific contrast situations for small-angle X-ray scattering experiments.

In this work, the PNIPAM shell acts as a low contrast spacer to guide potential assembly processes, while the inorganic core enhances the overall contrast of the particle. Furthermore, the thermoresponsive shell allows for precise control over the volume occupied by the microgels in dispersion, more accurately the volume fraction. This is especially beneficial for investigating microgels in dense packings.

Figure 2.3. schematically shows the synthesis of inorganic core and PNIPAM shell microgels, with silica (SiO_2) or gold (Au) as exemplary core materials. Both types of core particles were surface functionalized in order to increase the hydrophobicity of the surface and for silica cores to provide functional groups facilitating covalent bonding between core and microgel shell.[32, 59, 119] Here, NIPAM is the primary monomer and BIS acts as crosslinker in order to build the microgel shell. In general, the synthesis of thermoresponsive microgels is usually performed by precipitation polymerization, at temperatures above the LCST of the respective polymer. The reaction is started by the thermal initiator, potassium persulfate (PPS), incorporating negative charges in the polymer network. These provide colloidal stability even when the particles are in the collapsed state. For the encapsulation one can describe the reaction as seeded precipitation polymerization. It is presumed that oligomers which are already exhibiting LCST-behavior precipitate onto the hydrophobic cores, being the first step in the encapsulation process. The functionalized silica cores even provide polymerizable units on their surface which allow for covalent bonding between core and shell. From this point on, the shell starts to grow by further accumulating lower molecular weight oligomers on its surface as well as active chain-growth, accompanied by the formations of crosslinks by the consumption of free monomer and crosslinker. If the ratio between number of cores and monomer concentration is adjusted correctly, each inorganic core acts as seed for a single core-shell microgel.[119] This method provides high yields of core-shell microgels possessing single cores and fairly low number of pure microgels without cores. Exemplary TEM images are shown in **Figure 2.3b** and **c**.

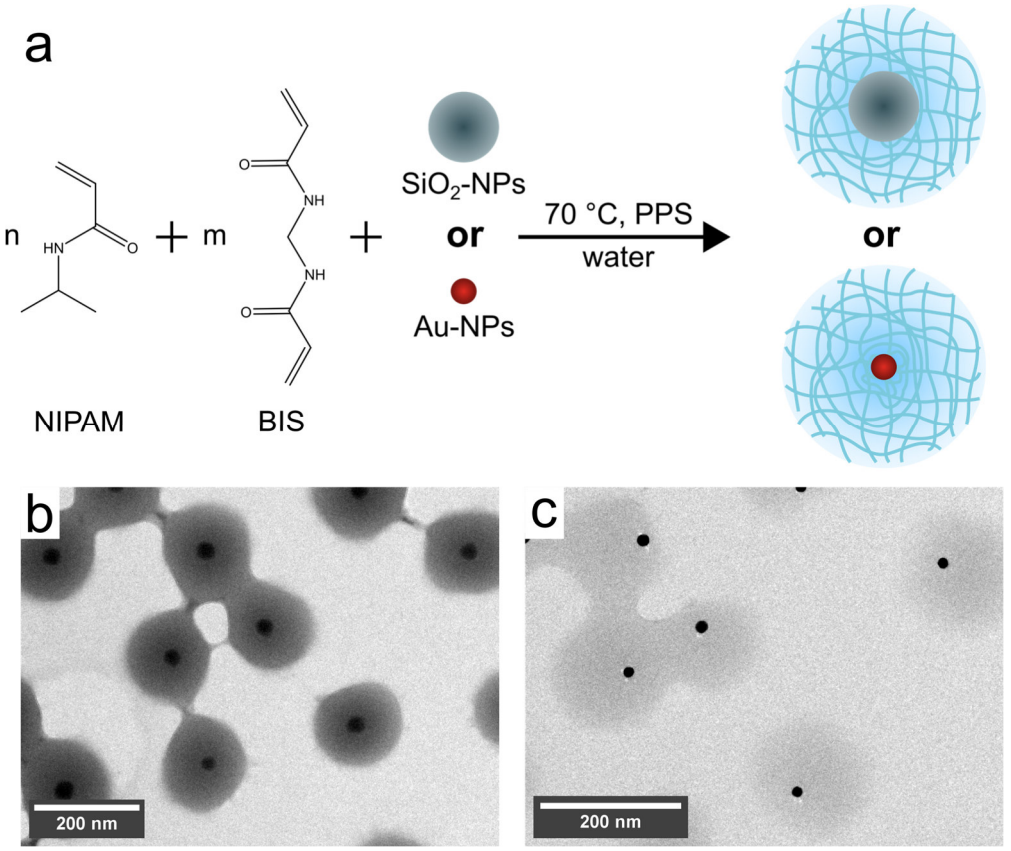

Figure 2.3 (**a**) Schematic illustration of the synthesis of core-shell microgel systems possessing inorganic cores, that were used in this work. (**b** and **c**) TEM images of silica and gold core-shell microgels with core diameters of 35 ± 3 nm and 13 ± 1 nm.

2.1.3 Microgels in Dense Packings

First insights into the phase behavior of colloids in dispersion are provided by the phase diagram of a hard sphere-like system shown in **Figure 2.4**, which is based on the work of Pusey and van Megen.[120] At low volume fractions (ϕ < 0.49), the dispersion is in a fluid, unordered phase as indicated by the blue spheres. From a volume fraction of 0.49, the system undergoes a transition towards the coexistence of a fluid and a crystalline phase (combination of blue and green spheres). Between volume fractions of 0.55 and 0.64 the system of spheres can form a crystalline or a glass phase (red spheres). Above a volume fraction of 0.64 up to the hard sphere limit of 0.74, only a crystalline phase is to be expected (green spheres). Therefore, the potential existence of crystalline structures can be expected when a dispersion of spheres exceeds a volume fraction of 0.49. Microgels being soft and deformable objects can express a different behavior than hard sphere-like colloids when placed into dense packings. The reason for this is their difference in the respective interaction potential. When hard particles are brought into contact, the interaction potential approaches infinity, which makes further compression impossible. Microgels express a soft interaction potential, which allows for compression which is characteristic for soft colloids. The phase behavior of microgels is investigated in 3D with concentrated dispersions of microgels in the bulk phase [43, 66, 80, 82] and also in 2D at interfaces.[58, 61, 117, 121] Due to their softness, microgels can be compressed above the maximum volume (0.74) or area fractions (0.91) being the upper limit for hard sphere-like systems.

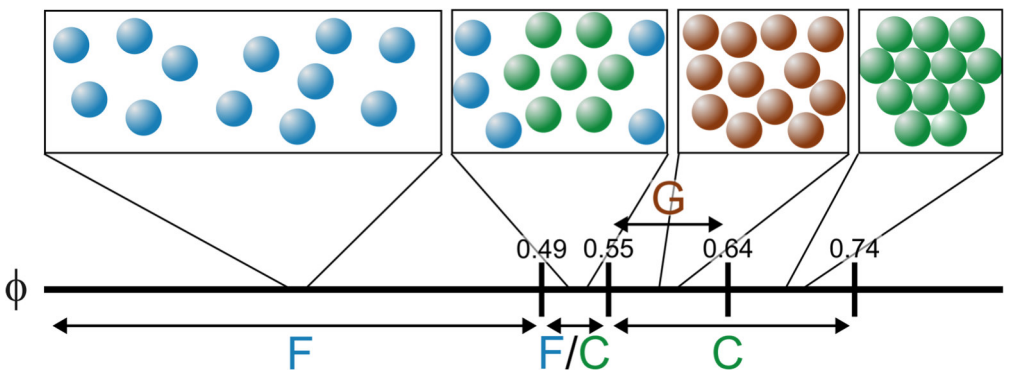

Figure 2.4 Schematic representation of the phase diagram for a dispersion of hard spheres. Blue spheres refer to the fluid phase, green spheres are related to the crystalline phases and the glass phase is indicated by red spheres.

For microgels, depending on the volume fraction of the dispersion, fluid and glassy phases were observed[122, 123] and in principle the phase behavior is comparable to hard sphere-like systems. Spherical microgels can also self-assemble into crystalline structures, which could be a primitive, body-centered-cubic (bcc), face-centered-cubic (fcc), hexagonally-closed-packed (hcp) or random hexagonally-closed-packed crystal (rhcp) structure for a monomodal system. Here the packing efficiency increases from primitive to fcc and hcp which are closed packed structures, with maximum packing efficiency for spheres. The closed packed crystal structures are shown in **Figure 2.5** with the indicated ABA (hcp) and ABC (fcc) stacking of hexagonal planes. In the top left of each stack a schematic unit cell of the respective crystal structure is shown. In literature, crystalline microgel dispersions often exhibit closed packed crystal structures, which might be attributed to the respective high packing efficiency.[59, 66, 71, 82] The interaction potential between microgels and the preparation of the obtained colloidal crystals has a distinct influence on the final structure of the dispersion. Very soft microgels, with a low degree of crosslinking, exhibited a bcc crystal structure[70], while for ionic microgels a coexistence between fcc and bcc structures was found.[69] These coexistence regions in the phase diagram were also indicated by computational simulations.[122] As the core-shell microgels discussed in this thesis feature a rather low core-to-shell ratio, a similar phase behavior to common microgels can be expected for comparable experimental conditions and nominal crosslinker contents.

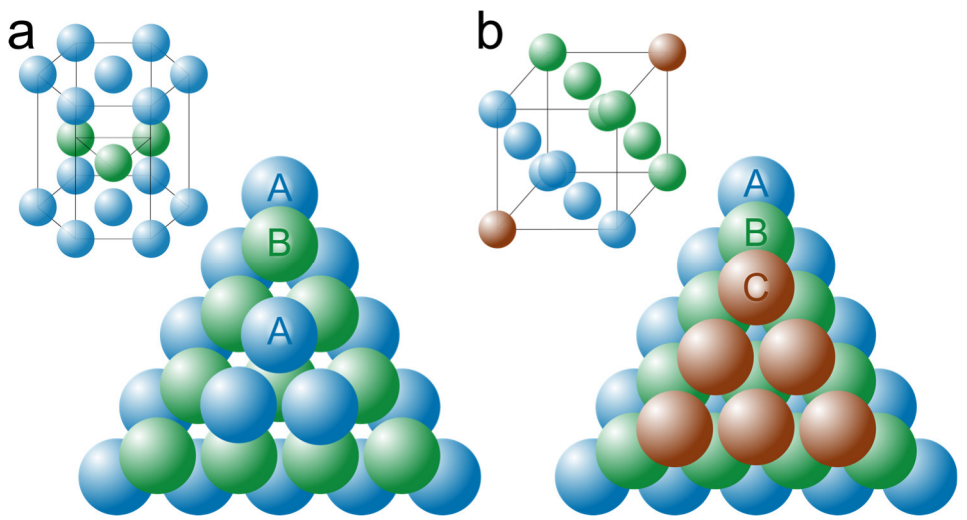

Figure 2.5 Schematic illustration of the closed packed crystal structures hcp (**a**) with its ABA stacking and fcc (**b**) with its ABC stacking of hexagonal planes.

In dense packings, microgels can undergo several processes which allow them to exceed the maximum packing fraction of hard spheres mentioned above.[118, 124] These processes are independent of the microgels being in a glassy or a crystalline phase and are shown in **Figure 2.6**. Here, a core-shell microgel colored in green is shown in its dilute state and surrounded by blue colored core-shell microgels in dense packings, expressing the respective response towards the crowded environment.[74]

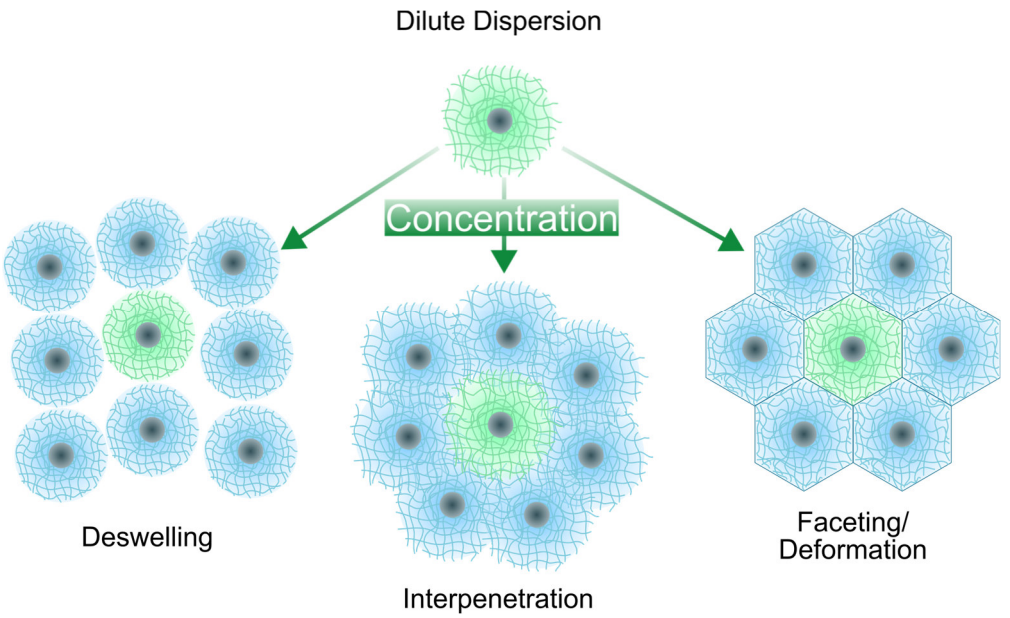

Figure 2.6. Potential responses of (core-shell) microgels towards dense packings. Deswelling (bottom left), interpenetration (bottom middle) and faceting or deformation (bottom right).

Microgels can undergo a deswelling process, reducing their total dimensions (**Figure 2.6** left). This is often referred to as osmotic deswelling, occurring when the bulk modulus of the microgels is exceeded by the osmotic pressure of the dispersion. Here, the bulk modulus of the microgels is related to their stiffness.[124] The increase in osmotic pressure can be ascribed to local concentration maxima of, for example, polymer or ions. At dense packings, the distance between microgels is drastically decreased and their periphery might begin to overlap, resulting in a local maximum of polymer concentration. Therefore, the polymer network responds with deswelling to resolve the local concentration maximum, as the microgels are not able to increase the average distance to their neighboring particles.

When the microgels possess charges, which are often incorporated by the initiator, this effect can occur, even before the microgels are in close contact with each other. Here, every microgel possesses an individual ion cloud and the overlapping of these ion clouds can also lead to local concentration maxima, increasing the osmotic pressure to a point where the microgels undergo osmotic deswelling.[125-127] If the microgels do not show deswelling in shell-to-shell contact, the particles might undergo interpenetration (**Figure 2.6** middle). The outer periphery of the microgels usually possesses a lower polymer density compared to the inner part of the particle. Therefore, these low-density regions of the polymer network can strongly overlap and the polymer networks can even interpenetrate each other.[78] When the microgels do not show deswelling or interpenetration under these conditions, they may exhibit changes in their shape. Withdrawing from their spherical shape, the microgels can facilitate higher packing efficiencies, accompanied by an increase in the polydispersity of the system. This process is considered as faceting or deformation (**Figure 2.6** right).[74, 128, 129] Due to these processes and their potential influence on the volume of the microgels one needs to distinguish between the real volume fraction occupied by the microgels ϕ and the generalized volume fraction ζ. The generalized volume fraction is solely based on the particle number concentration and the microgel size in the dilute regime. Therefore, the reduction of particle size, as consequence of an increase in particle concentration, is not considered.[80]

As a result of the explained processes and the size of microgels, the analysis of such systems in dense packings can become highly challenging.[11] Electron microscopy can be used to investigate such systems, but is mostly applied on dilute samples. In order to study microgels in dense packings and their swollen state cryo-electron microscopy techniques like cryo-scanning-electron-microscopy need to be apllied.[52, 130] If the particles possess a sufficient size, optical microscopy can also be applied to investigate microgels under these conditions.[76, 77, 128] This of course requires a certain size of the microgels and possibly super resolution microscopy techniques in addition to fluorescent-labeling. Here, super resolution microscopy even allows to resolve the deformation and interpenetration processes of microgels in dense packing.[76, 128] Without super resolution, faceting and interpenetration between particles make the investigation of microgels non-trivial, as both processes hamper the separate spatial resolution of particles.

In contrast to microscopy which directly provides real space images, scattering techniques are also widely applied to investigate microgels in dense packings, yielding results in reciprocal space with great statistics. In addition, scattering methods utilizing different types of radiation exhibit different contrast situations, making them highly versatile for investigating such customizable systems like microgels. More details on scattering methods regarding the investigation of colloidal dispersions are given in **chapter 2.2**.

Microgels are a beneficial system for studying the phase behavior of soft colloids. In the first place this is because of their variability, as softness, size, morphology and potential charges can be determined by the synthesis conditions and the addition of comonomers. Therefore, microgels are suitable systems for a broad range of experimental methods. The second and even more important fact is that dispersions of, for example, PNIPAM microgels can change their volume fraction as function of temperature. This allows for complex experiments where microgels can switch between phases and very low temperature changes can induce, for example, melting or recrystallization events within the microgel dispersion.[82, 131] With fast experimental methods like synchrotron small-angle X-ray scattering or microscopy techniques, microgels are an ideal model system to investigate the tunable phase behavior of soft colloids.

2.2 Scattering of Soft and Hard Colloids

Scattering methods are widely applied in colloid science to analyze the structural composition and properties of dispersions. When the scattering object is illuminated with an electromagnetic wave, the electromagnetic field induces an oscillatory motion in the electric charges of the scattering object. These accelerated electric charges radiate electromagnetic waves in all directions and this secondary radiation is called *scattered* radiation. If the energy of the incident radiation remains unaffected by the scattering process, it is classified as elastic scattering.[132]

The scattering vector $\vec{q}$ is introduced to quantify the direction of the scattered radiation which is based on the difference of the wavevectors of the incident radiation $\vec{k}_{\mathrm{in}}$ and the scattered radiation $\vec{k}_{\mathrm{out}}$.

$$\vec{q} = \vec{k}_{in} - \vec{k}_{out} \tag{2.1}$$

Figure 2.7 shows a sketch of the geometric definition of the scattering vector $\vec{q}$. The incident radiation ($\vec{k}_{\mathrm{in}}$) is scattered by a scattering center (blue sphere) into a direction ($\vec{k}_{\mathrm{out}}$) which is defined by the scattering angle *θ*.

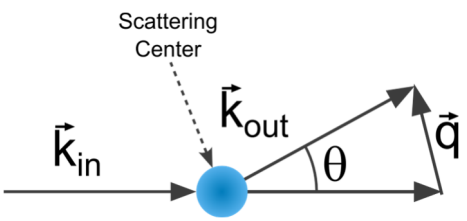

Figure 2.7 Construction of the scattering vector $\vec{q}$ based on the scattering angle *θ* and the wave vector of the incident ($\vec{k}_{\mathrm{in}}$) and scattered radiation ($\vec{k}_{\mathrm{out}}$).

The magnitude of the scattering vector $\vec{q}$ provides a quantitative measure for the length scale in a scattering experiment and is determined by the wavelength of the incident radiation *λ*, the refractive index *n* and the scattering angle *θ*. For SAXS and SANS experiments in this work, a refractive index of one was approximated and used to calculate q.

$$|\vec{q}| = q = \frac{4\pi n}{\lambda} \sin\left(\frac{\theta}{2}\right) \tag{2.2}$$

When a scattering object exceeds a certain size in respect to the applied wavelength, the scattering intensity becomes angle dependent. This is because of the scattering object being represented not by a single but multiple scattering centers which potentially show interference. For visible light, scattering objects exhibiting dimensions much smaller than the wavelength of the incoming radiation ($2R_{\text{scattering object}} < \lambda/20$), possess no angular dependency in terms of their scattering intensity and are classified as Rayleigh-scatterer. Here, the entire scattering object is considered as a single scattering center (**Figure 2.8**). In contrast, larger scattering objects consist of multiple scattering centers and exhibit distinct angular dependencies in their scattering intensity.[133]

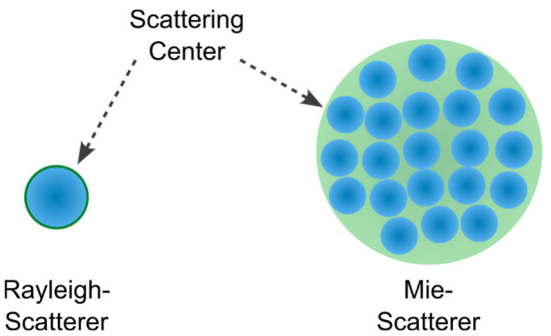

Figure 2.8 Schematic illustration of scattering objects consisting of one and multiple scattering centers. Blue spheres indicate scattering centers in the scattering object (green).

To describe the more complex situation of angle dependent scattering due to the distribution of multiple scattering centers in a single scattering object one can make use of a continuous density function $\rho(\vec{d}_{\text{SC}})$.

$$A(\vec{q}) = \int_0^\infty \rho(\vec{d}_{\text{SC}}) \exp(-i\vec{d}_{\text{SC}}\vec{q})\, d d_{\text{SC}} \tag{2.3}$$

Here, $\vec{d}_{\text{SC}}$ is the vector corresponding to the distance between scattering centers and $A(\vec{q})$ is the scattering amplitude. $A(\vec{q})$ is a measure for the scattering of an object consisting of multiple scattering centers. The microgels investigated in this work are of mostly spherical shape and as first approximation the scattering amplitude for a homogeneous sphere is given by:

$$A(q) = 4\pi R^3 \frac{\sin(qR) - qR\cos(qR)}{(qR)^3} \tag{2.4}$$

For a homogenous sphere, the scattering amplitude only depends on the magnitude of the scattering vector *q* and the radius of the sphere *R*. The scattering intensity I(*q*) is proportional to the square of the scattering amplitude. This is ascribed by the form factor P(*q*) which is typically used to describe the scattering properties of scattering objects. The form factor of a homogenous sphere is given by the Rayleigh-Debye-Gans approximation:[134]

$$P(q) = \left[3\frac{\sin(qR) - qR\cos(qR)}{(qR)^3}\right]^2 \tag{2.5}$$

Further, the total scattering intensity can be described by taking into account additional quantities like the contrast situation, number and volume of the scattering objects and potential structure factors. This is described by the following equation:

$$I(q) = NV^2 \Delta SLD^2 P(q) S(q) \tag{2.6}$$

With *N*, referring to the number of scattering objects in the probed volume. This volume is commonly described as scattering volume. *V* refers to the volume of the scattering objects. For X-rays or neutrons, the contrast difference between the scattering object and its environment can be described by the difference in scattering length density (*ΔSLD*). In the case of visible light, the contrast is related to the difference of the respective refractive indices. P(*q*) and S(*q*) correspond to the form factor and structure factor.

Figure 2.9 shows a schematic illustration of an ensemble of spherical scattering objects, consisting of multiple scattering centers. The scattering intensity I(*q*) as function of *q* and *R*, the radius of the scattering object, is shown as solid blue line. In addition to the form factor (P(*q*)) contribution, which is indicated by a solid green line, the scattering profile exhibits a structure factor (S(*q*)) contribution. For the sake of simplicity, the additional quantities (**Equation 2.6**) like particle number, volume and contrast are included in the form factor contribution. The structure factor contribution is indicated by the maximum around a *qR* of 3 in the scattering profile and the separated structure factor is shown as solid red line. While the form factor corresponds to the size and shape of the scattering objects, the structure factor is related to their spatial correlation and interparticle distance. For very dilute dispersions, the spatial correlation is usually very low and S(*q*) ≈ 1.

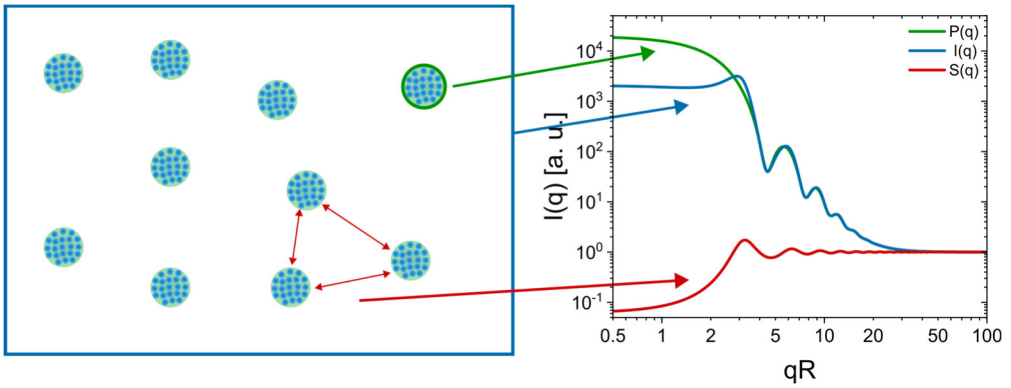

Figure 2.9 Schematic illustration of non-dilute dispersion of scattering objects and the respective scattering profile I(*q*) (solid blue line). Including the separated form factor P(*q*) (solid green line) and structure factor S(*q)* (solid red line) contributions. The form factor exhibits a size-polydispersity of 7.5 %.

In the following the form factor contribution to the scattering profile is explained in more detail before shifting the focus on the discussion of the structure factor.

As shown in **Figure 2.9**, the intensity of the form factor contribution (solid green line) is highly depending on *q*. At high *qR* the intensities are low, in the *qR* range between 4 to 20 multiple oscillations are present and a plateau with high intensity is reached at very low *qR*. Here, the position of the first form factor minimum is located at *qR* = 4.49. The progression of the scattering intensity at very low *qR* can be explained by **Equation 2.5**, as for *qR* tending towards zero P(*q*) = 1. Hence, the scattering intensity at very low *qR* can be considered as independent of the form factor and depends mostly on particle number, volume and contrast. At higher *qR* the scattering intensity is depending on *q*. The reason for this is that in the respective *qR*-regime, the scattering object cannot be described as a single scattering center and consists of a distribution of scattering centers (see **Figure 2.8**). Therefore, the phase relation of the scattered photons or particle waves changes, facilitating interferences which result in angle dependent scattering intensities.[133]

The form factor contribution to the scattering profile is also influenced by the size-dispersity of the investigated scattering objects. This is commonly observed in experiments as synthetic samples often possess some polydispersity. In order illustrate this, **Figure 2.10** shows the simulated scattering profiles for homogeneous spheres from low (blue) to high size-polydispersity (red) on the example of a Gaussian size distribution (**Equation 2.7**). Here, $\langle R \rangle$ is the average radius of the spheres in the distribution function and *R* corresponds to the radius of the individual spheres, while *σ* is related to the respective standard deviation.

$$D(R, \langle R \rangle, \sigma) = \frac{1}{\sqrt{2\pi\sigma^2}} exp\left(-\frac{(R-\langle R \rangle)^2}{2\sigma^2}\right) \tag{2.7}$$

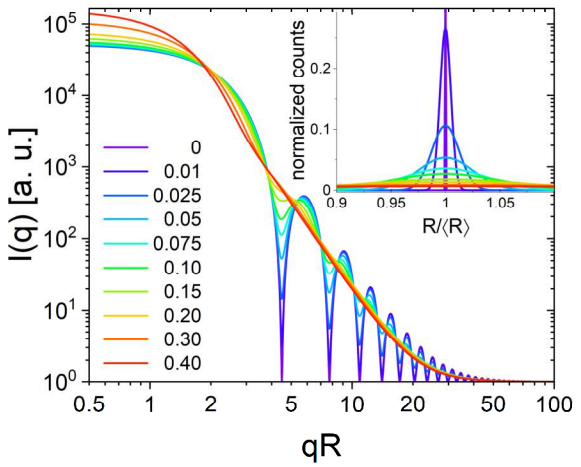

Figure 2.10 Influence of increasing size-polydispersity (*σ*) on the form factor (P(*q*)) of a homogenous sphere. The inset illustrates a selected section of the respective Gaussian size distribution.

For low polydispersity ($\sigma < 0.075$), the profiles indicated by violet to light blue color exhibit distinct and pronounced oscillations. When polydispersity is increased, the amplitude of the oscillations decreases and the respective form factor minima become less distinct (green to red profiles). For a standard deviation of approximately 0.2 (yellow profile), the form factor profile does not exhibit oscillations and the intensity follows a slope of q^{-4}. The increase in scattering intensity at low *qR* in the scattering profiles for systems with a high polydispersity is due to the size distribution being number weighted, while I(*q*) is intensity weighted.

This is provided by **Equation 2.6** and allows for the following relation between the size of a scattering object and its respective scattering intensity:

$$I(q) \propto R^6 \tag{2.8}$$

To study the scattering profile recorded from a dilute sample of scattering objects and extract information about shape and size, form factor analysis is applied. It is beneficial if the scattering profile exhibits some pronounced form factor oscillations which is usually the case for samples featuring low size-polydispersity. In some cases, scattering profiles do not exhibit these oscillations. This can be the result from either high polydispersity or a limited accessible *q*-range where the oscillations are not present. In this case, the Guinier approximation can give an impression on the scattering intensity $I(q)$ as function of q.[135] For a scattering object, the Guinier approximation is given in the following equation:

$$I(q) = I_{(0)} \exp\left(-\frac{q^2 {R_g}^2}{3}\right) \tag{2.9}$$

With R_g, the radius of gyration, being related to the center of mass of the scattering centers within the scattering object. Therefore, R_g does not provide direct access to the scattering objects dimension or shape, but R_g and the radius of a scattering object $R_{\text{scattering object}}$ exhibit fixed, shape dependent relations. For a homogeneous sphere, R_g is given by $R_g = R_{\text{sphere}}\sqrt{3/5}$.[135] In addition, the Guinier approximation is sufficient to describe the scattering intensity in the plateau-like section of the scattering profile at low qR.

The scattering objects investigated in this thesis are mostly microgels which need for more complex models to describe their scattering behavior. **Figure 2.11a** provides a comparison of scattering profiles based on two common form factor models which are used to describe the scattering properties of microgels. The profile of a homogeneous sphere is provided as reference. The *ΔSLD* profiles of the respective form factor models are normalized to the outer radius of the scattering objects and are given in **Figure 2.11b**. In the following, we want to describe and then compare these models beginning with the homogeneous sphere.

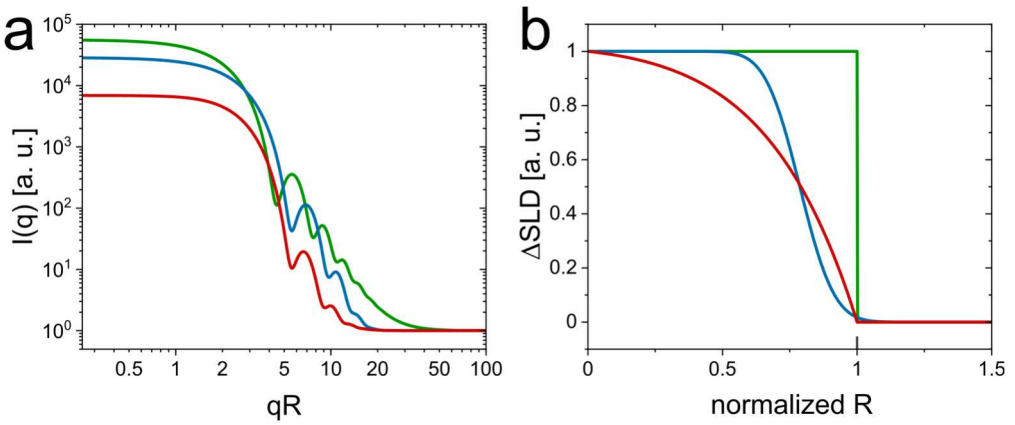

Figure 2.11 Form factors (**a**) and respective contrast profiles (**b**) referring to a homogeneous sphere (green), a fuzzy sphere (blue)[9, 30] and an exponential sphere model (red). In order to account for a realistic size distribution, size-polydispersity was set to 7.5 %. All scattering profiles are based on the same particle number concentration and total volume of the scattering object.

The homogeneous sphere model is indicated by a solid green line and does not ascribe for internal inhomogeneities of microgels. In contrast, **Figure 2.11b** shows that the fuzzy sphere model[9, 30] (FS-model, solid blue line) and the exponential sphere model (ExpS-model, solid red line) both account for a certain inhomogeneity in the *ΔSLD* profiles of the microgels.[29, 30, 103] The FS-model ascribes the gradient in density and the rather undefined periphery of a microgel by a constant *ΔSLD* section for the inner structure, followed by a Gaussian shaped decay of the *ΔSLD* profile. In the ExpS-model, the density profile follows an exponential decay, in order to simulate the potential internal structure of a microgel with high polymer density in the core and only low polymer density in the periphery. All three form factor models exhibit distinct oscillations but the first form factor minima of the FS- and the ExpS-model are shifted to higher *qR*, compared to the profile related to the homogeneous sphere. This is due to the increase in (polymer) density towards the center of the particle, as indicated by the respective *ΔSLD* profiles, shown in **Figure 2.11b**. The differences in scattering intensity between the profiles shown in **Figure 2.11a** are explained by the differences in the *ΔSLD* profiles, as the scattering profiles were calculated with the same particle number concentration. In conclusion, the homogeneous sphere model can only be used as a first approach to describe the experimentally recorded data but for a sufficient analysis more detailed models should be applied.

The FS- and the ExpS-model are well suited and widely applied form factor models, which provide a well description of scattering data recorded from microgels.[80, 129, 136]

After discussing the form factor contribution to the scattering profile, the focus is shifted towards the structure factor S(q). In **Figure 2.9**, the scattering profile (solid blue line) possesses a maximum in the scattering profile at a qR of 3. The origin of the maximum is a maximum in the radial distribution function, which is related to the structure factor (solid red line) by a Fourier transformation.[135] The simplest way to yield such a spatial correlation in an experiment, is to increase the number of scattering objects in the scattering volume and to reduce the interparticle distance to a point where a correlation can be detected. In most cases, the position of the first structure factor maximum is related to the interparticle distance between the scattering objects. The amplitude and width of the structure factor are related to the spatial correlation between the scattering objects. Therefore, structure factor maxima possessing a small width and high intensity correspond to a high spatial correlation. Crystalline structures are a common example for highly ordered systems which express sufficient long-range order. For unordered systems, like glasses or fluids a certain spatial correlation can be found at sufficiently high particle densities and short nearest-neighbor-distances.

In order to study the structure factor contribution in the scattering profile, it is often necessary to extract the structure factor from the scattering profile. This can be challenging as the position of the form and structure factor in terms of q are commonly very close to each other and can be superimposed. The extraction is often performed by dividing the scattering profile recorded in the concentrated state by a profile recorded int the dilute state. At sufficiently high concentrations the scattering profile $I(q)_{conc.}$ exhibits a structure factor while in the dilute state ($I(q)_{dil.}$) $S(q) = 1$. As shown in **Equation 2.10**, a scaling factor ($f_{scaling}$) is needed to account for the different number concentrations of both samples. It is notable that $I(q)_{dil.}$ can be exchanged with a sufficient form factor fit based on the respective scattering profile.

$$S(q) = \frac{I(q)_{conc.}}{f_{scaling}\, I(q)_{dil.}} \tag{2.10}$$

This is a convenient approach for scattering objects being unaffected by deformations, such as hard spheres, disks or rods where the form factor profile is independent of the packing fraction of particles. For soft particles like microgels, which are of major interest for this work, the form factor may change in dense packings as a consequence of deswelling or faceting.[74, 129] As a result, the extraction of structure factors from microgels in dense packings is particularly challenging.

Figure 2.12 provides the extraction of the structure factor regarding a crystalline (**a**) and a fluid (**b**) system, based on experimentally recorded scattering profiles from dispersions of core-shell microgels at temperatures of 20 °C and 40 °C.[131] Structure factors were extracted according to **Equation 2.10**. The crystalline system in **Figure 2.12a** exhibits more and distinct structure factor maxima compared to the fluid system in **Figure 2.12b**. This is due to the more pronounced structural correlation of particles assembled in crystalline lattices, compared to a fluid and unordered system where correlation is a matter of statistics. The relation between q, and the position of the structure factor maximum $S(q)_{max}$ is determined by the structural order of the system.

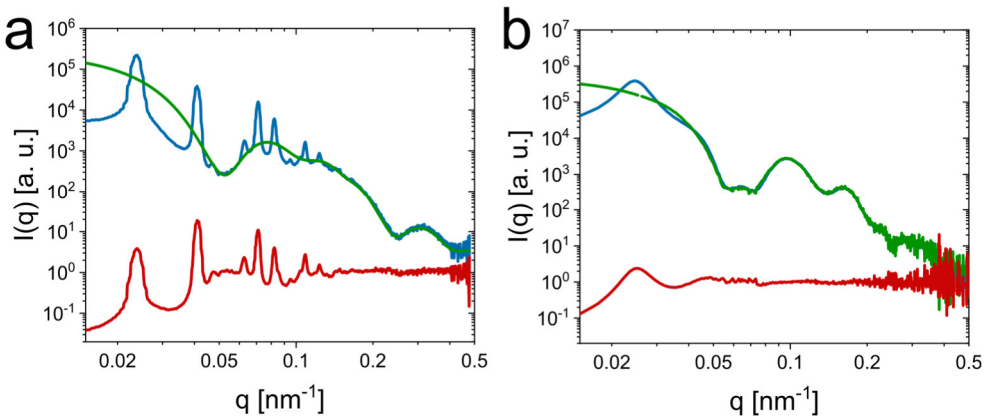

Figure 2.12 Structure factor (red) extraction from experimentally recorded scattering profiles (blue) of a crystalline (**a**) and fluid (**b**) sample of core-shell microgels recorded at 20 °C and 40 °C. The respective form factor (green) is based on a form factor fit. Data is adapted from Hildebrand et al.[131]

For a crystalline system, $S(q)_{max}$ is related to the distance *d*, between specific crystal planes defined by the miller indices *h*, *k* and *l* of the respective crystal lattice.

$$S(q)_{\max} = \frac{2\pi}{d_{\mathrm{hkl}}} \tag{2.11}$$

In case of an unordered system like a fluid or glass, the center-to-center distance between scattering objects can be approximated from $S(q)_{max}$ according to the following equation.

$$S(q)_{\max} = \frac{2\pi}{d_{\mathrm{c-c}}} \tag{2.12}$$

2.2.1 Small-Angle Scattering

The following chapter covers the fundamental setup of a small-angle scattering (SAS) experiment and a short explanation of how the choice of radiation can impact the experimental results. SAS methods can be applied on various disperse systems in a broad field of applications, for example in the fields of biological materials, polymers, colloids and nanocomposites.[135-140] In a SAS experiment, the intensity of the scattered or diffracted radiation is measured as function of the scattering angle θ, which is transformed into the magnitude of the scattering vector q (**Equation 2.2**). A schematic SAS setup is shown in **Figure 2.13** consisting of a beam generated by a polychromatic radiation source, followed by a monochromator. The monochromatic beam is collimated and focused on the sample. A collimator system is used to reduce the divergence of the beam, while an aperture is applied to control its shape and focus the radiation on the sample and detector. In SAS a 2D detector records the scattered radiation at multiple angles simultaneously, yielding a 2D scattering pattern. An experimentally recorded detector image is shown in **Figure 2.13** where form factor oscillations are present as pronounced rings of alternating high- and low intensities.

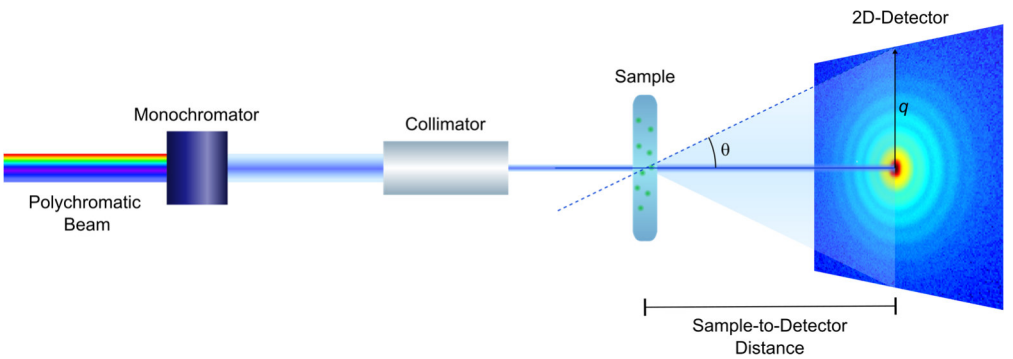

Figure 2.13 Schematic setup of a small-angle scattering experiment. Experimentally recorded SAXS 2D-pattern, indicating the 2D-detector, was recorded from a sample of core-shell microgels with silica cores provided by Arne Lerch.

Depending on the type of SAS, the beam consists of neutrons (SANS), electrons or photons in the range of X-rays (SAXS) to visible and near-infrared light (SALS). Beginning with visible light, conventional lasers and laser diodes provide monochromatic and coherent beams with a high photon flux, being well suitable for lab application due to their small sizes.

The provision of a sufficient neutron flux requires for large scale facilities which generate neutrons in nuclear reactors or spallation sources. Therefore, SANS is only available at scientific facilities like the Institut Laue-Langevin (ILL), the spallation neutron source (SNS) located in the Oak Ridge National Laboratory or the European spallation source (ESS). X-rays can be generated on laboratory scale with common X-ray sources like X-ray tubes or metal jet technology. Ultra-high flux X-rays combined with acquisition times in the millisecond time frame are only provided by modern synchrotrons, where the generated beam can exhibit excellent coherence, polarized light and high brilliance.[135]

The q-range accessible in a scattering experiment is the factor which determines the resolvable size-range of the investigated structures. According to **Equation 2.2**, the q-range can be defined by the wavelength of the applied radiation and the accessible range of scattering angles θ. In SAS, the range of recorded scattering angles can be adjusted by the sample-to-detector distance. This can also influence the instruments resolution in q. Therefore, SAXS and SANS can potentially resolve structures between a few nm up to several µm, highly depending on the instrument.[141, 142] Due to the influence of the applied wavelength on q, SALS operates in the same size domains as optical microscopy (0.8 to 80 µm), due to the longer wavelength of visible light (λ = 380-750 nm) compared to X-rays and neutrons (λ < 4 nm).

The applied type of radiation is also defining the contrast situation for the scattering experiment. While electrons, and photons exhibit interactions with the electrons of the respective materials, neutrons show interactions with the atom nuclei. For SAXS and SANS, the contrast is defined by the difference in the scattering length density (ΔSLD) between the scattering objects and the respective environment. The SLDs, in terms of X-rays are directly related to the electron density of the material. For neutrons, the SLDs depend on the strength of the interaction between the neutrons and the nuclei of the respective material which does not correspond to the elements position in the periodic table of elements.[135] The SLD can even vary between different isotopes of the same element. Hydrogen for example offers two drastically different contrast situations for the isotopes ^{1}H and ^{2}H (D). In SANS, this feature provides excellent contrast for hydrogenated samples dispersed in deuterated solvents and enables matching the SLD of a material for example in a H_2O/D_2O mixture.[79, 80] This becomes advantageous for samples consisting of different materials.

Regarding light scattering, contrast is defined by the difference of the refractive index *n* between the scattering object and the respective environment. For all contrast situations, the investigated sample must provide sufficient transmittance and therefore, the absorbance coefficient of the respective material needs to be considered.

Exemplary contrast situations in SAS for selected materials dispersed in H_2O, or dispersed in D_2O in case of SANS, are schematically shown in **Figure 2.14**. Each box is related to one material, where the color intensity of the inner circle refers to the contrast of the material compared to its respective environment, which is indicated by the excess area outside of the circle. In addition, the box is divided into three sections that are related to visible light (red, λ = 633 nm), X-rays (blue, λ = 0.12 nm) and neutrons (green, λ = 0.5 nm) as different types of radiation. Polystyrene and silica provide excellent contrast in light and neutron scattering as indicated by the strong color contrast between the inner circle and the outer part. This is due to their high refractive index and the large content of ^1H. Silica particles provide sufficient contrast for all types of radiation usually applied in SAS experiments.

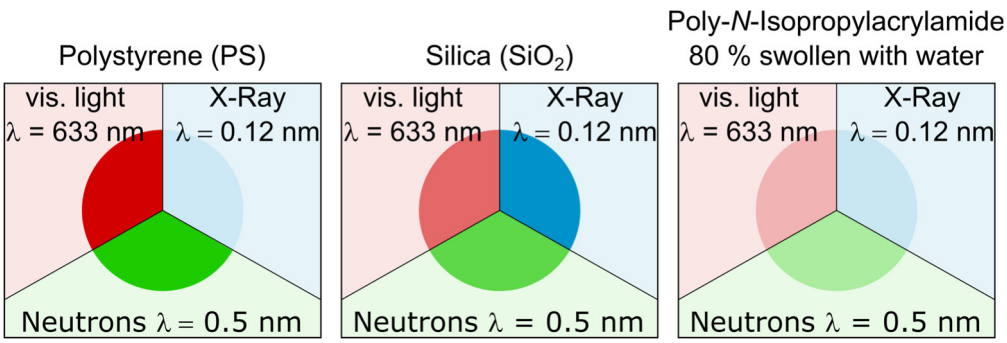

Figure 2.14 Exemplary contrast situations regarding polystyrene, silica and poly-*N*-isopropylacrylamide (swollen with 80 % mass content of water) with respect to H_2O or D_2O (neutrons), for different types of radiation: light (λ = 632 nm), X-rays (λ = 0.12 nm) and neutrons (λ = 0.5 nm).

As this work focuses on PNIPAM based core-shell microgels with silica cores, the contrast situation of PNIPAM microgels swollen with 80 % of H_2O, D_2O respectively, is also shown in **Figure 2.14**. Due to the high internal solvent content of the microgels, the contrast to the respective solvent is naturally decreased but still sufficient for the conduction of scattering experiments in all presented contrast situations. The displayed contrast situations show how hybrid particles, consisting of multiple materials can enhance the contrast and therefore the overall scattering intensity of a particle system for one specific or multiple scattering methods. In the case of SiO_2 core-shell microgels, the lower contrast of the swollen microgel is enhanced due to the presence of a core consisting of a high contrast material.

Especially for SAXS and SANS, the absolute scattering intensity of a sample can provide additional information about the investigated scattering objects. In order to record scattering data in absolute units, some sort of calibration is mandatory, for example with respect to glassy carbon. Here, a sample of glassy carbon with a defined thickness is used as reference, to calibrate a device for absolute intensity measurements.[143] For well-defined and homogenous particles with known composition and density, the particle number concentration becomes directly accessible through the scattering intensity, due to their direct correlation as shown in **Equation 2.6**. The extraction of the particle number concentration from scattering profiles recorded in absolute units can be performed according to following equation:

$$N_{\text{scat. obj.}} = \frac{I_{(0)}\, N_{\text{A}}\, \rho_{\text{scat. obj.}}{}^{2}}{M_{\text{scat. obj.}} m_{\text{scat. obj.}} \Delta SLD^{2}} \tag{2.13}$$

With Avogadro's number N_A, the density of the scattering object $\rho_{\text{scat. obj.}}$, $m_{\text{scat. obj.}}$ being the average mass of a scattering object and $M_{\text{scat. obj.}}$ its molecular weight. The scattering intensity at infinitely small q, $I_{(0)}$, is obtained from a Guinier analysis of the recorded scattering profile (**Equation 2.9**). To do so, it is necessary to exclude structure factor contributions in the q-range selected for the Guinier analysis of the scattering profile. When the particle morphology is more inhomogeneous, like for swollen microgels, with particle densities being hard to determine, absolute intensity measurements can give access to solvent contents and the actual polymer volume fraction within the microgel.[32]

2.2.2 Dynamic Light Scattering

After discussing small-angle scattering experiments and getting insights into form and structure factors, we want to focus on dynamic light scattering (DLS). DLS is widely applied as basic method, operating noninvasively, to obtain information about particle sizes on a length scale of a few nanometers to micrometers.[144, 145] There are devices offering simple conduction of measurements followed by automated analysis, and it is used as standard method in industry. **Figure 2.15a** shows the basic setup of a DLS system.

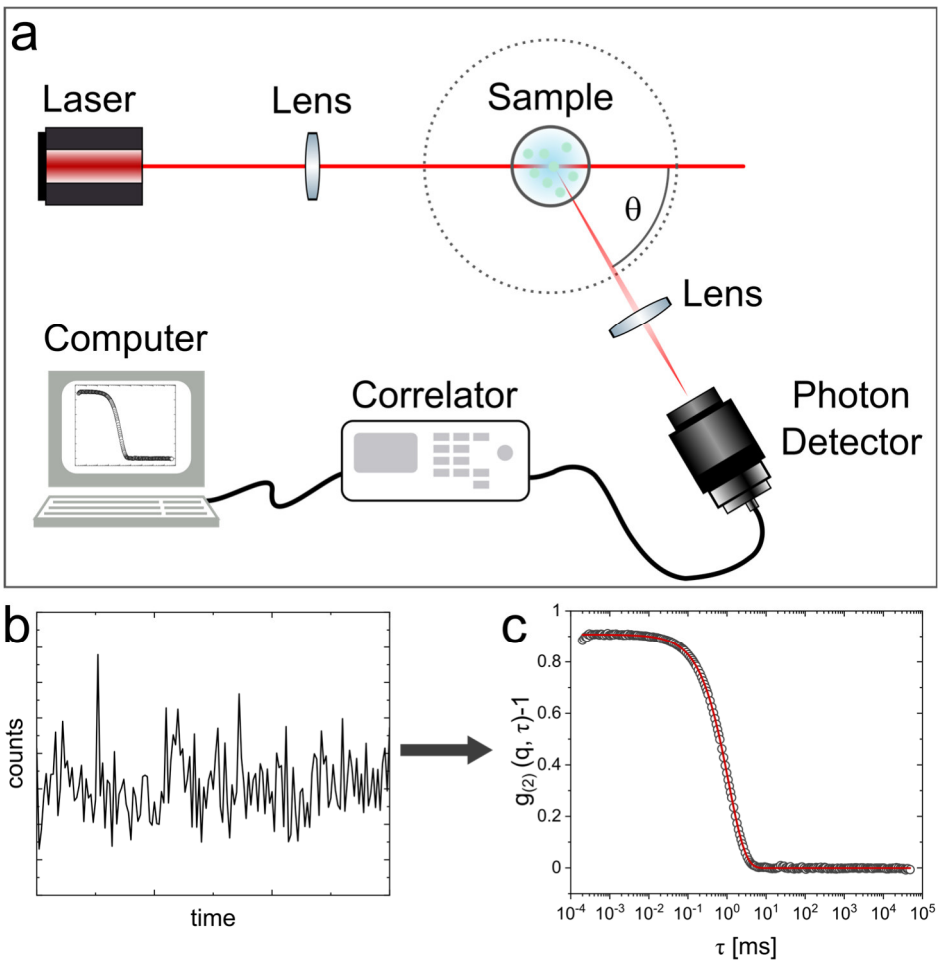

Figure 2.15 Schematic setup and procedure for DLS experiment. (**a**) Basic setup for a DLS measurement system. The ComponentLibrary by Alexander Franzen was used for this sketch.[146] (**b**) Intensity of the scattered light as function of time. (**c**) Normalized intensity-time autocorrelation function $g_{(2)}(q,\tau)$-1 as function of the delay time τ. The red line indicates a 2nd order cumulant-fit.

The laser beam is focused on a sample and the scattered light is detected by a photon detector. Usually, the scattered light is recorded at a fixed angle θ, but more versatile systems allow for angle dependent measurements. Independent of the angle, the measured scattering intensities are recorded as function of time and exhibit fluctuations (**Figure 2.15b**). These fluctuations are a result of the constant movement of the scattering objects in the probed volume, due to Brownian motion. When the interparticle distance changes, the phase difference between the light waves, emitted by the scattering objects is shifted. These phase shifts will cause alterations in the interferences between the propagating electromagnetic waves, influencing the measured intensities. The recorded fluctuations are transformed into a normalized intensity-time autocorrelation function $g_{(2)}(q,\tau)$ by a hardwire or digital correlator.

$$g_{(2)}(q,\tau) = \frac{\langle I(t)I(t+\tau)\rangle}{\langle I(t)\rangle^2} \tag{2.14}$$

Here, $I(t)$ and $I(t+\tau)$ are the respective scattering intensities at times t and $t+\tau$, with τ being the delay time. In principle, the autocorrelation function compares the evolution of the scattering intensity from the time t to following measurement points at $t + \tau$. A perfect correlation would reflect no changes of the intensity-time autocorrelation function over time. Here, the correlation would maintain a constant value of 1. Depending on how fast the scattering objects change in position, the correlation function will decrease, until reaching zero. Via the Siegert relation, one can convert the intensity-time autocorrelation function into the field-time autocorrelation function $g_{(1)}(q,\tau)$. Here, β refers to the intercept of the correlation function which is related to the dynamical contrast factor.

$$g_{(2)}(q,\tau) = 1 + \beta\left|g_{(1)}(q,\tau)\right|^2 \tag{2.15}$$

For monodisperse and isotropic scattering objects in dilute dispersion, $g_{(1)}(q,\tau)$ is following an exponential decay:

$$g_{(1)}(q,\tau) = \exp(-\Gamma\tau) \tag{2.16}$$

With the decay constant Γ and the magnitude of the scattering vector q, one can calculate the translational diffusion coefficient D_T of the dispersed particles according to the following equation:

$$D_T = \frac{\Gamma}{q^2} \tag{2.17}$$

From the diffusion coefficient, the hydrodynamic radius of the scattering objects can be derived based on the Stokes-Einstein equation:

$$R_{\mathrm{h}} = \frac{k_B T}{6\pi\eta D_{\mathrm{T}}} \tag{2.18}$$

With k_{B} referring to the Boltzmann constant, T being the absolute temperature and η corresponds to the dynamic viscosity of the dispersion medium.

However, the interpretation of DLS data is rather difficult as samples are often polydisperse and exhibit a certain size distribution, like for the intensity-time autocorrelation function in **Figure 2.15c** which is recorded from a microgel dispersion. Therefore, the measured autocorrelation function is a mean function of superimposed functions related to distributions of respective decay times $G(\Gamma)$ attributed to the size distribution of the sample.

$$g_{(1)}(q,\tau) = \int_0^{+\infty} G\,(\Gamma)\exp(-\Gamma\tau)\,d\Gamma \tag{2.19}$$

For a monomodal sample featuring some polydispersity, with a narrow size distribution, the method of Cumulants can be applied to analyze such data.[147] Basically, the Cumulant method uses a series expansion to describe the recorded autocorrelation function.

$$ln\left|g_{(1)}(q,\tau)\right| = -\bar{\Gamma}_1\tau + \frac{\mu_2}{2}\tau^2 - \frac{\mu_3}{3!}\tau^3 + \frac{\mu_4}{4!}\tau^4 \tag{2.20}$$

The mean value of the decay constant is defined by the first cumulant $\bar{\Gamma}_1$ and the second cumulant indicates the width of the decay constant distribution related to the actual size distribution of the scattering objects. A simplified approach to extract the decay rate and the second cumulant from the autocorrelation function is proposed by Frisken, with B being the baseline of the function:[148]

$$g_{(2)}(q,\tau) = B + \beta\exp(-2\bar{\Gamma}_1\tau)\left(1 + \frac{\mu_2}{2}\tau^2\right)^2 \tag{2.21}$$

The method of Cumulants reaches its limitations when the investigated sample is multi-modal and features more than one mean decay constant. Here, the CONTIN algorithm provides a numerical approach to describe the autocorrelation function and to extract decay constants, to a certain extend even for multimodal samples.[149]

In the following, the potential influence of the form factor on the results of a DLS experiment is explained using spherical particles as an example. In **Figure 2.16a**, the scattering intensity of spherical particles as function of the probed angle is shown in a polar graph for selected form factor radii ($R_{P(q)}$) between 10 and 500 nm. Scattering intensities in **Figure 2.16a** and **b** are both normalized to the Intensity at $\theta = 0°$ or infinitely small q. Small particles (< 20 nm, blue) exhibit Rayleigh scattering, as the scattering intensity remains constant at every angle, if:

$$particle\ diamter\ < \frac{\lambda}{20} \tag{2.22}$$

When the scattering objects increase in size ($R_{P(q)}$ > 50 nm, green to red), the scattering profiles show distinct oscillations which are ascribed to the form factor of the particles. In addition, the scattering intensity at higher angles is drastically decreased. This is also shown in **Figure 2.16b**, where the scattering intensities of the respective spherical particles are given as function of q. The grey section indicates the q-range which is accessible for typical DLS setups. Here it is important to note that the respective q-range highly depends on the respective wavelength of the laser (here 658 nm, θ from 10° to 176°) and the refractive index of the solvent used for sample preparation. It is shown that particles with $R_{P(q)} \leq 150$ nm are rather unaffected from form factor oscillations in the selected q-range because these oscillations are not present in the q-range of a DLS setup. The larger particles on the other hand exhibit pronounced form factor oscillations, which can potentially influence the result of a DLS measurement.

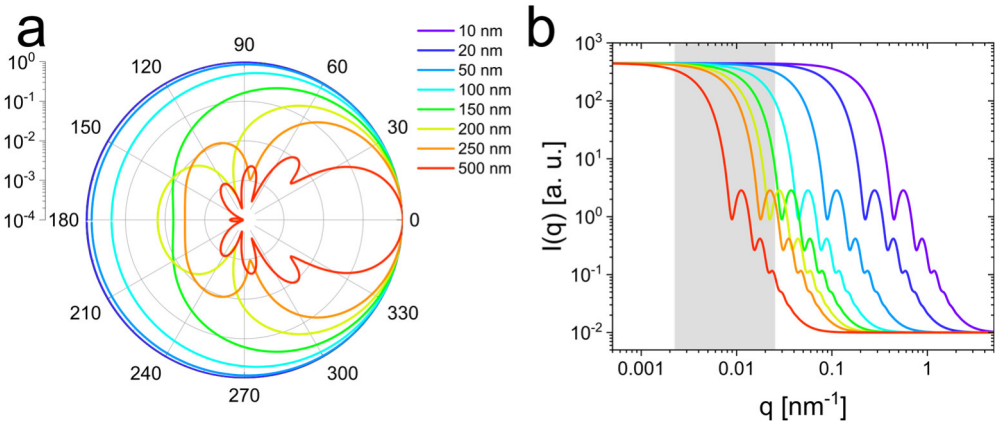

Figure 2.16 (**a**) Normalized (to an intensity of 1 at θ = 0°), polar graph for scattering profiles of hard spheres with increasing radius ($R_{P(q)}$) from 10 to 500 nm. (**b**) Respective, scattering profiles of hard spheres (size polydispersity of 0.075) as function of the scattering vector q normalized to an arbitrary scattering intensity at q = 0 nm^{-1}. The grey area indicates the q-range accessible based on a laser with a wavelength of 658 nm for θ from 10° to 176°. Graph in **a** is based on Mie scattering calculations conducted with the Mie scattering calculator by Scott Prahl.[150] The wavelength of the laser was 658 nm and the refractive index of sample environment was set to 1.332.

Due to scattering being intensity weighted, a small number of large scattering objects can easily dominate the recorded signal for a sample of small particles. Reconsidering **Figure 2.16**, the influence of a minority of large scattering objects on the DLS experiment is minimized at high angles where large scattering objects typically have low intensities. One can make use of this relation between angle-dependent scattering intensity and size, by investigating small particles at high angles. Here, potential larger aggregates possess a low scattering intensity and their influence on the DLS measurement can be minimized.

Performing a DLS experiment at a *q*-value close to the minimum of a form factor can have an influence on the results obtained from a DLS experiment. In **Figure 2.17** the form factor oscillations for a system of monodisperse hard spheres, at selected scattering angles are shown as function of the radius *R* (**Equation 2.5**). In contrast to the here presented form factor oscillations being related to monodisperse spheres, synthetic samples typically feature some polydispersity in their size distribution. The grey lines refer to mean particle radii of 150 and 280 nm, while the red area indicates a size distribution of 10%. This is a typical size range for microgels with a realistic size distribution.

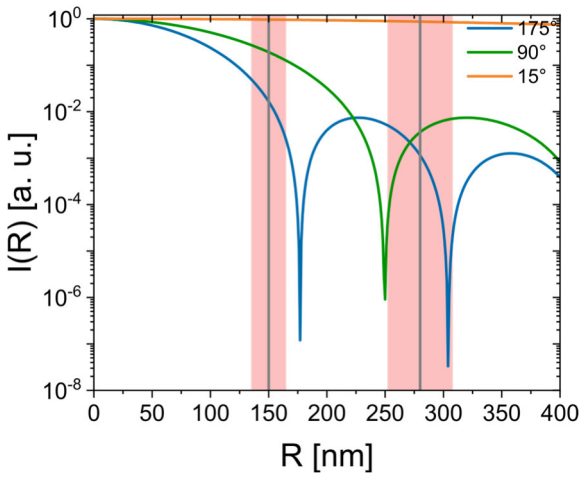

Figure 2.17 Form factor profiles of monodisperse hard spheres as function of the radius for selected scattering angles (λ = 658 nm and n = 1.332). Solid grey lines refer the radii of 150 and 280 nm with a size polydispersity of 10%, indicated by the red areas.

The results of the DLS measurement of the 150 nm particles should be rather unaffected by the selected scattering angle. This is due to the absence of form factor minima in the respective size range of the profile. This is different for the 280 nm particles, where the average radius of the sample is located close to a form factor minimum for scattering angles of 175° and 90°. For the potential measurement conducted at θ = 175° (blue), the scattering intensity decreases for radii larger than $R_{P(q)}$ = 280 nm, resulting in an underrepresentation of the larger fraction of particles for the detected scattering signal. Therefore, the hydrodynamic radius, obtained from the DLS measurement will be slightly smaller than the real R_h.

For θ = 90°, a form factor minimum is located at lower radii than the average particle radius and the scattering intensity of the smaller fraction of particles, within the respective size distribution, is expected to decrease. Therefore, the hydrodynamic radii obtained for the 280 nm particles will yield three slightly different values depending on the respective scattering angle. In comparison to the real R_h, the measurement conducted at 175° will yield a smaller R_h, while at 90°, the R_h will be larger. Only at 15°, for a monomodal sample without the presence of aggregates, the obtained R_h and the real R_h are expected to be the same.[144]

In conclusion, influences on the results of a DLS experiment in the discussed q-range, due form factor oscillations, can be avoided for particles with radii smaller than 150 nm. This is the case for the core-shell microgels discussed in this thesis, which possess a R_h of 147 nm at a temperature of 20 °C. When measuring the hydrodynamic radius of larger particles, these influences can be minimized by performing measurements at multiple angles. This becomes particularly important when the investigated particles, like many types of microgels, exhibit a responsive behavior towards external stimuli. For example, in the process of a temperature dependent DLS measurement, PNIPAM based microgels can undergo changes in their total dimensions over one magnitude. Because of the change in the radius of the microgels, the position of the form factor oscillations changes and might influence the obtained hydrodynamic radii at the respective temperatures. To measure the temperature dependent hydrodynamic radius of such samples one can make use of an angular dependent DLS setup. Via this method, the decay constant Γ can be determined for a high number of angles and plotted as function of q^2 (**Equation 2.17**). Consequently, the diffusion coefficient and the hydrodynamic radius can be extracted based on the measurements performed at multiple angles. This minimizes the potential influence of form factor minima on the measurements and results in reliable data.

3. Synopsis

In this work, core-shell microgels were used to investigate the phase behavior of soft colloids in dense packings. Synchrotron small-angle X-ray scattering (SAXS) is an excellent and fast method to receive insights into such colloidal assemblies, providing great statistics by probing a high number of particles simultaneously. Studying microgels in dense packings via SAXS is accompanied by three challenges. First, the separation of the structure factor from the scattering profile, which is challenging due to the form and structure factor contributions being superimposed. Secondly, the determination of the exact volume fraction and particle number concentration of the microgels which is of high importance when investigating their phase behavior. The third challenge is to gain insights in the response of microgels towards dense packings. Here, microgels can undergo several processes like deswelling, interpenetration and deformation.[118, 129] This information is provided by the form factor contribution to the scattering profile of the microgels recorded in dense packings. Furthermore, the extraction of the form factor contribution can also be beneficial for the successful separation of the structure factor from the recorded scattering data.

The first two challenges are addressed in the first publication (*SAXS Investigation of Core–Shell Microgels with High Scattering Contrast Cores: Access to Structure Factor and Volume Fraction*[81]), which contributes to this thesis. Here, a core-shell microgel system with a small gold core which possesses high contrast towards X-rays and a PNIPAM shell exhibiting low contrast was employed to study microgels in dense packings. At first the motivation behind this was related to the preparation of self-assembled plasmonic structures in bulk. Therefore, the aim was to prepare colloidal crystals and to get insights into the spatial correlation of the scattering centers, presumably the gold cores, in these assemblies. The recorded scattering patterns show up to three diffraction orders and surprisingly narrow Bragg peaks. These findings indicate a high spatial correlation of the gold cores which correspond to the cores being well positioned in the center of each microgel. Here, the shell guides the assembly process and acts as spacer between the gold cores, which also minimizes the superposition between form and structure factor oscillations as shown in **Figure 3.1**. In the low q-regime ($q < 0.09$ nm^{-1}), the scattering profile exhibits distinct structure factor maxima and no significant form factor oscillations can be detected. This facilitated the analysis of the structure factor and was the first approach to address the separation of the structure factor from the scattering profile.

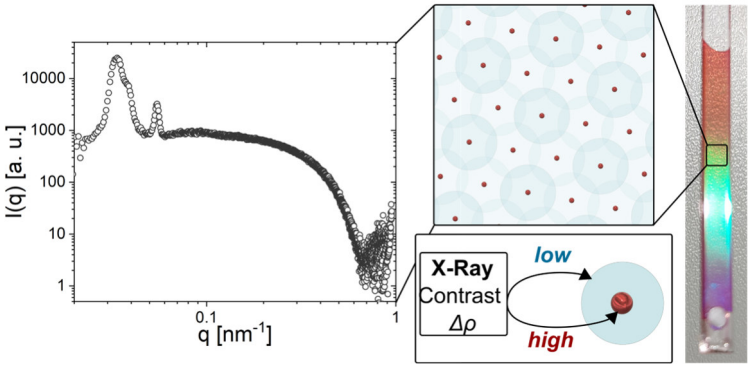

Figure 3.1 Table of contents figure from "SAXS Investigation of Core–Shell Microgels with High Scattering Contrast Cores: Access to Structure Factor and Volume Fraction"[81] From left to right: Exemplary scattering profile recorded from a dispersion of core-shell microgels in dense packing. Schematic illustration of core-shell microgels in a hexagonally ordered structure and the respective contrast situation of the particles regarding X-rays. Digital photograph of a core-shell microgel dispersion in a capillary used for SAXS measurements.

The second challenge regarding the determination of the volume fraction could be addressed due to the presence of the gold cores. These cores enabled the determination of the ratio between the mass content of core-shell microgels in dispersion and the respective particle number concentration *N*. According to **Equation 2.6**, the scattering intensity of the cores is directly proportional to the number of particles in the respective probed volume. When SAXS is measured in absolute units the number of cores (N_{core}) contributing to the scattering can be calculated with **Equation 3.1**, based on the scattering intensity I_0 at infinitely small *q*. Here, the core needs to show a pronounced form factor contribution that allows for a separate form factor analysis to extract $I_{(0)}$ from the recorded scattering profile. Therefore, the form factor oscillations of the core and the shell need to be separated with respect to *q*. This is limited by the size-, respectively the volume ratio between the core and shell of the core-shell microgel.

$$N_{\mathrm{core}} = \frac{I_{(0)}\, N_{\mathrm{A}}\, {\rho_{\mathrm{core}}}^2}{M_{\mathrm{core}}\, m_{\mathrm{core}}\, \Delta SLD^2} = N_{\mathrm{core-shell\ microgel}} \tag{3.1}$$

With the AuNP core density ρ_{core}, N_A Avogadro's number, M_{core} the molecular weight, m_{core} the mass of the core and ΔSLD the scattering length density differences.

This procedure is only possible because the core consists of a homogeneous material with a known density. Due to the vast majority of microgels possesses one single core, the number of cores equals the total number of particles. Therefore, this core-shell microgel system provides direct and easy access to particle number concentrations.

Based on the promising results from the gold core-shell microgels, the aim of the second publication (*Fluid-solid transitions in photonic crystals of soft, thermoresponsive microgels*[131]) was to improve the long-range order of the assemblies and to get insights into the response of the microgel shell towards the crowded environment. Synchrotron SAXS was used to record scattering profiles which possess structure factors with narrow Bragg peaks and pronounced form factor oscillations. The core-shell microgel system was modified in terms of core material and size, while maintaining a comparable core-to-shell size-ratio. Therefore, the advantages of the core-shell system, like the accessibility of particle number concentration, could be maintained. To increase the contribution of the microgel shell to the scattering profile in SAXS, the size of the shell (swollen state) was increased from an R_h of 105 nm to an R_h of 147 nm with respective core sizes of 6.5 nm and 18 nm. For a more feasible control over the core size, the material was changed from gold to silica. A comparison of the scattering properties of both core-shell microgels in SAXS is shown in **Figure 3.2**. The scattering profiles were simulated to facilitate a comparison of both core-shell microgels over a broad *q*-range and similar particle number concentrations. However, the parameters used to simulate the scattering patterns were obtained from form factor analysis of experimentally recorded SAXS profiles.[81, 131] The contributions of the core and shell to the scattering profiles are indicated by dashed and solid arrows. Shifts in the position of the form factor oscillation correspond to shifts in the different radii. For the silica core-shell microgel the contribution of the shell to the scattering profile is significantly increased and form factor oscillation are more pronounced. This was expected to be beneficial for investigating the response of the microgel shell towards dense packings and therefore adressing challenge number three.

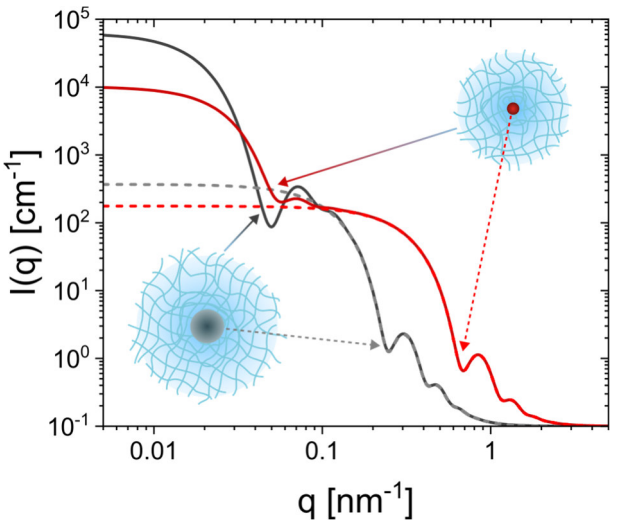

Figure 3.2 Comparison of the simulated scattering profiles of core-shell microgels in SAXS. Scattering profiles of the core-shell microgels (solid lines) in dilute state (T= 20 °C) and the respective core contribution (dashed lines) for gold (red) and silica (grey) as core materials. The profiles exhibit the same number concentrations and are simulated based on parameters obtained from the form factor fits of the respective core-shell microgel.[81, 131] Arrows indicate the first form factor minima of the microgel shell (solid arrows) and the core (dashed arrows) in the scattering profiles.

In order to record more pronounced structure factors in SAXS, the long-range order and the domain size of the colloidal crystals needed to be increased. Therefore, an annealing procedure with low cooling and heating rates of 1.5 K/h was employed to prepare colloidal crystals from the silica core-shell microgels. The self-assembled microgels exhibit multiple diffraction orders of narrow Bragg peaks in SAXS as shown in the detector image in **Figure 3.3a**. This underlines the success of the annealing procedure. The multiple diffraction orders in the SAXS pattern also enabled a detailed analysis of the domain sizes, lattice constants and crystal structure (hexagonally closed packed) of the colloidal crystals. The SAXS profiles recorded from crystalline assemblies of core-shell microgels show pronounced from factor oscillations associated to the microgel shell. Due to the narrow width of the Bragg peaks, these oscillations enabled a detailed form factor analysis of the core-shell microgels in dense packings. As response towards the dense packing, the microgel shell was found to undergo isotropic osmotic deswelling, before interparticle contact. This was associated to pronounced electrostatic interactions and the presence of an ion cloud possessing larger dimensions than the core-shell microgel.

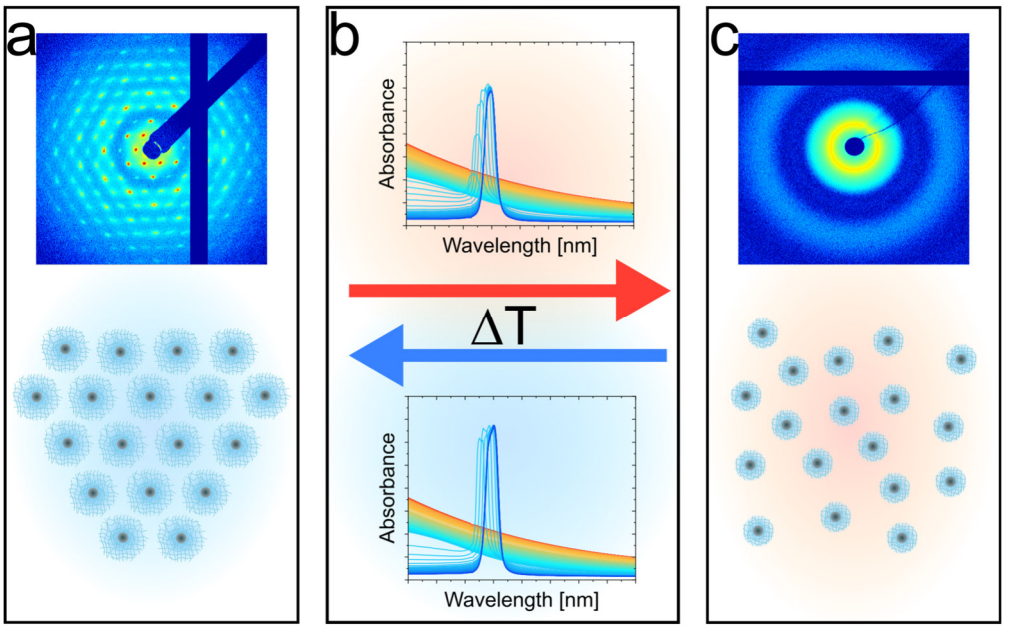

Figure 3.3 Modified table of contents figure from "Fluid-solid transitions in photonic crystals of soft, thermoresponsive microgels" [131] (**a**) Scattering pattern recorded from dispersions of core-shell microgels below the VPTT, forming a crystalline phase as indicated by the scheme of hexagonally ordered core-shell microgels. (**b**) The transition between fluid and crystalline/solid phases is shown by temperature dependent Vis-NIR spectra. (**c**) Scattering pattern recorded from dispersions of core-shell microgels above the VPTT, forming a fluid phase as indicated by the scheme of unordered and collapsed core-shell microgels.

In addition to SAXS, the photonic properties of the crystalline samples were utilized to study the phase behavior of the core-shell microgels. With lattice constants close to the wavelength of visible light, the samples possess narrow Bragg peaks in Vis-NIR absorbance spectroscopy which is shown by the blue curves in **Figure 3.3b**. The Bragg peaks can be used as indicator for the presence of crystalline structures in the investigated sample volume. Here, both methods are probing rather large sample volumes and provide representative insights into the phase behavior of core-shell microgels, which was further investigated with temperature-dependent optical spectroscopy. The decrease in Bragg peak intensity, followed by a complete disappearance, as response to an increase in temperature (blue to red color transition), is related to a phase transition of the dispersion between the crystalline and fluid phase.

The reversibility of the transition is shown by the spectra in **Figure 3.3b** for the heating (top) and cooling (bottom) process. Due to the thermoresponsive properties of the PNIPAM shell, the increase in temperature is accompanied by a decrease in size and respectively volume fraction of the core-shell microgels in dispersion. At a certain volume fraction, the packing density is no longer high enough to maintain the crystalline structure and the dispersion undergoes a phase transition. The crystalline and fluid phase are indicated by the schematic core-shell microgels in **Figure 3.3a** and **c**. This process can be followed by absorbance spectroscopy and the transition volume fraction was found to be at $\zeta = 0.45 \pm 0.05$. Therefore, thermoresponsive microgels are an ideal system to study the phase behavior of soft colloids, as the volume fraction can be controlled by temperature. The complete transition into the fluid phase was proven by additional SAXS measurements, performed at elevated temperatures, where the core-shell microgels are in the collapsed state (**Figure 3.3c**).

The analysis of the structure factors recorded from core-shell microgels in their collapsed state at dense packings (**Figure 3.3c**) and the osmotic deswelling before interparticle contact indicated the presence of a pronounced electrostatic contribution to the phase behavior of the microgels. This is related to charges being incorporated into the core-shell microgels during the synthesis, primarily by the radical initiator potassium persulfate. The third publication (*Temperature-dependent phase diagrams of weakly charged, thermoresponsive microgels under charged and charge-screened conditions*) focuses on the electrostatic contribution to the phase behavior of the core-shell microgels. Therefore, the influence of charge screening on the microgels in dense packings was studied. To achieve this, salt (0.5 mM potassium chloride, KCl) was added to the microgel dispersions increasing the concentration of ions and reducing the effective electrostatic interactions between the microgels. In order to ensure a successful screening of charges, the electrophoretic mobility of the microgels was recorded, revealing a drastic decrease in the electrophoretic mobility of the microgels in the swollen state. Core-shell microgels in the dilute state were investigated for the influence of salt on the size or morphology. Therefore, various scattering techniques like small angle neutron and X-ray scattering, as well as static and dynamic light scattering were applied. Here, the core-shell microgels show similar dimensions and an influence of the presence of salt on the morphology could not be detected.

SAXS and optical spectroscopy were used to study the potential influence of charge screening on the phase behavior of the core-shell microgels in dense packings. The recorded SAXS patterns and profiles indicated that the charge screening resulted in a shift of the phase boundary between the fluid and crystalline phase towards higher volume fractions. With exception of this shift, the core-shell microgels, in their swollen state, behave similar in the unscreened and charge-screened state. In both states the crystalline samples show SAXS patterns with high diffraction orders of Bragg peaks. Form factor analysis of the respective SAXS profiles showed that the core-shell microgels feature similar dimensions in these dense packings, independent of charge screening. At elevated temperatures, the collapsed microgels were in a fluid phase and the recorded structure factor was analyzed with a hard-core one-Yukawa-potential.[151, 152] The influence of charge-screening on the interaction potential is shown in **Figure 3.4**. Here, the length of the interaction potential *L*, reveals a significant influence of charge-screening on the effective interaction radius of the core-shell microgels. In absence of salt (red) the potential features a higher potential strength and length which is drastically reduced when charges are screened (black). It is likely that this reduction in the effective interaction radius is the reason for the shift in the phase boundaries found for the core-shell microgels in their swollen state. It can be assumed that this effect is less expressed in the swollen state of the microgels, where the charge density is slightly lower due to the larger dimensions of the particle.

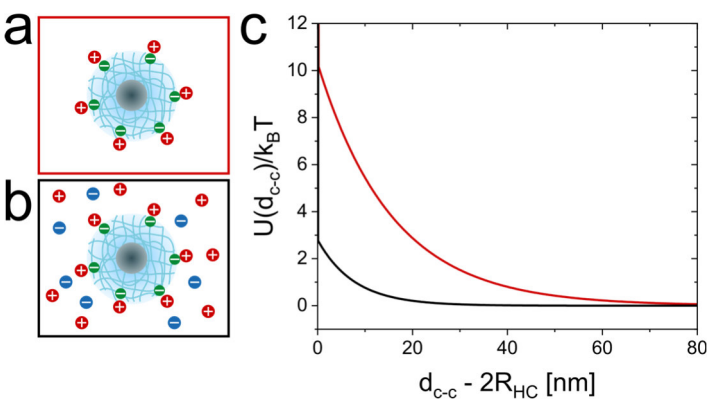

Figure 3.4 Schematic illustration of the collapsed core-shell microgels in the unscreened (**a**) and charge-screened state (**b**). The position and number of charges serves only as schematic illustration and is not based on experimental results. (**c**) Interaction potential (one-Yukawa potential[151]) as function of the interparticle spacing ($d_{c\text{-}c} - 2R_{HC}$) for silica core-shell microgels in the collapsed state for the unscreened (red) and charge-screened state (black).

Similar to the previous work, the photonic properties of the colloidal crystals enabled the investigation of the phase behavior via optical spectroscopy. Therefore, temperature-dependent Vis-NIR spectroscopy gave insights on the influence of charge-screening on the phase transition between crystalline and fluid phase. In order to investigate a broad range of volume fractions, a concentration series of core-shell microgels was prepared and the respective temperature regions where the samples undergo the phase transition (crystalline/fluid) could be extracted. Due to the particle number concentration becoming accessible via the scattering intensity of the silica core in SAXS, a precise mapping of the generalized volume fraction becomes feasible. As a result, the former indicated shift of the phase boundary between the crystalline and fluid phase, as well as the reduction of the effective interaction radius of the microgels, due to charge screening could be quantified. The pronounced influence of charges and respective charge screening can be detected in the temperature dependent phase diagrams presented in **Figure 3.5**. As indicated by the solid black line and the evolution of the crystalline region (light brown), it is shown that in absence of salt (**Figure 3.5a**), the core-shell microgels self-assemble into crystalline structures at very low volume fraction around 0.39 and high temperatures are needed for a transition into the fluid phase.

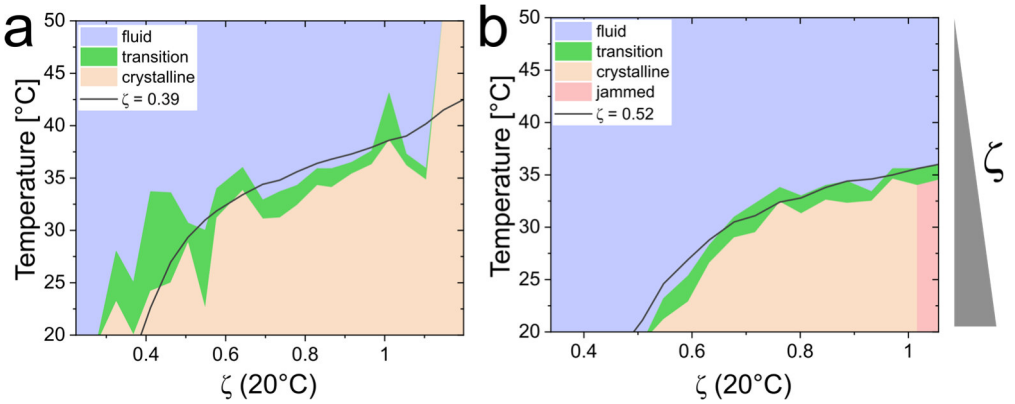

Figure 3.5 Phase diagram of core-shell microgels in absence (**a**) and presence of salt (**b**) with the transition temperature as function of the generalized volume fraction ζ at 20 °C. The blue area corresponds to the fluid regime and the crystalline regime is indicated in light brown. Between both regimes we find the transition area marked in green. For the area colored in red (**b**) no Bragg peaks could be found. The solid black lines indicate the expected transition temperature based on the respective average $\zeta_{transition}$. The grey bar on the right indicates the decrease in volume fraction for an increase in temperature.

When charges are screened (**Figure 3.5b**), the phase boundary is much more defined and core-shell microgels self-assemble into crystalline structures around the expected volume fraction, compared to a system of hard spheres (0.52 vs. 0.49). For a more detailed discussion see **chapter 6.4.5**. This work shows that even weakly charged microgels can exhibit distinct electrostatic contributions, which significantly influence their phase behavior.

The presented core-shell microgels are an ideal model system to investigate the phase behavior of soft colloids by means of scattering methods and optical spectroscopy. Particle number concentrations and volume fractions became accessible from the scattering intensity of the cores in SAXS. The presence of the cores also simplified the extraction of the structure factor from the scattering profiles. With sufficiently large shell sizes, SAXS gave even insights into the microgels response towards dense packings. It was also found that the weak charges of the core-shell microgels have an influence on the phase behavior. This was studied by structure factor analysis from SAXS profiles and temperature-dependent optical spectroscopy recorded from samples of core-shell microgels in dense packings under charged and charge-screened conditions.

3.1 Contributions to Joint Publications

Chapter 4: SAXS Investigation of Core–Shell Microgels with High Scattering Contrast Cores: Access to Structure Factor and Volume Fraction.

***Marco Hildebrandt**, Sergey Lazarev, Javier Pérez, Ivan A. Vartanyants, Janne-Mieke Meijer and Matthias Karg*

Published in *Macromolecules*, **2022**, 55, (7), 2959–2969. https://doi.org/10.1021/acs.macromol.2c00100

M.K., J.-M.M. and I designed the storyline of the study. I synthesized the core-shell microgels and conducted the characterization of the particles via dynamic light scattering, absorbance spectroscopy and analyzed the transmission electron microscopy images. J.-M.M. and S.L. performed synchrotron SAXS measurements, where J.P. assisted as responsive beamline scientist. I conducted the sample preparation. J.-M.M. and M.K. supported me during the analysis and interpretation of the synchrotron SAXS data. Additional SAXS data were acquired by me in order to extract particle number densities. Absorbance spectroscopy on densely packed samples was also performed by me. I designed and prepared all figures and wrote the first version of the manuscript. M.K and J.-M.M performed major editing and rewriting. All authors contributed with helpful discussions and proofread the manuscript.

Chapter 5: Fluid-solid transitions in photonic crystals of soft, thermoresponsive microgels

***Marco Hildebrandt**, Duong Pham Thuy, Julian Kippenberger, Tillmann L. Wigger, Judith E. Houston, Andrea Scotti and Matthias Karg*

Published in *Soft Matter*, **2023**, 19, (37), 7122-7135. https://doi.org/10.1039/D3SM01062G

M.K. and I designed the storyline of the study. D.P.T. synthesized the particles and performed preliminary experiments. Particle characterization, including dynamic light scattering, determination of particle number densities and the analysis of angle dependent dynamic light scattering data and transmission electron microscopy images was performed by me.

J.E.H. and A.S. conducted synchrotron SAXS measurements and did the data reduction. J.K. enabled and conducted angle dependent reflectance spectroscopy. T.L.W. assisted with the domain size analysis. Temperature dependent absorbance spectroscopy and the respective data interpretation was conducted by me. I performed the analysis of the synchrotron SAXS data, supported by M.K. I designed and prepared all figures and wrote the first version of the manuscript. M.K. performed major editing and rewriting. All authors contributed with helpful discussions and proofread the manuscript.

Chapter 6: Temperature dependent phase diagrams of weakly charged, thermoresponsive microgels under charged and charge-screened conditions

***Marco Hildebrandt**, Duong Pham Thuy, Anna Domgans, Andrea Scotti, Sylvain Prévost and Matthias Karg*

Manuscript in preparation for submission

M.K. and I designed the storyline of the study. D.P.T. and I synthesized the particles. D.P.T. performed preliminary experiments. Particle characterization, including dynamic light scattering, electrophoretic mobility measurements, determination of particle number densities and the analysis of static light scattering data and transmission electron microscopy images was performed by me. A.D. assisted with the sample preparation. A.S. conducted synchrotron SAXS measurements and did the data reduction. S.P. performed SANS measurements and the respective data reduction. Temperature dependent absorbance spectroscopy and the respective interpretation of the recorded data was conducted by me. I designed and prepared all figures and wrote the first version of the manuscript. M.K. performed major editing and rewriting. All authors contributed with helpful discussions.

4. SAXS Investigation of Core–Shell Microgels with High Scattering Contrast Cores: Access to Structure Factor and Volume Fraction

Published in *Macromolecules* **2022**, 55, 7, 2959–2969[81]

https://doi.org/10.1021/acs.macromol.2c00100

Marco Hildebrandt,[1] Sergey Lazarev,[2] Javier Pérez,[3] Ivan A. Vartanyants,[2] Janne-Mieke Meijer, [4,*] Matthias Karg[1,*]

[1]Institut für Physikalische Chemie I: Kolloide und Nanooptik, Heinrich-Heine-Universität Düsseldorf, Universitätsstraße 1, D-40225 Düsseldorf, Germany

E-Mail: karg@hhu.de

[2]Deutsches Elektronen-Synchrotron DESY, Notkestraße 85, 22607 Hamburg, Germany

[3]Synchrotron SOLEIL, L'Orme des Merisiers, Saint-Aubin, BP 48, 91192 Gif-sur-Yvette Cedex, France

[4]Department of Applied Physics and Institute for Complex Molecular Systems, Eindhoven University of Technology, P.O. Box 513, 5600 MB Eindhoven, The Netherlands

E-Mail: j.m.meijer@tue.nl

4.1 Abstract

To explore dense packings of soft colloids, scattering experiments are ideal to access the structure factor. However, for soft microgels determination of the structure factor is difficult because of the low contrast of the polymer network and potential microgel interpenetration and deformation that change the form factor contribution. Here, we employ small-angle X-ray scattering (SAXS) to study soft, thermoresponsive microgels with poly-*N*-isopropylacrylamide (PNIPAM) shells and gold nanoparticle cores. The scattering of the gold cores dominates the scattering patterns and allows precise determination of the microgel volume fraction over a broad range of concentrations. At high volume fractions we find distinct patterns with sharp Bragg peaks allowing extraction of the structure factor and characterization of the phases combined with UV-Vis spectroscopy. The unique scattering contrast of our core-shell microgels combined with SAXS opens up new ways to investigate dense packings of soft microgels including in situ studies of phase transitions.

4.1 Introduction

Microgels are composed of cross-linked polymer networks that are swollen by a solvent and possess a dual colloid-polymer nature.[8, 14, 16] Through the polymer composition, microgels can be rendered responsive towards various external stimuli such as pH, ionic strength and temperature.[7, 19, 20, 83, 153-155] The most prominent example for microgels that respond to changes in temperature undergoing a pronounced volume phase transition (VPT) is composed of poly-*N*-isopropylacrylamide (PNIPAM). PNIPAM microgels were first synthesized by Pelton and Chibante[24] and received great attention ever since for example as model system for soft colloids.[7, 72, 123, 156, 157] Furthermore, such responsive microgels are of interest for different applications, for instance photonic crystals,[72] 3D bioprinting,[46] color-changing systems,[44, 65] as well as viscosity modifiers and lubricants.[41, 42]

Similar to hard spheres, microgels can form crystalline phases in 2D and 3D assemblies. The fact that the microgel size can be tuned by external parameters and thereby allowing for in-situ changes of the volume fraction, ϕ, makes responsive microgels highly attractive for the study of crystallization and melting phenomena.[47, 82] Furthermore, the softness and deformability of microgels extend their phase diagram even above the hard sphere limit (ϕ = 0.74).

In 3D assemblies of hard spheres, the maximum packing density is reached when particles are in direct contact in close packed crystalline structures, namely fcc (face centred cubic) or hcp (hexagonally close packed). Higher packing fractions are not possible because hard spheres cannot be deformed and/or compressed. In contrast, upon contact, microgels can deform, shrink and/or interpenetrate resulting in apparent volume fractions above the hard sphere limit and even above unity, $\phi > 1$.[41] For the real volume fraction the changes in individual microgel volume at high packings needs to be considered. The difference between the apparent and the real volume fraction of soft and deformable microgels has been addressed recently by Scotti et al.[80] Clearly, understanding the influence of the softness and responsiveness of microgels on the structure and dynamics in dense dispersions is important for their applications as well as of fundamental interest to study, for example, crystallization, melting as well as glass or jamming transitions.

For relatively large microgels with sizes in the micron range, optical microscopy techniques have been used for investigating the local organization of microgel systems on a single particle level.[43, 65, 158] The overlapping of microgels in dense packings however limits the resolution in optical microscopy. In addition, different scattering methods, such as dynamics and static light scattering (DLS and SLS) or small-angle X-ray and neutron scattering (SAXS and SANS) were frequently employed to study the bulk structure and dynamics of microgel systems – mostly focusing on microgels too small to be observed with optical microscopy.[9, 66, 159] A major advantage of scattering methods over microscopy methods is that much higher particle numbers can be addressed in one measurement giving access to ensemble averages with great statistics. At high volume fractions, in particular, where microgels form colloidal crystals, scattering methods are much more powerful to resolve the long-range 3D order. However, it remains difficult to unambiguously decouple the form factor, $P(q)$, and the structure factor, $S(q)$, from scattering profiles. On the one hand both contributions appear on similar length scales (or ranges of scattering vector, q), thus requiring the form factor to be determined with great statistics. On the other hand, in contrast to hard spheres, the microgel form factor can change with concentration, in particular for dense packings due to interpenetration and/or deformation.[74, 78]

Furthermore, the form factor of microgels is much more complex than that of hard spheres due to the inhomogeneous distribution of the cross-linker leading to the well-known fuzzy sphere morphology[9, 32] and the overlap of their outer polymer segments at high concentrations.[76]

Recently, there has been an increased interest in microgels that contain metallic nanoparticles. Such hybrid microgels are attractive for the development of new materials with applications in photonics, plasmonic lasing, and opto-electronic devices.[47, 109, 160, 161] The interest has arisen because the nanoparticle core, for example silver or gold, can host localized surface plasmon resonances (LSPRs),[49, 162] while the interparticle spacing is controlled by the microgel shell that also governs the formation of 2D or 3D colloidal crystals.[47] For core-shell (CS) microgels consisting of gold nanoparticles (AuNPs) coated with a cross-linked PNIPAM shell it was shown that these behave as soft microgel systems, forming 2D and 3D crystal lattices.[48, 73, 90, 163, 164] The 2D lattices were found to show surface lattice resonances (SLR) when the inter-particle spacing was in the order of the visible wavelength leading to plasmonic-diffractive coupling.[63, 161, 165, 166] Due to the strong LSPR absorption of the AuNP cores, however, the use of optical microscopy methods is limited and so far the 3D crystal lattices have been mostly investigated with UV-Vis spectroscopy focusing on the Bragg reflection.[47] A recent study also explored SANS for the characterization of 3D colloidal crystals and found that the PNIPAM shell leads to the formation of a dominant fcc crystal lattice, irrespective of the presence of the small gold core.[73] However, in SANS the scattering arises from the polymer shell and therefore the same interferences between form and structure factor hampers the detailed analysis of the structure factor. It further remains unclear if the gold cores are truly located in the centers of microgel shells. Lapkin *et al*. recently studied a similar system focusing on the melting and crystallization of CS microgels at high volume fraction.[82] Thanks to the high scattering contrast cores, ultra small-angle X-ray scattering (USAXS) could be used to provide detailed information on the phase transition upon changes in temperature in situ. The appearance of sharp Bragg peaks in the crystalline regime allowed a detailed analysis of the melting and crystallization behavior.

In this work, we focus on studying PNIPAM microgels with small AuNP cores by SAXS. We exploit the large size and electron density difference between the cores and the swollen PNIPAM shells that will lead to the main scattering contribution arising from the AuNP cores. We investigate different low concentrations of the CS microgel system and demonstrate that the AuNP core allows for the precise determination of the apparent microgel volume fraction.

We also explore the formation of colloidal crystals driven by the microgel shells and investigate a broad concentration series. We determine the phase behavior and interparticle spacing as a function of microgel volume fraction. Finally, we compare our findings from SAXS with results from Bragg peak analysis using UV-Vis spectroscopy.

4.3 Experimental Methods

Chemicals

Gold(III) chloride trihydrate ($HAuCl_4$; Sigma-Aldrich, ≥99.9%), sodium citrate dihydrate (Sigma Aldrich, ≥99.0%), butenyl amine hydrochloride (Sigma Aldrich,97.0%), sodium dodecyl sulfate (SDS; Merck, ≥95.0%), *N*-isopropylacrylamide (NIPAM; TCI 98.0%), *N,N'*-methylenebis(acrylamide) (BIS; Aldrich, 99%), potassium peroxodisulfate (PPS; Sigma ≥99.0%), sodium chloride (NaCl; Fischer Chemical,; Ph. Eur.). Water was purified with a Milli-Q System (Millipore), resulting in a final resistivity of 18 MΩ cm.

Synthesis of Core-Shell Microgels

CS microgels with spherical gold cores and polymer shells consisting of chemically cross-linked PNIPAM were synthesized via seeded precipitation polymerization.[119] NIPAM (1.169 g; 10.3 mmol) and BIS (0.239 g; 1.6 mmol) were dissolved in 600 mL of Milli-Q water followed by degassing with argon at a temperature of 70 °C for 1.5 h. Before initiating the reaction with 12 mg PPS dissolved in 1 mL of water, 8.4 mL of a stock dispersion of spherical Au-NP seeds[48] with a mean radius of 7.4 nm (from transmission electron microscopy) and an elemental gold concentration of $[Au^0]$ = 0.02 mol/L were added to the reaction mixture. After the polymerization was initiated, the reaction was continued for 4 h. The final CS microgels were purified by three centrifugation steps, each for 3 h at 7500 rcf and redispersion in water to remove residues of salt, unreacted monomer and potentially non-cross-linked polymer. Finally, the CS microgels were freeze-dried. We take into account for a residual water content of 5.7% in the final freeze-dried sample.[73, 136]

Sample Preparation

CS microgel dispersions with different weight concentrations were prepared by diluting a highly concentrated stock dispersion made from freeze-dried CS microgels. In this way sample dispersions within the concentration range from 0.5 wt% to 22.5 wt% were prepared. Although care was taken to control all wt% concentrations, for the very dense samples we sometimes observed CS particle deposition on the capillaries. This loss of particles in combination with solvent evaporation could lead to changes in the wt%.

Transmission Electron Microscopy

Transmission electron microscopy (TEM) was conducted with a JEOL JEM-2100Plus TEM in bright-field mode operated with an acceleration voltage of 80 kV. Samples were prepared via drop casting of a dilute aqueous CS microgel dispersion on carbon coated copper grids (200 mesh, Electron Microscopy Science). The grids were dried at room temperature for several hours before investigation. The particle size was determined from the TEM images using the GMS 3 software from Gatan as well as ImageJ.[167, 168]

Dynamic Light Scattering

Temperature dependent dynamic light scattering (DLS) was performed with a Malvern Zetasizer Nano S (λ = 633 nm; θ = 173°). Three measurements at each temperature in a range of 15 to 65°C with a step of 1 K were taken with acquisition times of 60 s each. Dilute aqueous microgel dispersions were measured in standard polystyrene cuvettes with 1 cm pathlength. Hydrodynamic radii R_h (z-average) were determined with cumulant analysis provided by the instrument software.

Electrophoretic Mobility Determination

Electrophoretic mobility was measured with a Malvern Zetasizer Nano Z (λ = 633 nm; θ = 173°) at a temperature of 20°C. The CS microgels were dispersed in 10^{-4} M aqueous NaCl solution to provide a constant ionic background.

UV-Vis Absorbance Spectroscopy

UV-Vis spectra were recorded using a SPECORD S 600 (Analytik Jena) UV-Vis spectrophotometer. Dilute samples were measured in 1 cm PMMA cuvettes. Dense samples at high volume fractions were measured in 0.2 mm × 4.0 mm × 50 mm capillaries (VitroTubes). Measurements were performed at room temperature.

Small-Angle X-Ray Scattering

In-house SAXS measurements were performed on a Xeuss 2.0 (XENOCS) equipped with an X-ray beam of 8.048 keV, a sample to detector distance of 1 m and an acquisition time of 3600 s. Scattering patterns were collected with a Pilatus3R 300K with an area of 83.8 x 106.5 mm^2 and a pixel size of 172 x 172 μm^2. This setup provides a q-range of 0.03 $nm^{-1} < q < 3.5$ nm^{-1}. We want to mention that the resolution in the q-range of 0.03 – 0.1 nm^{-1} is much lower compared to synchrotron SAXS.

Dilute samples were measured in 1 mm round capillaries (WJM Glas) at a temperature of 20 °C. The measured signal was background corrected for the scattering of water, normalized to absolute scale using the thickness of the capillary and the scattering of glassy carbon as reference and finally radially averaged with the Foxtrot software provided by Xenocs.[169]

Synchrotron SAXS measurements on dense samples at high volume fractions were performed at the SWING beamline at the SOLEIL synchrotron in Saint-Aubin (France). An X-ray beam of 8 keV (λ = 0.155 nm) was employed with a sample to detector distance of 6497 mm. An Eiger 4M detector with an area of 155.2 × 165.5 mm^2 and a pixel size of 75 × 75 μm^2 was used to collect the 2D scattering patterns. This setup provides a q-range of 0.01 $nm^{-1} < q < 1.0$ nm^{-1}. Samples with different wt% were prepared in 0.2 mm × 4.0 mm × 50 mm capillaries (VitroTubes). These thin-walled rectangular capillaries provide short optical paths and also allow for measurements by SAXS and by UV-Vis absorbance spectroscopy on the same sample. Due to the high viscosity of high wt% samples, samples were heated to approximately 50 °C, which is well above the volume phase transition temperature (VPTT) of the microgel shells. At this temperature the volume fraction is significantly reduced due to the shrinkage of the PNIPAM shells lowering also the dispersion viscosity. By applying a small, reduced pressure to one opening of the capillaries, the dispersions were sucked inside the capillaries. The capillaries were sealed with two-component epoxy glue. Prior to investigation, all samples were annealed at a temperature of approximately 50 °C. Subsequently, the samples were slowly cooled to room temperature during at least 1 h. All samples were measured at a temperature of 20 °C with an acquisition time of 100 ms. Background corrections were performed on the recorded 2D SAXS patterns before analysis with the Foxtrot software provided by SOLEIL.[169]

Radially averaged scattering profiles were analysed with the SASfit software by Kohlbrecher.[170] The 2D SAXS patterns were analysed with the Software Scatter by Förster and Apostol.[171]

4.4 Results and Discussion

4.4.1 Characterization in the Dilute State

Seeded precipitation polymerization was used to synthesize CS microgels that have high electron density AuNP cores and low electron density hydrogel shells composed of chemically cross-linked PNIPAM. A schematic depiction of the CS morphology is shown in **Figure 4.1a.** In order to verify this CS structure experimentally and to determine the yield of encapsulation, the CS microgels were studied by TEM. **Figure 4.1b** shows a representative TEM image where the CS structure with the high contrast, spherical AuNP cores and the low contrast PNIPAM shells can be clearly identified. Due to drying effects on the TEM grids and the high vacuum conditions during the measurements, the microgel shells are in a collapsed state with dimensions much smaller than in dispersion under good solvent conditions (red, dashed circle in the TEM image). We also attribute the drying effects to be responsible for the AuNP cores not appearing in the centre of the microgels in TEM images (see **Figure 4.1b**). In addition, some microgels without cores could be observed (see **Figure S4.1** in the Supporting Information). The percentage of microgels that do not feature a AuNP core is low however (< 1 %) in agreement to findings in a previous work.[119] The mean radius of the AuNP cores, R_c, was determined as R_c = 6.6 ± 0.7 nm. A corresponding histogram of the core sizes determined by TEM analysis is shown in **Figure S4.2** in the Supporting Information. A UV-Vis extinction spectrum measured from a dilute dispersion of the AuNP cores (no shells) reveals a single dipolar LSPR with a resonance maximum at λ_{LSPR} = 524 nm (see **Figure S4.3** in the Supporting Information). Due to the rather small size of the AuNPs the LSPR is related to absorption of light while scattering, that scales with the sixth power of the particle radius, is negligible. The extinction properties change significantly when the much larger PNIPAM shell is added. **Figure 4.1c** shows the corresponding extinction spectrum of the CS microgels measured from dilute dispersion. While the LSPR of the AuNP cores is still visible as a peak at 524 nm wavelength, an increased absorbance is observed at lower wavelengths due to Rayleigh-Debye-Gans scattering of the larger PNIPAM shells.

This superposition of scattering from the PNIPAM shells and absorption from the AuNPs cores hampers the determination of particle number concentrations from extinction values.[136] We will later on show that SAXS is the ideal tool for extracting number concentrations with great precision. The total size of the CS microgels in dilute dispersion was determined by DLS. At 20 °C, i.e. in the swollen state, we measured a hydrodynamic radius, R_h, of 105 ± 1 nm. The VPT of the PNIPAM shell was studied using temperature-dependent DLS measurements. **Figure S4.4** in the Supporting Information shows the evolution of R_h as a function of temperature. With increasing temperature R_h decreases continuously until a plateau is reached when the shell is in a fully collapsed state at T > 50°C with R_h approaching approximately 65 nm. The VPTT is found at approximately 36 °C which agrees well to other PNIPAM microgels with similar cross-linking densities.[73, 136] The finding that we observe a pronounced temperature response for such high nominal cross-linker contents is in agreement with a recent study by Ponomareva et al. where similar CS microgels with varying size and cross-linker contents were studied in detail by different methods including light and neutron scattering.[32] The electrophoretic mobility of the CS microgels was investigated because it is known that electrostatic interactions can have an influence on the interparticle interactions.[172, 173] We find an electrophoretic mobility of -1.6 µm cm/Vs at 20 °C for the CS microgels. This slightly negative charge is related to the anionic initiator used in the synthesis. Therefore, we consider our microgels to be weakly electrostatically stabilized.

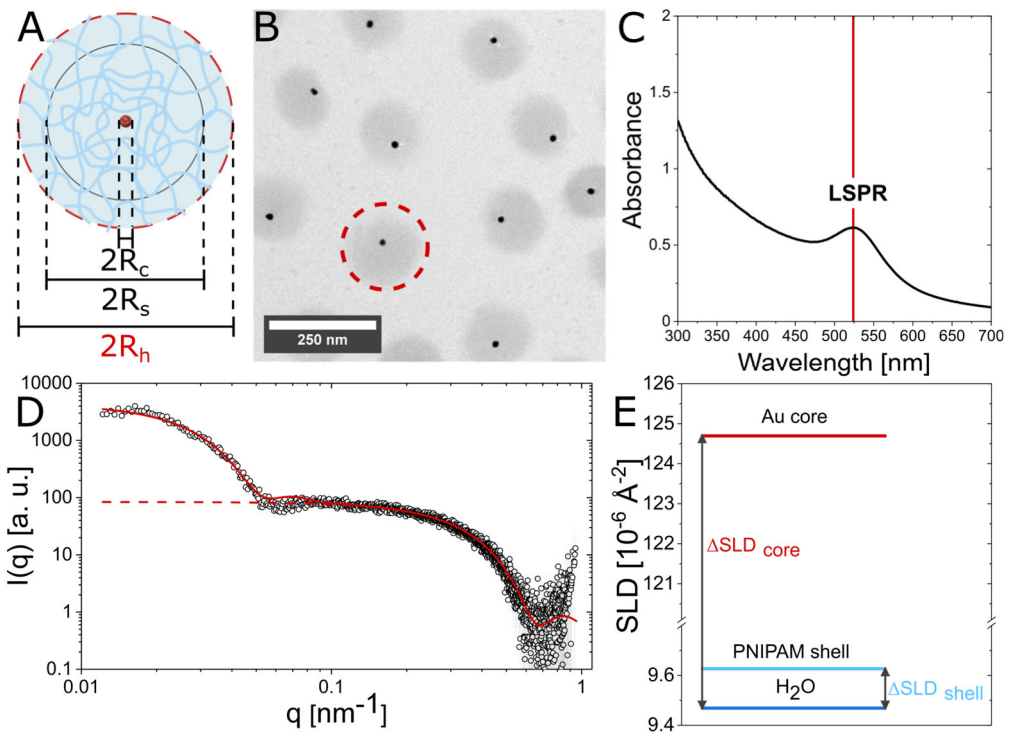

Figure 4.1 Characterization of Au-PNIPAM CS microgels. (**A**) Schematic illustration of the CS structure and the most relevant radii accessible by scattering experiments with R_c the radius of the AuNP core, R_s the radius of the CS microgel from SAXS and R_h the hydrodynamic radius. (**B**) Representative TEM image of the CS microgels. The red circle indicates the dimensions of the swollen PNIPAM shell as obtained from DLS. (**C**) UV-Vis absorbance spectrum of a dilute dispersion of CS microgels. The red line highlights the position of the LSPR. (**D**) Synchrotron SAXS profile from a dilute dispersion (0.5 wt%) of the CS microgels recorded at 20 °C. The dashed line corresponds to the form factor fit of the AuNP scattering contribution. The solid line corresponds to a form factor model that combines two polydisperse hard spheres with different size and different scattering contrast. (**E**) Scattering length density differences between Au, swollen PNIPAM microgel shell (80 % water content) and water as the dispersion medium. Note the break in scale due to the large difference between core and shell SLD. SLDs were obtained from the SLD calculator provided by NIST.[174]

To determine the form factor of the CS microgels and in particular to determine the contributions of core and shell scattering, we studied dilute microgel dispersions by SAXS. **Figure 4.1d** shows the radially averaged synchrotron SAXS profile measured at 20 °C. The scattered intensity $I(q)$ depends on the scattering contrast (ΔSLD) given by the scattering length density (SLD) for homogenous scattering objects, the particle number density N, the scattering object volume V_P, the form factor $P(q)$ and the structure factor $S(q)$, according to

$$I(q) = N(\Delta SLD)^2 V_p^2 P(q) S(q) \quad (4.1)$$

For dilute particle dispersions interparticle interactions can be considered negligible and $S(q) \approx 1$. In the mid to high q-region ($q > 0.1$ nm^{-1}) the SAXS profile is dominated by the form factor contribution of the AuNP cores. This contribution can be described by a simple polydisperse sphere model as the dashed red line in **Figure 4.1d** illustrates. In the following we will focus on the analysis of the core form factor and its forward scattering intensity. However, in the scattering profile we also observe an increase in scattering intensity in the low q-region ($q < 0.1$ nm^{-1}) that is related to scattering from the swollen PNIPAM shell. The contribution of the core is more distinct due to the difference in the SLD of the AuNP core and the PNIPAM shell as shown in **Figure 4.1e.** The difference in SLD of the AuNP cores and water exceeds that of the swollen PNIPAM shells with respect to water by almost three orders of magnitude, explaining the dominant contribution of the core in the mid to high q-region. The water content of PNIPAM microgels with different cross-linker densities up to 25 mol% (nominal) was investigated in detail by using SANS recently.[32] Even for such high nominal cross-linker amounts water contents of more than 80% in the swollen and more than 60% in the collapsed state were found. However, even though the shell possesses a lower contrast, it still contributes to the scattering profile at low q due to its much larger volume. As a simple approach to describe the core and the shell contribution we use the simple sum of two polydisperse spheres taking into account the difference in scattering contrast of the cores and shells (solid red line **Figure 4.1d**, for details see Supporting Information). Qualitatively this simple model describes the measured data sufficiently well. We want to note that a more complex form factor model that considers interference between core and shell and also accounts for the inhomogeneous cross-linker distribution in the shell would be more appropriate.[82, 116]

However, due to the rather small scattering contribution from the shell and the absence of pronounced form factor oscillations in the accessible *q*-range, we do not want to go deeper into such an analysis here. In the Supporting Information a form factor analysis comparing different models used to fit the scattering profile of the dilute CS microgel sample is given in **Figure S4.5**. In the following, the scattering signal from the cores only is what we will be using for further analyses in this study. From the fit of the core scattering contribution we find R_c = 6.5 ± 0.6 nm which is slightly smaller than the radius obtained from TEM (6.6 ± 0.7 nm). This difference can be explained by approximation of a perfect sphere in SAXS while we measure slightly anisotropic shapes in TEM. The form factor fit resulting from the linear combination of two polydisperse spheres describes the full scattering profile sufficiently well and we determine a radius of R_s = 77.9 ± 8.7 nm for the CS microgel. The reason R_s is significantly smaller than R_h is that the model does not take into account the fuzziness of the PNIPAM shell, while the outer low cross-linked region still contributes to the hydrodynamic dimensions. It is well known that PNIPAM microgels possess a gradient in cross-linker density due to the faster consumption of the cross-linker BIS during the precipitation polymerization.[30, 175] This gradient also leads to dangling end chains at the surface that contribute to R_h but are not resolved in SAXS due to their very low contrast.[78, 79, 83] This is also in good agreement with our previous results.[73, 82] Also, the radius of gyration R_g = 71.1 ± 1.7 nm determined from Guinier analysis is smaller than R_s (see **Figure S4.6** and discussion in the Supporting Information).This can also be ascribed to the gradient in cross-linker density. A similar difference is found when we compare R_g and R_h where we find the ratio R_g/R_h = 0.68, which is typically observed for microgels, for example studied by light scattering.[157]

Volume Fraction

Due to their soft and deformable nature as well as the dangling ends that allow for interpenetration in dense packings, the determination of the volume fraction, ϕ, of microgel dispersions is challenging and often defective. One approach to extract volume fractions from dilute microgel dispersions is relative viscosimetry.[36, 80] Here, owed to the strong scattering contrast of the AuNP cores, we can use the absolute SAXS intensity to determine the number concentration, *N* (see **Equation 4.1**), of the CS microgels very precisely in the low concentration regime. **Figure 4.2a** shows radially averaged scattering profiles recorded for dilute CS microgel dispersions ($S(q) \approx 1$) at 20°C with known concentrations (wt%).

The red solid lines correspond to the respective form factor fits of the AuNP core contribution. It is important to note that the scattering curves are not offset and the increase in $I(q)$ is a direct result of the increase in concentration and hence N. Because we normalized $I(q)$ to absolute intensity (cm^{-1}), the particle number density and hence ϕ_{core} can be determined from the intensity I_0 extrapolated to $q \rightarrow 0$ nm^{-1} according to:

$$N = \frac{I_0 \, N_A \, {\rho_{core}}^2}{M_{core} \, m_{core} \, {\Delta SLD}^2} \tag{4.2}$$

With ρ_{core} the AuNP core density, N_A Avogadro's number, M_{core} the molecular weight and m_{core} the mass of the AuNP core, and ΔSLD the scattering length density differences between gold and water (for more details see Supporting Information). Once N has been determined, the volume fraction of the CS particles, ϕ_{CS}, can be obtained from the number concentration N and the hydrodynamic radius R_h:

$$\Phi_{CS} = N \, \frac{4}{3} \pi \, {R_h}^3 \tag{4.3}$$

We employ R_h because Stieger et al.[9] showed that this is the most accurate size to describe soft microgels in the swollen state. The forward scattering intensities, $I_{0,}$ were determined from linear extrapolation of the scattering data in a Guinier plot where only the q-range relevant to scattering from the AuNP cores is considered. The inset in **Figure 4.2a** shows the Guinier plot for the differently concentrated samples and the corresponding linear fits (red lines). More details about the fitting procedure and a larger scale image of the inset in **Figure 4.2a** are provided in the Supporting Information (**Table S4.3** and **Figure S4.7**). For the fits we have ignored the scattering from the shell, visible at $q < 0.06$ nm^{-1}.

Figure 4.2b shows the resulting relation between the sample concentration in wt% and the extracted volume fraction of CS microgels, ϕ_{cs}, derived from N resulting from the SAXS data and using the hydrodynamic radius (R_h = 105 nm) in the swollen state at 20 °C. As expected, there is a linear relation between ϕ_{cs} and the CS microgel concentration in wt%. The slope of the linear fit to the data provides the scaling between the two quantities and allows us the calculation of the volume fraction for any given concentration in wt% (see also **Figure S4.8** in the Supporting Information). We find:

$$\phi_{CS} = (0.13 \pm 0.01) \, \text{mass concentration in wt\%} \tag{4.4}$$

A more detailed overview of concentrations and the respective volume fractions is presented in **Table S4.4** in the Supporting Information.

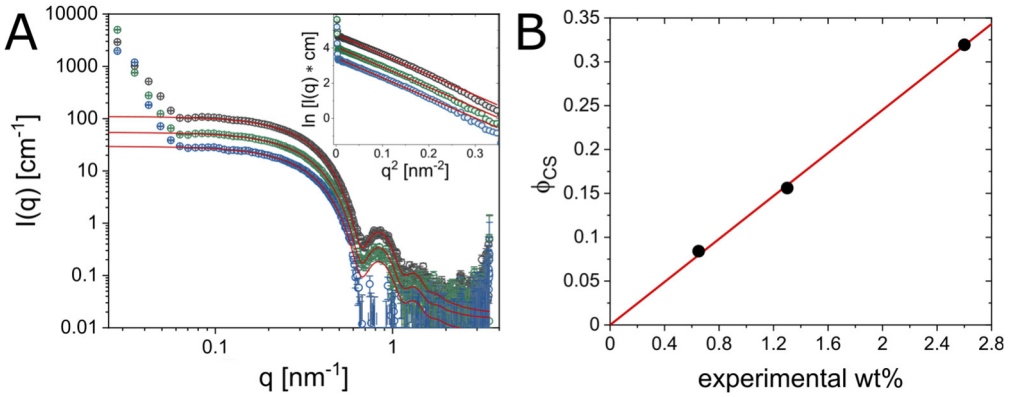

Figure 4.2 (**A**) Radially averaged SAXS profiles for differently concentrated dispersions of the CS microgels in the dilute regime. The concentrations were 0.62 wt% (blue), 1.23 wt% (green) and 2.45 wt% (dark grey). Red lines correspond to the form factor fits only taking into account the scattering contribution of the AuNP cores. The inset shows the SAXS data in the Guinier plot representation with the red lines corresponding to linear fits used for the extrapolation to obtain I_0 at $q \rightarrow 0$ nm^{-1}. (**B**) Determined volume fraction ϕ_{cs} for each experimental wt% (black circles) showing a linear relation (red line).

4.4.2 Separation of the Form Factor and Structure Factor

For dense packings of purely organic microgels without high contrast cores, form factor and structure factor typically overlap to some extent in the low q-range.[9, 66] Therefore, the determination of the structure factor is often difficult and requires, for example, contrast variation experiments.[78] While for hard spheres, the form factor will not be significantly affected by concentration, microgels can deform, interpenetrate and even change their size in dependence of concentration. This hampers the simple calculation of the structure factor by $S(q) = I_{conc.}(q) / I_{dil.}(q)$ with the measured scattering profiles of the dense sample ($I_{conc.}(q)$) and a dilute reference sample ($I_{dil.}(q)$) where $S(q) \approx 1$.[66] In our case, we deal with CS microgels that have a high contrast AuNP core. Due to the much greater volume of the PNIPAM shell with respect to the core, interparticle interactions of our swollen CS microgels are governed by the soft repulsive potential of the shells. Only at extremely high packing densities a contribution from the hard core might become relevant. In this work we focus on packing fractions where the phase behaviour is comparable to purely organic PNIPAM microgels without hard cores similar to our previous work.[73] Specifically, we look at a range of concentrations where we observe the self-organization into crystalline structures.[47, 82] Since the interparticle spacing, d, is much larger than the AuNP core size in these samples, we expect the dominating form factor of the cores and the structure factor of the crystalline assemblies to appear in significantly different ranges of q.

The as-prepared concentration range of CS particles we investigated spanned from 0.5 wt% to 22.5 wt%. Already visual inspection of these samples provides first insights into the phase behaviour. For the two most dilute concentrations with 0.5 wt% (ϕ_{cs} = 0.06) and 2 wt% (ϕ_{cs} = 0.24), fluid-like samples were obtained indicative by the absence of opalescence. In contrast, for concentrations higher than 2 wt% opalescence was observed indicating the formation of crystallites.[123, 176, 177] We also ascribe potential crystallization at lower volume fractions than expected ($\phi < 0.49$) to electrostatic interactions between the slightly charged CS microgels. **Figure 4.3a** shows scattering profiles from synchrotron SAXS measurements of all investigated samples. Like in the dilute concentration regime investigated with in-house SAXS, the mid to high q-regions (> 0.1 nm^{-1}) are dominated by the form factor contribution of the AuNP cores. The continuous increase in $I(q)$ at a given q in this region reflects the increase in number density N (see **Equation 4.1**).

Using the forward scattering intensity I_0 of the AuNP core scattering determined from the dilute sample and applying a correction that considers the residual water of the freeze-dried CS microgels we can use this dilute concentration of 0.5 wt% to precisely map N for each sample in the concentrated regime. In other words, we can determine the concentrations in the dense phases non-destructively and also account for local density fluctuations and potential sample inhomogeneities. **Table S4.5** in the Supporting Information lists the as-prepared and corrected wt% concentrations and corresponding volume fractions for all samples investigated. With our set of samples in the concentrated regime we cover a broad range of volume fractions ranging from ϕ_{cs} = 0.24 to ϕ_{cs} = 1.95. We want to note that values well above the hard sphere packing limit are possible because of the soft and deformable nature of the CS microgels.

Now turning to the low q-region in our synchrotron SAXS data, we observe clear structure factor contributions for all concentrated samples with $\phi_{cs} \geq 0.24$. Although the dilute sample (light brown circles in **Figure 4.3a**) does show an intensity increase with decreasing q in the low q-region related to the PNIPAM shells (**Figure S4.9** in the Supporting Information), the low q scattering of the dense samples is dominated by the structure factor that results from the periodic arrangement of the AuNP cores. In particular for volume fractions close to and higher than the hard sphere packing limit (ϕ = 0.74), we expect any form factor contributions from the shell to be negligible. In addition, since the shells will be in close contact and can deform at high ϕ_{cs} leading to a reduction in shell contrast.[76, 79] To confirm this assumption, we simulated scattering profiles assuming various shell contrasts and fixed core contrasts. From these simulated profiles we extracted the structure factors shown in **Figure S4.10** in the Supporting Information. No significant changes in the position of the first structure factor maximum, q_{max}, could be detected. A similar effect of disappearing contrast between shell and background can be seen in the UV-Vis spectra from such colloidal crystals where the scattering at lower wavelength is strongly supressed.[73] Assuming that the form factor and structure factor are well separated, we can now eliminate the form factor contribution by dividing all measured intensity profiles by the form factor of the AuNP cores, that is $I_{dil.}(q)$. **Figure 4.3b** shows the corresponding results for the sample with ϕ_{cs} = 0.66. The black circles represent the experimental scattering profile and the red dashed line corresponds to the form factor fit.

The extracted structure factor is represented by the blue circles. For $q > 0.08$ nm^{-1} the obtained structure factor is very close to unity highlighting that the form factor contribution was completely eliminated.

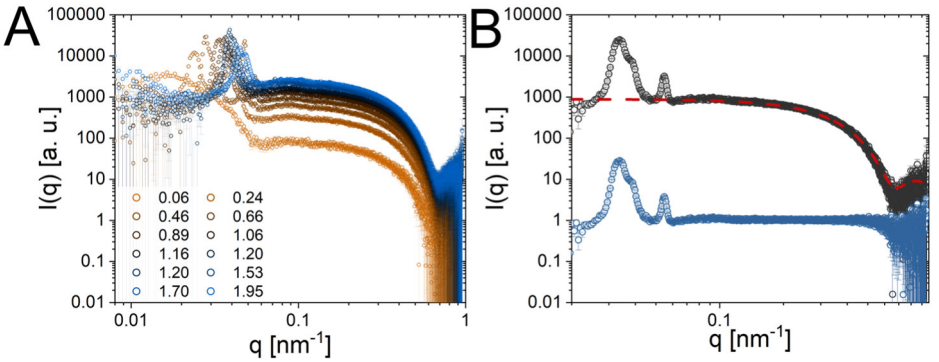

Figure 4.3 (**A**) Radially averaged synchrotron SAXS profiles for a broad range of CS microgel volume fractions listed in the legend. (**B**) Extracted structure factor of the sample with ϕ_{cs} =0.66 (blue circles) from the radially averaged intensity profile (black circles) via the fitted AuNP core form factor (red dashed line).

We now want to investigate the structure factors of the samples in more detail. To determine which crystal lattice was formed by the CS microgels, we first analysed the 2D SAXS patterns to determine the origin of the $S(q)$ peaks. As shown in the Supporting Information the 2D detector images of two selected samples reveal at least two orders of pronounced Bragg peaks with a six-fold symmetry indicating the formation of hexagonal close packed planes aligned to the capillary wall (see **Figure S4.15a** and **S4.15b** in the Supporting Information). Furthermore, the first order Bragg peaks are superimposed with a pronounced amorphous ring indicating a liquid-like contribution. Thus, these selected samples show the coexistence of crystalline and fluid-like phases in the probed scattering volume. For colloidal spheres it is well known that the stacking sequences of the close-packed hexagonal planes can lead to the formation of a random hexagonally close packed (rhcp) structure, which is a mixture of hexagonally close packed (hcp) and face centred cubic (fcc) stacking sequences, as the energetic differences are very small.[71, 82, 178] To get an idea of the dominant stacking sequence and lattice spacing we modelled the 2D SAXS patterns with the software Scatter (see **Figure S4.15c** and **S4.15d** in the Supporting Information).

We found a good agreement between the experimental and simulated patterns with a dominant fcc structure consisting of CS microgels with a homogeneous density shell and small domain sizes[179] (for more details see Supporting Information). This finding is in good agreement with the structure found for quite similar CS microgels in a previous SANS study.[73] We want to note that in other works on PNIPAM microgels rhcp phases were identified and that the presence of higher order Bragg peaks is needed to conduct a precise determination of the exact crystal system.[69, 71] The observation of sharp Bragg peaks indicates that the AuNP cores are well centred in the PNIPAM shells, since positional fluctuations would lead to the smearing or absence of clear structure factor peaks.

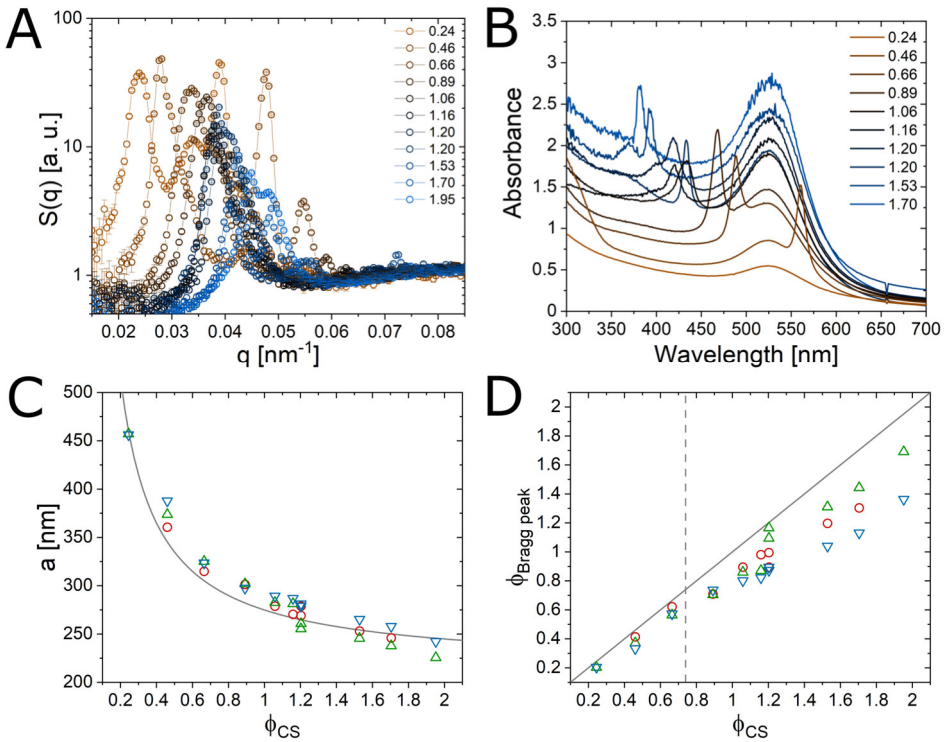

Figure 4.4. (**A**) Extracted structure factors for all crystalline samples. (**B**) UV-Vis absorbance spectra of all crystalline samples recorded in transmission geometry. Volume fractions regarding are listed in the legends. (**C**) Lattice constant ***a*** and (**D**) volume fraction $\phi_{Bragg\ peak}$ extracted from SAXS via the first (111) fcc (blue triangle) and second (220) fcc structure factor peak (green triangle), as well as from the diffraction peaks (λ_{diff}) in UV-Vis spectra (red circles). The black curve in (**C**) serves as guide to the eye and follows the expected scaling between ***a*** and ϕ_{CS}. The dashed, vertical line in (**D**) represents the hard sphere limit for close packed spheres, and the black, solid line corresponds to a linear dependence with a slope equals to one and a zero intercept. Error bars in (**C**, **D**) are the same size or smaller than the data points.

4.4.3 Phase Behaviour

We now want to focus on the crystalline structures and extract their lattice constants from the Bragg peaks obtained via UV-Vis spectroscopy and from the structure factor peaks determined by SAXS to get insights in the unit cell dimensions of the crystals. From the lattice constants we can also determine the volume fraction of CS microgels.

Figure 4.4a shows the experimentally determined structure factors from SAXS for samples of a broad range of volume fractions, i.e. ϕ_{cs} = 0.24 to ϕ_{cs} = 1.95. Having verified the alignment of the hexagonally packed planes to the capillary wall and a dominant fcc crystal structure, we can index the peaks in the structure factor profiles with their Miller indices *h*, *k* and *l*.[66] We can assign the first peak of *S*(*q*) to the quasi-forbidden (111) reflection for fcc[179] and the second peak to the (220) reflection. We do note that the first Bragg peaks could also be related to the presence of rhcp stacking that would lead to the appearance of the hcp (100) reflection[180, 181], but its position in *q* is very close to the (111) peak and therefore the two peaks are hard to distinguish. For simplicity and in agreement to our previous results from SANS[73] and works by others on microgel crystallization, we will continue with the fcc analysis.[66, 67] Here we also want to mention the work of Lapkin *et al*. where a similar system was investigated with larger focus on the crystal structures.[82] In **Figure 4.4a**, upon increasing ϕ_{cs} all peaks move to higher *q* values indicating a decrease in lattice constant. In addition, the intensity of the structure factor peaks decreases for increasing ϕ_{cs} which we attribute to a decrease in the degree of order. In addition, we provide the structure factors that are obtained by dividing using the form factor of the dilute sample in the Supporting Information **Figure S4.11**. Despite differences in intensity due to the shell contribution the structure factors and in particular the peak positions are in good agreement to the results in **Figure 4.4a**.

In addition to synchrotron SAXS, we investigated the diffraction properties of our samples using UV-Vis spectroscopy.[47, 73, 182, 183] **Figure 4.4b** shows the spectra of all samples. The relatively broad peak at $\lambda \approx 524$ nm in all spectra is related to the LSPR of the AuNP cores. In addition, sharp peaks originated from the Bragg reflection of the incident light by the (111) planes of the crystals can be observed. For instance, for ϕ_{cs} = 0.66 the Bragg peak occurs at approximately λ_{Bragg} = 488 nm.

Next, we quantitatively compare the results from both techniques, for example via the obtained lattice spacings, *a*. For this, we extracted the first two structure factor peak positions using the Gaussian fits to the data (see **Figure S4.12** and **S4.13** in the Supporting Information).

From the structure factor maxima q_{max}, we calculate the lattice spacing d_{hkl}:

$$d_{\mathrm{hkl}} = \frac{2\pi}{q_{\max}} \tag{4.5}$$

The lattice spacing d_{hkl} is assigned to different crystalline planes by the Miller indices *h, k* and *l*. With the lattice spacing we calculate the lattice constant *a* for *the* (111) peak according to:

$$a = d_{\mathrm{hkl}}\sqrt{h^2 + k^2 + l^2} = d_{\mathrm{hkl}}\sqrt{3} \tag{4.6}$$

The Bragg peak analysis by UV-Vis spectroscopy gives also access to the lattice spacing:

$$m\lambda_{\mathrm{Bragg}} = 2d_{\mathrm{hkl}}\sqrt{{n_{\mathrm{crystal}}}^2 - \sin\theta^2} \tag{4.7}$$

Here λ_{Bragg} is the spectral position of the diffraction peak, d_{hkl} the lattice spacing, $n_{crystal}$ the refractive index of the crystalline sample and θ the angle between the incoming plane and the normal to the crystal plane.[160, 171, 177] For the (111) crystalline plane one can simplify the calculation, since we assume the hexagonally close packed planes to be oriented parallel to the capillary wall so that $\theta = 0°$:

$$d_{111} = \frac{\lambda_{\mathrm{diff}}}{2n_{\mathrm{crystal}}} \tag{4.8}$$

We use $n_{crystal} = 1.345$ as the average refractive index of the colloidal crystals similar to our previous work.[73]

Figure 4.4c compares the determined lattice constants from SAXS and UV-Vis spectroscopy in dependence of the volume fraction of the samples. The data from both methods nicely collapse onto a single master curve showing a decrease from $a = 457$ nm at $\phi_{cs} = 0.24$ to $a = 226$ nm at $\phi_{cs} = 1.95$. The black line in **Figure 4.4c** serves as guide to the eye following the theoretical scaling between a and ϕ_{cs}, more details are given in the Supporting Information. Here we note that the volume fraction we use does not take into account any interpenetration and/or faceting of microgels when the volume fraction exceeds the hard sphere limit of $\phi = 0.74$ as recently discussed by Scotti et al.[74, 80]

In agreement to the scaling of a with $\phi_{cs}^{-1/3}$ we found the decrease of λ_{diff} to scale with $\phi_{cs}^{-1/3}$ which was previously observed for microgel systems (see **Figure S4.14** in the Supporting Information).[157]

We now want to compare the relation between the volume fraction ϕ_{cs} that we determined using the forward scattering of the AuNP cores in SAXS and the volume fraction $\phi_{Bragg\ peak}$ that we can calculate from the Bragg peak analysis of SAXS and UV-Vis data. Using the lattice constants, a and the hydrodynamic radii, R_h we get the following relation:

$$\phi_{\mathrm{Bragg\ peak}} = \frac{(3+1)\frac{4}{3}\pi {R_h}^3}{a^3} \tag{4.9}$$

Here an fcc lattice was considered and the (3 + 1) terms corresponds to the number of CS microgels in the fcc unit cell. In **Figure 4.4d** we compare $\phi_{Bragg\ peak}$ obtained from SAXS and UV-Vis data with ϕ_{cs}. The data from both techniques are in good agreement and we find a linear scaling between $\phi_{Bragg\ peak}$ and ϕ_{cs} for low volume fractions. At higher volume fractions exceeding the hard sphere limit of ϕ = 0.74 (dashed line in **Figure 4.4d**), we find that $\phi_{Bragg\ peak}$ is significantly smaller than ϕ_{cs}. This deviation indicates that microgel deformation and/or interpenetration starts to occur. In addition, we believe that the formation of wall crystals in coexistence with a disordered sample structure, as also indicated by the presence of the pronounced rings in the 2D SAXS patterns (**Figure S4.15** in the Supporting Information) can cause this discrepancy. The discrepancy between $\phi_{Bragg\ peak}$ determined from the (111) and the (220) reflections for samples exceeding the apparent volume fraction of 1 might be related to contributions from rhcp lattices as mentioned before. We can also not exclude that the form factor of the CS microgels in the dense regime might influence the peak positions to some extent.

Clearly, the phase behaviour and packing in dense microgel systems is difficult to quantify precisely. The benefits from scattering techniques for the investigation of soft colloids like microgels at higher volume fractions are clearly the good statistics by probing millions of particles at once. SANS is often used to investigate such samples but suffers from long durations for a single measurement. The combination of a hard inorganic core encapsulated in a soft and responsive microgel shell provides us with a powerful model system to make use of SAXS with acquisition times below 1 s and the separation between the form factor and structure factor, due to the difference in size and contrast between core and shell.

When normalized to absolute scattering intensities, the scattering signal of the core also provides detailed information about the number concentration of particles, which makes this system promising not only for dense packing, but also for studies in the dilute state were accurate control over the particle number is needed.

4.5 Conclusion

We have studied core-shell microgels in the dilute and densely packed regime using small-angle X-ray scattering. Owed to the pronounced difference in volume of the gold nanoparticle cores and the cross-linked poly-*N*-isopropylacrylamide shells as well as the stark difference in the scattering contrast, form factor and structure factor of crystalline samples are well separated. Using absolute scattering intensities and form factor analysis of the gold core contribution, we could determine microgel number concentrations very precisely. With this we could relate the experimentally given weight concentration to microgel volume fractions. We find that the microgels form crystals with a dominant fcc structure over a large range of ϕ_{cs}. The quantitative agreement between crystal analysis from SAXS and results from UV-Vis spectroscopy is very good, with the lattice constants of the crystal unit cells collapsing on a single master curve. There is an increasing deviation for higher volume fractions, in particular, above the hard sphere packing limit between the volume fraction obtained from the number concentration of the cores and the volume fraction determined from the lattice constant. This can be explained by having crystals in coexistence with a disordered sample structure indicated by distinct rings in the SAXS patterns and the occurrence of microgel deformation and interpenetration.

We propose that such core-shell microgels are ideal model systems to study the phase behaviour of microgels, in particular at high volume fractions. While the small gold nanoparticle cores dominate the mid to high q scattering in SAXS, they do not significantly affect the inter-particle interactions that are governed by the microgel shells. The short acquisition times of SAXS open up the possibility to investigate the impact of temperature changes on the microgels in dense packing, which induces melting and recrystallisation of the system, due to the temperature-dependent volume of the microgels[82], but has also been shown to change the particle interactions.[35] In addition, core-shell microgels with high contrast cores will allow further explorations of other fundamental phenomena such as jamming and the glass transition of soft colloidal systems. This is expected to lead to new insights in the field of soft colloidal systems.

Notes

The authors declare no competing financial interest.

ACKNOWLEDGMENTS

J.M.M. acknowledges financial support from the Netherlands Organization for Scientific Research (NWO) (016.Veni.192.119). M.K. acknowledges the German Research Foundation (DFG) for funding under grant KA3880/6-1. We acknowledge SOLEIL for provision of synchrotron radiation facilities and we would like to thank Javier Perez for assistance in using beamline SWING (Proposal number 20181613). The authors thank the Center for Structural Studies (CSS) that is funded by the Deutsche Forschungsgemeinschaft (DFG Grant numbers 417919780 and INST 208/761-1 FUGG) for access to the SAXS instrument. The authors acknowledge the DFG and the state of NRW for funding the cryo-TEM (INST 208/749-1 FUGG) and Marius Otten from Heinrich-Heine-University Düsseldorf for his assistance with the TEM measurements.

4.6 Supporting Information

General Characterization of Core-Shell Microgels

The morphology of the CS microgels and the successful encapsulation of single AuNP cores in each microgel was investigated by TEM. **Figure S4.1** shows TEM images of the CS microgels at different magnifications. These images were used to determine the encapsulation rate of the AuNP cores in the PNIPAM shells.

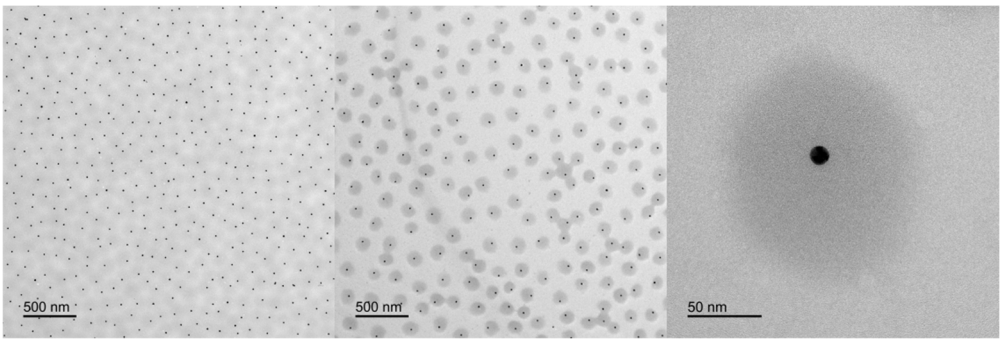

Figure S4.1. TEM images of CS microgels recorded at different magnifications.

Figure S4.2 shows the size distribution histogram of the AuNP cores as obtained from manual TEM image analysis using ImageJ.

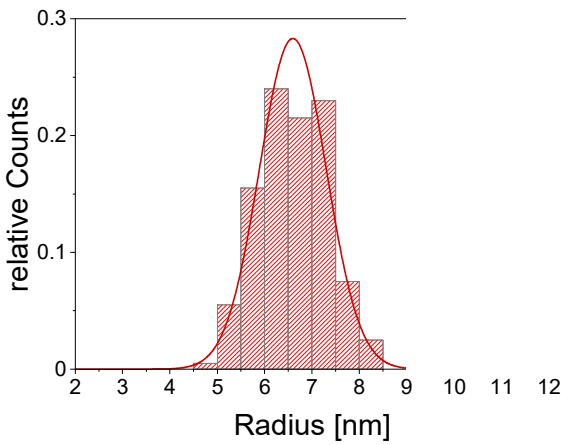

Figure S4.2. Size distribution of the AuNP cores as determined by TEM. The red line corresponds to a fit to the data using a Gaussian distribution function.

The optical properties of the AuNP cores and the final CS microgels were studied by UV-Vis spectroscopy. **Figure S4.3** shows UV-Vis absorbance spectra of the as-synthesized AuNP cores and the final Au-PNIPAM CS microgels. The Au^0 concentration of the AuNP core dispersion was determined via the absorbance at 400 nm, *Abs*(400), according to:[137]

$$c_{\mathrm{Au}^0} = \frac{Abs(400) \times F_{\mathrm{D}}}{\varepsilon} \tag{S4.1}$$

Here ε = 2330 $Lmol^{-1}cm^{-1}$ and F_D is the factor of dilution.

The peaks in absorbance at λ = 524 nm (vertical red lines) are related to the localized surface plasmon resonance (LSPR) of the AuNPs. For the CS microgels the LSPR is less pronounced due to the increased light scattering contribution of the polymer shell (**Figure S4.3B**).

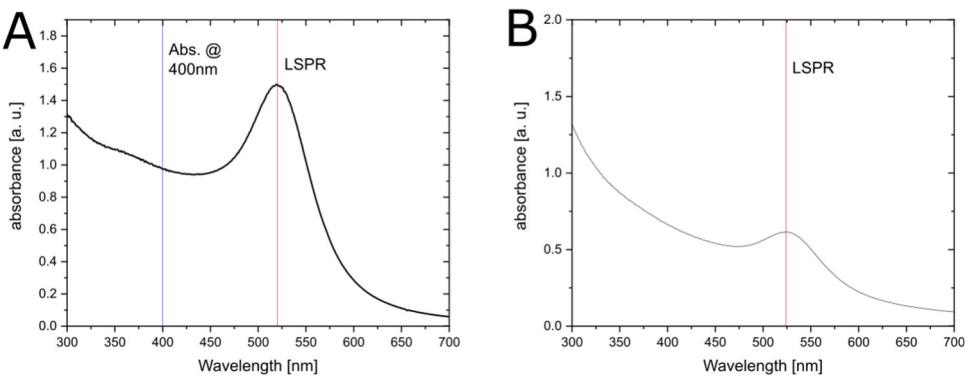

Figure S4.3. (**A**) Absorbance spectrum of the AuNP core dispersion (F_D = 50). (**B**) Absorbance spectrum of the CS microgels in dilute aqueous dispersion. The vertical red lines highlight the LSPR positions of the AuNPs.

The volume phase transition (VPT) of the CS microgels was followed by temperature-dependent DLS measurements. **Figure S4.4** shows the resulting evolution of the hydrodynamic radius, R_h, as a function of temperature. R_h decreases continuously with increasing temperature until reaching nearly constant values at temperatures of 60 °C and higher where the PNIPAM shells are in their collapsed state. The VPT temperature (VPTT) is approximately 36.2 °C. Even at high nominal cross-linker contents of 15 mol% and more PNIPAM microgels show distinct response to temperature.[32, 73]

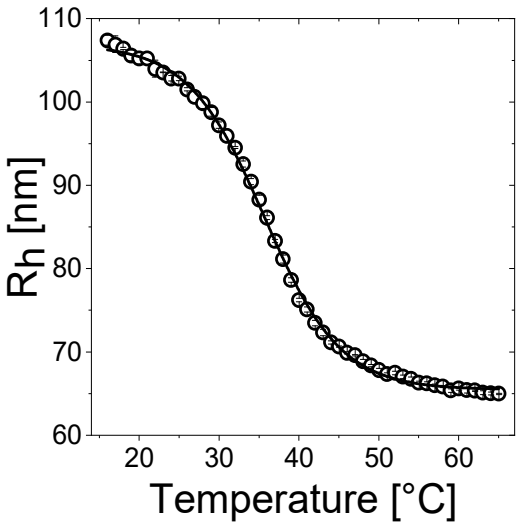

Figure S4.4. Hydrodynamic radii (R_h) of the CS microgels from DLS as a function of temperature. The solid black line corresponds to a fit using the Boltzmann sigmoidal function.

Form Factor Modeling

We measured the form factor of the CS microgels in dilute dispersion using SAXS. Due to the isotropic character of all recorded scattering data in the dilute regime, data were radially averaged to obtain the average scattering intensity, I, as a function of the magnitude of the scattering vector, q, given by:

$$|\vec{q}| = q = \frac{4\pi}{\lambda} sin\left(\frac{\theta}{2}\right) \quad \text{(S4.2)}$$

Here θ is the scattering angle and λ the wavelength of the X-ray beam.

For the investigated q-range the scattered intensity, $I(q)$, depends on the microgel number density, N, the volume of a single microgel, V_p, the scattering length density (SLD) difference between the scattering object and the solvent, ΔSLD, the form factor $P(q)$ of the scattering object and additional background contributions, I_B:

$$I(q) = N{V_P}^2(\Delta SLD)^2 P(q) + I_B \quad \text{(S4.3)}$$

Here we neglect any structure factor contributions, $S(q)$, since we are in the dilute regime, where $S(q) \approx 1$.

The form factor of a solid sphere with the radius *R* is given by:

$$P(q) = \left[3\frac{sin(qR)-qRcos(qR)}{(qR)^3}\right]^2 \quad \text{(S4.4)}$$

The form factor of a spherical shell is given by the radius of the core *R*, the thickness of the shell *ΔR* and the difference in scattering length dentistry between the matrix and the respective core and shell, ΔSLD_{core} and $\Delta SLD_{\text{shell}}$.

$$I_{shell}(q, R, \Delta R, \Delta SLD_{core}, \Delta SLD_{shell}) = [K(q, R + \Delta R, \Delta SLD_{shell}) - K(q, R, \Delta SLD_{shell} - \Delta SLD_{core})]^2 \quad \text{(S4.5)}$$

with

$$K(q, R, \Delta SLD) = \frac{4}{3}\pi R^3 \Delta SLD\ 3\frac{sin(qR)-qRcos(qR)}{(qR)^3} \quad \text{(S4.6)}$$

In order to account for polydispersity, the form factor and the volume are convoluted with a normalized Gaussian distribution function:

$$D\left(R, \langle R\rangle, \sigma_{\text{poly}}\right) = \frac{1}{\sqrt{2\pi\sigma_{\text{poly}}{}^2}} exp\left(-\frac{(R-\langle R\rangle)^2}{2\sigma_{\text{poly}}{}^2}\right) \quad \text{(S4.7)}$$

Here $\langle R\rangle$ is the average particle radius and σ_{poly} is the relative size polydispersity. In order to describe the measured form factor of the CS microgels, we used the simple sum of two homogeneous spheres. Thus, one polydisperse sphere accounts for the scattering of the AuNP cores, while the second one accounts for scattering from the PNIPAM shell. We want to highlight that this simple superposition does not consider for any interference between core and shell. Due to the large difference in contrast and size between the AuNP cores and the PNIPAM shells as well as the limited resolution of the microgel form factor, we used this very simplified model to estimate the total microgel size from our SAXS data. Since we do not attempt to describe the microgel form factor in detail in this work, we do not apply more complex core-shell or core-shell-shell models that are commonly used for microgels/core-shell microgels.[30, 82, 116] **Table S4.1** lists the obtained fit parameters for the core and the shell contribution obtained from a measurement of a diluted (0.5 wt%) sample at 20°C.

Table S4.1. Summary of fit parameters obtained from form factor analysis using SASfit.

	Core	Shell
R	6.5 ± 0.6 nm	77.9 ± 8.7 nm
ΔSLD	1.2 × 10^{-2} nm^{-2}	4.7 × 10^{-5} nm^{-2}
I_B	0.35 cm^{-1}	0.35 cm^{-1}
σ_{poly}	0.09	0.11

In addition to the sum of the two polydisperse spheres (red line), we show form factor fits based on a core-shell model in **Figure S4.5**. The two fits based on the core-shell model only differ in the polydispersity (σ_{poly} = 0.1 for the fit in green and σ_{poly} = 0.24 for the fit in blue). More details on the fits are listed in **Table S4.2**. We see that the fit exhibiting the higher polydispersity describes the data quite well but the unrealistically high polydispersity of σ_{poly} = 0.24 is in strong contrast to former SANS studies on very similar systems resulting in polydispersities close to σ_{poly} = 0.1. Here we want to note that the contrast of the polymer shell is much higher in SANS and should lead to more reliable results.[32, 73]

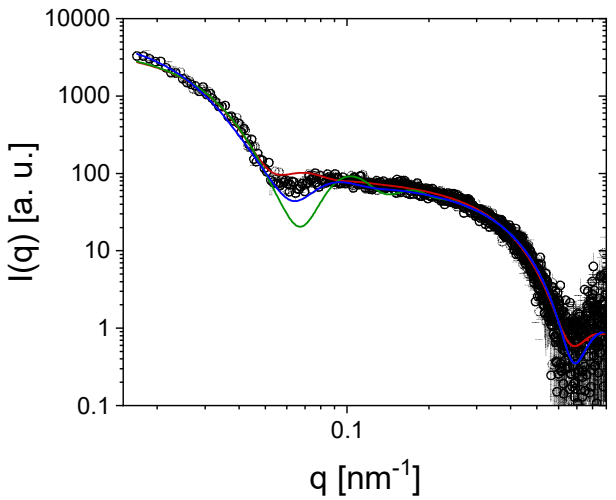

Figure S4.5. SAXS profile from dilute CS microgel dispersion (20°C). The solid lines correspond to the applied form factor fits. In red, the introduced fit based on the sum of two polydisperse spheres, in blue and green fits based on the core-shell model with polydispersities of σ_{poly} = 0.1 (green) and σ_{poly} = 0.24 (blue) of the respective shell.

Table S4.2. Summary of fit parameters obtained from form factor analysis based on the core-shell model using SASfit.

	Core-Shell	**Core-Shell**
R_{core}	6.5 nm	6.5 nm
R_{shell}	79.6 ± 8 nm	79.6 ± 19.2 nm
I_B	0.35 cm^{-1}	0.35 cm^{-1}
ΔSLD_{core}	1.2 × 10^{-2} nm^{-2}	1.2 × 10^{-2} nm^{-2}
ΔSLD_{shell}	3.2 × 10^{-5} nm^{-2}	3.2 × 10^{-5} nm^{-2}
$\sigma_{poly,\ shell}$	0.1	0.24

The radius of gyration R_g of the CS microgels was determined by analysis of the Guinier region at low q as shown in **Figure S4.6**.

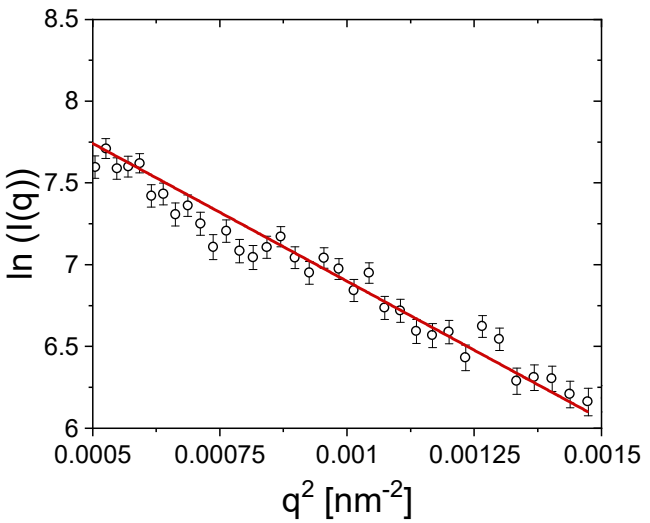

Figure S4.6. Guinier plot and linear fit (red line) of the low q SAXS data measured form a dilute CS microgel dispersion (0.5 wt%) at 20 °C.

The slope of the linear fit gives access to R_g:

$$I(q) = I_0 \times exp\left[\frac{-q^2 {R_g}^2}{3}\right] \quad \text{(S4.8)}$$

We obtain R_g = 71.1 ± 1.7 nm.

Due to the large difference in core and shell size, our SAXS data from dilute samples (see **Figure 4.2a** of the main manuscript) allow also to perform Guinier analysis in the mid to high *q*-range, where the scattering of the AuNP cores dominates. Thus, we can determine the values of R_g and also the forward scattering intensity, I_0. **Figure S4.7** shows the corresponding Guinier plots and linear fits to the data for three different CS microgel concentrations.

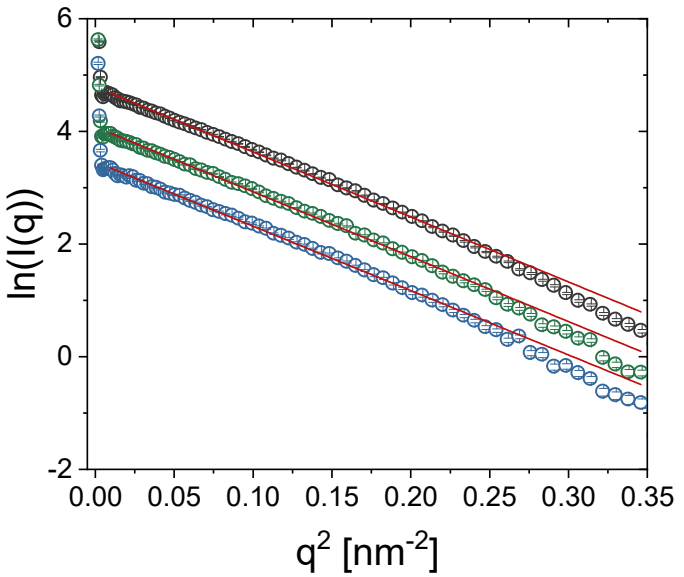

Figure S4.7. Guinier plots of the SAXS data measured from dilute CS microgel dispersions with 2.45 wt% (black circles), 1.23 wt% (green circles) and 0.62 wt% (blue circles). Linear fits (red lines) were applied to extract I_0 and R_g according to **Equation S4.6**.

The parameters from the linear fit and the resulting forward scattering I_0 and R_g are listed in **Table S4.3**.

Table S4.3. Parameters from Guinier analysis of the AuNP core scattering contribution at mid to high *q*.

	2.45 wt%	**1.23 wt%**	**0.62 wt%**
Intercept	4.79	4.07	3.45
Slope [nm^{-2}]	-11.55	-11.53	-11.44
I_0 [cm^{-1}]	120	59	32
R_g [nm]	5.89	5.88	5.86

As expected, the forward scattering scales with the microgel concentration. The obtained values of R_g are slightly smaller than the value obtained from the polydisperse sphere form factor analysis (R_{core} = 6.54 nm). This is expected for homogeneous spheres.

Determination of Number Density and Volume Fraction

With our absolute intensity in-house SAXS data and the theoretical scattering length densities of the AuNP cores and water, we can calculate the particle number density, N, based on the intensity I_0 at infinitely small q, i.e. the forward scattering intensity of the AuNP cores:

$$N = \frac{I_0 \, N_A \, \rho^2}{m \, M_w \, \Delta SLD^2} \tag{S4.9}$$

Here N_A is Avogadro's number, ρ the density of the AuNP cores (19.3 g·cm^{-3}), m the average mass of a single AuNP core and M_w its molecular weight. With the values of I_0 obtained from the Guinier analysis provided in **Figure S4.7**, we calculated N (**Table S4.4**).

Table S4.4. Number concentrations obtained from SAXS measurements of diluted samples with known concentrations.

	2.45 wt%	**1.23 wt%**	**0.62 wt%**
N [10^{13} ml^{-1}]	6.59	3.22	1.73

Since we know from detailed TEM analysis that each CS microgel contains one single AuNP core, the obtained number density of the AuNP cores is equal to the number density of CS microgels, i.e. the number of cores is equal to the number CS microgels. This allows to determine the volume fraction of CS microgels, ϕ_{CS}:

$$\phi_{CS} = N \, \frac{4}{3}\pi \, {R_h}^3 \tag{S4.10}$$

Figure S4.8 shows the determined values of ϕ_{cs} as a function of the weight concentration (wt%). The linear fit to the data (black line) for the differently concentrated samples in the dilute regime allow for an extrapolation to higher concentrations. We find the following relation:

$$\phi_{\mathrm{CS}} = (0.13 \pm 0.01)\ \text{mass concentration in wt\%} \tag{S4.11}$$

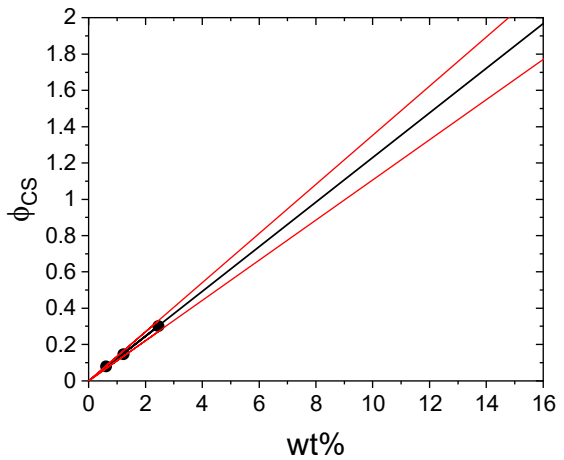

Figure S4.8. Volume fraction of CS microgels ϕ_{cs} determined for samples in the dilute regime from in-house SAXS measurements. The black line is a linear fit to the data. The red lines indicate a 10% error corridor.

The very valuable relation provided by **Equation S4.11** and the fact that we can precisely determine the forward scattering of the AuNP core contribution allows us to determine the local concentration of dense samples probed by the rather small X-ray beam in the synchrotron SAXS experiments. As reference for the mapping of the concentrations, we choose the most dilute sample (0.5 wt%). This sample was prepared by dilution of a stock dispersion prepared from freeze-dried CS microgels. We considered a residual water content in the freeze-dried sample of 5.7%.[73] **Table S4.5** lists the results for all sample concentrations studied in this work. The as-prepared, expected concentrations, are the concentrations that were aimed at by weighing in freeze-dried microgels and dispersing the microgels in the respective amounts of water. The forward scattering intensities from the AuNP core scattering contribution, I_0, were determined by Guinier analysis of the mid to high-q scattering region as demonstrated in **Figure S4.7**.

Table S4.5. Determination of sample concentration and volume fraction based on the forward scattering of the AuNP core contribution in the synchrotron SAXS measurement and the relation given by **Equation S4.11**.

as-prepared expected concentration [wt%]	I_0 [a.u.]	**concentration based on I_0** [wt%]	**concentration[a] corrected for water content** [wt%]	**volume fraction ϕ_{cs}**
0.5	88.6	0.5	0.47	0.06
2	353	1.99	1.88	0.24
4	665	3.75	3.54	0.46
6	961	5.42	5.11	0.66
8	1290	7.28	6.86	0.89
10	1530	8.63	8.14	1.06
11	1675	9.45	8.91	1.16
12.5	1739	9.81	9.25	1.20
11	1740	9.82	9.26	1.20
15	2210	12.47	11.76	1.53
17.5	2464	13.9	13.11	1.70
22.5	2822	15.92	15.02	1.95

[a]Values were corrected for a residual water content of 5.7% (by mass).

Structure Factor Analysis

We now turn to the synchrotron SAXS investigation of dense samples in the crystalline regime. We first want to address the potential influence of the scattering contribution from the CS microgels at low q as observed from the synchrotron SAXS measurements in the dilute regime. To do so we divide the experimental scattering profile of the dilute sample by the fitted polydisperse sphere form factor of the AuNP cores $P_{core}(q)$. The residual scattering profile shown in **Figure S4.9** should correspond solely to scattering from the PNIPAM shells. The shell contribution is only visible for $q < 0.07$ nm^{-1}. Here we observe a continuous increase in scattering intensity with decreasing q.

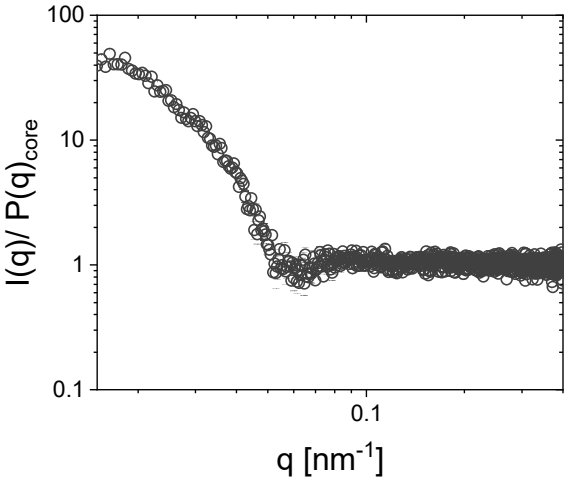

Figure S4.9. Shell contribution to the scattering intensity after division by $P_{core}(q)$ as measured with synchrotron SAXS.

We now want to discuss whether such residual scattering from the PNIPAM shells hampers the analysis of the structure factor with a particular focus on the peak positions of $S(q)$. While for systems of hard, non-deformable scattering objects $S(q)$ is typically easily accessible by simply dividing scattering profiles of dense samples by profiles of dilute samples, where $S(q) \approx 1$, the situation is more complex for soft microgels. In the dense packing regime, microgels can deform and/or interpenetrate and thus, the form factor is different as compared to the dilute state. We want to determine whether this is also the case for our SAXS data of the CS microgels where scattering of the shells is weak and core scattering dominates. To do so, we simulated scattering profiles in SASfit using the form factor and contrast parameters as listed in **Table S4.1** and a structure factor corresponding to a volume fraction of 0.64 and a hard sphere radius of 115 nm. The specific hard sphere radius and volume fraction are chosen to give the most realistic description of the system and are obtained from the lattice spacing *a*. We used a structure factor based on the Percus-Yevick model for hard sphere fluids.[184] These simulated scattering profiles where then divided by the dilute state form factor only where we apply different contrasts for the PNIPAM shell. A contrast of 1 Δ*SLD*(shell) corresponds to the values given in **Table S4.1**. A contrast of 0 Δ*SLD*(shell) corresponds to scattering of the AuNP cores only. **Figure S4.10** shows the resulting structure factors for different shell contrasts.

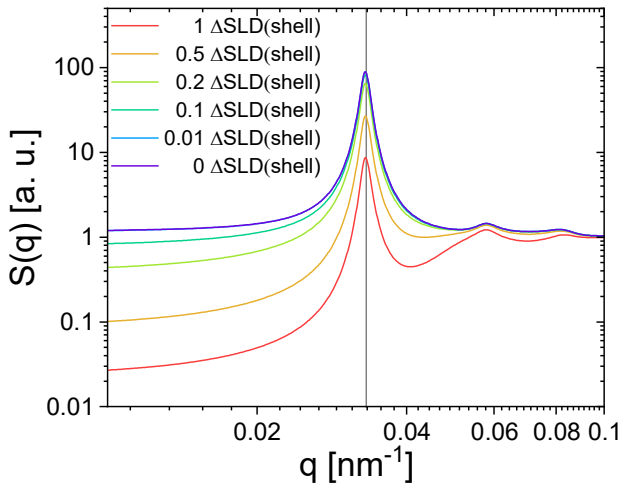

Figure S4.10. Calculated structure factors from SASfit simulations for decreasing shell contrasts. The vertical black line highlights the position of the first structure factor peak.

While we see a pronounced influence in structure factor intensity at low q, the position of the structure factor peaks, q_{max}, remain unaffected by the shell scattering contribution. The first structure factor peak appears at q_{max} = 0.0331 nm^{-1}, independent of the considered shell contrast. Even for the simple division by the AuNP core form factor (0 Δ*SLD*(shell)), we obtain the same peak positions. Therefore, all structure factors of dense samples shown in the main manuscript were obtained by dividing the experimental SAXS profiles by the AuNP core form factor contribution only.

Here we also want to provide the structure factor extracted by dividing the scattering profile of the dense samples $I_{conc.}(q)$ by the scattering profile of the dilute sample $I_{dil.}(q)$ where $S(q) \approx 1$. **Figure S4.11** shows the resulting structure factors in the same q-range as used in **Figure 4.4a** in the main manuscript. We see a shift of the structure factor towards high q with increasing volume fraction. Overall, we find very similar peak positions and shapes as in **Figure 4.4a**. The most prominent differences refer to the peak intensities and overall structure factor intensity at very low q where the shell scattering from the dilute sample is strongest. This is also clearly seen in **Figur S4.10**.

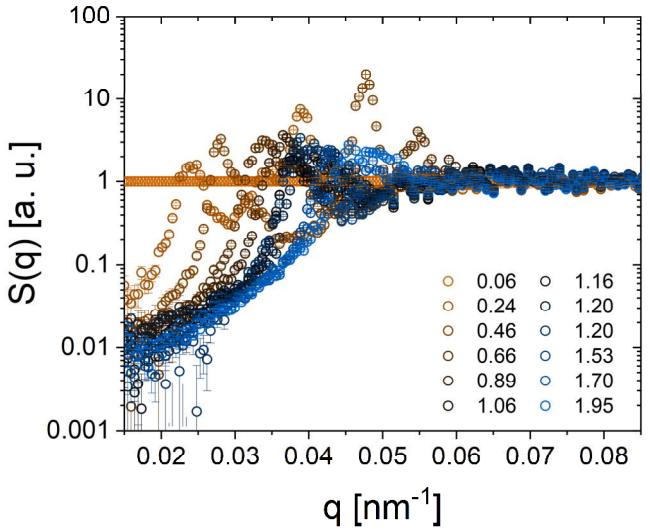

Figure S4.11. $S(q)$ extracted by dividing $I_{conc.}(q)$ through $I_{dil.}(q)$ obtained from the experimentally measured SAXS profile of a dilute CS microgel dispersion (20°C).

In **Figure S4.12** we exemplarily show the obtained structure factor for a CS microgel sample at ϕ_{cs} = 0.66.

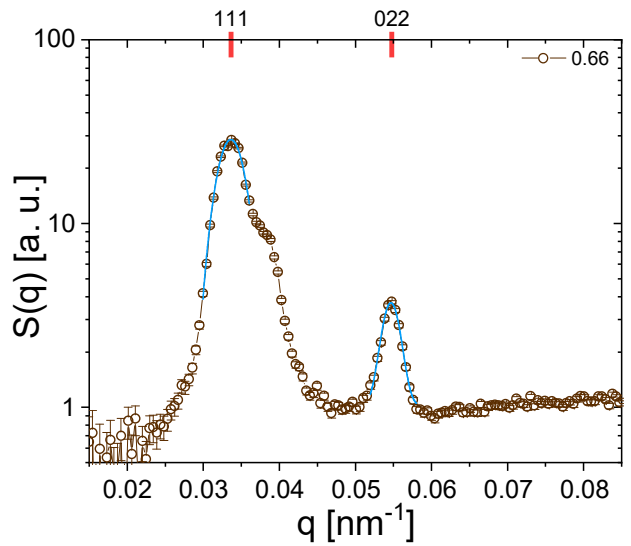

Figure S4.12. S(q) obtained from a sample at a volume fraction of 0.66 and the Peak assignment of the 111 and the 022 peak for a fcc crystals structure including Gaussian fits which were used to extract the structure factor maxima.

The first two structure factor maxima are clearly visible and correspond to the (111) and (022) peaks. The high-*q* shoulder of the (111) peak corresponds to the amorphous ring from the fluid-like scattering contribution. To extract the positions of the structure factor maxima, we applied Gaussian fits to the data in selected ranges of *q* (blue lines in **Figure S4.12**).

For higher volume fractions the intensity of the (022) peaks drops significantly as shown in **Figure S4.13**. Nevertheless, we could still analyze the peak positions by performing Gaussian fits to the data.

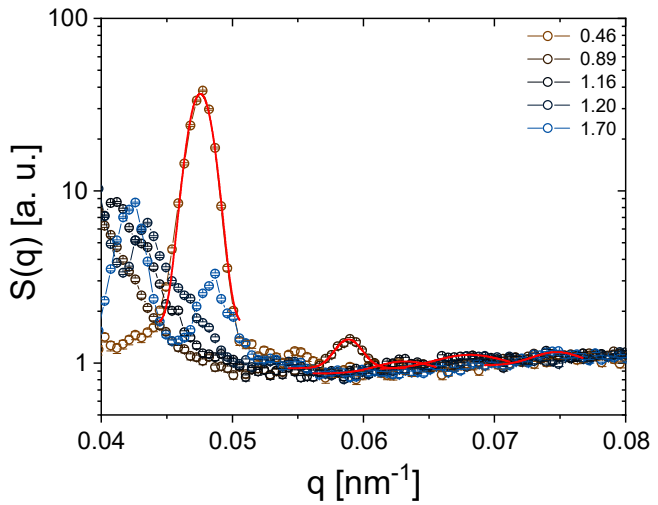

Figure S4.13. Structure factors in a selected *q*-range and analysis of the (022) peaks by Gaussian fits (red lines).

In total we analyzed the structure factor of 11 different samples covering a broad range of volume fractions. In addition to Bragg peak analysis from SAXS, we also studied the sample diffraction by using UV-Vis spectroscopy. The results from both methods are summarized in **Tables S4.6** and **S4.7**.

Table S4.6. Positions of the first two structure factor maxima (q_{max}), positions of Bragg peaks from UV-Vis spectroscopy (λ_{Bragg}) and the resulting lattice spacings (d).

ϕ_{CS}	q_{max}(111) [nm^{-1}]	q_{max}(002) [nm^{-1}]	λ_{Bragg} [nm]	d(111) [nm]	d(022) [nm]	$d_{UV\text{-}Vis}$(111) [nm]
0.24	0.0239	0.0389		263	162	
0.46	0.0281	0.0476	560	224	132	208
0.66	0.0336	0.0547	489	187	115	182
0.89	0.0366	0.0589	468	172	107	174
1.06	0.0376	0.0629	433	167	100	161
1.16	0.0379	0.0632	420	166	99	156
1.20	0.0390	0.0696	418	161	90	155
1.20	0.0387	0.0682	433	162	92	161
1.53	0.0410	0.0724	393	153	87	146
1.70	0.0422	0.0747	382	149	84	142
1.95	0.0449	0.0788		140	80	

Table S4.7. Lattice constants (a) and the resulting volume fractions of the CS microgels calculated from the lattice spacings of **Table S5**.

ϕ_{CS}	a [nm] **(111)**	a [nm] **(022)**	$a_{UV\text{-}Vis}$ [nm]	ϕ_{cs} **(111)**	ϕ_{cs} **(022)**	ϕ_{cs} **UV-Vis**
0.24	456	457		0.20	0.20	
0.46	388	374	361	0.33	0.37	0.41
0.66	324	325	315	0.57	0.56	0.62
0.89	298	302	301	0.74	0.70	0.71
1.06	289	283	279	0.80	0.86	0.90
1.16	287	281	270	0.82	0.87	0.98
1.20	279	255	269	0.89	1.17	0.99
1.20	281	261	279	0.87	1.09	0.90
1.53	265	246	253	1.04	1.31	1.20
1.70	258	238	246	1.13	1.44	1.30
1.95	242	226		1.36	1.69	

For most of the samples we find very good agreement between the determined volume fractions from structure factor analysis (SAXS) and diffraction analysis by UV-Vis spectroscopy. Only in some cases we observe a mismatch with more than 10% deviation. The mismatch is highest for the higher volume fractions and is attributed to a less precise analysis of the weak (022) structure factor peak in SAXS. The volume fractions obtained from UV-Vis spectroscopy are defective to the average refractive index of the dense samples. Deviations to the SAXS data might be explained by the fact that we did not consider the concentration dependence of the refractive index. Nevertheless, the good agreement between the data for most of the samples, highlights the robustness of our structure factor analysis.

Figure S4.14 shows the experimentally determined Bragg peak positions (λ_{Bragg}) from UV-Vis spectroscopy plotted as a function of $\phi^{-1/3}$. A linear fit (solid line) describes the experimental data well indicating that all samples contain crystalline domains with the same crystal structure.

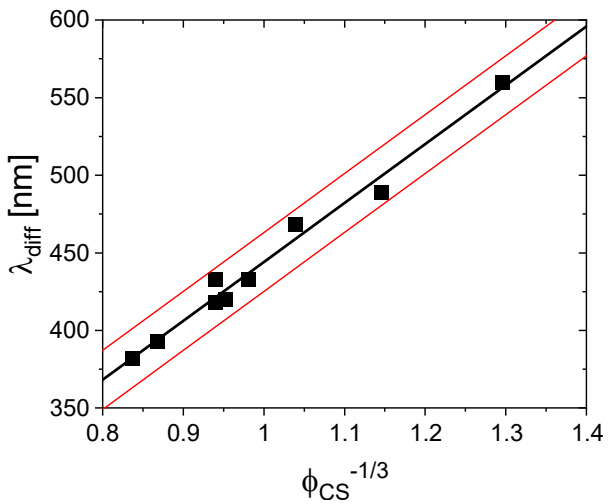

Figure S4.14. Results from Bragg peak analysis by UV-Vis spectroscopy. Plotted are the positions of the Bragg peaks (λ_{Bragg}) as function of $\phi^{-1/3}$. The black line represents a linear fit while the red lines show the respective error range.

The position of λ_{Bragg} depends on the lattice spacing (d_{hkl}), the refractive index of the crystalline sample ($n_{crystal}$) and the angle between the incoming beam and the sample:

$$\lambda_{\mathrm{diff}} = 2\, d_{\mathrm{hkl}} \sqrt{{n_{\mathrm{crystal}}}^2 - \sin\theta^2} \tag{S4.12}$$

We prepared samples in rectangular capillaries that were studied in standard transmission geometry. For an fcc (or rhcp) crystal structure, we expect the 111 plane to be parallel to the walls of the capillary. Therefore, the 111 plane is orthogonal to the beam in transmission geometry ($\theta = 0°$). Therefore, **Equation S4.12** simplifies to:

$$\lambda_{\mathrm{diff}} = 2\, d_{\mathrm{hkl}}\, n_{\mathrm{crystal}} \tag{S4.13}$$

The lattice constant *a* and the lattice spacing d_{hkl} are related by the following equation:

$$a = d_{\mathrm{hkl}} \sqrt{h^2 + k^2 + l^2} \tag{S4.14}$$

Combining **Equations S4.13** and **S4.14** we get:

$$a = \frac{\lambda_{\mathrm{diff}} \sqrt{h^2+k^2+l^2}}{2\, n_{\mathrm{crystal}}} \tag{S4.15}$$

The volume fraction of an fcc crystal with 3 + 1 spheres per unit cell can be calculated with the lattice constant *a* and the radius of the spheres *R*.

$$\phi = \frac{(3+1)\frac{4}{3}\pi R^3}{a^3} \tag{S4.16}$$

Using *a* according to **Equation S4.15**, we get:

$$\phi = \frac{(3+1)\frac{4}{3}\pi\, R^3}{\left(\frac{\lambda_{\mathrm{diff}} \sqrt{h^2+k^2+l^2}}{2\, n_{\mathrm{crystal}}}\right)^3} \tag{S4.17}$$

With **Equation S4.17** providing the relation between the volume fraction and the position of the diffraction peak, we can directly show the linear dependency between λ_{diff} and $\phi_{cs}^{-1/3}$ as experimentally verified in **Figure S4.14**:

$$\left(\frac{\lambda_{\mathrm{diff}} \sqrt{h^2+k^2+l^2}}{2\, n_{\mathrm{crystal}}}\right)^3 = \frac{(3+1)\frac{4}{3} R^3}{\phi} \tag{S4.18}$$

$$\lambda_{\mathrm{diff}} = \frac{2\, n_{\mathrm{crystal}} \sqrt[3]{(3+1)\frac{4}{3} R^3}}{\sqrt{h^2+k^2+l^2}}\, \phi^{-\frac{1}{3}} \tag{S4.19}$$

Regarding the scaling of ϕ_{cs} with the lattice constant *a* shown in **Figure 4.4c** in the main manuscript, we can rewrite **Equation S4.16** in the following way:

$$a^3 = \frac{16}{3}\pi {R_\mathrm{h}}^3 \frac{1}{\phi} \tag{S4.20}$$

$$a = \sqrt[3]{\frac{\pi 16}{3}} R_\mathrm{h} \phi^{-\frac{1}{3}} \tag{S4.21}$$

Here, we use the hydrodynamic radii (R_h) of the CS microgels. According to **Equation S4.21** the lattice constant would approach zero for high enough volume fractions. In reality, our soft and deformable CS microgels can only be packed to a certain limit. To take this into account, we add the offset *B* to describe our experimental findings:

$$a = \sqrt[3]{\pi \frac{16}{3}} R_\mathrm{h} \phi^{-\frac{1}{3}} + B \tag{S4.22}$$

Equation S4.22 is used to the guide to the eye shown in **Figure 4.4c** in the main manuscript. We used a value of B = 215 nm as offset. Regarding a fcc crystal structure this would result in a hard sphere radius of 76 nm which is close to the CS microgel radius of 77.9 nm that we determined from SAXS.

Characterization of Crystalline Samples

Due to the anisotropic scattering signal from dense samples, we can also apply analysis of the 2D detector images from SAXS. **Figure S4.15A** and **S4.15B** show the 2D SAXS patterns of two crystalline samples with ϕ_{cs} = 0.66 and ϕ_{cs} = 1.20. Both patterns show at least two orders of sharp Bragg peaks with six-fold symmetry indicative of hexagonally ordered planes aligned parallel to the capillary walls. In addition, a distinct amorphous ring is visible indicating the coexistence with fluid-like/disordered regions in the samples. Furthermore, some weak Bragg peaks are visible that are most likely caused by small, differently oriented crystal domains and will be excluded from further analysis.

Figure S4.15C and **S4.15D** show the overlay of the experimental scattering patterns with simulated ones obtained from Scatter.[171] Using an fcc crystal structure with small domain sizes[179] (~1 µm) we find qualitatively good agreement. We used a core shell model in our simulations with a homogeneous shell. This is comparable to our approach of fitting the form factor. The homogeneous shell is described by a constant scattering length density of the polymer shell in its radial density profile, which is not addressing the fuzzy sphere morphology known for microgels. The particle sizes used in the simulation were R_{core} = 6.5 nm and R_{total} = 91 nm for ϕ_{cs} = 0.66 and R_{total} = 83 nm for ϕ_{cs} = 1.20, respectively (see **Table S4.8**). The facts that both particle sizes are smaller than R_h =105 nm and that R_{total} decreases with ϕ_{cs} indicate that the microgels are in close contact and densely packed. The agreement between simulated and experimental scattering patterns is reasonable and points towards fcc as the crystal structure. This finding is in agreement with a previous SANS study of similar CS microgels.[73] However, we want to highlight that a precise analysis of the crystal lattice would require scattering data with many more orders of Bragg peaks.

While in our previous SANS study the main scattering contribution to $S(q)$ was related to scattering from the microgel shells, here the dominant contrast in SAXS comes from the small AuNP cores. The fact that we observe such sharp and pronounced Bragg peaks underlines that the AuNP cores are well centered in the microgels. In contrast pronounced variation in core location would lead to strong smearing of the structure factor.

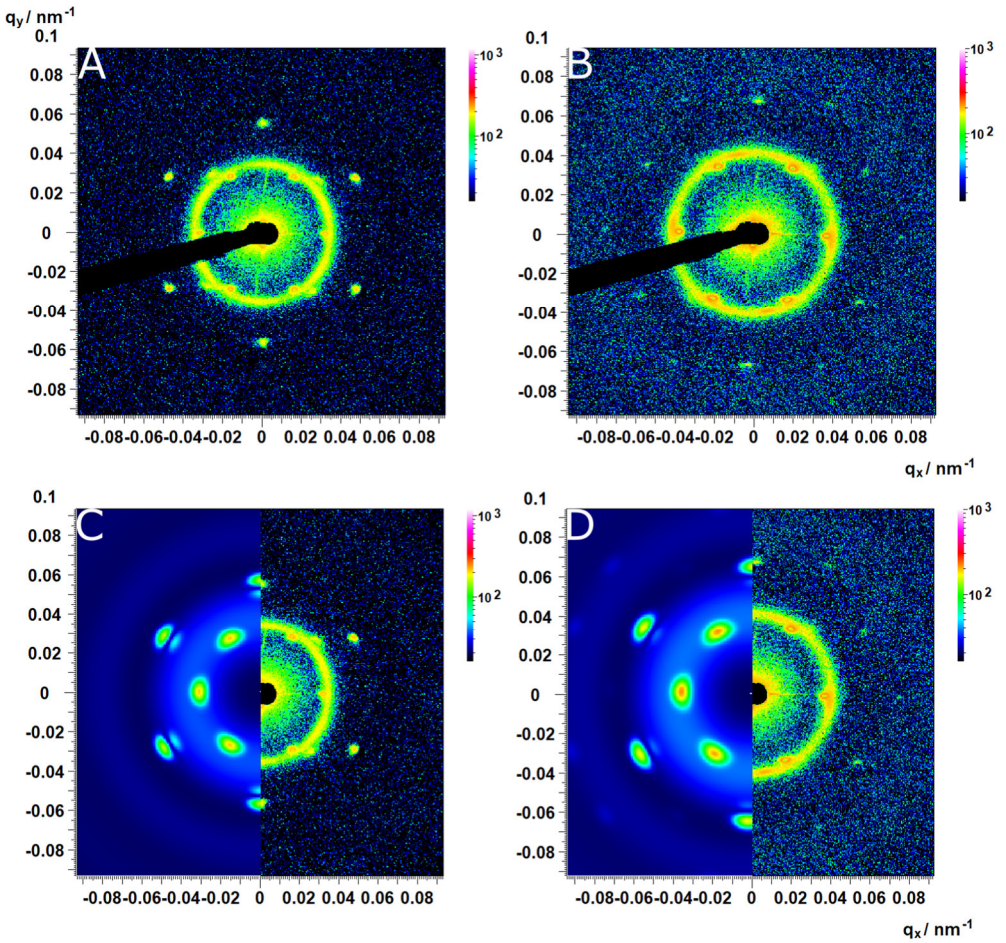

Figure S4.15. 2D SAXS patterns of the ϕ_{cs} = 0.66 (**A**) and ϕ_{cs} = 1.20 samples (**B**). (**C**, **D**) Scattering patterns simulated with Scatter software (left half) on top of the 2D SAXS patterns shown in (**A**) and (**B**) respectively.

Table S4.8. List of the parameters used for the simulation of the 2D scattering patterns of crystalline samples with the Scatter software.

	ϕ_{CS} = 0.66	**ϕ_{CS} = 1.20**
Crystal lattice	fcc	fcc
Unit cell *a* [nm]	322	281
Radial domain [nm]	1100	950
Azimuthal domain [nm]	750	650
Maximum hkl	2	3
Form Factor	Sphere (core + homogenous shell)	Sphere (core + homogenous shell)
R_{core} [nm]	6.54	6.54
σ_{core}	0.07	0.07
R_{CS} [nm]	91	83
ρ (ratio between SLDs)	0.01	0.01

5. Fluid-Solid Transitions in Photonic Crystals of Soft, Thermoresponsive Microgels

Published in *Soft Matter* **2022**, 19, 37, 7122-7135[131]

https://doi.org/10.1021/acs.macromol.2c00100

M. Hildebrandt,[1] D. Pham Thuy,[1] J. Kippenberger,[1] T. L. Wigger,[1] J. E. Houston,[2] A. Scotti,[3] and M. Karg[1]*

[1]Institut für Physikalische Chemie I: Kolloide und Nanooptik, Heinrich-Heine-Universität Düsseldorf, Universitätsstraße 1, D-40225 Düsseldorf, Germany

E-Mail: karg@hhu.de

[2]European Spallation Source ERIC, Box 176, SE-221 00 Lund, Sweden

[3]Institute of Physical Chemistry, RWTH Aachen University, Landoltweg 2, 52056 Aachen, Germany

5.1 Abstract

Microgels are often discussed as well-suited model system for soft colloids. In contrast to rigid spheres, the microgel volume and, coupled to this, the volume fraction in dispersion can be manipulated by external stimuli. This behavior is particularly interesting at high packings where phase transitions can be induced by external triggers such as temperature in case of thermoresponsive microgels. A challenge, however, is the determination of the real volume occupied by these deformable, soft objects and consequently, to determine the boundaries of the phase transitions. Here we propose core-shell microgels with a rigid silica core and a crosslinked, thermoresponsive poly-*N*-isopropylacrylamide (PNIPAM) shell with a carefully chosen shell-to-core size ratio as ideal model colloids to study fluid-solid transitions that are inducible by millikelvin changes in temperature. Specifically, we identify the temperature ranges where crystallization and melting occur using absorbance spectroscopy in a range of concentrations. Slow annealing from the fluid to the crystalline state leads to photonic crystals with Bragg peaks in the visible wavelength range and very narrow linewidths. Small-angle X-ray scattering is then used to confirm the structure of the fluid phase as well as the long-range order, crystal structure and microgel volume fraction in the solid phase. Thanks to the scattering contrasts and volume ratio of the cores with respect to the shells, the scattering data do allow for form factor analysis revealing osmotic deswelling at volume fractions approaching and also exceeding the hard sphere packing limit.

5.2 Introduction

Microgels and nanogels are composed of chemically and/or physically crosslinked polymer chains and are swollen by large amounts of solvent under good and typically even bad solvent conditions.[7, 8] With this large solvent content and their soft polymeric network structure the physical properties of microgels are complex featuring characteristics that are common for colloids, surfactants and macromolecules.[14-16, 22, 72, 185] Depending on the polymer composition, microgels can react to different external stimuli like temperature, pH or ionic strength.[23, 83, 186] The most prominent example of temperature responsive microgels is based on poly-*N*-isopropylacrylamide (PNIPAM). PNIPAM microgels undergo a pronounced volume phase transition (VPT) at a transition temperature of 32 °C or higher depending on the crosslinker density.[123, 124, 187] This behavior is related to the lower critical solution temperature (LCST) of PNIPAM in water.[188, 189] The precipitation of PNIPAM at temperatures above the LCST is also the basis for the rather straightforward synthesis of related microgels by (seeded) precipitation polymerization.[24, 119] The resulting microgels typically possess an inhomogeneous internal network structure resembling a gradient in crosslinking and consequently a polymer density that is decreasing in the outer periphery of the microgels. This gradient is the result of the faster consumption of the crosslinker during the precipitation polymerization and leads to a higher crosslinked core and a loose outer shell that also contains dangling chains.[25, 30, 79] This structure was also found for the polymeric shell of core-shell microgels that contain rigid nanoparticle cores such as gold[32] and silica.[115] In recent years the structural evolution of microgels in dense packings, either in 2-dimensional confinement or 3-dimensional samples in bulk dispersion, has attracted significant interest.[8, 121, 190] Despite their softness, microgels can (self-) assemble into highly ordered structures and, for example, crystalline phases similar to hard spheres were observed.[47, 66, 68, 72, 82, 90, 123, 124, 191] In contrast to rigid colloids, responsive microgels allow for external control of the microgel volume fraction due to their VPT behavior, *i.e.* for a given number concentration, *N*, for example temperature can be used to alter the volume fraction and thereby induce phase transitions.[36, 82] This behavior renders microgels particularly interesting for fundamental studies on crystallization, crystal melting and jamming. Surprisingly, little is known about the minimal temperature change needed to induce the fluid/solid and solid/fluid transitions.[47, 82, 192]

A challenge related to structural investigations at high volume fractions is the deswelling and faceting that alters the form factor of the microgels in dependence of their concentration.[76, 78, 125, 127, 129, 193-195] This behavior in combination with the inhomogeneous internal network structure and the high solvent contents hamper the determination of the volume fraction. The easier accessible quantity is the generalized volume fraction that considers the microgel volume in the dilute, non-interacting state.[36, 196] In-situ studies on phase transitions consequently require knowledge of the form as well as structure factor in dense packings that typically requires deuteration strategies and complex contrast variation using X-ray and neutron scattering.[78, 79]

In this work, we use silica-PNIPAM core-shell (CS) microgels to study fluid-solid transitions in dense packings. Our aims are (i) to determine transition temperatures where fluid-solid transitions occur, (ii) to study the structure and long-range order of both phases and (iii) to determine the microgel size and volume fraction in the concentration range where osmotic deswelling is expected to alter the microgel form factor. To do so, we use a combination of absorbance spectroscopy and synchrotron SAXS measurements for samples of various concentrations in the regime of dense packing. Importantly, the shell-to-core size ratio of the CS microgels was chosen to provide contrast for both, the shell and the core in SAXS investigations. This allows for the direct determination of structure as well as form factors at high volume fractions from single, individual scattering profiles. In the solid regime, we use Bragg peak analysis to study the crystal structure and domain size. Therefore, this work provides not only an ideal, new model system to tackle fundamental challenges related to studying and understanding phase transitions but also provides a direct link between the optical properties and the structure and long-range order of the CS microgel assemblies. This comparison is well justified because of the rather larger probed volumes in non-microfocus SAXS and standard optical spectroscopy giving access to the ensemble behavior rather than only local phenomena.

5.3 Experimental Section

Chemicals

L-arginine (PanReacAppliChem, ≥ 99%), cyclohexane (Fisher Scientific, analytical reagent grade), tetraethyl orthosilicate (TEOS, Sigma Aldrich, 98%), 3-(trimethoxysilyl)propyl methacrylate (MPS, Sigma Aldrich, 98%), *N*,*N*-methylenebis(acrylamide) (BIS, Sigma-Aldrich, 99%), potassium persulfate (PPS, Sigma-Aldrich, 99,0%) and heavy water (D_2O, Sigma Aldrich, 99.9%) were used as received without further purification.

N-isopropylacrylamide (NIPAM, TCI, >98%) was recrystallized from cyclohexane prior to use. Water was always used in ultra-high purity provided by a Milli-Q system (Merck Millipore) with a resistivity of 18.2 MΩ cm.

Synthesis of Silica Cores

Silicon dioxide seed particles were synthesized by an interphase-mediated condensation reaction,[114] where 82 mg (0.47 mmol) of L-arginine were dissolved in 78 mL of water in an 100 ml Erlenmeyer flask and an organic phase was added by the addition of 4.05 mL of cyclohexane. The reaction mixture was equilibrated for 30 minutes at 60°C in an oil bath and stirred only gently in order to prevent the aqueous and organic phase from mixing. Afterwards, 4.95 mL (22.2 mmol) of TEOS were added to the organic phase and the reaction was allowed to proceed for 72 h. The resulting silica particles were then surface-functionalized with MPS to increase the hydrophobicity as needed for the later precipitation polymerization. To do so, the aqueous phase was used without any purification and 9 mL of cyclohexane were added to the dispersion. After equilibration for 30 minutes at 60°C, 90 µL of MPS were added to the organic phase. After stirring for 24 h, the aqueous phase was separated and the mass content of the dispersion was determined. The obtained MPS-functionalized seeds were used without further purification.

Synthesis of CS Microgels

CS microgels were synthesized by free-radical precipitation polymerization using 4000 mg (35.4 mmol) NIPAM monomer, 817 mg (5.3 mmol) of BIS as crosslinking comonomer and 122 mg MPS-functionalized seeds dispersed in 600 mL of water. The reaction medium was degassed with nitrogen for 45 minutes at a temperature of 70°C. Then, 50 mg (0.19 mmol) of PPS dissolved in 1 mL of water were added in one shot to initiate the polymerization. The reaction was conducted for 6 h. The CS microgels were purified and concentrated by three centrifugation and redispersion (water) steps at 10000 rcf for 3 h followed by dialysis against pure water for at least seven days with multiple water exchanges.

Sample Preparation

CS microgel dispersions with defined mass contents used for absorbance spectroscopy and SAXS measurements were prepared by freeze-drying the respective amount of a stock dispersion with known mass content and redispersion of the microgels in the respective volume of D_2O or H_2O. CS microgel dispersions with only low mass contents were prepared by dilution of a stock dispersion. Dense samples at high concentrations were prepared in 0.2 mm x 4.00 mm x 10 mm rectangular, flat-wall capillaries (VitroTubes). The respective CS microgel dispersions were sucked into the capillaries by applying a small reduced pressure from one side of the capillary. Afterwards, the capillaries were flame-sealed with a hydrogen torch. After sample preparation, the samples were annealed using a temperature cycle. First, the samples were heated from 20 °C to 50 °C with a rate of 1.5 °C/h. Then the temperature was kept constant at 50 °C for 1 h. Finally, the samples were cooled back to 20 °C with a rate of 1.5 °C/h. These samples were used for SAXS and temperature-dependent absorbance spectroscopy. For SAXS measurements above 20 °C, we prepared CS microgel dispersions in 1 mm round capillaries (WJM Glas) and sealed with epoxy glue. The mass content of dilute CS microgel dispersions prepared for form factor measurements was adjusted to yield a volume fraction of around 0.03, in both swollen and collapsed state. A sample list is given in **Table S5.1** in the supporting information.

SAXS

Synchrotron SAXS experiments were performed on the CoSAXS beamline at the MAX IV synchrotron in Lund (Sweden). The instrument was equipped with an Eiger2 4M detector exhibiting a sensitive area of 155.1 × 162.2 mm^2 with total pixel sizes of 75 × 75 μm^2. SAXS measurements were recorded with acquisition times of 10 ms. The energy of the X-ray beam was 12.4 keV and the sample-to-detector distance was set to 6.85 m resulting in an effective *q*-range from 0.015 nm^{-1} to 0.5 nm^{-1} for the measurements performed at 20 °C. For the experiments performed at 40 °C the sample-to-detector distance was set to 11.04 m resulting in an effective *q*-range from 0.01 nm^{-1} to 0.5 nm^{-1}. Due to limited available beamtime and limitations in precisely controlling the sample temperature with our unusual sample geometry, experiments could only be performed at 20 and 40 °C. Detector images were radially averaged using a mask accounting for the inactive section of the detector boundaries and the beamstop. The resulting SAXS profiles were background corrected for D_2O.

In addition, SAXS measurements on selected samples were performed on a Xeuss 2.0 (XENOCS) equipped with a Pilatus3R 300K detector exhibiting a sensitive area of 83.8 × 106.5 mm^2 with total pixel sizes of 172 x 172 μm^2. The sample-to-detector distance was set to 1.2 m and the energy of the X-ray beam was 8.048 keV leading to an effective *q*-range of 0.03 nm^{-1} to 2 nm^{-1}. All measurements were performed in order to extract scattering intensities in absolute units with 1 mm glassy carbon as reference. Here we note that only the SAXS profiles based on measurements performed with the Xeuss 2.0 and using glassy carbon as reference exhibit absolute units. All data from synchrotron SAXS measurements of CS microgels in dense packings are reported in arbitrary units as the data analysis focusing on the form and structure factor does not require absolute scaling. Scattering profiles were recorded with acquisition times of 3600 s. The resulting SAXS profiles were corrected for the respective solvent as background. Samples were measured in round capillaries with a diameter of 1 mm and a wall thickness of 0.01 mm (WJM Glas). The concentration used for the CS microgels was 10 wt%, while silica particles were investigated in dilute state.

Radial averaged scattering profiles were analyzed with the SasView software.[197] The 2D SAXS patterns were simulated with the software Scatter by Förster and Apostol.[171]

Absorbance Spectroscopy

UV-Vis-NIR absorbance spectroscopy was performed on a SPECORD S600 (Analytik Jena) equipped with a temperature-controlled sample changer. We want to note that we measured the exact same samples by absorbance spectroscopy as by synchrotron SAXS.

Angle-Dependent Reflectance Spectroscopy

Reflectance spectroscopy was performed with a home-built setup consisting of a tungsten-lamp as light source and the Flame VIS-NIR Spectrometer (Ocean Insight) as detector. Both, detector and the light source were equipped with visible-NIR fibers to ensure free movement of the detector and light source in a goniometer-like fashion. The sample holder and fiber guides were 3D printed using a Prusa MK3 FDM printer. Measurements were performed in reflectance with the incident angle matching the angle of detection.

Dynamic Light Scattering

Temperature-dependent dynamic light scattering (DLS) measurements were performed with the Zetasizer Nano S (Malvern Panalytical) equipped with a laser of 633 nm wavelength and scattered light was detected in an angle of 173°. Measurements were conducted between 17°C and 60°C with steps of 0.2 °C. Three measurements with acquisition times of 60 s each were performed at each temperature step. The measurements were recorded in semi-macro cuvettes (polymethylmethacrylate, VWR) with CS microgel mass contents of 0.05 wt% in water. The hydrodynamic radii (z-average) were determined by cumulant analysis provided by the instrument software.

Angle-dependent DLS measurements were done on a 3D LS Spectrometer (LS Instruments, Switzerland) operated in 2D mode (pseudo cross-correlation) equipped with a HeNe laser (632.8 nm) as light source while the scattered light was detected with two avalanche photodetectors. A CS microgel dispersion, filtered through a 5 µm syringe filter (PTFE, Carl Roth) with a mass content of 0.01 wt% was prepared in a cylindrical glass cuvette (10 x 75 mm, borosilicate, Fisher scientific). Beforehand, the glass cuvette was treated with 2 vol% Hellmanex solution, followed by cleaning in an acetone fountain.

Finally, samples were placed in a temperature-controlled decalin bath (JULABO CF31, PT100 close to sample position) and measured in angles between 30° and 140° in 5° steps with acquisition times of 60 s. The recorded data was analyzed by the CONTIN algorithm[149] as implemented in AfterALV v.1.0e (Dullware).

Electrophoretic mobility Determination

The temperature-dependent electrophoretic mobility of the CS microgels dispersed in water was determined using a Litesizer 500 from Anton Paar.

Transmission Electron Microscopy

Transmission electron microscopy (TEM) was performed with a JEOL JEM-2100Plus TEM in bright-field mode. The acceleration voltage was set to 80 kV. Aqueous CS microgel dispersions were drop-casted on carbon-coated copper grids (200 mesh, Electron Microscopy Science) and dried for several hours at room temperature before investigation. TEM images were exported with the GMS 3 software from Gatan and the particle size was determined using ImageJ.[168]

5.4 Results and Discussion

5.4.1 Characterization in the Dilute Regime

We synthesized CS microgels that feature spherical silica nanoparticle cores and crosslinked PNIPAM shells. **Figure 5.1** summarizes the basic characterization in the dilute (non-interacting) regime. A schematic illustration of the microgel structure and the most relevant dimensions for this work are shown in **Figure 5.1a**. The SAXS profile in **Figure 5.1b** reveals the form factors measured at 20°C and 40 °C with contributions from the core in the high *q* range and contributions from the shell in the mid to low *q* range. Form factor analysis on the basis of a CS model with a homogeneous core and a shell with an exponentially decaying density profile (red line) provided a core radius of R_{core} = 18 ± 2 nm and a total radius of the CS microgels of 138 ± 14 nm at 20 °C. More details on the form factor analysis including the application of other models can be found in the Supporting Information (**Table S5.3** and **Figure S5.1**). Due to the thermoresponsive behavior of PNIPAM based microgels, the CS microgels collapse above the volume phase transition temperature (VPTT). This is also reflected by the scattering profile recorded at 40 °C, i.e. well above the VPTT. In this state a simple CS model with homogeneous core and shell can be used to describe experimental scattering data. The respective fit to the data yields a total radius of 90 ± 8 nm. For more details on the fitting parameters see **Table S5.2** in the Supporting Information.

Temperature-dependent DLS measurements reveal the typical VPT behavior of the PNIPAM shell in aqueous dispersion (**Figure 5.1c**). In the swollen state (20 °C) the CS microgels possess a hydrodynamic radius of R_h = 147 ± 3 nm. The radius continuously decreases with increasing temperature reaching a value of 97 ± 1 nm at 50 °C. The VPTT is approximately 35.0 °C. We want to note that we used 15 mol% of BIS in the synthesis (nominal) which explains the slightly higher temperature of the VPT as compared to 'classical' PNIPAM microgels. This is in agreement with findings from previous studies on comparable systems.[32, 73] Since the precision of the hydrodynamic dimensions in the swollen and collapsed state is of utmost importance for the further analysis in this work, we used angle-dependent DLS in addition to the fixed angle results. The good agreement between both sets of measurements can be seen in **Figure S5.2** in the Supporting Information.

In addition, we recorded the temperature-dependent electrophoretic mobility of the CS microgels under dilute conditions (**Figure S5.3**) revealing the expected behavior with rather low mobilities (- 1.23 µmcm/Vs, 20 °C) in the swollen state, followed by a decrease when the particles undergo the VPT (- 2.23 µmcm/Vs, 40 °C). Here, the negative electrophoretic mobility is related to the initiator PPS, introducing negative charges and a decrease in negative mobility is associated to an increase in charge density of the microgels.

Figure 5.1d shows a representative TEM image of the CS microgels where the cores and shells can be clearly distinguished due to their difference in contrast. The image supports that each microgel contains a single nanoparticle core with an average radius of R_{core} = 17.5 ± 1.6 nm. SAXS measurements of the bare silica cores (**Figure S5.4**) are in good agreement with the results from TEM leading to an average radius of 17.8 ± 1.8 nm. A histogram from size analysis of a large number of microgels along with additional TEM images is provided in the Supporting Information (**Figure S5.5**). We found that less than 1% of the microgels feature more than one or no core. As expected, the microgel shells significantly shrink due to the sample preparation and the high vacuum conditions during TEM investigation. This is illustrated by the red circle in **Figure 5.1d** that highlights the swollen state dimensions determined by DLS.

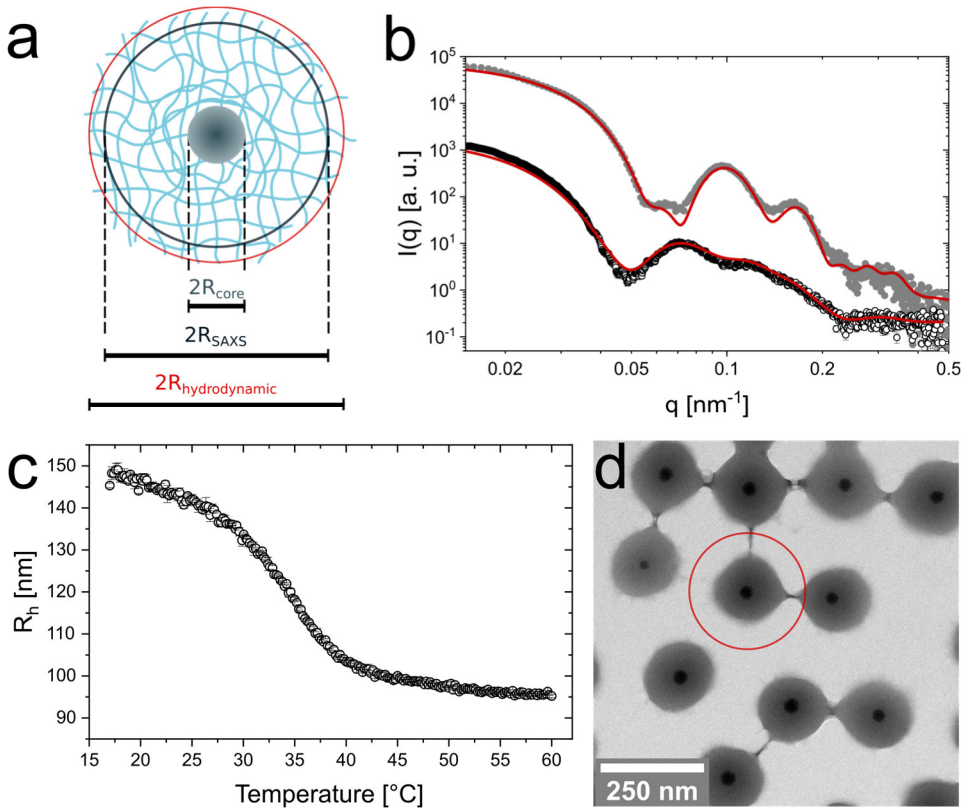

Figure 5.1. Characterization of the CS microgels in the dilute state. (**a**) Schematic illustration of a single CS microgel with the most relevant radii. R_{core} is the radius of the core, R_{SAXS} the total microgel radius from SAXS and R_h is the hydrodynamic radius. (**b**) Synchrotron SAXS profile measured from a dilute dispersion (0.45 wt%) at 20 °C (black circles) and (1.25 wt%) at 40°C (grey dots). In case of the profile recorded at 20 °C, the solid line corresponds to a form factor model containing a homogeneous, isotropic core and a shell with an exponentially decaying density profile. A core-homogeneous-shell model was applied to fit the profile recorded at 40 °C. (**c**) Hydrodynamic radius as function of temperature (black circles) obtained from temperature-dependent DLS measurements (**d**) Representative TEM image. The red circle indicates the total dimensions obtained from DLS at 20°C.

5.4.2 Fluid-Solid Transitions in Dense Packings

Similar to hard spheres, microgels including our CS microgels are expected to crystallize at large enough packing fractions. Due to the total size of our CS microgels approaching visible wavelength scale, absorbance spectroscopy is a convenient tool to monitor the phase behavior.[47, 73] **Figure 5.2a** shows Vis-NIR absorbance spectra of samples with 5.4 to 10.9 wt% CS microgels obtained directly after sample preparation (dashed lines) and after the SAXS investigation in the solid regime (solid lines) which is addressed later in this work. Prior to the SAXS investigation of the solid regime, the samples were annealed at 50 °C followed by slow cooling to 20 °C. More details on the annealing procedure and the parameters that we have identified for the best annealing conditions can be found in the Supporting Information (**Figure S5.6**). The annealing process reduces the linewidths of the narrow Bragg peaks, enhances their maximum intensity indicating a reduction in incoherent scattering. At the same time, only small spectral shifts are observed. For the lowest concentration (5.4 wt%) a Bragg peak is not constantly present (**Figure S5.7**). This can be attributed to a liquid-crystal coexistence phase and potentially local concentration differences right after sample preparation. During the annealing, the crystallites melt and the resulting fluid homogenizes resulting in a fluid phase that even remains after slow cooling to room temperature where the volume fraction is significantly increased. This behavior indicates that the volume fraction of this particular sample in the swollen state is close to the threshold volume fraction where crystallization occurs. In **Figure S5.7** in the Supporting Information, additional absorbance spectra recorded at different points in time can be found while **Figure S5.8** shows results from angle-dependent reflectance measurements. The reflectance data show the expected blue shift of the Bragg peak for increasing angle of incidence (with respect to the normal).

What happens during the heating and cooling cycles in our annealing protocol can be nicely followed by absorbance spectroscopy. It is notable that the sample volume probed in Vis-NIR spectroscopy is much larger than the volumes probed by microscopy[192] or microfocus SAXS[82] and, therefore, our approach provides a more representative ensemble picture of the phase behavior of the CS microgels. Detailed information about the temperature cycling can be found in the Supporting Information (**Figure S5.9**).

Figure 5.2b shows as an example the spectra recorded during the heating in 0.3 °C steps starting at 20 °C for the sample with 7.3 wt% CS microgels. During the first approximately 10 °C of heating the Bragg peak remains nearly unchanged in position, intensity and full width at half maximum (FWHM). When approaching a temperature of 30 °C and higher (inset in **Figure 5.2b**), we can see a decrease of the Bragg peak accompanied by a blue shift and broadening. These changes are related to a significant shrinking of the PNIPAM shell that reduces the microgel volume fraction ϕ. This is related to the VPT of the microgels (see **Figure 5.1c**). At temperatures of 31.7 °C and higher, the Bragg peak cannot be observed anymore indicating that only a fluid phase is left. To follow this phase transition more closely, **Figure 5.2c** shows the evolution of the Bragg peak absorbance with temperature for a heating (red symbols) and cooling (blue symbols) series. The data for both, the heating and cooling cycle, almost perfectly overlap with very little hysteresis and slightly smaller inflection points for the cooling cycle (30.7 °C in contrast to 31.6 °C for the heating cycle). Surprisingly, the temperature window where the solid-fluid (fluid-solid) transition occurs is very narrow as indicated by the green vertical bar. Within approximately 2 °C the crystals completely melt during the heating cycle and reversibly recrystallize during the cooling cycle. In addition, a change in temperature of a few millikelvin is enough for the dispersion of CS microgels to undergo the change from a partially crystalline (green transition area) to a completely fluid phase. It is important to note that data shown were not normalized or anyhow modified. We simply take in account the maximum absorbance values at the respective position of the Bragg peak with only the incoherent background scattering being subtracted. This background subtraction is the reason why the plotted intensities remain nearly unchanged for temperatures outside the green-colored area. Following only the development of the coherent signal reveals the very sharp and reversible phase transition. The same heating/cooling study was also performed for the samples containing 9.1 and 10.9 wt% CS microgels. The respective data can be found in the Supporting Information (**Figure S5.10** and **Table S5.4**). In addition, we performed time-dependent Vis-NIR absorbance spectroscopy in the temperature range of the phase transition between the fluid and solid state, to verify that the samples reached equilibrium at the time of the measurement. As presented in **Figure S5.11** in the Supporting Information, the intensity of the Bragg peak changes within the first 100 s, after reaching the target temperature and from this point on stays constant.

Therefore, not only the CS microgels show a fast response towards temperature,[198] but also the phase behavior exhibits a rather fast response towards temperature changes (~100 s), and the suspension quickly reaches equilibrium when temperature steps are sufficiently small. Here, we conclude that the samples are at equilibrium when spectra are recorded after 720 s equilibration time.

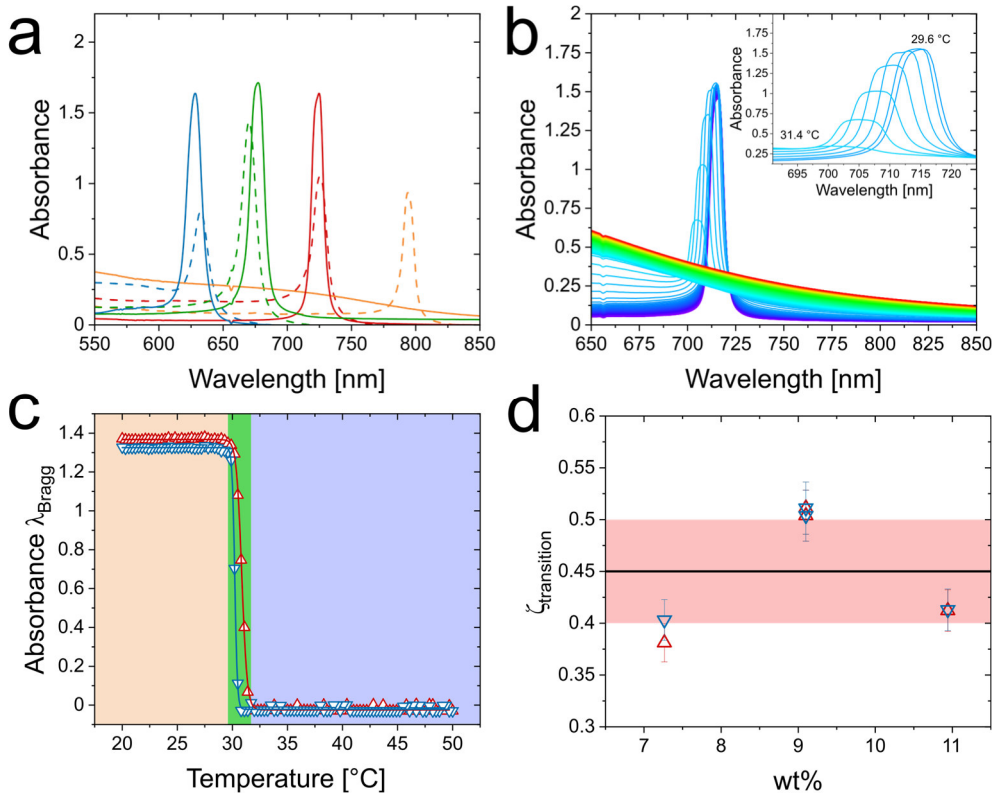

Figure 5.2. Phase behavior of CS microgels. (**a**) Vis-NIR absorbance spectra of CS microgel dispersion with mass contents of 5.4 wt% (orange), 7.3 wt% (red), 9.1 wt% (green) and 10.9 wt% (blue) after preparation (dashed lines) and after SAXS experiments (straight lines, crystalline state). (**b**) Temperature-dependent Vis-NIR absorbance spectra of 7.3 wt% CS microgel dispersion. Spectra were recorded from 20°C (violet) to 50°C (red) in 0.3 °C steps. The inset shows the temperature-dependent evolution of the Bragg peak at temperatures between 29.6°C and 31.4°C. (**c**) Temperature-dependent evolution of the intensity of the Bragg peak for the heating (red triangles) and cooling procedure (blue triangles). The green area indicates the temperature range where the Bragg peak disappears/reappears. (**d**) Threshold value of the generalized volume fraction where the transitions between fluid and crystalline phases occur in dependence of the mass contents of the respective samples. The horizontal, black line indicates the average volume fraction of 0.45 needed for crystallization and the red area is related to the respective standard deviation.

Similar to our previous works on gold-PNIPAM CS microgels,[32, 81] we can use the SAXS scattering contribution of the nanoparticle cores (here: silica) to determine the microgel number concentration, *N*. A detailed explanation for the data treatment and calculations is given in the Supporting Information (**Figures S5.12-14** and **Tables S5.5-8**). Having access to *N* allows us to determine the generalized volume fraction ζ that is based on the hydrodynamic microgel volume in the dilute, non-interacting regime available from our DLS data. **Figure S5.15** in the Supporting Information shows the evolution of ζ with temperature. We can now use the transition temperatures determined from the spectroscopic data, listed in **Table S5.4** of the Supporting Information, to determine the values of ζ where the solid-fluid (fluid-solid) transitions occur. **Figure 5.2d** shows the respective results for the heating and cooling cycles as a function of mass content of the samples. The data for the three different concentrations scatter around the average value of $\bar{\zeta}_{\text{transition}}$ = 0.45 ± 0.05 (black line in **Figure 5.2d**) without a clear trend. The hysteresis between cooling (blue symbols) and heating (red symbols) is the largest for the sample at a concentration of 7.3 wt% and almost not observable for 9.1 and 10.9 wt%. Here, the 2 °C interval, where the CS microgels undergo the phase separation corresponds to an approximate change in ζ of around 0.05 ± 0.01. As the transition temperatures are close to the VPT, we propose that the microgels are nearly in the collapsed state and thereby can be hardly collapsed further. We want to note that the volume fractions are well below the random close packing and, therefore, the generalized volume fraction can correspond to the real packing fraction.[80, 125] Our mean value of 0.45 is slightly smaller than the freezing volume fraction of hard spheres (0.494).[120] We attribute this small deviation to an electrostatic contribution due to the anionic radical initiator used in the precipitation polymerization rendering the CS microgels charged.

5.4.3 Structure in the Fluid Regime

We performed synchrotron SAXS measurements on the dense samples at 40 °C, i.e. where the PNIPAM shells are collapsed. According to the analysis from absorbance spectroscopy, all samples should be in a fluid-like state at this temperature (see **Figure S5.10** in the Supporting Information) as Bragg peaks were not observed. **Figure 5.3a** shows a 2D detector image of a 9.1 wt% CS microgel dispersion recorded at 40 °C. A distinct fluid structure factor contribution, as well as some oscillations related to the form factor are visible in the isotropic scattering pattern. Additional detector images recorded from samples with different mass contents are provided in the Supporting Information (**Figure S5.16**). The results agree very well to the observation from absorbance spectroscopy. The radially averaged scattering profile is shown in **Figure 5.3b** (black circles). The profile shows a pronounced structure factor contribution in the range of low q (< 0.05 nm^{-1}). The mid to high q regime is dominated by the form factor of the CS microgels (see also **Figure 5.1b**). Scattering profiles for samples with 5.4 to 12 wt% CS microgel content are shown in **Figure S5.17** in the Supporting Information. The data reveal the expected changes in the structure factor, i.e. a shift of the first structure factor maximum to larger q for increasing concentration. At the same time the form factor contribution remains unchanged. This implies that the microgel do not change due to osmotic deswelling in the collapsed state, at least in the range of concentrations studied. Consequently, the structure factor can be calculated directly from the scattering intensities of the dense samples ($I_{conc}(q)$) using the known form factor ($S(q) = I_{conc}(q)/P(q)$). Due to a small structure factor contribution in the experimental scattering profile of the dilute CS microgel dispersion (1.25 wt%) recorded at 40 °C (see **Figure S5.18**), we did not use the experimental data in the range of low q (< 0.025 nm^{-1}) for this calculation. In the latter case, the theoretical form factor as shown by the fit in Figure 1b was used. **Figure 5.3b** shows the resulting structure factor (green circles) for the 9.1 wt% sample. The vertical dashed line highlights the value in q separating the range in q where the form factor fit was used for the calculation (q < 0.025 nm^{-1}) and the range where the experimental data (1.25 wt%) were used (q > 0.025 nm^{-1}). More details on this data treatment are provided in the Supporting Information (**Figure S5.19**). The Percus-Yevick[184] (PY) hard sphere structure factor fit describes the determined structure factor almost perfectly.

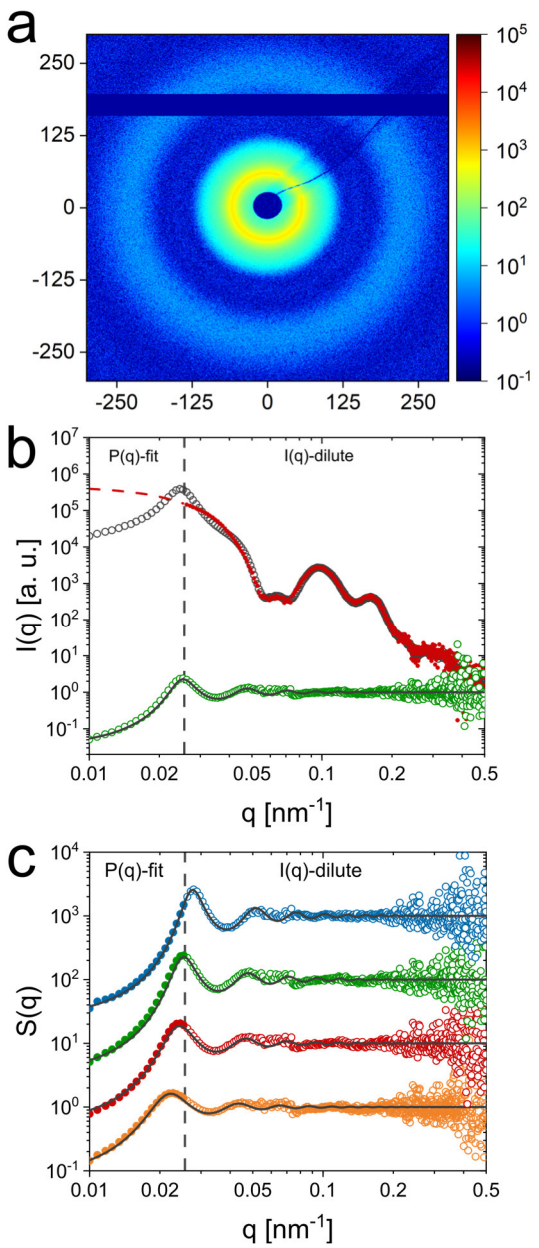

Figure 5.3. Synchrotron SAXS analysis of dense CS microgel dispersions, recorded above the VPTT at 40°C. Samples from 5.4 to 9.1 wt% were prepared in D_2O and the 12 wt% dispersion in H_2O. (**a**) 2D detector image (pixels as units) with a pronounced contribution of a liquid structure factor. The horizontal bar in dark blue corresponds to the inactive area between the panels of the SAXS detector. These areas are masked during data reduction. (**b**) Structure factor (green circles) extracted from the scattering profile of a 9.1 wt% CS microgel dispersion recorded at 40 °C (black circles). The dashed red line corresponds to form and the solid black line to the structure factor fits (Percus-Yevick) and red dots correspond to the (rescaled) experimental scattering profile of the dilute CS microgel dispersion at 40 °C. The dashed vertical line highlights the threshold value where either the form factor fit (q < 0.025 nm^{-1}) or the experimental scattering signal of the dilute CS microgel dispersion (q > 0.025 nm^{-1}) was used for the structure factor calculation. (**c**) Extracted structure factors for CS microgel dispersions from scattering profiles recorded at 40 °C of 5.4 wt% (orange circles), 7.3 wt% (red circles), 9.1 wt% (green circles) and 12 wt% (blue circles). The solid black lines correspond to structure factor fits (Percus-Yevick). The structure factor profiles are shifted vertically for the sake of clarity.

Figure 5.3c compares the extracted structure factors for the samples in the range of 5.4 to 12 wt% with increasing concentration from bottom to top. All data can be nicely fitted by the PY structure factor model. We also observe the expected shift of the first structure factor maximum to larger q for increasing concentration. At the same time, we observe a reduction in structure factor peak width. Results from the structure factor analysis are summarized in **Table S5.9** in the Supporting Information. The effective hard sphere volume fraction increases from 0.32 for 5.4 wt% to 0.46 for 12 wt%. At the same time, the effective hard sphere radius decreases from 142 to 124 nm – values that are significantly larger than the value of the hydrodynamic radius in the collapsed state (40 °C) as determined from DLS. The significant deviation between R_h and the effective hard sphere radius obtained from the fit of the data with the PY model indicates a pronounced influence of electrostatic interactions between the CS microgels, which are not considered in the classical hard sphere model. Therefore, the extracted values for the hard sphere volume fractions and for the effective hard sphere radii do not reflect the real packing fraction and size of the CS microgels. For a more realistic description a more complex model would be required, ideally together with support from theoretical calculations or computer simulations. However, the focus of the present work is rather on the fluid-solid transition than on the role of electrostatic interactions. The latter will be carefully addressed in a follow-up work. Noteworthy, when the CS microgels undergo the VPT, the effective charge density also increases, as reflected by the electrophoretic mobility (**Figure S5.3**). This enhances the influence of electrostatics in the phase behavior of the microgels.

We attribute the decrease in hard sphere radius to an increasing electrostatic screening as the microgel and consequently the counterion concentration increases. **Figure S5.20** in the Supporting Information shows only the low q region of the structure factors and reveals the good match between PY structure factor fit and experimental data towards q = 0 nm^{-1}. This underlines the hard sphere-like behavior of the CS microgels in the collapsed state. In swollen state experimental structure factors of microgels were shown to deviate from the hard sphere approximation which was related to the soft character of the interaction potential.[199]

5.4.4 Structure in the Solid Regime (Crystalline)

The absorbance spectra of **Figure 5.2a** indicate that the crystallinity is significantly improved by the applied temperature annealing protocol. To verify this and to determine the crystal structure, we used synchrotron SAXS. **Figure 5.4a** shows the 2D detector image recorded for the 9.1 wt% sample at 20 °C, as a representative example. Pronounced and sharp Bragg peaks of at least 10 orders of diffraction are observed. Furthermore, the six-fold symmetry of the diffraction pattern is clearly visible indicating the alignment of hexagonal close-packed planes parallel to the capillary wall.[82] Apparently, SAXS studies on microgels and CS microgels in dense packings are scarce and from reported 2D diffraction patterns typically only up to four orders of diffraction are observed.[81, 82, 200] Although not directly comparable due to the different experimental smearing and detector resolution, analysis of colloidal crystals of microgels by small-angle neutron scattering (SANS) revealed diffraction with Bragg peaks of four diffraction orders.[73] The long-range order and superior crystallinity of our system can also be observed for the 7.3 and 10.9 wt% sample as shown in the Supporting Information (**Figure S5.21)** Here, the combination of the presented SAXS pattern and the Vis-NIR spectra recorded from the same samples (**Figure 5.2a**) allow for a direct correlation between the order of the assemblies and the obtained spectra. Previous works on colloidal crystals in microgel suspensions made use of optical spectroscopy to follow and/or identify crystallization but could not provide a direct link between optical properties and crystal structure as well as degree of order. Notably, the synchrotron SAXS (non-microfocus) and Vis-NIR spectroscopy applied here, both illuminate a relatively large volume. Therefore, the scattering data and optical spectra provide a representative ensemble picture of the crystalline assemblies of the CS microgels. **Figure 5.4b** shows the radially averaged data (black circles) corresponding to the detector image shown in **Figure 5.4a**. The structure factor with pronounced and well distinguishable Bragg peaks is clearly visible in the mid to low q region (q < 0.15 nm^{-1}). In addition, the form factor minima related to the core ($q \approx 0.23$ nm^{-1}) and the microgel shell ($q < 0.1$ nm^{-1}) are clearly visible. Due to the distinct intensity minima, we can model the form factor even in the densely packed state where analysis is typically difficult/not possible due to changes in the microgel size and shape (osmotic deswelling and faceting)[74, 75, 129] and the superposition with the structure factor. The red line in **Figure 5.4b** corresponds to our modeled form factor.

Here, the CS structure of our microgels simplifies the modeling process, because the core contribution is well resolved and isolated from the shell as well as structure factor contribution. Consequently, also the particle number density, N, can be precisely determined through the form factor contribution of the core. The contribution of the shell can be modeled based on the distinct form factor minimum at $q \approx 0.05$ nm^{-1}. With the resulting form factor, $P(q)$, in the concentrated regime, we can calculate the structure factor by dividing the measured scattering intensity by $P(q)$ similar as has been presented before in the fluid regime.

The extracted structure factor is shown in **Figure 5.4b** (green circles). In the high q region $S(q)$ approaches the expected value of 1. This underlines that the modelled form factor describes the high q region precisely. In the limit of low q, $S(q)$ approaches very low values close to zero. Extrapolation to $q = 0$ nm^{-1} reveals a value $S(0) = 0.03$.

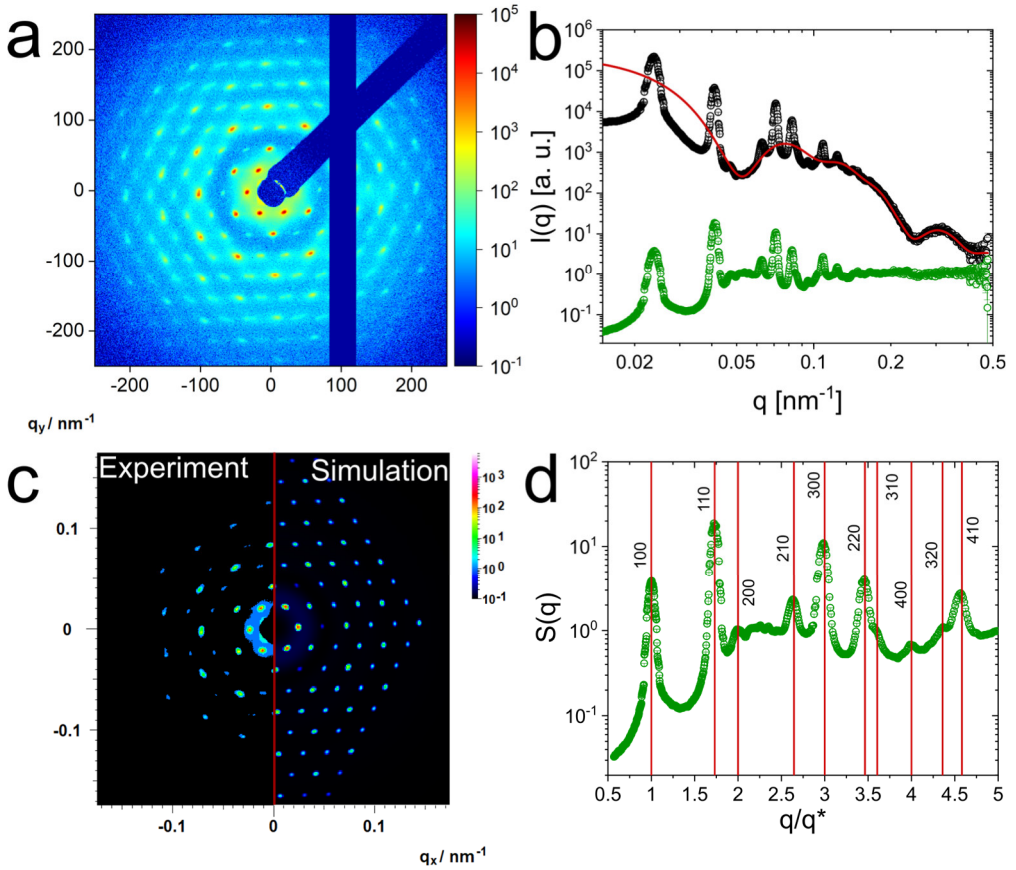

Figure 5.4. Synchrotron SAXS analysis of crystalline sample with 9.1 wt% CS microgels. (**a**) 2D detector image (pixels as units) with pronounced Bragg peaks of several orders. The dark blue bars are the boundaries of the detector panel (vertical) and the arm of the beam stop (diagonal). (**b**) Corresponding radially averaged data (black circles). The red solid line corresponds to the modelled form factor. The green circles correspond to the to the structure factor extracted from the 2D radial average of panel (**a**). (**c**) Measured scattering data (2D) on the left and the corresponding hcp simulation on the right. (**d**) Structure factor from experiment with theoretical peak positions (vertical red lines) corresponding to a hcp crystal structure. The x-axis is normalized to the position of the first peak of the structure factor (q^* = 0.0238 nm^{-1}).

The large number of Bragg peaks allows us to simulate theoretical scattering patterns in direct comparison to the recorded 2D detector images. **Figure 5.4c** shows the good agreement with a hcp lattice. The Bragg peaks from simulation do not only match the experimental data in terms of peak positions and intensities but also the azimuthal and radial peak widths match closely. Detailed information on the simulation parameters and additional simulations performed on the 7.3 and 10.9 wt% samples are presented in **Table S5.10** and **Figure S5.22** in the Supporting Information.

To further support the hcp structure, the agreement between measured peak positions and theoretical ones for a hcp lattice is also seen in **Figure 5.4d**. Here, the experimental structure factor is plotted with a normalized q axis. Normalization was done based on the position of the first structure factor maximum, q^*. The vertical, red lines correspond to the calculated positions for a hcp lattice:

$$\frac{q}{q^*} = \frac{d_{hkl}}{d_{100}} = \frac{\sqrt{\frac{4}{3}(h^2+hk+k^2)+\frac{a^2}{c^2}l^2}}{\sqrt{\frac{4}{3}}} \tag{5.1}$$

Here, d_{hkl} refers to the lattice spacing with Miller indices h, k and l. In order to describe the dimensions of the unit cell a refers to the lattice constant and c to the height of the unit cell. The first Bragg peak to be expected is assigned to the d_{100} lattice and for a closed packed structure of spheres the ratio between c and a is fixed to a value of $(8/3)^{1/2}$. The theoretical Bragg peaks which we could not identify in our scattering profile as well as a comparison to an fcc lattice are shown in **Figure S5.23** in the Supporting Information. It is known that hard spheres crystallize into close-packed hexagonal layers, e.g. fcc lattices. Because of the small free-energy difference between fcc and hcp, random stacking is often observed, i.e. rhcp structures.[178, 181, 201] For microgels a similar behavior has been reported in literature.[69, 71, 82] These works show the simultaneous presence of fcc and hcp structures which can be considered as rhcp structure. For hard spheres it was found that the nucleation process can influence the proficiency of the system for crystallizing into a fcc or hcp structure.[202] Therefore, we suggest the sole presence of the hcp crystal structure to be attributed to the slow annealing procedure of our samples, which we assume is of high relevance for the nucleation process.

A similar analysis for samples in a range of concentrations from 5.4 to 10.9 wt% is presented in **Figure 5.5a**. Here the q axis is again normalized by q^*. Only in case of the 5.4 wt% sample that revealed a mostly fluid character after long temperature annealing, the data were normalized by the second structure factor maximum (110 plane). The first structure factor maximum located at $q \approx 0.02$ nm^{-1} is mostly attributed to a fluid like structure factor while the second one at $q \approx 0.03$ nm^{-1} exhibits a small width and more distinctive shape and therefore is considered as a Bragg peak. We relate the Bragg peak to small residual crystallites. In **Figure S5.24** we show a fit of the fluid-like structure factor. From this, we conclude that the volume fraction of the CS microgels in the 5.4 wt% dispersion is very close to the freezing concentration. As **Figure 5.2c** indicates, only small change in temperature are required to induce the start of the crystallization or, vice-versa, melting.

For all samples with mass contents above 5.4 wt%, we find a nearly perfect agreement between the experimental and the theoretical positions of the Bragg peaks assigned to the hcp crystal structure. In **Figure 5.5b,** we show the linear relation of the Bragg peak position, q_{hkl}, and the d-spacing between lattice planes for hcp structures. The slopes of the linear fits provide the respective lattice constants, a, according to:

$$q_{hkl} = \frac{2\pi}{a}\left(\frac{4}{3}(h^2 + hk + k^2) + \frac{3}{8}l^2\right)^{\frac{1}{2}} \tag{5.2}$$

Table S5.11 in the Supporting Information lists the determined values of a. In addition, the lattice constant is accessible from the simulations of the 2D detector images like shown in **Figure 5.4c** as well from the positions of the Bragg peaks from absorbance spectroscopy, λ_{diff}:

$$a = \frac{\lambda_{\mathrm{diff}}\sqrt{\frac{4}{3}(h^2+hk+k^2)+\frac{3}{8}l^2}}{2\,n_{\mathrm{crystal}}} \tag{5.3}$$

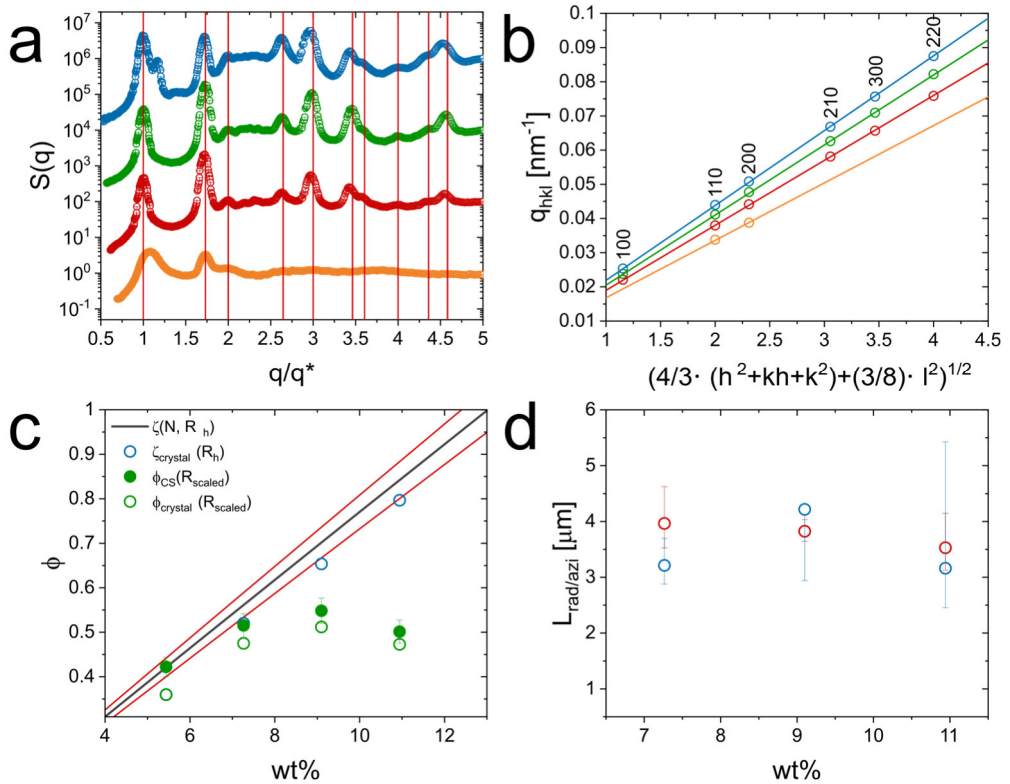

Figure 5.5. Extraction of the lattice constant *a* and the volume fraction ϕ of the CS microgels in the colloidal crystals. (**a**) $S(q)$ of CS microgel dispersions with mass contents of 5.4 wt% (orange circles, q^* = 0.0195 nm^{-1}), 7.3 wt% (red circles, q^* = 0.0221 nm^{-1}), 9.1 wt% (green circles, q^* = 0.0238 nm^{-1}) and 10.9 wt% (blue circles, q^* = 0.0255 nm^{-1}). The straight vertical lines correspond to the theoretical Bragg peak positions assigned to the hcp crystal structure. The x-axis is normalized to the position of the respective first structure factor maximum except for the 6 wt% sample (orange circles) where the position was normalized by the position of the second peak. The profiles are offset along the ordinate for clarity. (**b**) Extraction of the lattice constant *a* via the linear dependence of the position of the Bragg peak on the *d*-spacing. (**c**) Volume fraction ϕ of the CS microgel in dependence of the mass content. The black line corresponds to the generalized volume fraction, based on particle number concentration and R_h of the CS microgel. The red lines indicate the standard deviation. The blue circles and green dots are related to the volume fraction of the particles in the crystal based on the lattice constant and R_h (blue) respectively $R_{h,scaled}$. Green circles indicate the volume fraction based on particle number concentration and $R_{h,scaled}$. (**d**) Radial (red) and azimuthal (blue) sizes of the coherently scattering domains.

For the hcp crystal structure, we assign the Bragg peak from the absorbance spectra to the 002 lattice. **Figure S5.25** in the Supporting Information shows the good agreement of the lattice constants, *a*, as obtained from analysis of SAXS data and absorbance spectra. The lattice constant decreases from 322 nm (7.3 wt% sample) to 284 nm (10.9 wt% sample). We can now calculate the volume fraction of the crystalline samples, ϕ_{crystal}, based on the unit cell dimensions:

$$\phi_{\text{crystal}} = \frac{(3+3)\frac{4}{3}\pi(R_h)^3}{\frac{3\sqrt{3}\sqrt{\frac{8}{3}}a^3}{2}} = \frac{8\,\pi(R_h)^3}{3\sqrt{2}a^3} \tag{5.4}$$

Figure 5.5c compares the determined volume fractions based on the hydrodynamic radius in the dilute state, i.e. the generalized volume fraction, ζ (blue circles and black line) and using radii that we determined from the form factor analysis of the SAXS data directly in the densely packed state. The latter values allow us to rescale the hydrodynamic radius, R_h, using the obtained radii from SAXS in the dilute ($R_{\text{SAXS dil.}}$) and concentrated state (R_{SAXS}):

$$R_{\text{h,scaled}} = \frac{R_{\text{SAXS}}}{R_{\text{SAXS dil.}}} R_{\text{h}} \tag{5.5}$$

We see a good agreement between the volume fractions calculated based on R_h with the number concentration *N* (black line) and the volume fraction calculated with R_h and the unit cell dimensions (blue circles) shown in **Figure 5.5c**. The red lines indicate the standard deviation of the calculated ζ based on the number concentration. The values of ζ obtained from the unit cell dimensions lie within the respective standard deviation. This underlines the reliability of the extraction of ζ via the number concentration obtained from the scattering of the core in SAXS.

The calculated values of the effective volume fractions are presented in **Figure5.5c** as green symbols. The calculation is either based on the particle number concentration from SAXS measurements (filled, green symbols) or based on the lattice constants as obtained from SAXS measurements on crystalline samples (open, green circles). The data follow the same trend with slightly smaller volume fractions obtained from the crystal structure analysis. Again, the difference lies within the standard deviation with exception for the 5.4 wt% sample, where the lattice constant is related to small crystallites not representing the average bulk volume fraction of the dispersion. When reaching the threshold of crystallization (**Figure 5.2d**) we observe a significant deviation of the volume fraction from the generalized volume fraction.

This is most pronounced for the 9.1 and 10.9 wt% samples where the volume fraction approaches values of approximately 0.52 which is far away from the closed packed volume fraction of 0.74 for hard spheres. This is in agreement to the values reported by Scotti based on comprehensive analysis of microgels in dense packing using SANS.[80]

In addition, we show the respective volume fractions based only on R_{SAXS} without any normalization to the hydrodynamic radius R_h in the Supporting Information (**Figure S5.26**). Due to the smaller total size of the CS microgels as observed by SAXS, the determined volume fractions are significantly smaller although still following the trend seen in **Figure 5c**.

To analyze the domain sizes of the crystalline samples, we use the Williamson-Hall analysis[203] that is based on the azimuthal and radial widths of the Bragg peaks as shown in **Figure S5.27** in the Supporting Information. This analysis revealed very low strains below 1% for our colloidal crystals and coherently scattering domain sizes between 3 and 4 µm (**Figure 5.5d**). These values are in good agreement with the slightly smaller domain sizes from analysis of the 2D detector images using Scatter. Based on the total size of our CS microgels we estimate that these domain volumes contain approximately 2000 microgels per single domain.

5.4.5 Osmotic Deswelling in the Solid Regime (Crystalline)

As reported in the literature, the concentration of counterions, which determines the osmotic stress of the suspension, grows with increasing microgel concentration for ionic microgels[125-127] and also for microgels that are often considered neutral but typically carry some charges from the ionic initiator.[194, 204] As a consequence, when the bulk modulus of the microgels is lower than the external osmotic pressure the microgels start to deswell, even when they are not in direct contact.[12, 80, 194, 195] In our case, the CS microgels carry chargeable groups that are only attributed to the used anionic radical initiator. The electrophoretic mobility measured at 20 °C and dilute conditions is – 1.23 µmcm/Vs. Thus, our microgels can be considered as weakly charged in the swollen state. Due to the unique contrast situation of our CS microgels for SAXS, we can extract the form factor even in the regime of dense packings, i.e. where $S(q) \neq 1$. The measured SAXS profiles (symbols) and the modeled form factors (solid lines) are presented in **Figure 5.6a**. The high q region can be very reliably described with the form factor model due to the contribution of the core. Since the rigid cores do not change in size, shape and its size polydispersity remains constant, the form factor contribution of the cores does not change. This is highlighted by the vertical solid line that marks the position of the form factor minimum due to the core contribution. In the mid and, in particular, low q region where the structure factor contribution is strong, the fit and experimental data seem to deviate. This however is only caused by the absence of the structure factor in the model. The first minimum of the form factor contribution of the shell is still well-resolved and not hampered by the structure factor. Therefore, we get very good agreement between fit and data around the minimum (approximately 0.05 nm^{-1}). The parameters used for the form factor modeling are listed in **Table S5.12** in the Supporting Information. As the grey arrow indicates, the minimum associated to the microgel shell shifts towards lower q with decreasing concentration. This means that the particle size decreases with increasing concentration. In other words, the microgel shells shrink as the particle number density increases.

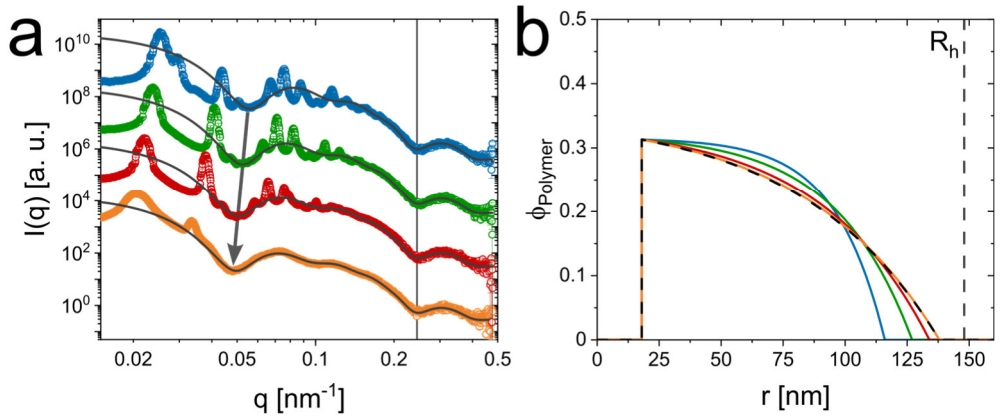

Figure 5.6. Osmotic deswelling of the CS microgels in dense packings. (a) Scattering profiles from samples with mass contents of 5.4 wt% (orange circles), 7.3 wt% (red circles), 9.1 wt% (green circles) and 10.9 wt% (blue circles) recorded at a temperature of 20 °C. The grey lines correspond to the respective form factors and the grey arrow illustrates the shift of the form factor minimum related to the shell, while the black, vertical line indicates the fixed position of the form factor minimum related to the core. The profiles are offset along the ordinate for clarity. (b) Radial density profiles of the polymer volume fraction at the respective mass contents (similar color coding to **a**). The black dashed profile corresponds to the CS microgels in the dilute state and the black dashed, vertical line highlights the hydrodynamic radius.

Figure 5.6b shows radial polymer density profiles as the result from the form factor analysis. The respective polymer volume fractions are extracted from a radial density profile of the scattering length density shown in **Figure S5.28** in the Supporting Information. Here we also present the constant integrals of the radial density profiles. The rigid silica cores have a mean radius of 18 nm. Consequently, in **Figure 5.6b** the polymer volume fraction is zero for $r < 18$ nm. Within the shell region ($r > 18$ nm) the polymer volume fraction decreases from very similar values of 0.31, independently on the mass content of the samples, to zero, following the exponential decay of the *SLD* in the corresponding form factor model. With an increase in mass content, we can detect a decrease of R_{SAXS} from 138 nm to 116 nm and a more pronounced decline in the exponential decay, indicating a deswelling process. The fact that we can accurately determine interparticle-distances, based on the lattice constant of the crystalline structure formed by the CS microgels, reveals that deswelling occurs far before interparticle contact.

This again indicates the presence of a pronounced electrostatic influence on the microgel behavior, even when the particles are in the swollen state, exhibiting rather low electrophoretic mobilities. The influence of electrostatics on potential deswelling of microgels (here in the dilute state) was also shown by Bergman et al. where changes in the ionic strength of the dispersion resulted in a deswelling of charged microgels.[83] Reconsidering the phase behavior of the CS microgels at 40 °C in addition to the deswelling, we conclude that the microgels must exhibit a pronounced electrostatic contribution. Therefore, the deswelling of the CS microgels, most likely, is a result of the overlapping between the individual ion-clouds exhibited by the microgels, increasing osmotic pressure, forcing the microgels to deswell. As we could not detect an increase in the polydispersity of the CS microgels for the deswelling process, in combination with the electrostatic contribution and due to the dense packing of the CS microgels inside of the colloidal crystal we conclude that the microgels undergo an isotropic osmotic deswelling.[33, 80, 129] This leads to the decrease in radius and the more pronounced decline of the polymer volume fraction as described above. From literature it is known that the internal microgel architecture including the nominal crosslinker content dictates whether isotropic deswelling or faceting of the microgels is observed.[124] For microgels with high nominal crosslinker contents (≥ 5 mol% BIS), like in our case, it is known that isotropic deswelling occurs before faceting.[79, 80] A similar behavior was found for hollow microgels that showed isotropic osmotic deswelling when the particle concentration in the dispersion was increased. In this case it was attributed that deswelling is favored over faceting due to the presence of the cavity inside the microgel which allows for rearrangement of the polymer chains within the microgel.[74, 118] Ultra low crosslinked microgels, expressing pronounced soft behavior, show faceting when they are dispersed in a crowded environment, rather than undergoing isotropic deswelling before microgels make contacts.[70, 80]

5.5 Conclusion

Core-shell microgels with polymeric shells that are significantly larger than the incompressible core are ideal candidates to study fluid-solid transitions by small-angle scattering without the need of selective deuteration and contrast variation.[78-80] We have shown that SAXS is particularly powerful given that the core as well as the shell provide sufficient contrast with respect to the solvent environment. In our case this was realized by silica-PNIPAM core-shell microgels with shell-to-core size ratios on the order of 8 (swollen state). The form factor contribution of the silica cores in the range of large q is well separated from the scattering of the shell and also from structure factor contributions in dense packings. Due to the overall microgel dimensions approaching the wavelength of visible light, crystallization of the microgels can be easily followed optically due to the photonic properties. We used absorbance spectroscopy as an efficient and easily available method to study solid-fluid/fluid-solid transitions induced by heating/cooling of the samples. Analysis of the data revealed very narrow temperature windows where the phase transitions occur with almost no hysteresis between heating and cooling within a change in volume fraction of about 0.05. The freezing point is registered at a volume fraction of 0.45 ± 0.05. The deviation from the value of hard spheres was explained by electrostatic interactions. The structures of the fluid and solid phases were studied by synchrotron SAXS. Structure factors extracted in the fluid regime indicate the presence of a pronounced electrostatic contribution in the phase behavior of the CS microgels. In addition, we did not observe any osmotic deswelling in dense packings of collapsed microgels. In contrast, the samples in the solid regime showed sharp Bragg peaks and many different diffraction orders upon very slow temperature annealing of the samples. Analysis of the scattering data revealed hcp structures and domain sizes in the micrometer range. Due to the combination of synchrotron SAXS and optical spectroscopy on the very same samples, both methods probing rather large sample volumes, we were able to provide a representative correlation between the optical properties and ensemble structure of the CS microgel assemblies. From the scattering profiles of the crystalline samples, we could also directly determine the form factor of the CS microgels. Data analysis revealed osmotic deswelling with an extend that increases with increasing concentration.

The unique combination of our silica-PNIPAM core-shell microgels and properly chosen shell-to-core size ratio with synchrotron SAXS is ideally suited to determine form as well as structure factors even in packings exceeding the hard sphere limit. Due to the great resolution of SAXS and the extremely short acquisition times, in situ studies on phase transitions over a broad range of packing densities will be possible in future works. A comprehensive follow-up work addressing in more detail the role of electrostatics in the phase behavior of our core-shell microgels using charged and charge-screened conditions is currently underway.

Conflicts of Interest

There are no conflicts of interest to declare.

Acknowledgements

The authors acknowledge the German Research Foundation (DFG) and the state of NRW for funding the cryo-TEM (INST 208/749-1 FUGG) and Marius Otten from Heinrich-Heine-University Düsseldorf for his assistance with the operation and image recording. The authors thank the Center for Structural Studies (CSS) that is funded by the DFG (Grant numbers 417919780 and INST 208/761-1 FUGG) for access to the SAXS instrument. A. S. thank the DFG for financial support of project A3 (Project No. 191948804) within the SFB 985 – Functional Microgels and Microgel Systems. The authors acknowledge Déborah Feller for her assistance with the operation of the angle-dependent dynamic light scattering setup. A. V. Petrunin, T. Höfken, and P. Mota-Santiago helped with the SAXS measurements. The SAXS measurements were performed on the CoSAXS beamline at the MAX IV laboratory (Lund, Sweden) under the proposals 20200777 and 20220526. The Research conducted at MAX IV, a Swedish national user facility, is supported by the Swedish Research council under contract 2018-07152, the Swedish Governmental Agency for Innovation Systems under contract 2018-04969, and Formas under contract 2019-02496. This work benefited from the use of the SasView application, originally developed under NSF award DMR-0520547. SasView contains code developed with funding from the European Union's Horizon 2020 research and innovation programme under the SINE2020 project, grant agreement No 654000.

5.6 Supporting Information

List of Samples

Core-shell (CS) microgel dispersions were prepared with various mass contents and filled into different capillaries depending on the type of measurements. Detailed information about the sample composition and the used capillaries are listed in **Table S5.1**. In order to maintain comparability between the samples prepared in H_2O and D_2O we used the same volume of solvent for dispersions made with the same mass of CS microgels. Thus, the dispersions possess the same particle number concentration in H_2O and D_2O. As an example, the 10.9 wt% sample prepared in D_2O and the 12 wt% sample prepared in H_2O have the same particle number concentration.

Table S5.1. List of the CS microgel dispersions prepared for the different experiments.

Mass content [wt%]	Dispersant	Capillary	Experiment
0.45	D_2O	rectangular	SAXS (20 °C)
5.4	D_2O	rectangular	SAXS (20 °C) / absorbance (various *T*)
7.3	D_2O	rectangular	SAXS (20 °C) / absorbance (various *T*)
9.1	D_2O	rectangular	SAXS (20 °C) / absorbance (various *T*)
10.9	D_2O	rectangular	SAXS (20 °C) / absorbance (various *T*)
1.25	H_2O	round	SAXS (40 °C)
5.4	D_2O	round	SAXS (40 °C)
7.3	D_2O	round	SAXS (40 °C)
9.1	D_2O	round	SAXS (40 °C)
12	H_2O	round	SAXS (40 °C)
10	H_2O	round	SAXS (determination of *N*)

Form Factor Analysis

We measured SAXS from dilute and concentrated core-shell (CS) microgel dispersions and radially averaged the scattering data to obtain the scattering intensity *I*, as function of the magnitude of the scattering vector *q*.

$$|\vec{q}| = q = \frac{4\pi}{\lambda} sin\frac{\theta}{2} \tag{S5.1}$$

The scattering angle is given by θ and λ is the wavelength of the X-rays.

In general, for the investigated *q*-range, the scattering intensity *I*(*q*), possessing the unit m^{-1} if measured in absolute units, can be described by the following equation:

$$I(q) = N{V_{\mathrm{particle}}}^2 \Delta SLD^2 P(q) S(q) + I_{\mathrm{B}} \tag{S5.2}$$

With *N* [m^{-3}] corresponding to the particle number density, $V_{particle}$ [m^3] the volume of the scattering object and *ΔSLD* [m^{-2}] the difference in scattering length density (*SLD*) between the scattering object and the respective solvent. *P*(*q*) is the form factor of the scattering object, *S*(*q*) is the structure factor and I_B [m^{-1}] describes additional incoherent background contributions. For dilute dispersions, the structure factor can be neglected as *S*(*q*) ≈ 1.

We note that here, the contrast of the investigated samples using SAXS is defined by the *SLD*s of the respective materials and the applied wavelength of the X-rays. Despite *SLD* being a *q*-dependent physical quantity, it is a suitable and well accepted quantity to describe contrast situations in SAXS as we already demonstrated in our previous work[81] and done so elsewhere.[138, 205]

The form factor modeling was performed with the SasView software.[197]

To describe the form factor of our CS microgels, we used a CS model:[206]

$$I(q) = \frac{scale}{V_{\mathrm{particle}}}\left[3V_{core}SLD_{\mathrm{core}}k(qR_{\mathrm{core}}) + 3V_{particle}SLD_{\mathrm{shell}}k\left(qR_{\mathrm{particle}}\right) - 3V_{core}SLD_{\mathrm{shell}}k(qR_{\mathrm{core}}) - 3V_{\mathrm{particle}}SLD_{\mathrm{solvent}}k\left(qR_{\mathrm{particle}}\right)\right]^2 + I_{\mathrm{B}} \quad \text{(S5.3)}$$

with

$$k(qR) = \frac{\sin(qR) - qR\cos(qR)}{(qR)^3}$$

With *scale* as scaling factor (corresponding to the volume fraction if measured in absolute units), *V* representing the volume of the respective scattering object and R_{core} and R_{particle} corresponding to the total radius of the core and the overall CS microgel. Here, R_{particle} is the sum of R_{core} and the thickness of the shell $\Delta t_{\mathrm{shell}}$. For the here probed *q*-range, the contrast is related to the *SLD*s of the respective materials. Due to their homogeneous and isotropic structure, the *SLD* of the solvent and the core is kept constant. *K*(*qR*) refers to the form factor oscillations of a spherical scattering object. In case of the CS microgels in their collapsed state, we used a constant *SLD* for the shell. For the CS microgels in their swollen state, we used an exponential decay in the *SLD* profile of the shell.

The exponentially decay ©n the scattering length density of the shell ©s described by:

$$SLD_{\mathrm{shell}}(R) = B\ exp\left(\frac{-A(R-R_{\mathrm{core}})}{\Delta t_{\mathrm{shell}}}\right) + C \quad \text{(S5.4)}$$

With $\Delta t_{\mathrm{shell}}$ being the thickness of the shell, and *A* being the decay constant. *B* and *C* are defined as:

$$B = \frac{SLD_{\mathrm{out}} - SLD_{\mathrm{in}}}{e^A - 1} \quad \text{(S5.5)}$$

$$C = \frac{SLD_{\mathrm{in}}e^A - SLD_{\mathrm{out}}}{e^A - 1} \quad \text{(S5.6)}$$

Here, SLD_{in} and SLD_{out} are the *SLD*s at $R_{\mathrm{in}} = R_{\mathrm{core}}$ and $R_{\mathrm{out}} = R_{\mathrm{particle}}$

The scattering length of the shell derived from the exponential *SLD* profile is given by:

$$f_{\mathrm{shell}} = 3\mathrm{BV}(R_{\mathrm{shell}})e^{A}h(\alpha_{\mathrm{out}},\beta_{\mathrm{out}}) - 3BV(R_{\mathrm{core}})h(\alpha_{\mathrm{in}},\beta_{\mathrm{in}}) + 3CV(R_{\mathrm{shell}})\frac{\sin(qR_{\mathrm{shell}})-qR_{\mathrm{shell}}\cos(qR_{\mathrm{shell}})}{(qR_{\mathrm{shell}})^3} - 3CV(R_{\mathrm{core}})\frac{\sin(qR_{\mathrm{core}})-qR_{\mathrm{core}}\cos(qR_{\mathrm{core}})}{(qR_{\mathrm{core}})^3} \quad \text{(S5.7)}$$

where

$$\alpha_{\mathrm{in}} = A\frac{R_{\mathrm{core}}}{\Delta t_{\mathrm{shell}}} \quad \text{(S5.8)}$$

$$\alpha_{\mathrm{out}} = A\frac{R_{\mathrm{shell}}}{\Delta t_{\mathrm{shell}}} \quad \text{(S5.9)}$$

$$\beta_{\mathrm{in}} = qR_{\mathrm{core}} \quad \text{(S5.10)}$$

$$\beta_{\mathrm{out}} = qR_{\mathrm{shell}} \quad \text{(S5.11)}$$

and

$$h(x,y) = \frac{x\sin(y)-y\cos(y)}{(x^2+y^2)y} - \frac{(x^2-y^2)\sin(y)-2xy\cos(y)}{(x^2+y^2)^2y} \quad \text{(S5.12)}$$

The polydispersity of the core and the shell of our CS microgels are included using a Gaussian distribution of the respective radii. Here, $\langle r\rangle$ is related to the average particle radius, and σ_{poly} describes the relative size polydispersity.

$$D\left(R,\langle R\rangle,\sigma_{\mathrm{poly}}\right) = \frac{1}{\sqrt{2\pi{\sigma_{\mathrm{poly}}}^2}}exp\left(-\frac{(R-\langle R\rangle)^2}{2{\sigma_{\mathrm{poly}}}^2}\right) \quad \text{(S5.13)}$$

Due to the distinct difference in core and shell size, we can also fit the core contribution only. To describe the scattering intensity of the silica cores, we applied a simple polydisperse sphere model:

$$I(q) = \frac{scale}{V_{\mathrm{particle}}}\left[3V(R)\Delta SLD\frac{\sin(qR)-qR\cos(qR)}{(qR)^3}\right]^2 + I_{\mathrm{B}} \quad \text{(S5.14)}$$

The parameters used for the fits are listed in **Table S5.2**.

Table S5.2. Parameters applied to fit the scattering profiles of the dilute CS microgel dispersions in their swollen (T = 20 °C) and collapsed state (T = 40 °C).

Parameters	Core-exponential-shell (swollen state)	Core-homogeneous-shell (collapsed state)
scale	0.029	2.733
I_B [a. u.]	0.2	0.003
R_{core} [nm]	18	18
Δt_{shell} [nm]	120	72
SLD_{core} [10^{-6} Å^{-2}]	17.75	17.75
$SLD_{shell, in}$ [10^{-6} Å^{-2}]	9.89	10.30
$SLD_{shell, out}$ [10^{-6} Å^{-2}]	9.43	-
$SLD_{solvent}$ [10^{-6} Å^{-2}]	9.43	9.43
σ_{core}	0.1	0.1
σ_{shell}	0.1	0.08
A	2.2	-

We began the fitting procedure using fixed values for the background (I_B), R_{core}, σ_{core}, $SLD_{solvent}$, and SLD_{core}. Prior to the first fitting-steps, reasonable values for the Δt_{shell}, SLD_{shell} and σ_{shell} were assumed to get a starting point for the fitting-procedure. Next, the parameters were fitted in the following order: *scale*, SLD_{shell}, Δt_{shell}, *A* (decay constant), σ_{shell}. The values obtained from each fitting-step were applied for the following step. In each step, only the respective parameter was set free to change, while the other parameters were kept constant. As the model consists of many parameters, setting all parameters free resulted in a fit no longer describing the data sufficiently well when using SasView. Therefore, the procedure was repeated until the fit described the experimental data sufficiently well.

Prior to the synchrotron SAXS experiments, R_{core} and σ_{core} were determined from inhouse SAXS measurements presented in **Figure S5.13**. The q-range in the experiment was limited in the high-*q* regime and we were only able to fit the scattering of the core. Due to this, the values were already known and could kept constant in the fitting-procedure regarding the CS microgels.

We also applied other form factor models including the core-shell microgel model that is based on the widely accepted fuzzy-sphere model to describe the inhomogeneous morphology of microgel shell.[207, 208] **Figure S5.1** compares the results for a simple CS model (homogeneous shell) in orange, the core-shell microgel model that is described by a box like profile for the core and the inner homogeneous region of the microgel shell with respective constant *SLD*s followed by an error function like decay similar to the fuzzy sphere model in green[208] and the previously discussed CS model with exponentially decaying shell in red. These additional form factor fits were performed with the SASfit software.[170]

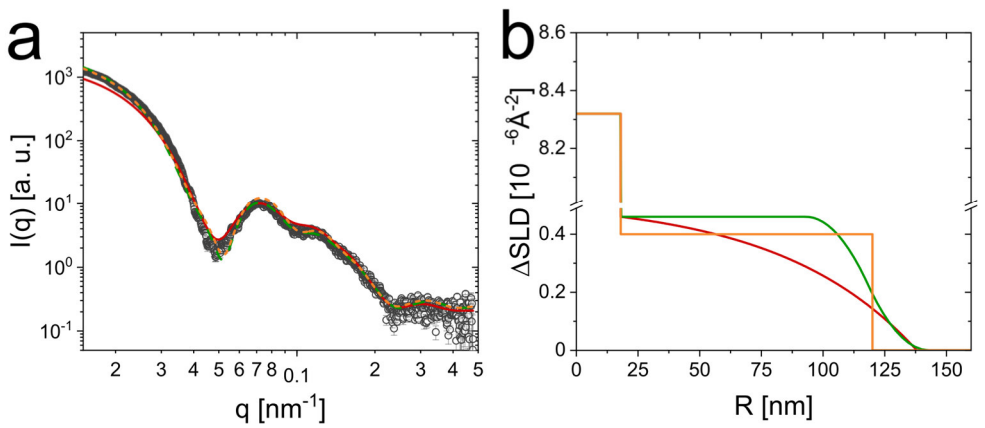

Figure S5.1: Comparison of different form factor models. (**a**) SAXS profile recorded from a dilute CS microgel dispersion with solid lines corresponding to fits using a core-shell model with an exponentially decay in the *SLD* of the shell (red, **Eq. S5.3** and **Eq. S5.4**), the core-shell microgel model[208] (green, dashed line) and a core-shell model with homogeneous *SLD* profiles for the core and the shell (orange, dashed line). (**b**) Radial profiles of the difference in *SLD*s, based on the shown form factor fits with the same color coding as in (**a**).

Figure S5.1a shows that all three applied CS models can describe the SAXS profile of our CS microgels quite well. Deviations occur in the low and mid *q*-range where the shell scattering dominates. The parameters used to fit the scattering intensities are listed in **Table S5.3**. The radial density profiles extracted from the respective CS models are shown in **Figure S5.1b**. All models exhibit a high *ΔSLD* value related to the core until a radius of 18 nm. From this point on, we can see an exponential decay for the core-exponential-shell model (red) and a constant *ΔSLD* for the core-shell model (orange).

The core-shell microgel model (green) exhibits the box like profile with a constant *ΔSLD* followed by a decay ascribed to the fuzzy surface of a microgel.[208] The core-exponential-shell and the core-shell microgel model result in similar total radii of 138 ± 14 nm and 143 ± 27 nm, while the core-shell model yields a much smaller radius with just 120 nm. Despite the fact that the simple CS model with homogeneous *SLD* profiles for core and shell describes the experimental data very well, we do not further consider this model because the homogeneous density profile of the shell is rather unrealistic given the known crosslinker gradient towards the periphery of the microgel shell.[32] In order to obtain reasonable fits with the core-shell microgel model, a polydispersity as large as 20% was imposed on the homogeneous box profile, which is very unrealistic according to our results from dynamic light scattering, where the polydispersity was below 10%. Therefore, despite the good description of the experimental data with this model, we decided to not further consider this rather complex form factor model with a large number of fits parameters. We conclude that the core-exponential-shell model leads to more realistic results for the size, morphology and polydispersity of the CS microgels. Furthermore, due to the lower number of possible fit parameters, we decided to use the core-exponential-shell model in the following of this work.

Table S5.3. Fit parameters obtained from different form factor models.

Parameters	**Core-exp.-shell[206]**	**Core-shell microgel[208]**	**Core-shell**
R_{core} [nm]	18	18	18
[1]Δt_{shell} [nm]	120	75	102
[2]$sigma_{out}$ [nm]	-	25	-
[3]SLD_{core} [10^{-6} Å^{-2}]	17.75	17.75	17.75
[3]SLD_{shell} [10^{-6} Å^{-2}]	9.89	9.89	9.83
[3]$SLD_{solvent}$ [10^{-6} Å^{-2}]	9.43	9.43	9.43
[3]σ_{core}	0.1	0	0
σ_{shell}	0.1	0.2	0.15
[2]A	2.2	-	-

[1] According to the SASfit manual Δt_{shell} is given as W_shell and SLD_X refers to eta_X being the scattering length density of the respective material. Parameters corresponding to the core-shell microgel model according to the SASfit manual not being listed here are set to zero.

[2] Parameters without any given value are not present in the respective model.

[3] In SASfit polydispersity can only be applied on one parameter, therefore we choose the thickness of the shell (Δt_{shell}) being the more relevant quantity in this case.

Dynamic Light Scattering

In addition to the temperature dependent DLS measurements shown in **Figure S5.2a**, we performed angle-dependent DLS measurements below and above the volume phase transition temperature (VPTT) at 20°C and 45°C, respectively. The decay constants, Γ, were computed from the normalized field-time autocorrelation functions using the CONTIN algorithm[149] via the AfterALV software (v1.06d, Dullware, Amsterdam, The Netherlands).

Plotting the values of Γ against q^2 (**Figure S5.2b**) we can extract the translational diffusion coefficient, D_T, with high precision:

$$D_T = \frac{\bar{\Gamma}}{q^2} \tag{S5.15}$$

The Stokes-Einstein equation can then be applied to determine the hydrodynamic radius R_h:

$$D_T = \frac{kT}{6\pi\eta R_h} \tag{S5.16}$$

Here, k is the Boltzmann constant, T is the absolute temperature and η is the viscosity of the solvent.

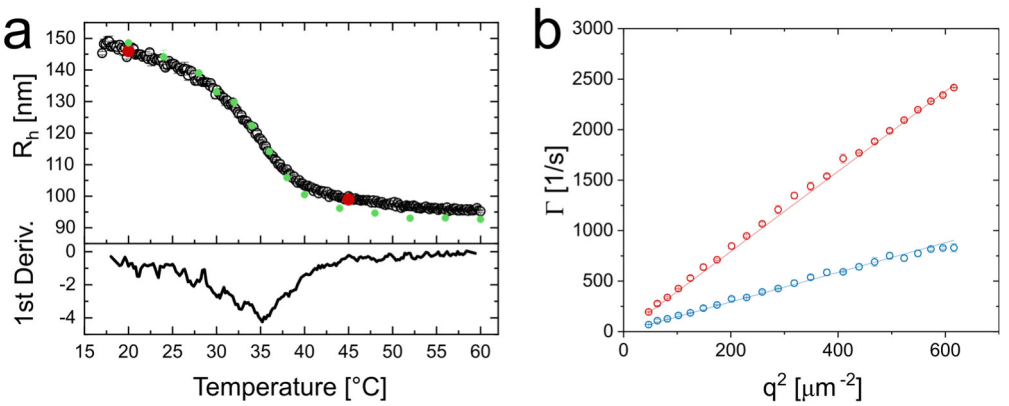

Figure S5.2. (**a**) Hydrodynamic radius as function of temperature obtained from fixed angle measurements in H_2O (black circles, Zetasizer), D_2O (green circles, Zetasizer) and angle-dependent DLS (red circles, H_2O). (**b**) Decay constants from angle-dependent DLS as function of q^2. The blue circles correspond to the data recorded at 20 °C and the red circles were recorded at 45 °C. The straight lines correspond to linear fits to the data.

Translational diffusion coefficients of $1.47 \cdot 10^{-12}$ m^2/s and $3.97 \cdot 10^{-12}$ m^2/s were extracted from the linear fits and correspond to R_h of 146 ± 1 nm at 20°C and 99 ± 1 nm at 45 °C presented as red circles in **Figure S5.2a**. The obtained values form angle-dependent DLS match well to the results from the temperature dependent measurements with a R_h of 147 ± 3 nm at 20 °C and 100 ± 1 nm at 45 °C. In addition, we extracted a VPTT of 35.1 °C for the CS microgels based on the 1st derivative of the temperature dependent DLS data. To investigate isotope effects on the thermoresponsive properties of the CS microgels we performed temperature dependent DLS measurements in D_2O as solvent. The R_h is shown as function of the temperature as green circles in **Figure S5.2a**. A deviation from the hydrodynamic radii recorded in H_2O is only visible for temperatures above 38 °C as the particles exhibit a R_h of 100 ± 1 nm in D_2O and 103 ± 1 nm in H_2O at a temperature of 40 °C. Up to the temperature of 38 °C, the hydrodynamic radius determined in H_2O describes the size of the CS microgels sufficiently well, independent of the here used solvents.

Figure S5.3 shows the electrophoretic mobility of the CS microgels in aqueous dispersion. At low temperatures, in the swollen state, the microgels possess rather small, negative values of mobility, until a temperature of 35 °C. Here, the mobility strongly decreases until reaching a constant value at about 55 °C. The decrease in mobility is associated to the reduction in size of the CS microgel when undergoing the VPT. Here, the surface area decreases and thus the effective charge density over the CS microgel increases. Please note that the CS microgel is negatively charged and an increase in charge per area is reflected by a decrease in electrophoretic mobility.

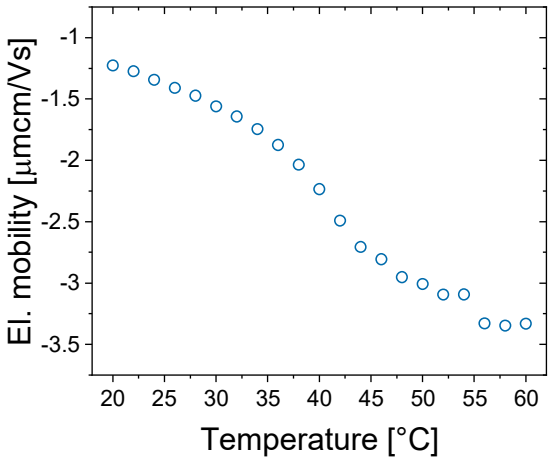

Figure S5.3. Electrophoretic mobility of the CS microgels in dilute, aqueous dispersion as function of temperature.

SAXS Investigation of the Silica Cores

The scattering profile of the SiO_2 cores prior to the encapsulation in the PNIPAM shell is presented in **Figure S5.4** and shows multiple form factor oscillations between q = 0.15 – 1.0 nm^{-1}. We fitted the scattering data with a homogeneous sphere model (red solid line) yielding a radius of 18 ± 2 nm with a polydispersity of 10%.

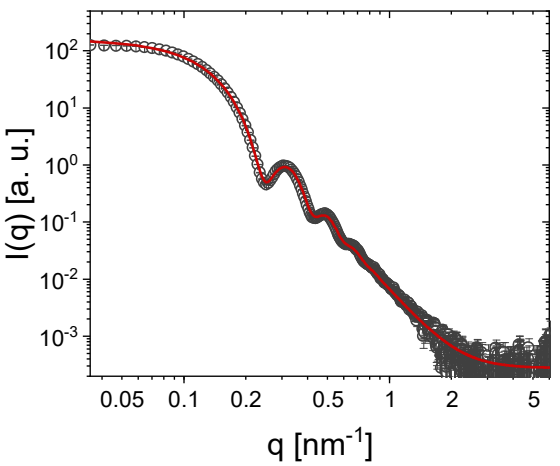

Figure S5.4. Scattering profile of the SiO_2 cores prior to the encapsulation in PNIPAM shells. The solid line is related to a hard sphere form factor fit (**Eq. S5.14**).

Transmission Electron Microscopy Investigation

The successful encapsulation of the silica cores and general morphology of the CS microgels was investigated with transmission electron microscopy (TEM). We used the images shown in Figure S5a-c to determine the encapsulation rate of the SiO_2 nanoparticles (NPs), the average core size and its size distribution which is presented in **Figure S5.5d**. The histogram is based on manual image analysis using the image analysis software imageJ.[209] The size distribution can be described with a Gaussian distribution function resulting in an average radius of 18 ± 2 nm.

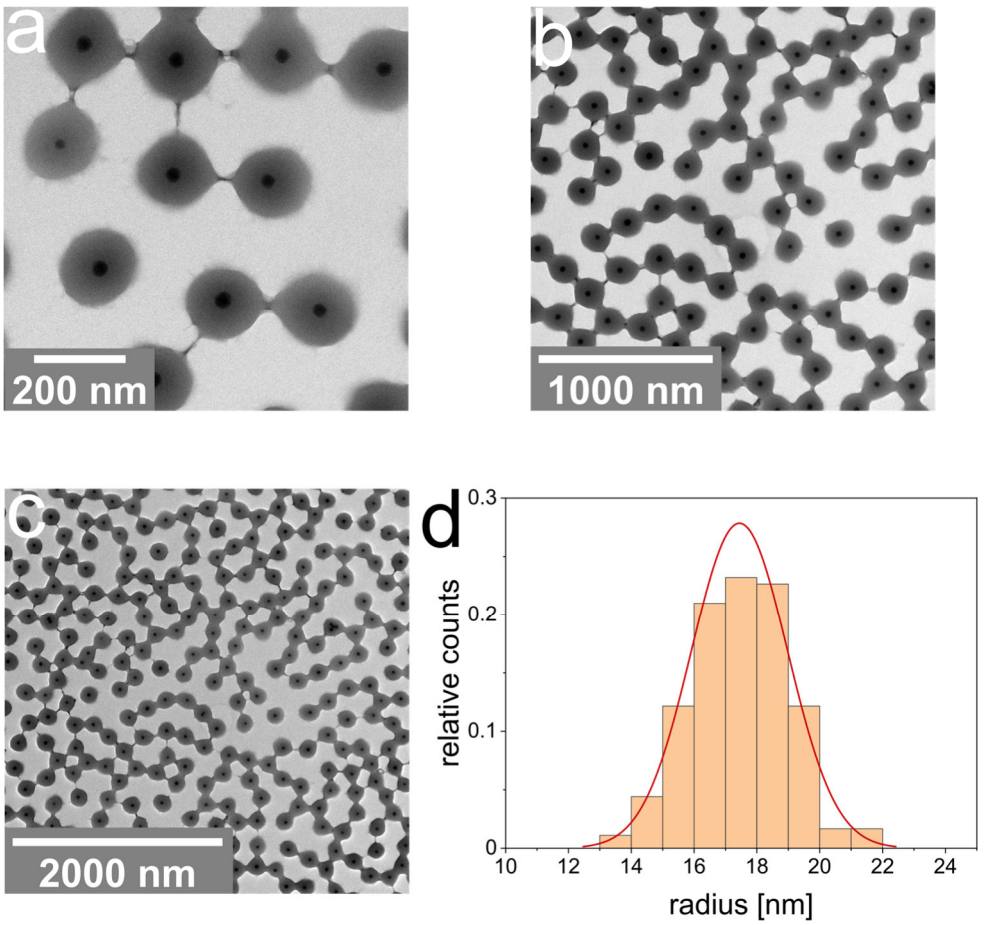

Figure S5.5. Representative TEM images of the CS microgels at different magnifications (**a**-**c**) and a histogram related to the size distribution of the SiO_2 cores with a fit to the data using a Gaussian distribution function (red line) (**d**).

Sample Annealing

After sample preparation at room temperature, we performed a detailed annealing procedure where the temperature is increased from 20 °C to 50°C with a rate of 1.5 K/h using a high precision circulating water bath. At 50 °C the temperature is kept constant for one hour and is then again lowered to 20°C with a cooling rate of 1.5 K/h. The time dependent evolution of the temperature is shown in **Figure S5.6**.

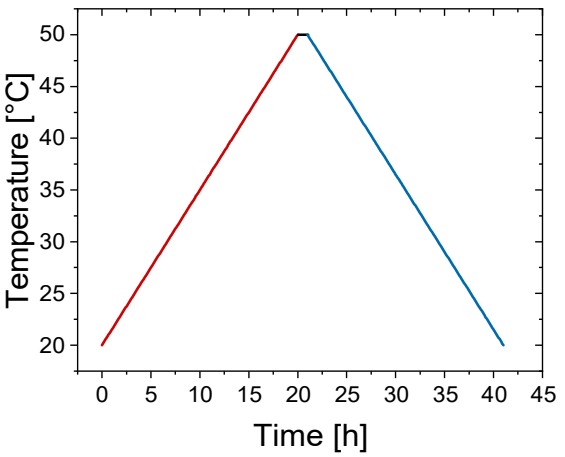

Figure S5.6. Temperature profile used for sample annealing.

Vis-NIR Absorbance Spectra from Different Points in Time

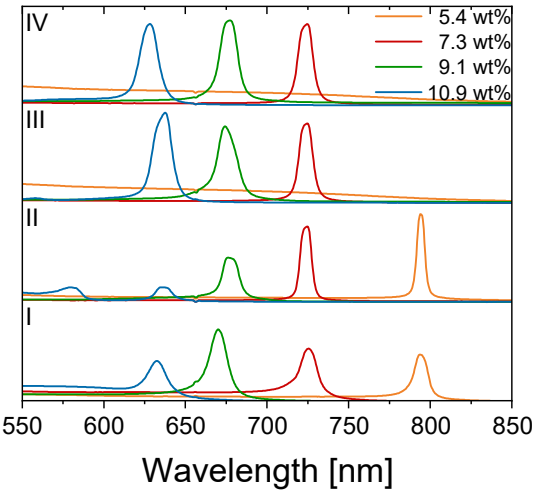

Figure S5.7. Vis-NIR absorbance spectra recorded at different points in time. From the bottom to the top: Directly after sample preparation (I), after annealing (II), half a year after sample preparation (III) and directly after SAXS measurements (IV).

Vis-NIR absorbance spectra were recorded at different points in time at 20°C, to verify the stability of the colloidal crystals (CC). The spectra at the bottom of **Figure S5.7** (I) were recorded directly after sample preparation and show Bragg peaks for all samples. After the annealing procedure (II) the spectra exhibit sharper Bragg peaks for the 5.4 and 7.3 wt% samples indicating an increased crystallinity. The samples with 9.1 and 10.9 wt% show a decrease in the intensity of the Bragg peak. We attribute this to the absence of large crystalline domains in the monitored sample volume. We note that the samples were measured in specific sample holders which do not allow for any changes in the position of the capillary. Afterwards samples were directly stored at 4°C. The next series of absorbance spectra (III) was recorded half a year after sample preparation and all samples excluding the 5.4 wt% exhibit distinct Bragg peaks. We conclude that the 5.4 wt% sample does not show stable colloidal crystals in long time equilibrium state. The improvement in the Bragg peak quality, in the observed volume, might be attributed to a temperature change of the samples during the transfer of the samples to a different location. Here, some rearrangements within the sample might occur resulting in higher quality Bragg peaks in the probed volume.

Spectra recorded after the SAXS measurements (IV) show similar appearance compared to (III). A distinctive change in the Bragg peak position of the CS microgel dispersions is not detectable over the complete series of measurements.

Crystal Analysis by Vis-NIR and Angle-Dependent Specular Reflectance Spectroscopy

We measured concentrated dispersions of CS microgels that exhibit distinct and narrow Bragg peaks at wavelengths, λ_{Bragg}, that are related to the respective diffraction order m, the incident angle θ and the spacing between the respective lattice planes d_{hkl}. Theoretically, the Bragg peak position is described by a combination of Snell's law and Bragg's law:[210]

$$m\lambda_{\mathrm{diff}} = 2\, d_{\mathrm{hkl}} \sqrt{{n_{\mathrm{crystal}}}^2 - \sin\theta^2} \qquad \text{(S5.16)}$$

We used an average refractive index for the CS microgel dispersion of $n_{crystal}$ = 1.345 as reported in literature for a similar system.[73]

Exemplary angle-dependent specular reflectance spectroscopy measurements were conducted with the 9.1 wt% sample. In **Figure S5.8** we show the relation between the angle of the incident beam and the position of the Bragg peak. The black vertical lines indicate the theoretically expected Bragg peak positions for a d_{hkl} = 251 nm. An absorbance spectrum recorded in transmission geometry to represent the Bragg peak position at an angle of 0° is shown in red. We see a distinct blue shift of the Bragg peak with an increase in the respective angle. The experimental data and the theoretical peak positions are in good agreement.

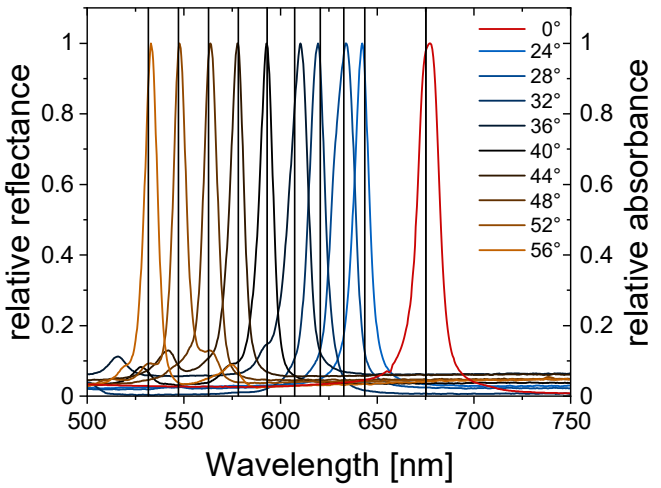

Figure S5.8. Normalized angle-dependent specular reflectance measured form the 9.1 wt% sample. The red spectrum is related to an absorbance measurement in transmission geometry (0 °). Black vertical lines indicate the theoretical peak positions based on a hcp lattice.

When the samples are measured in transmission geometry and θ corresponds to the angle between the optical normal and the incident beam $\theta = 0°$ leading to:

$$\lambda_{\mathrm{Bragg}} = 2\, d_{\mathrm{hkl}}\, n_{\mathrm{crystal}} \tag{S5.17}$$

Assuming a hexagonal closed packed (hcp) crystal structure the spacing between lattice planes, d_{hkl} is connected to the lattice parameters a and c by:

$$d_{hkl} = \frac{a}{\sqrt{\frac{4}{3}(h^2+hk+k^2)+\frac{a^2}{c^2}l^2}} \tag{S5.18}$$

Here, h, k and l correspond to the Miller indices. In case of a closed packed lattice of isotropic spheres the ratio between c and a is fixed to a value of $(8/3)^{1/2}$. This is due to the geometry of the unit cell at dense packing of spheres with a volume fraction of 0.74. With the known ratio we can rewrite **Equation S5.18** to yield the lattice constant a:

$$a = d_{hkl}\sqrt{\frac{4}{3}(h^2+hk+k^2)+\frac{3}{8}l^2} \tag{S5.19}$$

With the **Equations S5.17** and **S5.19,** we can extract the lattice constant *a* from the position of the Bragg peak in the Vis-NIR absorbance spectrum.

$$a = \frac{\lambda_{\mathrm{diff}} \sqrt{\frac{4}{3}(h^2+hk+k^2)+\frac{3}{8}l^2}}{2\, n_{\mathrm{crystal}}} \tag{S20}$$

When we assign the 002 plane to the Bragg peak, we can write **Equation S5.20** in the following way:

$$a = \frac{\lambda_{\mathrm{diff}} \sqrt{\frac{3}{2}}}{2\, n_{\mathrm{crystal}}} \tag{S5.21}$$

The volume fraction ϕ of an hcp crystal with 3 + 3 spheres contributing to one unit cell can be calculated with the lattice constant *a* and the radius *R* of the spheres.

$$\phi = \frac{(3+3)\frac{4}{3}\pi R^3}{\frac{3\sqrt{3}\sqrt{\frac{8}{3}}a^3}{2}} \tag{S5.22}$$

Temperature Dependent Vis-NIR Absorbance Spectroscopy

We performed temperature dependent Vis-NIR spectroscopy with crystalline CS microgel dispersions which exhibit Bragg peaks. The spectra were recorded between 20 °C and 50 °C in steps of 0.3 °C. The samples were equilibrated for twelve minutes before each measurement. Due to the slow heating and cooling rates, we can assume that the sample is close to equilibrium conditions during the whole procedure. This is illustrated in **Figure S5.9a**, while in **Figure S5.9b** a small section of the procedure is shown to clarify the stepwise approach. We note that **Figure S5.9** excludes the time needed for the sample holder to change temperature, and the time for conducting the measurement itself.

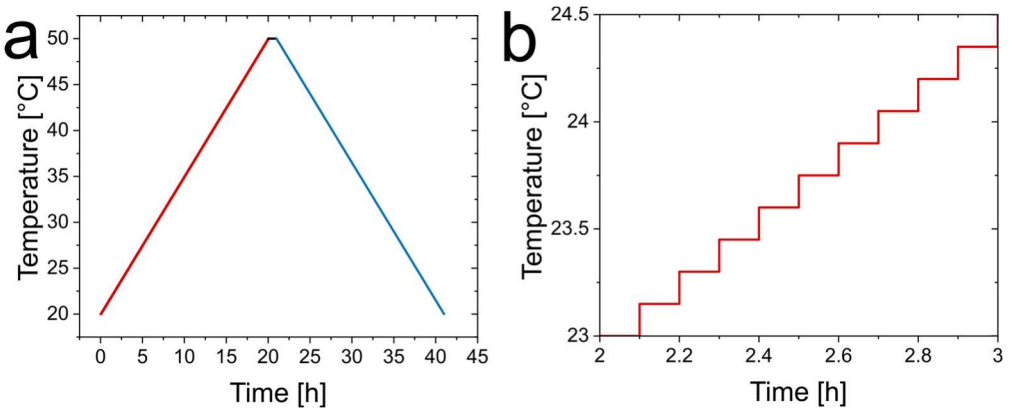

Figure S5.9. Temperature profiles used for Vis-NIR absorbance measurements. (**a**) Time dependent evolution of the temperature and a small section (**b**) showing the stepwise increase of the temperature.

The temperature dependent Vis-NIR spectra are shown in **Figure S5.10** and were recorded between 20 °C and 50 °C in 0.3 °C steps indicated by the color transition from dark blue (20 °C) to red (50 °C). The four rows correspond to the mass contents of 7.3 wt% (a), 9.1 wt% (b, c) and 10.9 wt% (d) CS microgel dispersions. Noteworthy, for 9.1 wt% an additional sample was measured to verify the reproducibility of the measurements. For each sample, we observe a decrease in the absorbance of the Bragg peak in a certain temperature range, which is visible in the absorbance spectra and marked in green for the respective plots of the Bragg absorbance as function of the temperature. In this temperature range, the sample undergoes the phase transition from a crystalline to a disordered system. Based on the conducted experiment, we can extract the transition temperature of the respective CS microgel dispersion (**Table S5.4**). This is done by applying linear fits on the green colored transition section were the Absorbance of the Bragg peak decreases and the blue colored section where the Bragg peak absorbance is 0. The intercept of both fits on the x-axis is listed as transition temperature.

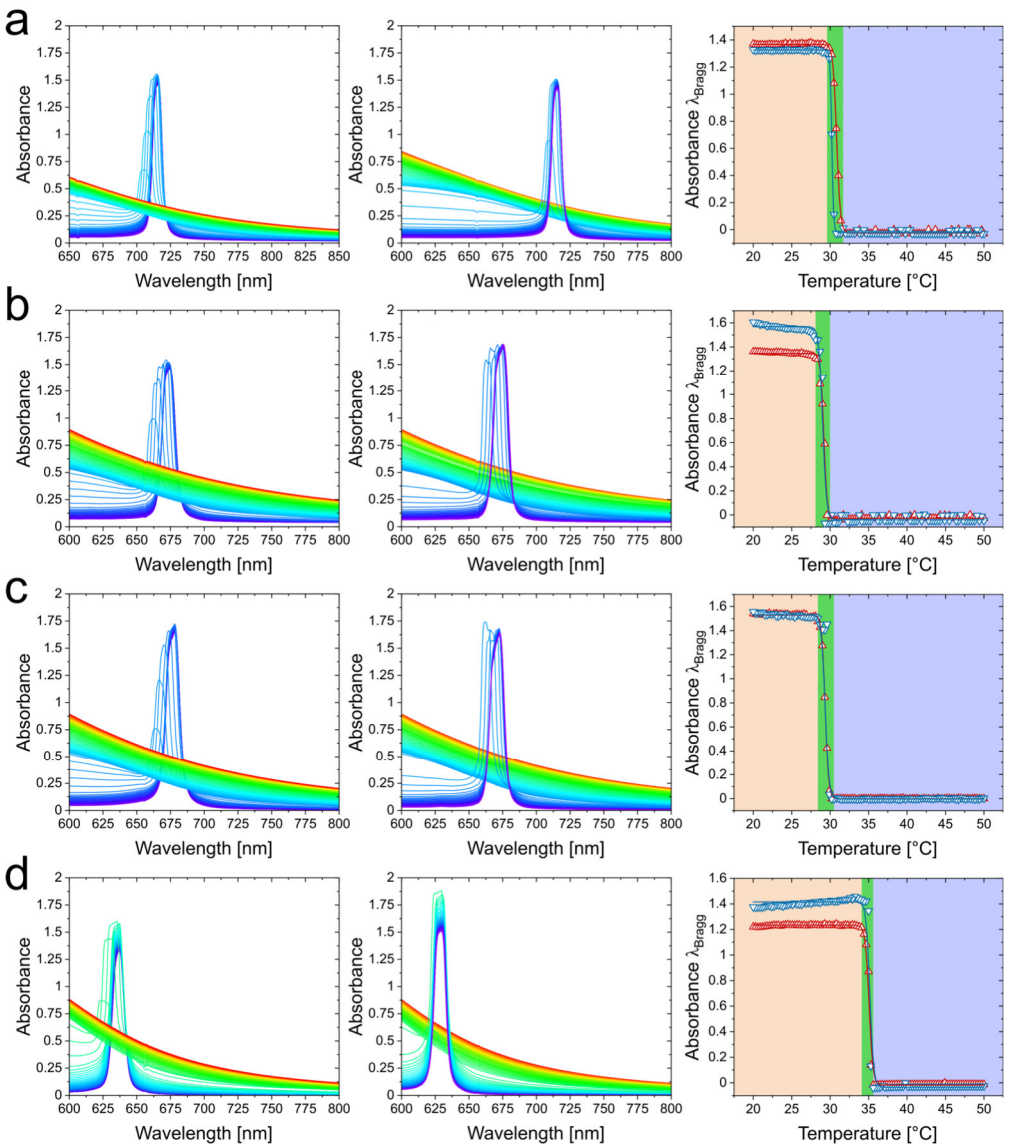

Figure S5.10. Temperature dependent Vis-NIR absorbance spectra and the respective Bragg peak intensity as function of the temperature from 7.3 wt% (**a**), 9.1 wt% (**b**, **c**) and (**d**) 10.9 wt% CS microgel dispersion. The spectra in the left row correspond to a heating cycle while the spectra in the middle column correspond to a cooling cycle. Spectra were recorded from 20°C to 50°C and vice versa with 0.3°C steps indicated by the color transition from blue to red.

Table S5.4. Transition temperatures of the respective CS samples.

Mass content [wt%]	$T_{transition}$ (heating) [°C]	$T_{transition}$ (cooling) [°C]
7.3	31.6	30.7
9.1	29.8	29.9
9.1	30.2	30.3
10.9	35.7	35.5

Figure S5.11a shows the time-dependent evolution of the Bragg peak at fixed temperatures. In **Figure S5.11b**, the absorbance of the Bragg peak at fixed temperatures is plotted as function of time. It is clearly visible that the Bragg peak decreases within the first 100 seconds and remains at a constant value for the rest of the observed time window (a total time of 1800 s). This implies that for the performed temperature-dependent Vis-NIR spectroscopy measurements, with equilibration time of 720 s between each temperature step, the CS microgel dispersion has reached its equilibrium state.

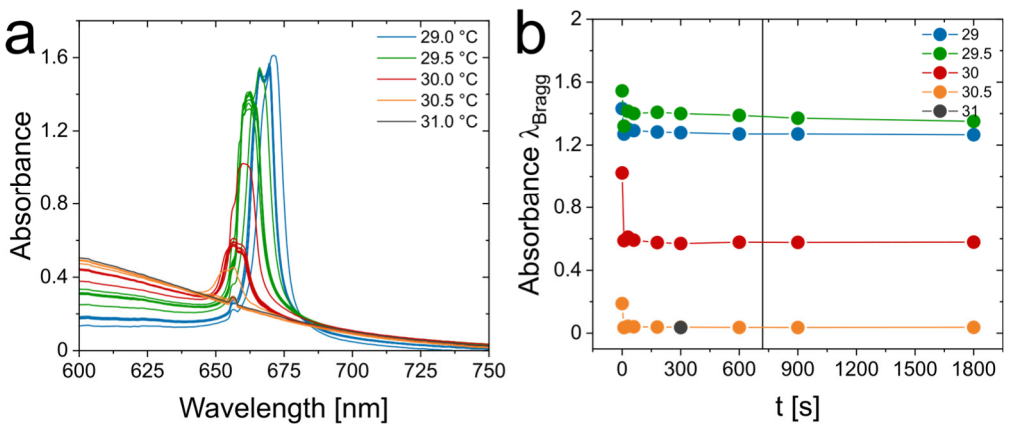

Figure S5.11. Time-dependent evolution of the Bragg peak at fixed temperatures recorded from a 9.4 wt% CS microgel dispersion. (**a**) Time-dependent Vis-NIR absorbance spectra recorded at fixed temperatures after a prior, fast temperature increase by 0.5 K. (**b**) Time-dependent evolution of the Bragg peak absorbance.

Density of the Silica Cores

In order to extract the number concentration from SAXS profiles the density of the scattering objects is required. In our case, the form factor of the core is used for the analysis and thus the density of the silica cores was determined. To do so, the dispersion of silica cores was purified via dialysis against ultra-pure water and the density of a series of dilute dispersions with various concentrations was measured. From a plot of the reciprocal density of the respective dispersions against the respective mass content, the density of the SiO_2 NPs can be extracted with the following equation:

$$\rho = \frac{1}{w_f m + b} \implies \frac{1}{\rho} = w_f m + b \tag{S5.23}$$

Here, ρ is the density of the dispersed particles, w_f being the mass fraction and m and b are related to the slope and the y-intercept of the linear fit as shown in **Figure S5.12,** where the reciprocal density of the dispersion is plotted as function of the silica mass fraction.

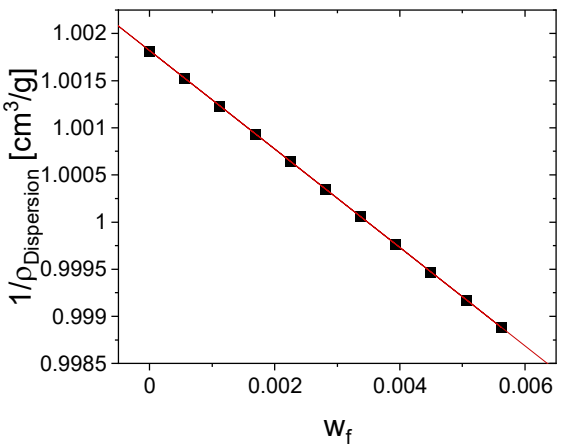

Figure S5.12. Reciprocal density of dilute SiO_2 NP dispersions against the mass content of the respective dispersion. The red line corresponds to the linear function used to fit the data.

The linear function describes the data very well and a slope of -0.52204 cm^3/g and a y-intercept of 1.00182 cm^3/g is obtained. According to **Equation S5.23** a density of 2.08 g/cm^3 for the SiO_2 NPs can be determined.

Extraction of Number Concentrations from SAXS

Additional SAXS measurements were performed with the intensity in absolute units on four (I-IV) concentrated CS microgel dispersions to determine the number concentrations based on the scattering contribution of the SiO_2 cores.[32, 81] A total number of four samples with the same mass content were investigated to ensure that the performed measurements lead to representative results and to obtain a standard deviation regarding the number concentration. The SAXS profiles of the CS microgel dispersions (10 wt%, H_2O), including form factor fits (solid lines) are shown in **Figure S5.13**. The applied polydisperse sphere model describes the data sufficiently well in the respective *q*-range and the fit parameters are listed in **Table S5.5**. We see the first form factor minimum at approximately 0.2 nm^{-1} and discrepancies between the measured data and the form factor fit below q = 0.06 nm^{-1}. The deviation is related to scattering of the shell which is not described by the model used here. The data of the four different CS microgel dispersions superimpose each other, as well as the form factor fits. This is expected as all samples possess the same concentration. Even though 10 wt% ©s a concentration high enough that strong structure factor contributions will occur, our analysis is reasonable since we focus on the form factor of the cores that are much smaller than the total CS microgel dimensions. In other words, the structure factor from the lattice of CS microgels and the form factor of the small cores appear in different regimes of *q*. In particular the pronounced form factor oscillations visible in **Figure S5.13** are not affected by the structure factor. Therefore, we can use the analysis of relatively high and thus well strongly scattering samples to deduce the number concentration of cores and consequently the CS microgels based on the assumption that each CS microgel contains a single silica core. Consequently, the number concentration of the cores is the same as the number concentration of the CS microgels.

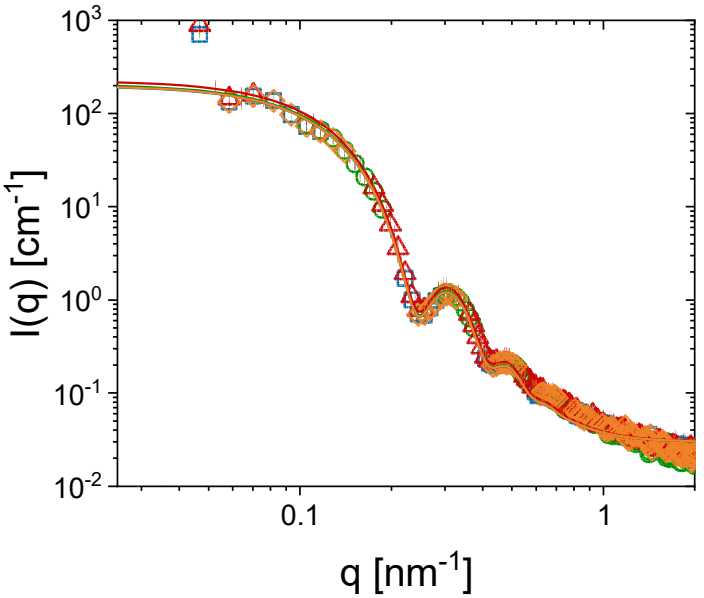

Figure S5.13. SAXS profiles of four different samples (each 10 wt% CS microgels) and the respective form factor fits (sphere-model, **eq. S14**) to the core scattering contribution (solid lines).

Table S5.5. Fit parameters obtained from the form factor fits. The Errors of the parameters are smaller by two orders of magnitudes compared to the obtained valuers and therefore not listed.

	I	II	III	IV
scale	0.00107	0.00108	0.00111	0.00121
I_B [cm^{-1}]	0.03	0.03	0.03	0.03
SLD (SiO_2) [10^{-6} $Å^{-2}$]	17.75	17.75	17.75	17.75
SLD (H_2O) [10^{-6} $Å^{-2}$]	9.47	9.47	9.47	9.47
R [nm]	18	18	18	18
σ_{poly}	0.1	0.1	0.1	0.1

In order to calculate the number concentration N, the scattering intensity at infinitely small q, I_0 needs to be known. Therefore, the SAXS data in absolute units are plotted in a Guinier plot, *i.e.* $\ln(I(q))$ as function of q^2 according to:

$$\ln\big(I(q)\big) = \ln(I_0) - \frac{q^2 {R_G}^2}{3} \tag{S5.24}$$

In addition to I_0, we can extract the radius of gyration R_G from a linear fit to the data. As presented in **Figure S5.14**, we performed the Guinier analysis not only on the scattering profile but also on the performed form factor fits of the core. This is due to the form factor oscillations of the shell, which occur for $q^2 < 0.015$ nm^{-2} and might influence the results of the Guinier analysis. To prevent possible corruption of the extracted I_0 due to the scattering of the shell we used the I_0 extracted from the Guinier analysis of the form factor fits of the core. The results from the Guinier analysis are presented in **Table S5.6** and **Table S5.7.**

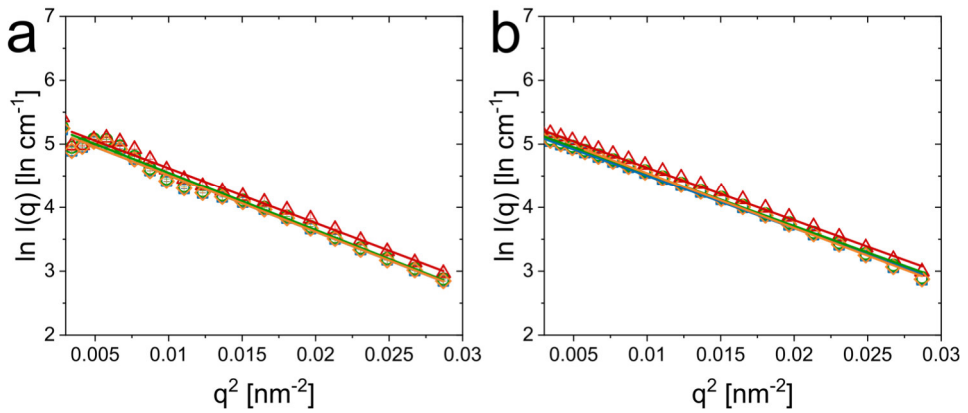

Figure S5.14. Guinier plots of the scattering data (**a**) and the respective form factor fits (**b**).

Table S5.6. Results from the linear fits applied on the Guinier plots of the SAXS data.

	I	II	III	IV
I_0 [cm^{-1}]	221 ± 10	233 ± 10	242 ± 10	221 ± 9
R_G [nm]	16.4 ± 0.3	16.5 ± 0.3	16.1 ± 0.3	4 ± 0.3

Table S5.7. Results from the linear fits applied on the Guinier plots of the form factor fits.

	I	II	III	IV
I_0 [cm^{-1}]	206 ± 2	215 ± 2	235 ± 2	224 ± 3
R_G [nm]	15.8 ± 0.1	15.8 ± 0.1	15.8 ± 0.1	16.2 ± 0.1

Both approaches give comparable results with a radius of gyration close to 16 nm. The radius of gyration is expected to follow $R_g = \sqrt{\frac{3}{5}}\, R_{HS}$ and, therefore, to be smaller than the radius we extracted from form factor fits. With a R_g of 16 nm we see a small deviation of 2 nm from the expected value. This is attributed to the selected q-range where the Guinier analysis was performed due to limitation in the experimentally accessible lowest q. Regarding I_0, we obtained slightly higher intensities from the linear fits applied on the Guinier plot of the experimental data. This is due to the scattering intensity in the low q-regime is not only related to the scattering of the core. Here, the form factor oscillations of the shell are interfering with the scattering signal of the core in the selected q-regime. Thus, the measured intensities are influenced by the scattering of the shell and therefore lead to higher scattering intensities at infinitesimal low q.

Since we now know the forward scattering intensity, I_0, we can combine this with the Avogadro's number N_A, the density of the silica cores ρ (2.08 g/cm^3), the mass of a single scattering object, m (5.08 10^{-17} g) based on the radius of the scattering object and the density of the respective material, the molecular weight, of the scattering object, M_w (3.06 10^7 g/mol) based on the mass of the scattering object, and the difference in scattering length density between the solvent and the scattering object ΔSLD to calculate the number concentration N according to **Equation S5.25:**

$$N = \frac{I_0\, N_A\, \rho^2}{m\, M_w\, \Delta SLD^2} \tag{S5.25}$$

The extracted number concentrations, as well as the average number concentration $\bar{\bar{N}}$ and the respective standard deviation SD are listed in **table S5.8**.

Table S5.8. Number concentrations extracted from the scattering intensity of CS microgels dispersions (10wt%)

	I	II	III	IV	$\bar{N}$	*SD*
N (*I*(*q*)) [10^{13} 1/mL]	5.31	5.58	5.81	5.31	5.50	0.21
N (*P*(*q*)) [10^{13} 1/mL]	4.95	5.15	5.64	5.36	5.27	0.26

The average number concentration is 5.5 ± 0.2 10^{12} 1/mL and is, within the experimental errors, virtually the same as the number concentration extracted from the form factor fits with 5.3 ± 0.3 10^{12} 1/mL. We ascribe the difference between the two values due to the contributions of the polymer shell on the *P(q)* and, therefore, we will use the number concentration extracted from the form factor fits for further calculations.

From the number concentration and the hydrodynamic radius R_h of the CS microgels we can calculate the generalized volume fraction ξ:

$$\xi = N\frac{4}{3}\pi {R_h}^3(T) \tag{S5.26}$$

Due to the PNIPAM shell, the hydrodynamic radius and the generalized volume fraction of the CS microgels depend on the temperature as shown in **Figure S5.15**.

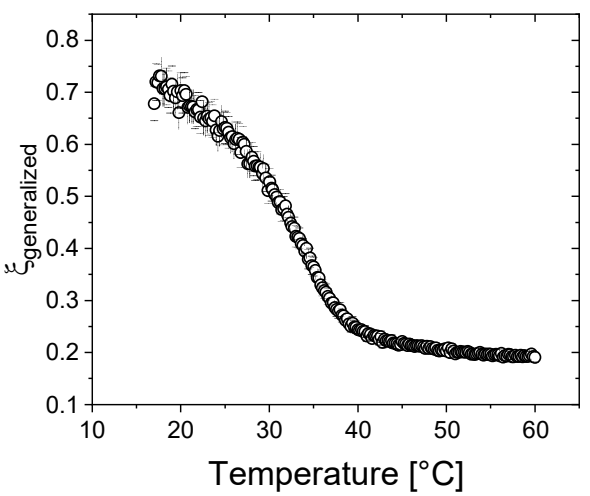

Figure S5.15. Generalized volume fraction as function of the temperature on the example of a 10 wt% CS microgels dispersion.

The hydrodynamic radius, measured via temperature dependent DLS, directly corresponds to the relation of the generalized volume fraction and the temperature.

Structure Factor Extraction in the Fluid Regime

Absorbance spectroscopy has revealed that all CS microgel dispersions (5.4 – 12 wt%) are not in a crystalline state at 40 °C. Thus, we assume that the sample possess a fluid-like structure. To verify this, we conducted SAXS measurements at 40 °C. The 2D detector images of all concentrated samples are shown in **Figure S5.16**. All scattering patterns exhibiting a fluid-like structure factor contribution as well as intensity minima related to the form factor of the collapsed CS microgels. No Bragg peaks were observed so the dispersions are in a purely unordered phase.

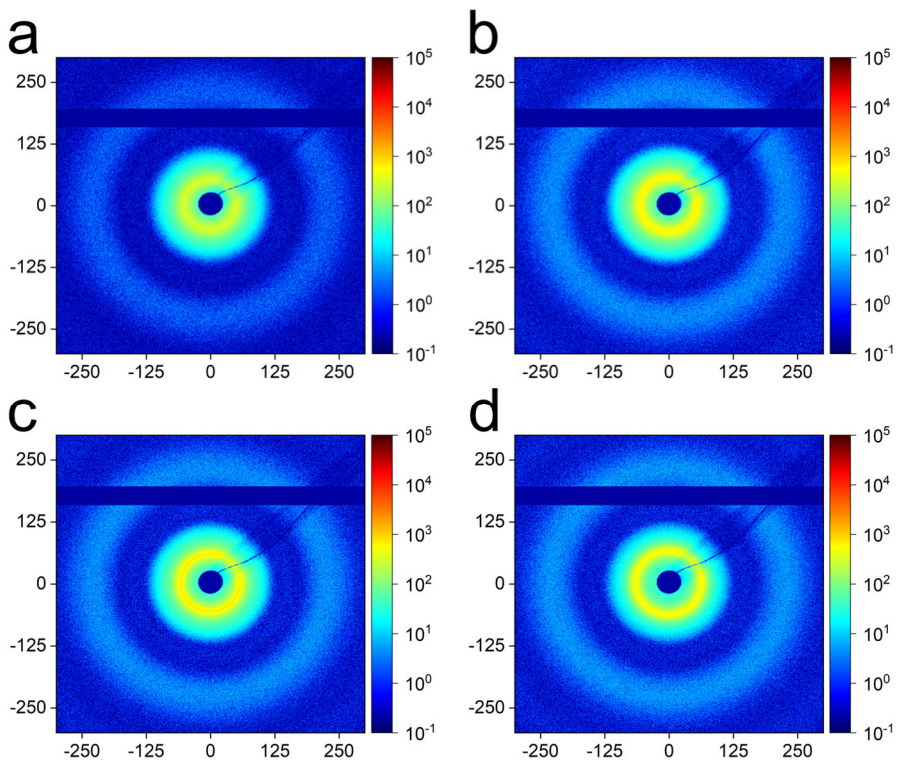

Figure S5.16. 2D detector images of CS microgel dispersions with mass contents of (**a**)5.4, (**b**) 7.3, (**c**) 9.1 and (**d**) 12 wt%.

Radially averaged scattering profiles of the CS microgels with mass contents between 5.4 and 12 wt% recorded at 40 °C are shown in **Figure S5.17**. While the form factor at mid to high *q* remains unchanged for increasing concentration, the first structure factor maximum in the low *q* region shifts towards higher *q* as indicated by the grey arrow.

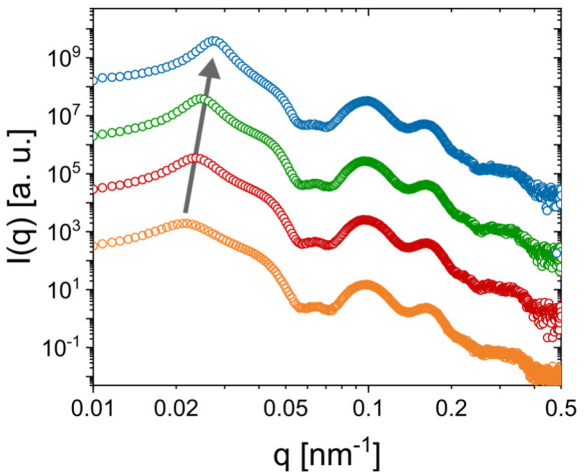

Figure S5.17. Scattering profiles of samples with 5.4 wt% (orange circles), 7.3 wt% (red circles), 9.1 wt% (green circles) and 12 wt% (blue circles, H_2O) recorded at 40 °C. The grey arrow indicates the shift of the structure factor maximum towards higher *q* with an increase in mass content.

We also measured a sample at a much lower concentration (1.25 wt%) at 40 °C, i.e. at conditions where the microgel shell is collapsed. To our surprise the scattering pattern shown in **Figure S5.18** exhibits a weak structure factor maximum at $q \approx 0.02$ nm despite the low concentration. Due to this, we did not use the complete scattering profile for the extraction of the structure factor from scattering profiles recorded of the dense samples. The structure factor contribution can be described by the Percus-Yevick hard sphere structure factor model resulting in a volume fraction of 0.16 and a hard sphere radius of 176 nm.

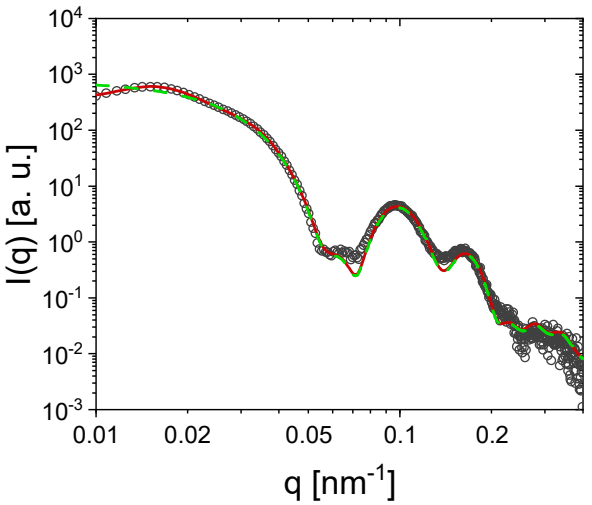

Figure S5.18. Scattering profile (black circles) recorded from a 1.25 wt% CS microgel dispersion at 40°C. The solid red line corresponds to a combination of form and structure factor fit including a core-homogeneous-shell model and the Percus-Yevick model, respectively. The green dashed line represents a form factor fit without any structure factor.

The structure factor can be calcul”ted ’rom the scattering profiles of the concentrated samples $I_{conc}(q)$ using the known form factor $P(q)_{dilute}$ determined from the dilute sample:

$$S(q) = \frac{I_{\mathrm{conc}}(q)}{scale \cdot P(q)_{\mathrm{dilute}}} \qquad \text{(S5.27)}$$

Here *scale* is a scaling factor used to account for the number concentration, scattering contrast as well as the volume of the scattering object (see **Equation S5.2**). Due to small deviations of the form factor fit and the oscillations of the scattering profile, the extracted structure factors show distinct deviation from unity in the mid to high range of q. Here, the deviations are present even for q > 0.05 nm^{-1} where we expect only low amplitudes of the oscillations related to the structure factor. In order to conduct a more realistic structure factor extraction, we used the form factor fit for the extraction in the low q regime (q < 0.025 nm^{-1}) which is shown as green dashed line in **Figure S5.18** and the scattering profile of the dilute CS microgel dispersion for the mid and high q-regime (q > 0.025 nm^{-1}) as indicated in **Figure S5.19b**.

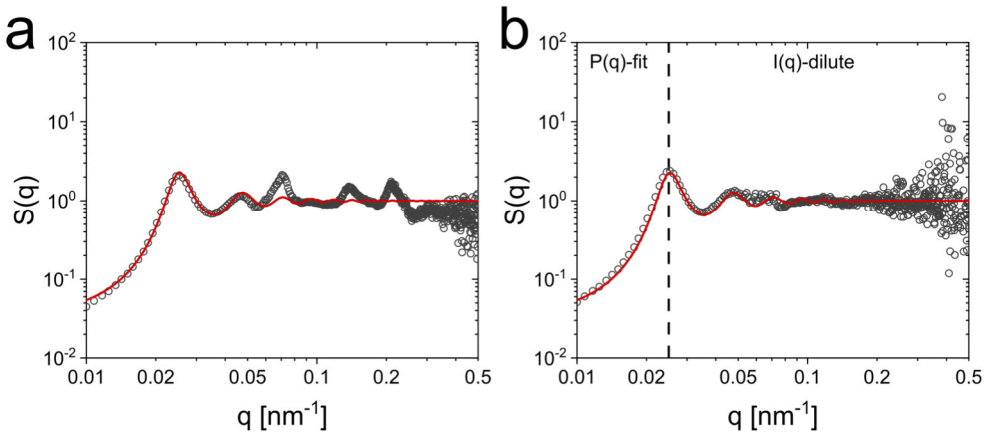

Figure S5.19. Extracted structure factors from a 9.1 wt% CS microgel dispersion recorded at 40 °C. (**a**) Extraction based on the form factor fit obtained from fitting the scattering profile of the dilute CS microgel dispersion. (**b**) Extraction based on the form factor fit for q < 0.025 nm^{-1} and the scattering profile of the CS microgel in the dilute state for q > 0.025 nm^{-1}. The red lines show the structure factor fit (Percus-Yevick).

We fitted the extracted structure factors with the Percus-Yevick hard sphere model. The resulting volume fractions and hard sphere radii are listed in **Table S5.9**.

Table S5.9. Parameters obtained from structure factor fits applied to the scattering profiles recorded from CS microgel dispersions at 40°C.

	5.4 wt%	**7.3 wt%**	**9.1 wt%**	**12 wt%**
R_{HS} [nm]	142 ± 11	135 ± 6	133 ± 5	124 ± 4
ϕ_{HS}	0.32 ± 0.08	0.38 ± 0.06	0.43 ± 0.05	0.46 ± 0.04
$S(q)_{q=0}$	0.08	0.05	0.03	0.023

Figure S5.20 shows the extracted structure factors along with the PY structure factor fits in the regime of low q where deviations between fit and data are expected for soft particles. In our case, fits and data match also in the low q regime indicating that our collapsed CS microgels effectively interact like hard spheres.

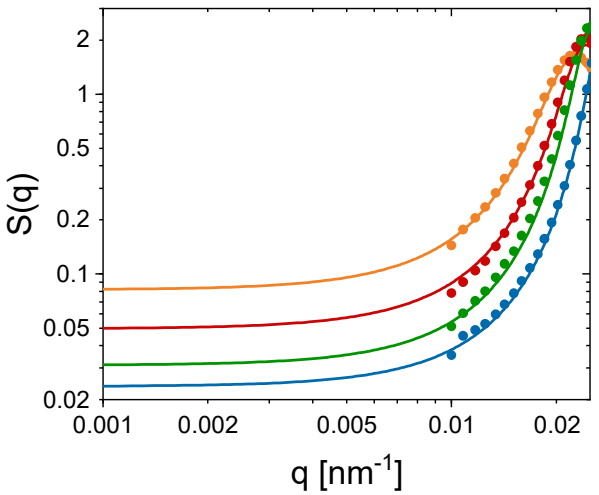

Figure S5.20. Low *q* region of experimentally determined structure factors (symbols) and Percus-Yevick fits (solid lines) from SAXS measurements of 5.4 wt% (orange dots), 7.3 wt% (red dots), 9.1 wt% (green dots) and 12 wt% (blue dots) samples at 40 °C.

SAXS Patterns and Simulations for CS Microgels in the Solid (Crystalline) State

The recorded 2D detector images of samples with 5.4, 7.3, 9.1 and 10.9 wt% measured at 20 °C (swollen state) are presented in **Figure S5.21**. For the 5.4 wt% sample, at the first glance, we see an isotropic scattering pattern in **Figure S5.21a**, indicating a fluid-like structure. At a closer look, diffraction peaks are visible close to the beamstop, i.e. at low *q*. The large number of peaks and their rather random azimuthal distribution points to a multicrystalline character of the sample. This indicates that this sample is in the fluid-crystalline coexistence region with small, randomly oriented crystallites. Due to the dominant presence of a fluid-like structure factor contribution we consider the 5.4 wt% sample primarily as a fluid, which is in agreement to our findings from absorbance spectroscopy (see main manuscript). For the 7.3, 9.1 and 10.9 wt% samples, we see pronounced sharp Bragg peaks of multiple diffraction orders in **Figure S5.21b-d**. The hexagonal symmetry of these diffraction patterns indicates close packed structures. The large number of diffraction orders indicates long range order and thus large crystalline domains.

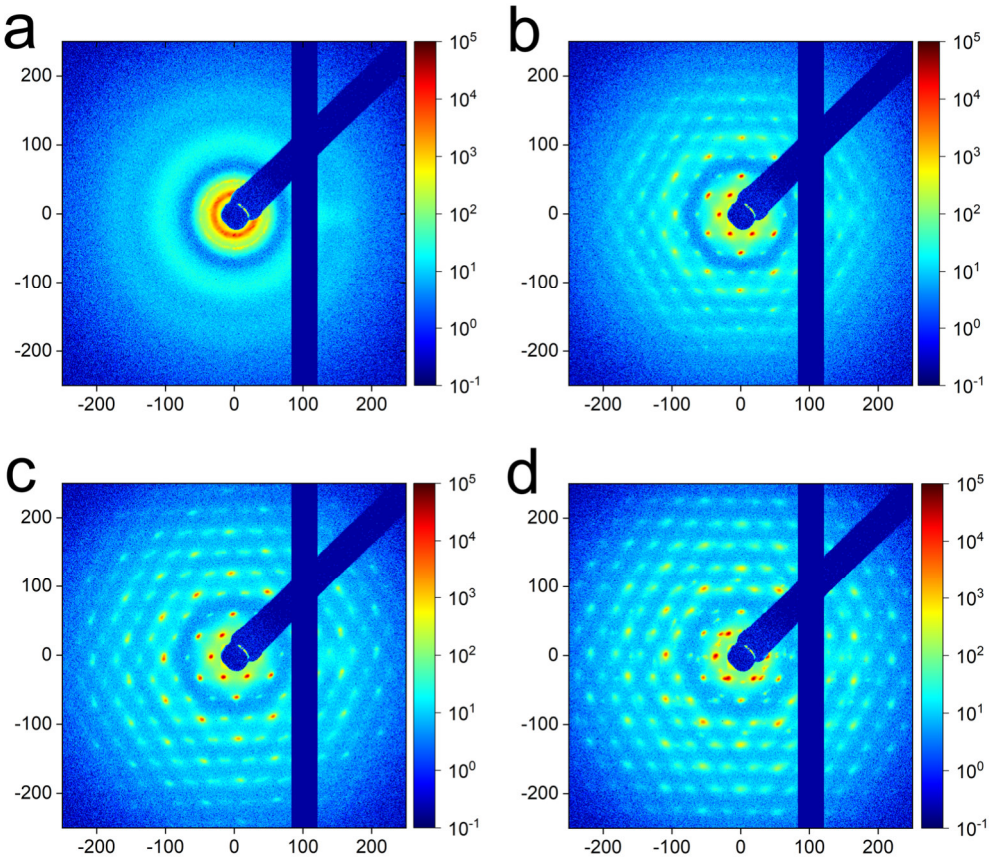

Figure S5.21. 2D detector images of samples with 5.4 wt% (**a**), 7.3 wt% (**b**), 9.1 wt% (**c**) and 10.9 wt% (**d**) CS microgels, recorded at a temperature of 20 °C.

In order to identify the crystal structure, we simulated scattering patterns using the software *scatter*.[171] We see an excellent agreement between the recorded (left half) and the simulated pattern (right half) for an hcp structure in **Figure S5.22**.

The simulations were performed with the 002 plane of the hcp crystal positioned orthogonal to the incident beam. The parameters used in simulations are listed in **Table S5.10**. We took into account a small particle displacement of 5 nm within the lattices. In **Table S5.10**, “max. hkl” refers to the orders of Bragg peaks attempted to simulate and ρ refers to the ratio in scattering length density between the polymer shell and the core ($\rho = SLD_{shell} / SLD_{core}$).

For simplicity, we used a core-shell model with a homogeneous shell to describe the form factor of the CS microgels. Differences in R_{SAXS} used in this simulation and R_{SAXS} obtained from the form factor analysis are ascribed to the different models used to describe the form factor of the CS microgels.

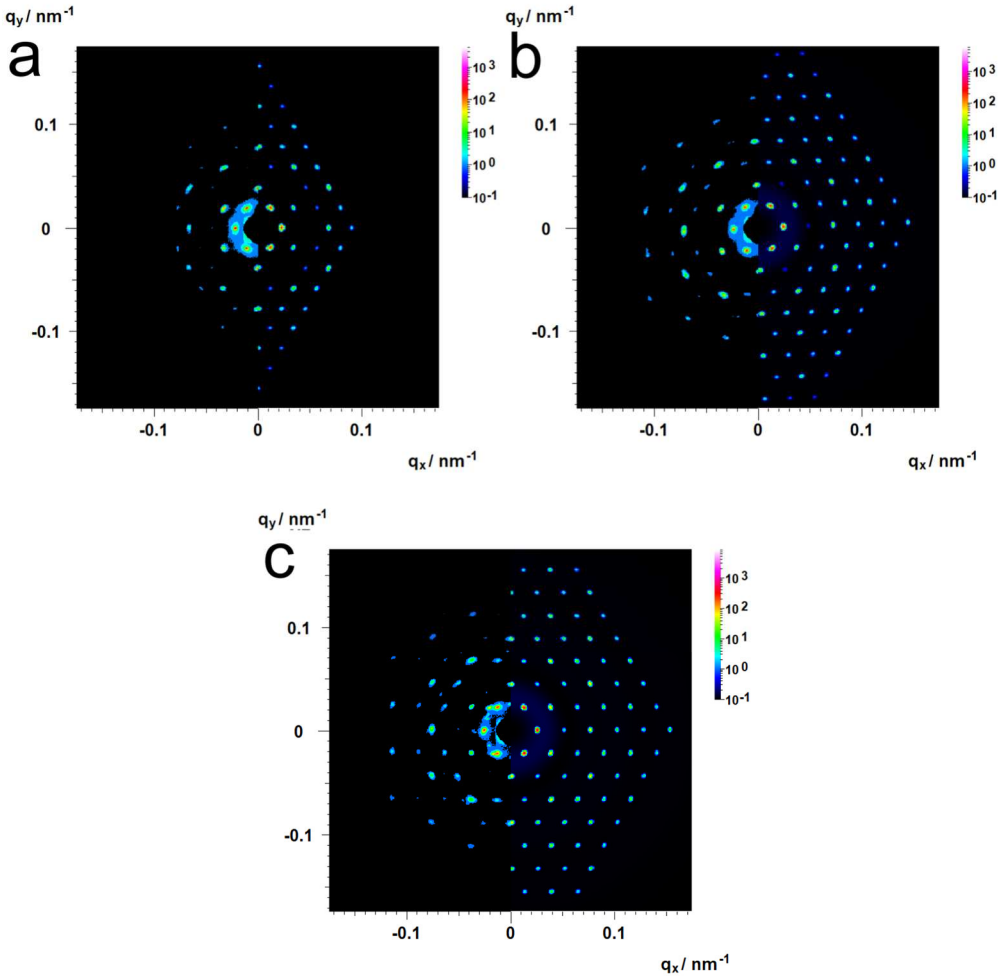

Figure S5.22. Experimental (left half) and simulated (right half) scattering patterns of samples with 7.3 wt% (**a**), 9.1 wt% (**b**) and 10.9 wt% (**c**) CS microgels. Simulations were performed using a hcp crystal structure with the beam direction orthogonal to the 002 plane.

Table S5.10. Parameters used to simulate the scattering pattern with a hcp crystal structure.

	7.3 wt%	**9.1 wt%**	**10.9 wt%**
unit cell [nm]	322	303	284
radial domain size [nm]	2700	3000	3200
azimuthal domain size[nm]	2000	2200	2500
displacement [nm]	5	5	5
max. hkl	4	6	6
R_{core} [nm]	18	18	18
σ_{core}	0.1	0.1	0.1
R_{SAXS} [nm]	121	114	104
ρ	0.04	0.04	0.04

Comparison of Peak Positions for Close Packed Crystal Structures

We now want to compare our detected Bragg peaks with the theoretically allowed ones including other crystal structures than hcp. For this, we use the extracted structure factors from the 9.1 wt% sample as an example. The structure factors were extracted by dividing the measured scattering intensity of the dense sample by the form factor contribution of the silica cores (green circles) as well as the form factor of the total CS microgel (blue circles). We plotted all possible peaks corresponding to a hcp structure as vertical lines in the normalized scattering profiles in **Figure S5.23a**. The profiles were normalized to the position of the first structure factor maximum. The red lines correspond to the Bragg peaks that we could detect in our measured profiles while the grey lines indicate the position of additional, theoretically allowed, peaks. Here, we note that the first structure factor maximum is attributed to the 100 peak, as in the given crystal orientation, the presence of peaks related to 002 and 101 planes is not expected. The peak position is not influenced by the protocol used for the extraction of the structure factor. This is clearly shown as the peak maxima of all three datasets are located on the same positions in *q*.

Since the fcc and hcp crystal structure are energetically very similar and both structures were reported for dense phases of soft microgels, it is worth to compare these to the measured scattering profiles. In **Figure S5.23b**, the redlines indicate the theoretical position of peaks related to an hcp, the grey lines for fcc, and the green lines for peaks shared by both crystal structures. The grey lines do not match with the positions of the recorded Bragg peaks and even for peak positions shared between fcc and hcp structures (green) we only see a match between experimental peaks and theoretical positions at q/q^* = 1.73 and 3. For a rhcp structure, we would expect to detect at least some Bragg peaks solely attributed to an fcc structure. Thus, we can exclude a fcc structure and find no indications for the presence of a rhcp structure. To highlight this ruther we show a selected region of the profiles in the low q/q^* range in **Figure S5.23c**. In addition, **Figure S5.23d** highlights only the observed peaks with vertical lines for the hcp structure (red) and the shared peaks between both fcc and hcp structures (green). Here we want to note that the q/q^* normalization regarding the fcc peak positions needed to be performed on the Bragg peak related to the (220) plane. Due to the structural similarities between the hcp and the fcc structure, the crystal plane, referred to as 220 regarding fcc is similar to the 110 plane in hcp, expressing a diffraction peak at the same position. Therefore, these peaks are very convenient for a normalization of the q-range, towards comparison of fcc and hcp peaks.

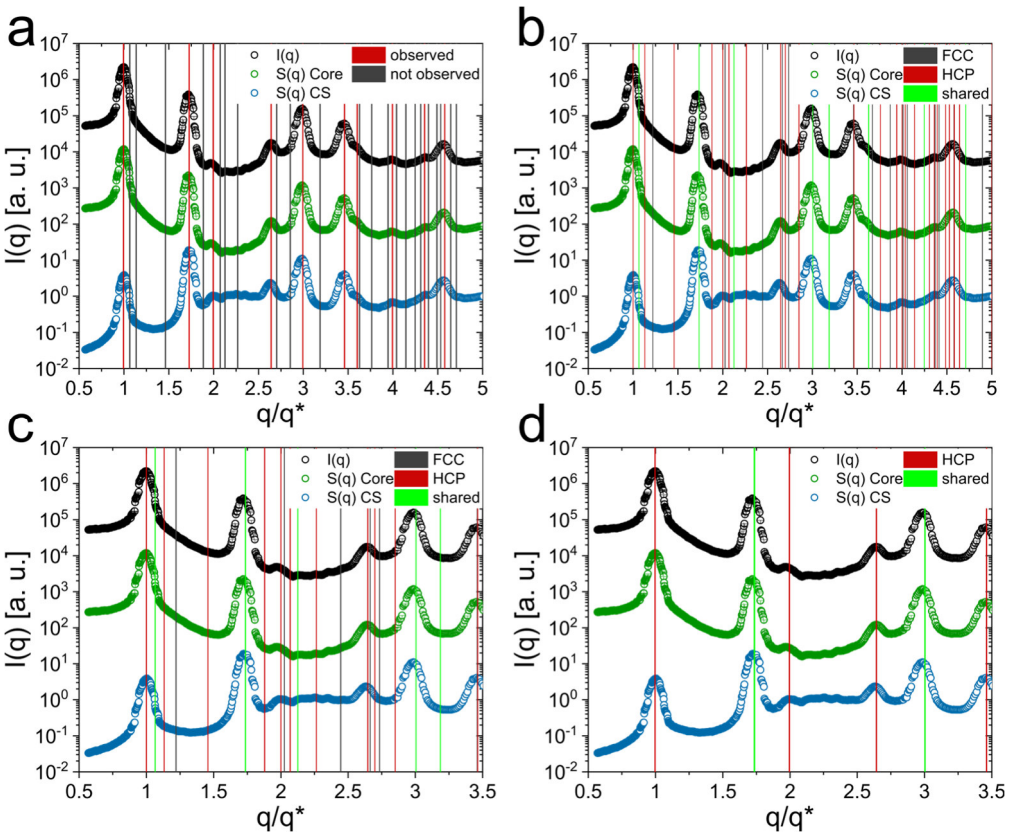

Figure S5.23. Scattering profiles (black circles) and the extracted structure factors using the form factor of just the core (green circles) and of the total CS microgel (blue circles). (**a**) The vertical lines correspond to the theoretically allowed peak positions for an hcp crystal structure. Red lines are related to the experimentally observed peaks while the grey lines indicate the position of additional theoretically allowed peaks. (**b**) Red lines correspond to peak positions of an hcp structure, grey lines are related to an fcc structure and the green lines indicate peaks shared in position between both close packed structures. (**c**) Same as (**b**) but with a smaller q/q^* range focusing on the low q region. (**d**) Same as (**c**) but with a focus on the observed peak positions only, for hcp (red) and the shared peaks with the fcc structure (green).

CS Microgel Dispersion Close to the Freezing Volume Fraction

The 5.4 wt% CS microgel sample exhibits a distinct fluid-like structure factor, but also a Bragg peak around $q \approx 0.03$ nm^{-1} indicating the coexistence with crystallites. In addition to the modeled form factor, we applied a structure factor fit to describe the fluid-like contribution (Percus-Yevick, $S_{\text{fluid}}(q)$) .[184] Here, we want to note that we applied a decoupling approximation instead of a local monodisperse approximation regarding the calculation of the structure factor.[211] Thus, we take into account the polydispersity of our system. The analysis yields a hard sphere radius of 158 nm and a volume fraction ϕ of 0.44. In **Figure S5.24** we see a good agreement between the fit (black line) and the scattering profile (orange circles). We attribute the deviation between R_{SAXS} and the hard sphere radius to the fuzziness of the microgel shell and potential electrostatic interaction between the CS microgels. The structure factor related to the presence of small crystalline residuals ($S_{\text{crystal}}(q)$) was extracted according to:

$$S_{\text{crystal}}(q) = \frac{I(q)}{N(\Delta SLD)^2 V_{\text{p}}{}^2 P(q) S(q)_{\text{fluid}}} \tag{S5.28}$$

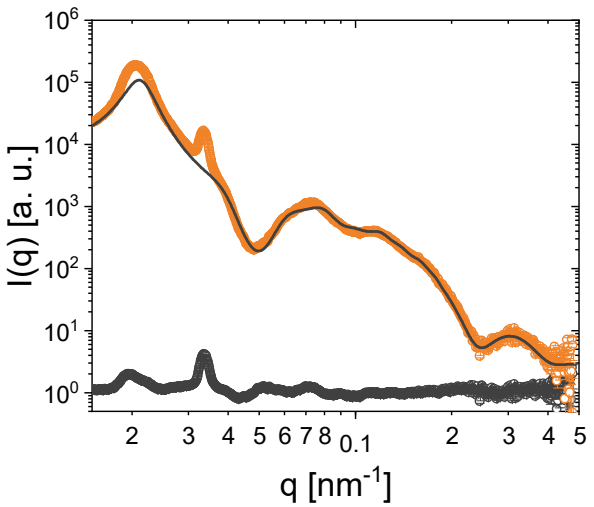

Figure S5.24. Scattering profile of the 5.4 wt% CS microgel dispersion (orange circles), the respective fit composed of the modeled form factor and the hard sphere structure factor (black line) and the residual structure factor associated to crystalline structures.

The extracted structure factor $S_{crystal}(q)$, related to the small crystallites only exhibits two Bragg peaks which in this case does not allow for a precise crystal structure analysis. Based on the CS microgel dispersions possessing higher mass contents we suppose closed packed structures like hcp or fcc.

Lattice compression

From the linear relationship between q_{hkl}, the position of the Bragg peak and the d-spacing of the crystal lattices we can extract the lattice constants a from the slope of the linear fit. From this we can calculate the lattice constant a. The slopes and respective lattice constants are listed in **Table S5.11**.

Table S5.11. Slopes and respective lattice constants extracted from linear fits of the Bragg peak position as function of the lattice spacing.

	5.4 wt%	7.3 wt%	9.1 wt%	10.9 wt%
Slope [nm^{-1}]	0.0168	0.0190	0.0205	0.0219
a [nm]	374	331	306	287

We compare the lattice obtained from 2D simulations of the SAXS patterns and the linear relationship between the Bragg peak positions and q_{hkl} in **Figure S5.25**. In addition, we also added the lattice constants calculated based on the Bragg peaks obtained from Vis-NIR absorbance spectroscopy. All extracted lattice constants are in good agreement with each other.

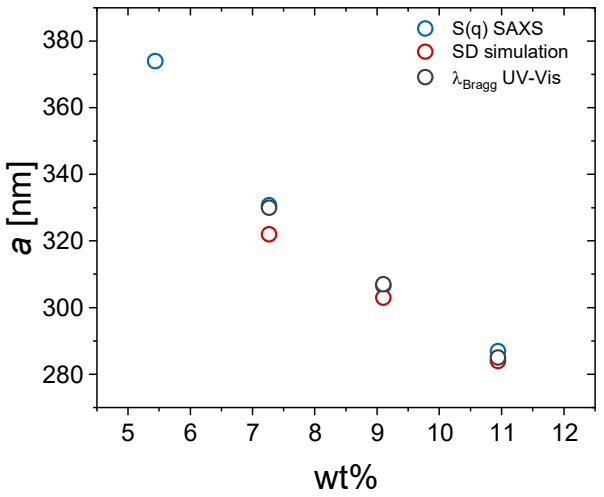

Figure S5.25. Lattice constants based on the hcp crystal structure extracted from $S(q)$, 2D simulation of the diffraction pattern and the Bragg peak from Vis-NIR absorbance measurements.

Volume Fraction of CS Microgels in the Colloidal Crystals

In addition to the volume fractions calculated based on R_h as well as R_{SAXS} normalized to R_h, we also calculated the volume fraction based solely on R_{SAXS}. Based on the scattering intensity of the SiO_2 cores we obtained the relation between particle number density and the mass content of the CS microgels. With the radius $R_{SAXS,\,dil.}$ Of the CS microgels we calculated the generalized volume fraction illustrated as black line in **Figure S5.26**. In addition, we calculated the volume fraction $\phi_{crystal}$ of the CS microgels based on the lattice constant a and $R_{SAXS,\,dil.}$ To compare $\xi_{generalized}$ and $\phi_{crystal}$ according to **Equation S5.22**. We see a good agreement between $\xi_{generalized}$ and $\phi_{crystal}$ which shows the high reliability of the SAXS measurements conducted to extract particle number concentrations. When we include the isotropic osmotic deswelling of the CS microgels at dense packings we see a distinct deviation between the respective volume fractions and $\xi_{generalized}$ for mass contents above 7.3 wt%. The effective volume fractions of the CS microgels seems to stay constant around 0.43 where we identified the solid phases.

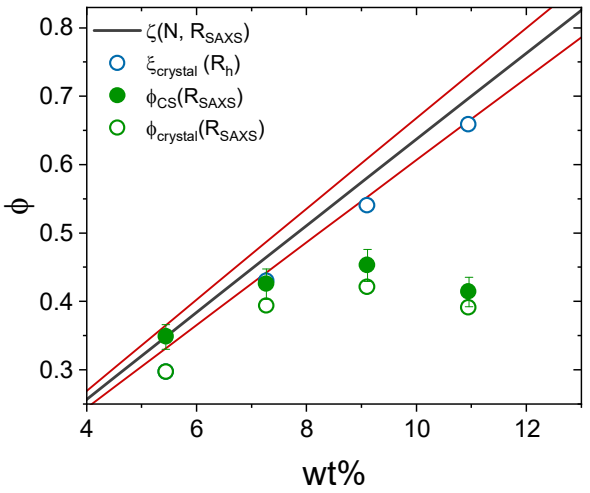

Figure S5.26. Relation between volume fraction and mass content of the CS microgels. The solid black line is related to the generalized volume fraction extracted from particle number concentration and $R_{SAXS,\ dil.}$ Obtained from the P(q) of the dilute CS microgel dispersion. The red lines indicate the respective standard deviation. Green and blue circles are related to the volume fraction of the CS microgels based on the unit cell dimensions. For the blue circles the CS microgel volume is based on R_{SAXS} from dilute dispersion, while for the green circles R_{SAXS} is obtained from the respective modeled form factor in dense packing. The green dots indicate the volume fraction of the CS microgels based on the particle number concentration and the radius extracted from the respective modeled form factor in dense packing.

Williamson-Hall Analysis

We performed a Williamson-Hall analysis to extract the radial and azimuthal sizes of the coherently scattering domains.[203] **Figure S5.27** shows the square of the FWHM of the Bragg peaks $w_{rad/azi}$ as function of the position of the Bragg peak in q^2. The FWHM and peak positions, regarding the radial domain sizes were extracted by the application of a Gaussian-fit-function on the Bragg peaks in the structure factor profiles. While for the determination of the azimuthal domain size we performed automated image analysis to apply gaussian fits on the azimuthal profiles of the respective Bragg peaks. A linear fit was applied on the obtained data according to:

$$w_{\mathrm{rad/azi}}{}^2(q) = \left(\frac{2\pi}{L_{\mathrm{rad/azi}}}\right)^2 + g_{\mathrm{rad/azi}}\, q^2 \qquad \text{(S5.29)}$$

Here $L_{rad/azi}$ is related to the size of coherently scattering domains and $g_{rad/azi}$ is related to strains of the crystallites. $L_{rad/azi}$ can be extracted from the intercept of the linear fit and is presented in **Figure S5.27**. The extraction of $g_{rad/azi}$ leads to strains below 1% which is reflected by the small slope of the linear fits. From this we conclude that we have domain sizes of 3 to 4 µm with nearly no strains present for our colloidal crystals based on CS microgels.

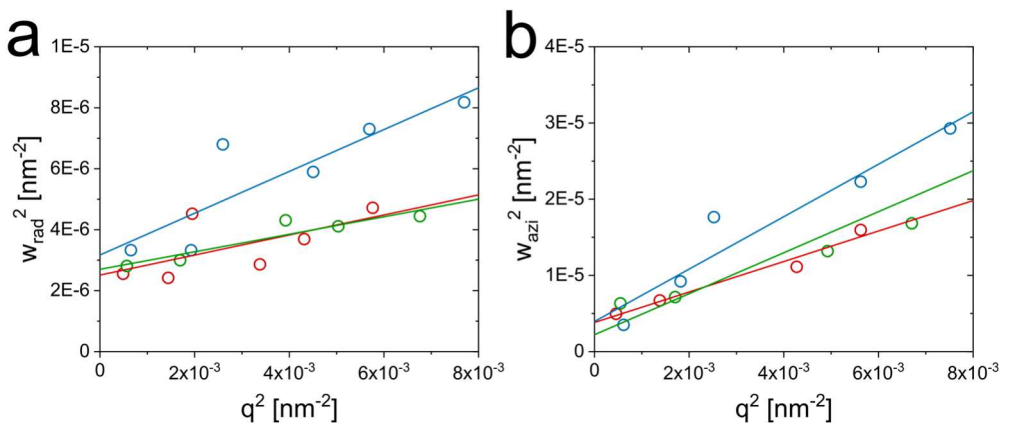

Figure S5.27. Williamson-Hall analysis applied on the Bragg peaks to extract the size of the coherently scattering domains of the colloidal crystals in (**a**) radial and (**b**) azimuthal sizes. Square of the FWHM from the Bragg peaks obtained from a gaussian fit as function of q^2. Data obtained from CS microgel dispersion with mass contents of 7.3 wt% is shown in red, green is related to 9.1 wt% and blue to 10.9 wt%. The solid lines correspond to linear fits to the data.

Form Factor Modeling and Radial Density Profiles of CS microgels at Dense Packing

The distinct form factor oscillations in the scattering profiles of the CS microgel dispersions with high mass contents from 5.4 to 10.9 wt% enabled a detailed form factor analysis, based on the same core-exponential-shell model which was used to fit the scattering profile of the CS microgels in the dilute state. The parameters applied for the form factor modeling are listed in **Table S5.12**.

Table S5.12. Parameters used for the form factor modeling (**Eq. S5.3** and **S5.4**) of the CS microgel dispersions in the concentrated regime.

Parameters	5.4 wt%	7.3 wt%	9.1 wt%	10.9 wt%
scale	0.28	0.34	0.36	0.39
IB [a. u.]	0.2	0.2	0.2	0.2
R_{core} [nm]	18	18	18	18
Δt_{shell} [nm]	120	116	109	98
SLD_{core} [10^{-6} Å^{-2}]	17.75	17.75	17.75	17.75
$SLD_{shell,\ in}$ [10^{-6} Å^{-2}]	9.89	9.89	9.89	9.89
$SLD_{shell,\ out}$ [10^{-6} Å^{-2}]	9.43	9.43	9.43	9.43
$SLD_{solvent}$ [10^{-6} Å^{-2}]	9.43	9.43	9.43	9.43
σ_{core}	0.1	0.1	0.1	0.1
σ_{shell}	0.08	0.08	0.08	0.08
A	2.2	2.6	3.5	4.9

In addition, we were able to extract the radial density profiles of the CS microgels from the modeled form factor shown in **Figure S5.28a**. The density profile exhibits high *ΔSLD* values until reaching a radius of 18 nm, representing the SiO_2 core. From this point we see an exponential decrease in contrast *ΔSLD* which is related to the inhomogeneous structure of the microgel shell. With an increase in concentration the decline of the shell contrast gets more and more pronounced, also resulting in a decrease of the thickness of the shell. We integrated the regime of the density profile associated with the microgel shell for all profiles, presented in **Figure S5.28b**, in order to ensure constant mass and the validity of the *ΔSLD* profiles.

Here we want to note that the *SLD*s of SiO_2 and the PNIPAM microgel shell were obtained from the *SLD* calculator provided by NIST.[174]

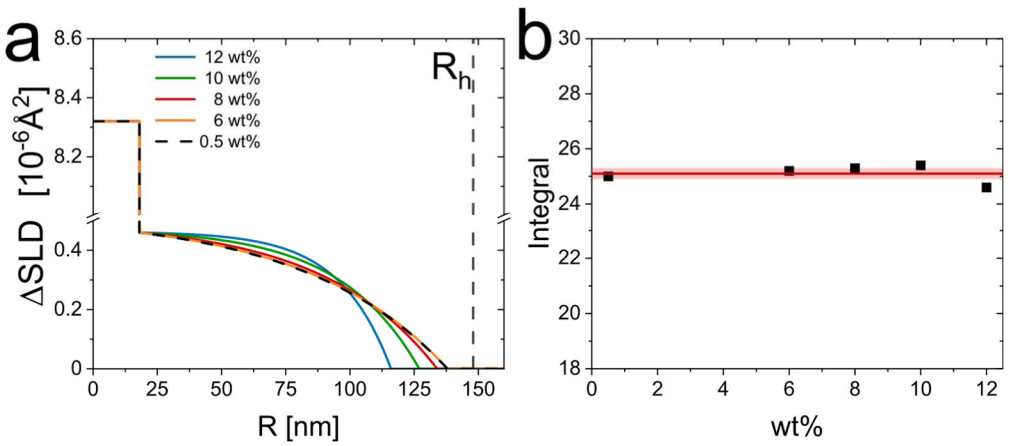

Figure S5.28. (a) Radial *ΔSLD* profiles extracted from the modeled and fitted form factors of the CS microgels in dense packings and dilute state based on the core-shell model, exhibiting an exponential decay in the *SLD* profile of the shell (**Eq. S5.3**). For the sake of clarity, we added a break on the y-axis, due to the strong differences in *ΔSLD* between the core and the shell. (b) The integrals of the microgel shell extracted from the radial *ΔSLD* profile in dependence of the respective mass content.

6. Temperature-Dependent Phase Diagrams of Weakly Charged, Thermoresponsive Microgels under Charged and Charge-Screened Conditions

Manuscript in preparation for publication

M. Hildebrandt[1], D. Pham Thuy[1], A. Domgans[1], A. Scotti[2], S. Prévost[3], M. Karg[1]*

[1]Institut für Physikalische Chemie I: Kolloide und Nanooptik, Heinrich-Heine-Universität Düsseldorf, Universitätsstraße 1, D-40225 Düsseldorf, Germany

E-Mail: Karg@hhu.de

[2]Institute of Physical Chemistry, RWTH Aachen University, Landoltweg 2, 52056 Aachen, Germany

[3]Institut Laue-Langevin - 71 avenue des Martyrs CS 20156, 38042 GRENOBLE Cedex 9 - France

6.1 Abstract

Thermoresponsive microgels featuring pronounced responses towards external stimuli, while possessing a soft and deformable character exhibit a complex phase behavior. Here we employed weakly charged microgels with small silica cores to investigate the influence of charge screening and temperature on the phase behavior of a poly-*N*-isopropylacrylamide (PNIPAM) based microgels. The presence of the silica core allows us to access particle number concentrations and precisely determinate the particle volume fraction. We used scattering methods featuring different contrast situations like small-angle X-ray, neutron and light scattering (SAXS/SANS/LS) to investigate the microgels for potential morphological changes between the charged and charge-screened state. SAXS measurements on microgels in dense packings performed below and above the volume phase transition temperature (VPTT) revealed the influence of charge-screening on the crystalline and the fluid phase of the system. Due to the photonic properties of the colloidal crystals, the transition of the microgels between the crystalline and fluid phase could be investigated by temperature-dependent absorbance spectroscopy. Here, the temperature-dependent evolution of the Bragg peak, exhibited by the crystalline microgel dispersions in optical spectroscopy, enabled us to record a full temperature-dependent phase diagram of the core-shell microgels.

6.2 Introduction

Microgels and nanogels are composed of a crosslinked polymer network, which is swollen by large amounts of solvent.[7, 8, 11] Due to their total dimensions and soft, polymeric nature, with high internal solvent contents, microgels feature characteristics attributed to colloids, macromolecules and surfactants.[10, 12-16] Microgels are also known for their responsiveness towards external stimuli like pH, temperature and ionic strength, which can be introduced and influenced by the polymer composition.[7, 18, 83, 87, 88, 212] First introduced by Pelton and Chibante[24] microgels based on poly-*N*-isopropylacrylamide (PNIPAM), are one of the most prominent examples of such responsive systems, composed of a polymer that exhibits a lower critical solution temperature in water around 32 °C.[28] pNIPAM based microgels have a volume phase transition (VPT), where the particles releases significant amounts of solvent above 32 °C, leading to a drastic reduction in volume, as the environment changes from good to bad solvent conditions.[96, 213, 214] In addition, typical PNIPAM-based microgels exhibit a gradient in crosslinking density, as the crosslinker *N*,*N'*-methylenebisacrylamide (BIS) is consumed faster during synthesis, leading to a rather undefined fuzzy-like surface structure with dangling polymer chains.[16, 30] Interestingly and despite their soft nature, microgels in dense packings can (self-)assemble into crystalline structures, whether in 2D at liquid interfaces or in 3D in bulk, similar to hard spheres.[47, 61, 64, 66, 67, 72, 120] A great advantage of responsive microgels is that, in contrast to hard spheres, the volume fraction of the particles can be influenced in-situ, changing the respective external stimulus like temperature.[82] This makes microgels an ideal model system to investigate crystallization processes and the phase behavior of soft colloidal objects. Therefore, the phase diagram of such systems can be expected to be complex, as the volume fraction, as well as the particle-to-particle interaction potential become a function of temperature and not only of particle number concentration.[122] Despite microgels in dense packings were intensively investigated in the past, an experimentally recorded full, temperature-dependent phase diagram as function of the volume fraction is not published by now.[77, 215] Receiving more experimental insight into the phase behavior of soft colloidal system can also provide additional parameters for numerical simulations in the field of microgels.[216] In order to investigate microgels in dense packings, small-angle scattering experiments can elucidate the overall structure of the system, provided by the structure factor ($S(q)$).[66, 81, 199, 200]

This includes information about fluid and crystalline phases such as crystal structures or coexistence of fluid and crystalline regimes.[81, 82] The common challenge for the investigation of microgels in dense packings is the separation between form and structure factor, being difficult for soft colloids, as the particle shape and, therefore, the form factor, can change depending on the packing density, respectively the volume fraction. Indeed, microgels can undergo the processes of deswelling, faceting and interpenetration.[74, 76, 129, 204] One approach to solve this issue is to make use of contrast variation methods in SANS and measure mixtures of deuterated and hydrogenated microgels in order to separately record the structure factor and the form factor of the microgel at dense packing.[78-80] Recently, we have shown that microgels with very small, inorganic cores provide an alternative approach by making use of SAXS, to investigate microgels in dense packings, providing access to particle number concentration and simplifying the extraction of the structure factor.[81, 82, 131] We could show that using high scattering contrast gold cores damper the form factor oscillations, minimizing interferences between structure and form factor. With the application of a modified core-shell microgel system possessing small silica cores and a larger microgel shell we were able to prepare colloidal crystals exhibiting multiple diffraction orders in SAXS. Due to the small width of the Bragg peaks, the scattering profiles exhibit well resolved form factor oscillations providing access to information about the particle morphology and size in dense suspensions. In general, these suspensions can be characterized by their volume fraction ϕ, which ascribes for changes in the microgel volume due to deswelling, interpenetration or faceting. As an alternative one can make use of the generalized volume fraction ζ which is solely based on the particle dimensions in the very dilute regime and particle number concentration.

In addition to their thermoresponsive properties, microgels can also exhibit a decent polyelectrolyte character as potential charges can be introduced into the polymer network. Microgels are usually considered weakly charged when charges are only introduced by the initiator,[217] like potassium or ammonium persulfate (PPS/APS) providing negative charges or for example 2,2'-Azobis(2-methylpropionamidine) dihydrochloride (V50) which introduces positive charges in the microgel.[89] If functional groups, exhibiting charges like carboxylic acids are introduced during the synthesis, by addition of comonomers, these microgels are often considered as ionic microgels.[87]

Bergman et al. investigated the influence of charges on the morphology of PNIPAM-co-acrylic acid based microgels by varying the number of charges, making use of the pH-dependent protonation degree of the carboxylic acid functionalities and the variation of ionic strength of the dispersion.[83] Here, distinct changes in the internal morphology of the microgels were found, accompanied by a reduction in size as response towards an increase in the ionic strength of the dispersion. The ionic strength was altered by the simple addition of a defined amount of potassium chloride (KCl). A recent study from Petrunin et. al on microgels in dense packings showed that charges can have a significant influence on the microgels response towards crowded environments.[21] Weakly charged microgels undergo slight deswelling followed by faceting and deformation while ionic microgels show deswelling before interparticle contact. Zhou et al. studied the size of the counterion cloud attached to weakly charged microgels by SANS and found similar dimensions for the counterion cloud and the total size of the microgel.[217] Therefore, it was concluded that the counterion cloud is mostly located in the outer periphery of the microgel and is a potential contributor to the microgels phase behavior. Electrostatic interactions between particles play an important role in the stabilization of microgel dispersions. At lower temperatures, in the swollen state, microgels are stabilized by a stearic contribution related to the fuzzy outer part of the polymer network and an electrostatic contribution associated to the presence of charges in the microgel. When the microgels undergo the VPT and polymer-polymer interaction become favored, only the electrostatic contribution ensures the stability of the system. However, when charges are screened due to the presence of ions, colloidal stability can be lost above the VPT. Therefore, conducting a temperature-dependent experiment with screened charges of the microgels, especially at dense packings, needs for a careful adjustment of the ionic strength in order to maintain colloidal stability over a broad range of temperatures and volume fractions.

In this work, we investigate the influence of charge-screening on the phase behavior of microgels in dense packings. We prepared aqueous dispersions of weakly, negatively charged microgels and increased the ionic strength of the system, by the addition of KCl. Based on our previous work, we make use of core-shell (CS) microgels possessing a silica-core and a thermoresponsive PNIPAM-shell.[131] This microgel system, being optimized for SAXS, provides a sufficient separation of the form factor oscillations related to the core and the shell. It also exhibits a generally beneficial contrast situation, as well as access to particle number concentration. [32, 81] The CS microgels were investigated for morphological changes, as a result of screened charges via SAXS, SANS and light scattering methods below and above the VPT, probing the majority of potential contrast situations. The influence of the charge-screening was also investigated by temperature-dependent measurements of the electrophoretic mobility. In addition, the phase behavior of CS microgels in dense packings below and above the VPTT was investigated by synchrotron SAXS, revealing crystalline phases with multiple diffraction orders of Bragg peaks and a full transition into the fluid phase above the VPTT. The influence of charge-screening on the temperature-dependent phase behavior of the CS microgels was investigated by temperature-dependent Vis-NIR spectroscopy. Here, the dispersions of CS microgels exhibit Bragg peaks in the absorbance spectra which are related to the presence of crystalline structures. Based on these measurements, we were able to record a full, temperature-dependent phase diagram of the CS microgels as function of the generalized volume fraction ζ. The charge-screening has a drastic influence on the phase behavior and results in a shift of the phase boundaries.

6.3 Materials and Methods

Chemicals

L-arginine (PanReacAppliChem, ≥ 99%), cyclohexane (Fisher Scientific, analytical reagent grade), tetraethyl orthosilicate (TEOS, Sigma Aldrich, 98%), 3-(trimethoxysilyl)propyl methacrylate (MPS, Sigma Aldrich, 98%), *N*-isopropylacrylamide (NIPAM, TCI, >98%) *N*,*N'*-methylenebis(acrylamide) (BIS, Sigma-Aldrich, 99%), potassium persulfate (PPS, Sigma-Aldrich, 99,0%), potassium chloride (KCl, VWR chemicals, Reag. Ph. Eur.) and heavy water (D_2O, Sigma Aldrich, 99.9%) were used as received without further purification.

Water was always used in ultra-high purity provided by a Milli-Q system (Merck Millipore) with a resistivity of 18.2 MΩ cm.

Synthesis and Sample Preparation of Core-Shell Microgels

For details on the synthesis of CS microgels and the sample preparation, we refer to a previous work of our group.[131] Synchrotron SAXS experiments were performed with CS microgels dispersed in D_2O, excluding the samples with volume fractions of 0.84, recorded at 40 °C, which were dispersed in H_2O. No significant impact of the solvent on the swelling behavior of the CS microgels could be detected.[131] CS microgel samples investigated by Vis-NIR absorbance spectroscopy were all dispersed in H_2O. Dispersions of CS microgels with screened charges were prepared with aqueous solutions of the monovalent and inert salt potassium chloride (KCl), exhibiting a concentration of 0.5 mM (Debye length: λ_D = 13.7 nm). Please note that the ionic strength of the final dispersion is expected to be higher than 0.5 mM, as the CS microgels possess charges, accompanied by counterions, introducing additional ions into the dispersion.

A second batch of CS microgels (CS2) was synthesized to record temperature dependent phase diagrams. Details on the microgel preparation, particle characterization (**Figure S6.5**, **Tables S6.10** and **S6.11**) and extraction of the particle number concentration (**Figure S6.6** and **Tables S6.6** to **S6.9**) are given in the Supporting Information.

SANS

SANS experiments were performed on the D11 instrument at the Institut Laue-Langevin in France (Grenoble). The instrument was equipped with a ^{3}He gas detector (CERCA) with a sensitive area of 96 × 96 cm^2 and a total pixel size of 3.75 × 3.75 mm^2. The neutron wavelength was set to 0.6 nm and sample-to-detector distances of 1.7, 10.5 and 38.0 m were used to cover an effective q-range of 0.02 nm^{-1} to 5 nm^{-1}. Here, the instrumental resolution regarding q is based on the neutron beam width, the pixel size and the wavelength spread ($\Delta\lambda/\lambda$ = 9% (FWHM)). Acquisition times were 120 s, 300 s and 900 s, respectively. Aqueous dispersions of CS microgel (0.45 wt% in D_2O) were measured in cylindrical quartz glass cuvettes (Hellma, Germany, d = 1 mm). The recorded scattering profiles were background corrected for D_2O and merged with respect to the profile recorded at the largest sample-to-detector distance.

SAXS

Synchrotron SAXS experiments were conducted on the CoSAXS beamline at the MAX IV synchrotron in Sweden (Lund). An Eiger2 4M detector with a sensitive area of 155.1 × 162.2 mm^2 and total pixel sizes of 75 × 75 µm^2 was used to record the scattering patterns. The energy of the X-ray beam was 12.4 keV for all performed experiments. The sample-to-detector distance was set to 6.85 m for measurements performed at a temperature of 20 °C and to 11.04 m for the measurements conducted at 40 °C. This yields effective q-ranges of 0.015 nm^{-1} to 0.5 nm^{-1} and 0.01 nm^{-1} to 0.5 nm^{-1}, respectively. CS microgel dispersions investigated at 20 °C were measured in 0.2 mm x 4.00 mm x 10 mm rectangular, flat-wall capillaries (VitroTubes), while the dispersions measured at 40 °C were prepared in 1 mm round capillaries (WJM Glas). The recorded detector images were radially averaged and background corrected for D_2O.

Additional SAXS measurements were performed on a Xeuss 2.0 (XENOCS). The instrument was equipped with a Pilatus3R 300K detector possessing a sensitive area of 83.8 × 106.5 mm^2 with total pixel sizes of 172 x 172 µm^2. Here, the energy of the X-ray beam was 8.048 keV and the sample-to-detector distance was set to 1.2 m, resulting in an effective q-range of 0.03 nm^{-1} to 2 nm^{-1}. The acquisition time was set to 3600 s and glassy carbon (1 mm) was used as reference to yield scattering intensities in absolute units.

CS microgel dispersions with mass contents of 10 wt% were measured in 1 mm round capillaries (WJM Glas). The resulting SAXS profiles were background corrected for the respective solvent.

The radially averaged scattering profiles were analyzed with the SasView software[197] and the structure factors were fitted with SASFit (v0.94.12).[218]

Light Scattering

Temperature-dependent DLS was performed with a Zetasizer Nano S from Malvern Panalytical, equipped with a laser of 633 nm wavelength. The scattered light was detected at an angle of 173°. Dilute dispersions (0.05 to 0.01 wt%) of CS microgels, filtered through a 5 µm syringe filter (PTFE, Carl Roth) were measured in semi-macro cuvettes (polymethylmethacrylate, VWR) at temperatures between 17 °C and 60 °C in 0.2 °C steps with equilibration times of 60 s after each step. Intensity-time autocorrelation functions were recorded in triplicate with acquisition times of 60 s. Hydrodynamic radii (Z-average) were determined by cumulant analysis provided by the instrument software.

Static light scattering was measured on an angle-dependent 3D LS spectrometer (LS Instruments, Switzerland) equipped with a HeNe laser (632.8 nm). Measurements were performed in cylindrical glass cuvettes (10 x 75 mm, borosilicate, Fisher scientific), treated with 2% Hellmanex solution, followed by cleaning in an acetone fountain prior to use. CS microgel dispersions with mass contents of 0.01 wt% were filtered through a 5 µm syringe filter (PTFE, Carl Roth) and filled in glass cuvettes. The samples were placed in a temperature-controlled decalin bath (JULABO CF31, PT100 close to sample position). Measurements were performed in angles between 20° and 140° in 2° steps with acquisition times of 10 s.

Electrophoretic Mobility

Temperature-dependent electrophoretic mobilities and respective zeta potentials of the CS microgels were determined with a Litesizer 500 (Anton Paar). CS microgel dispersions with mass contents of 0.05 wt% were filtered through a 5 µm syringe filter (PTFE, Carl Roth) and degassed in an ultrasonic bath for 600 s. The dispersions were filled into omega-cuvettes (Anton Paar) for zeta-potential measurements. The electrophoretic mobility was recorded at a voltage of 100 V and temperatures between 20 to 60 °C in 2 °C steps with equilibration times of 300 s.

Transmission Electron Microscopy

Transmission electron microscopy (TEM) was conducted with a JEM-2100Plus (JEOL) operating in bright-filed mode with an acceleration voltage of 80 kV. Dilute, aqueous dispersions of CS microgels were drop-casted on a carbon-coated copper grid (200 mesh, Electron Microscopy Science) and dried for several hours at ambient conditions.

Absorbance Spectroscopy

Vis-NIR spectroscopy was performed on a SPECORD S600 (Analytik Jena GmbH). Temperature-dependent measurements were conducted in a temperature-controlled sample changer at temperatures from 20 to 50 °C, in steps of 0.3 °C, with equilibration times of 720 s.

6.4 Results and Discussion

6.4.1 Characterization of the Core-Shell Microgels in the Dilute Regime

CS microgels, possessing spherical silica nanoparticles as cores and crosslinked PNIPAM as hydrogel shells, were investigated in a low ionic strength environment (water 18.2 MΩcm) and in an aqueous dispersion containing KCl (0.5 mM). KCl, being an inert and monovalent salt, possessing no pronounced chaotropic properties according to the Hofmeister series, is an ideal choice in order to screen charges exhibited by the CS microgels. The concentration of KCl was set to 0.5 mM as at this concentration the CS microgels still maintained colloidal stability above the VPTT. **Figure 6.1** shows different scattering methods applied to study the size and morphology of the CS microgels in the dilute regime, where no inter-particle interactions are expected. TEM images confirming the CS morphology are presented in **Figure S6.1** in the supporting information. Analysis of different TEM images yielded a core radius of R_{TEM} = 18 ± 2 nm. The thermoresponsive behavior of the CS microgels was investigated via temperature-dependent DLS measurements. The hydrodynamic radii (R_h) of the CS microgels with unscreened charges (c_{KCl} = 0 mM, blue) and screened charges (c_{KCl} = 0.5 mM, green) were plotted as function of temperature in **Figure 6.1a**. Here, the R_h followed the expected sigmoidal trend, as the size of the microgels is reduced when temperature increases. Until a temperature of 40 °C, the evolution of R_h is very similar for the unscreened and charge-screened state with the CS microgels exhibit hydrodynamic radii of $R_{h,\ 0\ mM}$ = 147 ± 1 nm and $R_{h,\ 0.5\ mM}$ = 145 ± 1 nm, respectively. For higher temperatures, CS microgels dispersed in KCl solution exhibit a slightly lower R_h compared to the sample dispersed in absence of salt. We attribute this to a screening of the negative charges, incorporated into the polymer network during synthesis by the PPS initiator, slightly increasing the deswelling capacity of the microgel. The volume phase transition temperature (VPTT) is unaffected by the charge screening and remains at a temperature of 35 °C. **Figure 6.1a** shows the temperature-dependent evolution of the hydrodynamic radius (R_h) and the electrophoretic mobility in the presence and absence of salt. When the CS microgels reduce their surface area, while they undergo the VPT, the number of charges per area is increased which results in a higher electrophoretic mobility at elevated temperatures.

Adding KCl to the CS microgel dispersion results in a decrease of the electrophoretic mobility over to whole range of investigated temperatures. It is also clearly shown that in the presence of 0.5 mM KCl, the electrophoretic mobility is close to zero until approaching the VPT. Therefore we conclude that the electrostatic interactions between the CS microgels are drastically decreased when charges are screened.[219] The respective zeta-potentials are shown in **Figure S6.2** in the supporting information. In comparison to the VPTT, the temperature where the electrophoretic mobility undergoes significant changes is shifted towards higher temperatures, which for PNIPAM based microgels, is in accordance with literature.[86, 87, 89]

From the R_h determined by temperature dependent DLS we can calculate the normalized, generalized volume fraction $\zeta_{generalized}$ shown in **Figure 6.1b**.[80] $\zeta_{generalized}$ is calculated based on the R_h of the CS microgels and their particle number concentration N ($5.27 \cdot 10^{12}$ wt%$^{-1}$mL^{-1}) extracted from the scattering intensity of the SiO_2 cores in SAXS. Details on the extraction of N and the calculation of ζ are given in the Supporting Information of our previous work on the same CS microgels.[131] It is shown that the volume fraction of the CS microgels is reduced around 70 % during the temperature induced collapse of the particles. Here, ζ was normalized to its value at a temperature of 20 °C. In addition, the temperature dependent evolution of ζ was found to be similar for CS microgels in presence or absence of salt.

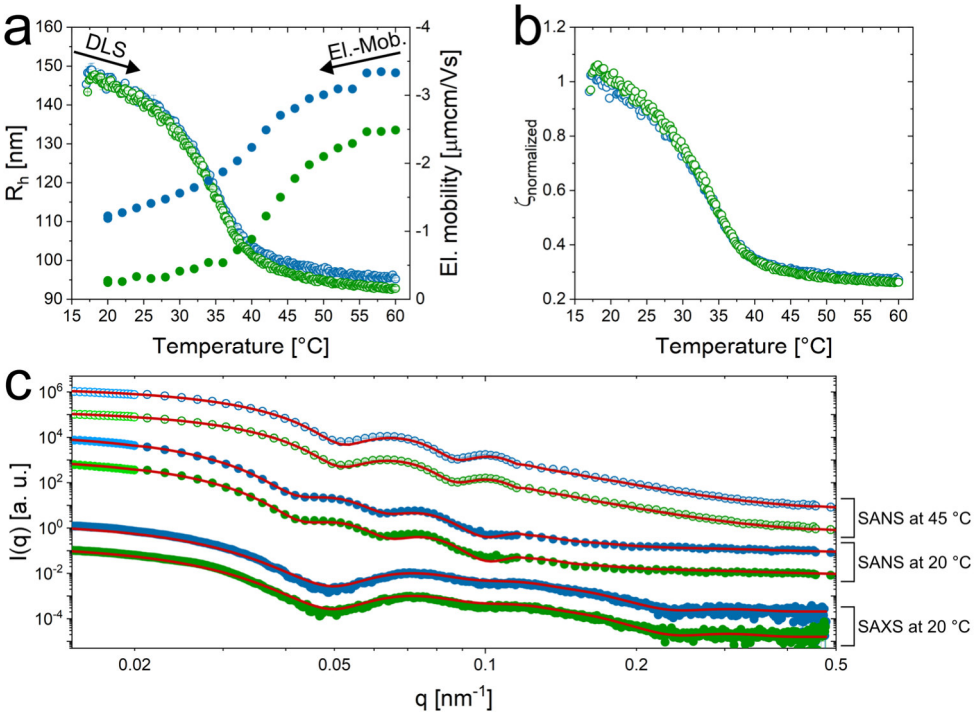

Figure 6.1. Characterization of CS microgels in the dilute state without charge-screening (blue) and in the presence of KCl (green). (**a**) Temperature-dependent evolution of R_h (empty symbols) and electrophoretic mobility (filled symbols) of CS microgels in aqueous dispersion. (**b**) Normalized, temperature-dependent generalized volume fraction ζ of the CS microgels. The data was normalized to ζ at 20 °C. (**c**) Scattering profiles of CS microgels from SAXS and SANS recorded at 20 °C (full symbols) and 45 °C (empty symbols). Additional data points obtained from SLS were merged to the SANS profiles and are shown in the respective lighter color. The red lines indicate the respective form factor fits. Temperature-dependent DLS and SAXS data at c_{KCl} = 0 mM, were adapted from our previous work.[131]

We performed small-angle X-ray and neutron scattering (SAXS/SANS) on CS microgel dispersions with mass contents of 0.45 w%, as well as static light scattering (SLS) measurements on 0.01 wt% CS microgel dispersions in presence and absence of salt. Therefore, we were able to cover a broad *q*-range and make use of different contrast situations, together with DLS providing a detailed, scattering methods based, analysis of the CS microgels presented here. The SAXS profiles, shown in **Figure 6.1c**, were recorded at a temperature of 20 °C. Form factor (P(*q*)) minima related to the microgel shell are located close to *q* of 0.05 nm^{-1}, while the form factor minima related to the SiO_2 cores are present at *q* = 0.25 nm^{-1}.

The solid red lines correspond to the form factor fits with a CS model with an exponential decay in the scattering length density (SLD) of the shell. This model was chosen to account for the gradient in the crosslinker distribution within the polymer network. The form factor fits are in very good agreement with the experimentally recorded data. Here, the form factor fits, yield R_{core} = 18 ± 2 nm and a total radius of 138 ± 14 nm for the CS microgels, independent of the presence or absence of salt. We applied the same form factor model on the scattering profiles, resulting from the merged SLS (lighter colors) and SANS (darker colors) data in **Figure 6.1c**, recorded at 20 °C. In order to describe the internal fluctuations of the polymer network, we also added a Lorentzian function (Ornstein-Zernike contribution) to the model. Here the first form factor minimum associated to the shell is located at q = 0.04 nm^{-1}, followed by additional form factor oscillations. Despite the lower resolution as compared to the SAXS data, the SANS profiles still reveal the presence of the cores by a small increase in scattering intensity between q = 0.1 and 0.2 nm^{-1}. The deviation in the position of the first form factor minimum, related to the shell, between SANS and SAXS is attributed to the inhomogeneity of the polymer network and the differences in the respective contrast situation. Regarding the merged scattering profiles from SANS and SLS, both profiles fit very well with each other and extend the accessible q-range of our SANS data towards lower q further reaching the Guinier plateau. The form factor fits (red solid lines) sufficiently describe the scattering profiles of the CS microgels and at a temperature of 20 °C, no influence of the applied concentration of KCl can be found. A total radius of 138 ± 11 nm is found, being in perfect agreement to the results from SAXS. This is also reflected by the fitting parameters obtained during form factor analysis, listed in the **Tables S6.1** and **S6.2** given in the supporting information. The SANS and SLS profiles are mostly related to scattering of the microgel shell. Despite the higher contrast of the SiO_2 core in SAXS, the PNIPAM shell features a distinct contribution to the SAXS profile. This is related to the size-ratio between core and shell in combination with the contrast situation of the respective scattering objects contributing to the total scattering intensity. More details are given in **Table S6.3.** Merged SANS and SLS profiles recorded at a temperature of 45 °C are also shown in **Figure 6.1c**. The symbols in green are associated to the samples containing salt (c_{KCl} = 0.5 mM). At 45 °C, the CS microgels are in their collapsed state, possessing a more homogeneous network structure.

Under these conditions the internal water content and consequently the size is drastically decreased.[32] The scattering profiles are well described by a simple CS form factor model with homogeneous radial SLD profiles for core and shell (solid red lines). The form factor fit provides a total radius of 88 ± 7 nm for the collapsed CS microgels, which is in good agreement with R_{SAXS}(40 °C) = 90 ± 7 nm (**Figure S6.3**). In addition, we found no differences in terms of the CS microgels size or morphology in the collapsed state, regarding absence or presence of salt based on the recorded scattering data.

Furthermore, the scattering data at low q allow for a Guinier-analysis (**Figure S6.4**). Radii of gyration (R_g) between 95 and 100 nm were found in the swollen state and radii of 70 to 75 nm in the collapsed state. Due to the gradient in the cross-linking density, for microgels in their swollen state, it is common to compare the R_g/R_h ratio[27, 31], which is approximately at 0.67 for the here presented system. This is in good agreement with literature for comparable microgel systems.[73] In conclusion, we obtain similar results from form factor analysis performed on SAXS and SANS profiles, recorded from dilute CS microgel dispersions in presence and absence of salt. The total radii are about 138 nm in the swollen and 88 to 90 nm in the collapsed state. Via DLS we could clearly prove colloidal stability of the dispersion in presence of salt in the collapsed and swollen state. Here, the screening of charges results in a small decrease of R_h in the collapsed state. In contrast, the presence of salt has a pronounced influence on the electrophoretic mobility of the CS microgel, decreasing to nearly 0 µmcm/Vs in the swollen state (20 °C) and therefore reducing potential for electrostatic interactions.

6.4.2 Swollen Core-Shell Microgels in Dense Packings

Having shown that the presence of small amounts of additional charges, introduced by the addition of salt, have little to no effect on the CS microgel size and form factor in the dilute state, we now want to address the behavior in dense packings. **Figure 6.2** shows 2D detector images as recorded by synchrotron-SAXS of samples with increasing volume fraction under charged and charge-screened conditions. Scattering pattern recorded in the absence of salt were adapted from our previous work.[131] The respective generalized volume fraction (ζ) of the CS microgels at a temperature of 20 °C are indicated in between the scattering patterns recorded in the absence of salt (top) and in the charge-screened state (bottom). Here, the generalized volume fraction

is calculated based on the particle number concentration N, extracted from the scattering intensity related to the cores in SAXS and R_h at 20 °C (0 mM KCl).

As the particle number concentration of the CS microgels was already determined in a previous work of our group, the detailed explanation is given in the respective supporting Information.[131] A compassion between ζ for c_{KCl} = 0 mM and c_{KCl} = 0.5 mM at temperatures of 20 °C and 40 °C is given in **Table S6.10** in the Supporting Information. At ζ = 0.42, both scattering patterns are dominated by a fluid-like structure factor (S(q)). When ζ is increased to 0.56, the sample in the unscreened state already exhibits multiple diffraction orders of Bragg peaks, related to the presence of colloidal crystals of CS microgels. In contrast, the scattering pattern of the sample with screened charges exhibits a pronounced fluid structure factor, as well as some low intensity Bragg peaks. We conclude that the CS microgels are in a fluid/crystalline coexistence regime for the probed ζ. It is clearly shown that the screening of charges, exhibited by the CS microgels, has a distinct influence on the phase behavior of the microgels. The screening results in an increase of the volume fraction, needed for the system to self-assemble into a crystalline structure. This is a clear indicator for a reduction of the effective interaction radius of the CS microgels, which is attributed to electrostatic interactions with surprisingly long range. The presence of a distinct electrostatic contribution to the self-assembly process of the CS microgels, especially at low volume fractions, was also indicated in our previous work.[81, 131] When ζ is further increased, the scattering patterns are very similar, exhibiting multiple orders of Bragg peaks and no influence of charges can be detected. Here, the six-fold symmetry of the Bragg peaks indicates the alignment of hexagonal closed packed planes of CS microgels, forming colloidal crystals, parallel to the wall of the capillary.[81, 82, 200]

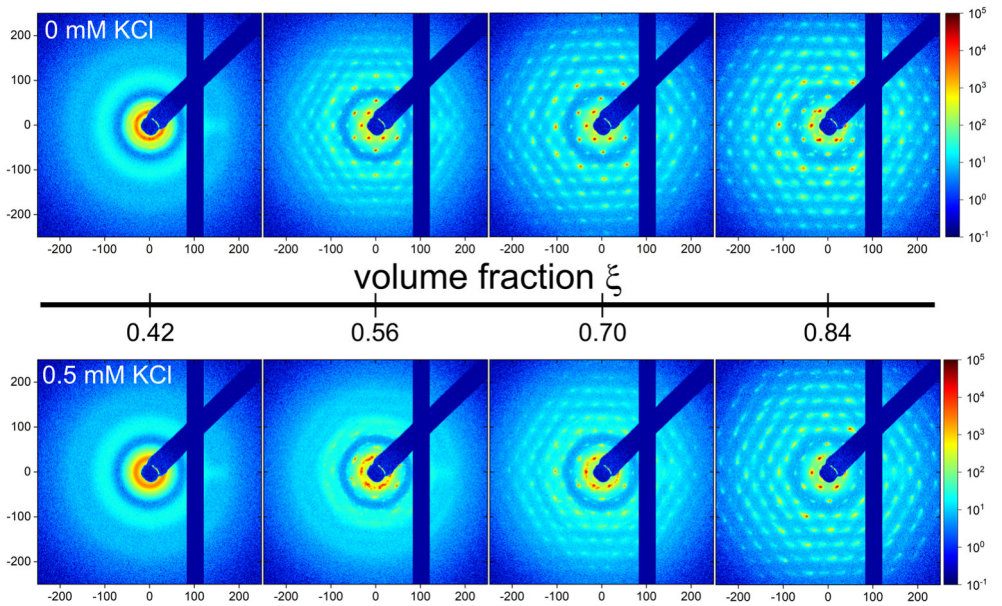

Figure 6.2. SAXS pattern of CS microgels in the unscreened (top) and charge-screened state (bottom) in dense packing with increasing generalized volume fraction ζ(20°C). The volume fraction is calculated based on number concentration N and R_h at 20°C in the unscreened state. SAXS patterns (top) were adapted from our previous work.[131]

In addition to the scattering patterns recorded at 20 °C, **Figure S6.7** in the supporting information shows scattering patterns of CS microgel dispersions with the same particle number concentration (N) recorded at 40 °C, i.e., in the collapsed state of the microgels. It is clearly shown that all samples in the probed range of volume fractions are in the fluid state at the respective temperature.

Radial averaged scattering profiles extracted from the SAXS patterns in **Figure 6.2** are shown in **Figure 6.3a**. In addition to the Bragg peaks, the scattering profiles exhibit pronounced form factor oscillations which allow for form factor analysis. The form factor minima at q = 0.25 nm^{-1} and 0.05 nm^{-1}are related to the SiO_2 core and the shell, respectively. When ζ is increased, the form factor minimum related to the shell is shifting towards higher q, indicating a decrease in size of the microgel, which we attribute to osmotic deswelling.[194] As expected for a non-deformable object, the position of the form factor minima, in q, related to the core stays constant.

According to our previous study, we ascribe the osmotic deswelling of the CS microgels, to the osmotic stress of the microgel dispersion, scaling with volume fraction. Due to the sharp Bragg peaks, the form factor oscillations in the presented SAXS profiles are very pronounced, enabling us to perform form factors analysis of the CS microgels in dense packings, where $S(q) \neq 1$. Form factors were described with the same CS model with an exponentially decaying scattering contrast of the shell that was used to fit the scattering data in the dilute regime. The modeled form factors are indicated as solid black lines in **Figure 6.3a** and describe the form factor oscillations very well for the high and mid q-range ($q \geq 0.04$ nm^{-1}). The respective fit parameters are listed in **Table S6.12** and **S6.13**. Deviations between fits and experimental data at low q ($q < 0.04$ nm^{-1}) are attributed to the structure factor contribution to scattering profiles. As the form factor minima related to the scattering contribution of the PNIPAM shells shift towards higher q for an increase in ζ, a decrease in the total radius of the CS microgels from 138 to 116 nm can be found. This is accompanied by a more pronounced decline in the exponential decay of the shell[131] and reflects a conservation of the polymer volume fraction of the microgel. The lighter colors in **Figure 6.3** are associated to CS microgel dispersions with screened charges and the form factor oscillation are similar to oscillations exhibited by the CS microgels measured in absence of salt. This is proven by form factor analysis, where we cannot find differences within particle size or morphology depending on the KCl concentration. This indicates that the increase in ionic strength does not influence the osmotic deswelling of the CS microgels for the investigated conditions as already reported in the literature for purely pNIPAM microgels.[194, 204, 217]

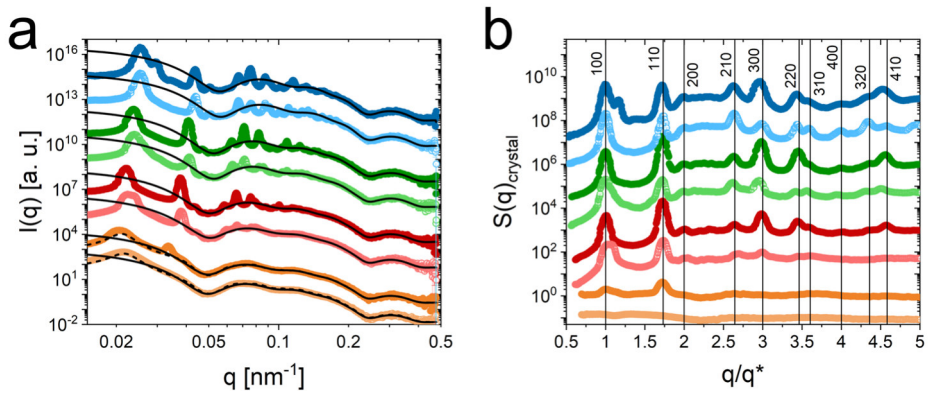

Figure 6.3. Results from synchrotron-SAXS measurements of CS microgels in dense packings at 20°C. (**a**) SAXS profiles for samples with ζ (20 °C) of 0.42 (orange), 0.56 (red), 0.70 (green) and 0.84 (blue). ζ is calculated based on R_h in the unscreened state. The respective dark colors correspond to samples of CS microgels measured in absence of salt while the lighter colors correspond to the microgels with screened charges. Solid black lines are form factor fits. Dashed lines correspond to a PY structure factor fit. (**b**) Normalized crystalline structure factors extracted from the SAXS profiles measured at 20 °C. Same color code as for the SAXS profiles. The straight vertical lines indicate the theoretical positions of the Bragg peaks for an hcp crystal structure. Normalization was performed on the position of the first structure factor maximum related to the hcp crystal structure (ζ (20 °C), q^* charged/charged-screened: 0.42, 0.0195/0.0195; 0.56, 0.0221/0.0221; 0.70, 0.0238/0.0241; 0.84, 0.0255/0.0254).

The scattering profiles for ζ = 0.42 in **Figure 6.3a** exhibit a fluid structure factor contribution in addition to a weak Bragg peak for the dispersion with CS microgels in the unscreened state (orange). In order to account for the fluid structure factor contribution we combine the Percus-Yevick (PY) structure factor with the form factor fit, which is shown as dashed black line.[184] For unscreened CS microgels, the structure factor contribution yields a volume fraction ϕ(PY) of 0.44 and a hard sphere radius R_{HS} = 158 nm, while in the charge-screened state the values of ϕ(PY) = 0.42 and R_{HS} = 152 nm are slightly smaller. These differences point to a significant screening of charges and thus reduction in the range of inter-microgel interactions in the case of added salt. Here, the primary aim of applying the PY model on the scattering data was the extraction of the crystalline structure factors. As the PY model is not capable of describing the influence of electrostatics on the phase behavior, the obtained results can only be interpreted in a qualitative manner and not quantitatively.

Nevertheless, the decrease in the effective interaction radius can be attributed to the screening of charges and a reduction of electrostatic interaction between the CS microgels.

With the modeled form factors and the application of the PY-fits on the low ζ data (orange) in **Figure 6.3a** we are able to extract the crystalline structure factor ($S(q)_{crystal}$). This was done by dividing the scattering profiles by the modeled form factors. The extracted structure factors are shown in **Figure 6.3b**, where the q-axis was normalized to the position of the first structure factor maximum q^*, related to a Bragg peak. Scattering profiles which do not possess a distinct Bragg peak related to the 100 crystal plane, were normalized on the 110 peak with respect to the ratio between 100 and 110 being 1.73.[131] The sample with ζ = 0.42 in the charge-screened state (light orange), exhibits no Bragg peaks and the normalization was conducted similarly to the sample with the same ζ. The normalization enables a direct comparison of the structure factors independent of ζ and the resulting changes in interparticle distance. Due to this we can indicate the theoretical positions of the Bragg peaks as vertical black lines and relate the Bragg peaks to the respective Miller indices *hkl*, for a hexagonally closed packed (hcp) crystal system.

For details on the $S(q)$ extraction, the normalization procedure and the determination of the crystal structure we refer to our previous work.[131]

The sample with ζ = 0.42 under charge-screened conditions (light orange) does not exhibit any crystalline contributions. For ζ = 0.42 with unscreened charges, the extracted crystalline structure factor exhibits two Bragg peaks of weak intensity, indicating the presence of a crystalline phase in coexistence with the fluid phase. All extracted structure factors for $\zeta \geq 0.56$ possess distinct and sharp Bragg peaks, which match well to the theoretical peak positions. This indicates the presence of an hcp crystal structure for our samples, independent of ζ and charge-screening. For $\zeta \geq 0.70$ (green and blue symbols) the scattering profiles and extracted structure factors are very similar and do not show a pronounced influence of the charge-state. Here, all extracted structure factors exhibit multiple orders of sharp and distinct Bragg peaks.

The CS microgels with ζ = 0.56 show less orders of Bragg peak under charge-screened conditions, compared to dispersion prepared in absence of salt. In addition, the Bragg peak intensity is lower which might indicate that the generalized volume fraction ζ of the dispersion is close to the phase boundary between fluid and crystalline state. This is also reflected by the respective SAXS pattern in **Figure 6.2**. Based on the scattering profiles and patterns we conclude that the CS microgel dispersions with ζ = 0.42 in the unscreened state and ζ = 0.56 under charged-screened conditions are close to the phase boundary between fluid and crystalline state.

With the known relation between the Bragg peaks and the respective Miller indices, we can extract the lattice constants of the colloidal crystals in dependence of ζ and the screening state. The dependence of the Bragg peak position and the Miller indices is shown in **Figure S6.8** in the Supporting Information. Lattice constants decreasing from 374 to 287 nm were obtained for increasing volume fractions. The addition of salt did not influence the lattice spacing (**Table S6.14**). We also performed Williamson Hall analysis on the scattering data in order to extract the size of the coherently scattering domains of the colloidal crystals (**Figure S6.9**).[203] Here, domains sizes in a range between 2 to 4 µm were found (**Figure S6.10**).

6.4.3 Collapsed Core-Shell Microgels in Dense Packings

In addition to the scattering profiles recorded at 20 °C, where most of the investigated CS microgel samples were crystalline, we performed SAXS measurements at 40 °C, i.e., where the microgel shells are in the collapsed state. Importantly, the same samples as for measurements at 20 °C were used in these experiments. Thus, for each sample the number concentration N is fixed while the volume fraction changes in dependence of the swelling state of the microgel shells. The respective SAXS profiles are shown in **Figure 6.4a**. For q > 0.05 nm^{-1}, the scattering profile is dominated by the form factor oscillations related to the collapsed shell and the contribution of the core. The form factor contributions to the scattering profiles are very similar, independent of ζ or changes in charge-screening. In the low q-regime, the scattering profiles exhibit a pronounced structure factor contribution. The first form factor minimum related to the shell is located at q = 0.056 nm^{-1}. This is found for all investigated samples and related to the reduced water content of the CS microgels in the collapsed state.

Due to this, the CS microgels are less affected by osmotic deswelling and the position of the first form factor minimum stays constant. In contrast to the form factor contribution to the scattering profile, the screening of charges strongly influences the respective structure factor contribution to the scattering data. Samples in absence of salt (darker colors) exhibit a pronounced structure factor, shifting towards higher q when ζ is increased. When the samples are investigated in the charge-screened state, the structure factor oscillations become less pronounced. For a detailed analysis, we extracted the structure factors, following the procedure recently reported by us.[131] The extracted structure factors are shown in **Figure 6.4b** and exhibit a shift of the maxima towards higher q with increasing ζ. In addition, when comparing structure factors with similar ζ under charged and charge-screened conditions it is noticeable that the maxima for the screened state are shifted towards higher q and the structure factor oscillations are less pronounced. The extracted structure factors were fitted (grey solid lines) with a hard-core one-Yukawa potential rescaled mean spherical approximation model (1Y-RMSA)[151, 152, 218] which describes a fluid of hard spheres where the electrostatic repulsion is ascribed by a single repulsive potential. The fits are in good agreement with the data and the respective fit parameters are listed in **Tables S6.20** and **S6.21** in the Supporting Information. The structure factor analysis reveals a hard-core radius of about 110 nm for the CS microgels which is slightly larger than the respective R_h of 103 nm. Based on a recent work from Zhou et al. we assume that this increase might be related to ion cloud of the CS microgels.[217] The extracted potentials reveal a pronounced influence of the charge-screening and are shown in **Figure S6.11** in the Supporting Information. In absence of salt, the potentials express a rather long range, and the potential strength is decreased to the factor of 1/e at 15.5 ± 2.7 nm beyond the hard-core radius. For the charge-screened state the strength of the potential is drastically decreased, as well as the range which reaches 1/e of the initial strength at 8.1 ± 0.5 nm. This reflects a drastic decrease in the effective interaction radius of the CS microgels due to charge screening. In addition, a comparison of the 1Y-RMSA model with the PY-[184] and the Hayter-Penfold rescaled mean spherical approximation model[220] is provided in **Figure S6.11** in the Supporting Information.

One can assume that the influence of the salt screening might be more pronounced for the microgels in their swollen state as the effective charge in the outer periphery of the microgel and, therefore, the electrophoretic mobility is lower (**Figure 6.1a**). In conclusion, the results from SAXS measurements reveal that the ionic strength of the dispersion drastically influences the effective interaction radius of the CS microgels in their collapsed state. We attribute this to a screening of the charges in the outer periphery of the CS microgels in presence of KCl that reduces the electrostatic interaction.

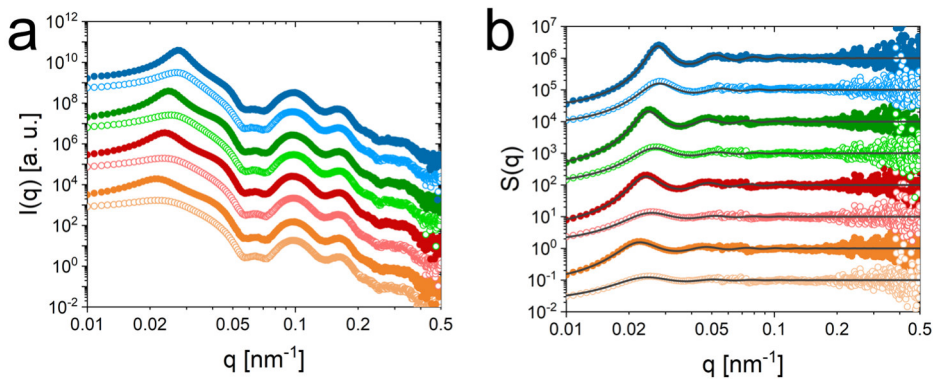

Figure 6.4. Results from synchrotron-SAXS measurements of CS microgels in dense packings at 40°C with ζ (20 °C) of 0.42 (orange), 0.56 (red), 0.70 (green) and 0.84 (blue). ζ was calculated based on R_h in the unscreened state. The respective dark colors correspond to aqueous dispersion in absence of salt while the lighter colors are related to dispersion with screened charges. (**a**) SAXS profiles of CS microgels. (**b**) Structure factors extracted from the SAXS profiles. The solid black lines correspond to structure factor fits based on the PY model. Data of the CS microgels in the unscreened state were adapted from our previous work.[131]

6.4.4 Following Phase transitions by Optical Spectroscopy

A time and cost-efficient approach to investigate the phase behavior of the CS microgels in dense packings is temperature dependent optical spectroscopy. As the colloidal crystals possess lattice constants slightly below the wavelength of visible light, they exhibit Bragg peaks in the Vis-NIR region.[47, 72, 73, 81] Vis-NIR spectra of the investigated samples are shown in **Figure 6.5a**. For c_{KCl} = 0 mM all samples exhibit distinct and sharp Bragg peaks. In the presence of salt (c_{KCl} = 0.5 mM) Bragg peaks are observed for all samples except for ζ = 0.49.

This is in good agreement with our findings from SAXS at 20 °C, where we found Bragg peaks for all samples in the unscreened state and a fluid phase for the charge-screened dispersion with ζ = 0.42. Independent of c_{KCl}, the Bragg peaks shift towards lower wavelength as ζ is increased and there is not a clear dependence on the presence or absence of salt. This is in agreement with our findings from SAXS. The shift of the Bragg peaks with concentration is related to the decrease of the lattice constant *a*. Additional spectra from all samples used for SAXS experiments at 20 °C and tables listing Bragg peak positions and lattice constants *a*, can be found in the Supporting Information, **Figure S6.12** and **Table S6.22** and **S6.23**.

Vis-NIR spectra recorded from a dispersion of CS microgels with ζ = 0.70 in absence of salt at various temperatures are shown in **Figure 6.5b**. The increase in temperature from 20 to 50 °C is represented by the coloration of the spectra from blue to red. At low temperatures, the Bragg peak at 687 nm remains nearly unaffected until 31.1 °C, where the peak begins to shift towards lower wavelength and decreases in intensity. The peak disappears completely at 32.6 °C and higher (see also inset in **Figure 6.5b**). Thus, the phase transition from crystalline (Bragg peak) to fluid (no Bragg peak) occurs in a temperature window as small as 2 °C. Detailed information about the procedure of these measurements including temperature steps and equilibration times are given in the Supporting Information of our previous work.[131] Here, we also presented time-dependent measurements in the range of the transition temperature to verify that the samples are in equilibrium at the time of the measurement. When temperature is increased, the CS microgels decrease in size due to the thermoresponsive behavior of the PNIPMA shell and consequently the volume fraction decreases for a given number concentration of CS microgels (**Figure 6.1b**). This can lead to complete melting of the crystalline samples given that the threshold volume fraction for crystallization is passed. After the disappearance of the Bragg peak, the absorbance increases slightly until the temperature reaches 50 °C. This is due to a change in the scattering intensity of the CS microgels during shell collapse.[32, 221]

We now aim to monitor the phase transitions (solid-fluid and fluid-solid) by using background corrected absorbances as function of temperature. The background correction was used to consider only the coherent contribution to the absorbance at the Bragg peak position. In this way, the incoherent scattering background related to the light scattering of the CS microgels could be subtracted.

Figure 6.5c shows the evolution of the absorbance for the samples with ζ = 0.70 without (top) and with charge-screening (bottom). The red triangles correspond to the heating cycle, while blue triangles refer to the cooling cycle. The green colored areas indicate the regions of the phase transition where the absorbance drops/rises significantly for the heating/cooling cycle. In the absence of salt, the nearly constant absorbances outside the phase transition region from the heating and cooling cycle overlap nicely. Small differences can only be observed in the phase transition region with a small hysteresis where recrystallization in the cooling cycle occurs a slightly lower temperatures then the melting during the heating cycle. Interestingly, in the charge-screened state the transition region appears at lower temperatures, approximately 5 °C shifted compared to the salt-free case. As both samples possess the same particle number concentrations N and generalized volume fraction ζ, a decrease in the transition temperature is associated to a change in effective interaction radius of the CS microgels.

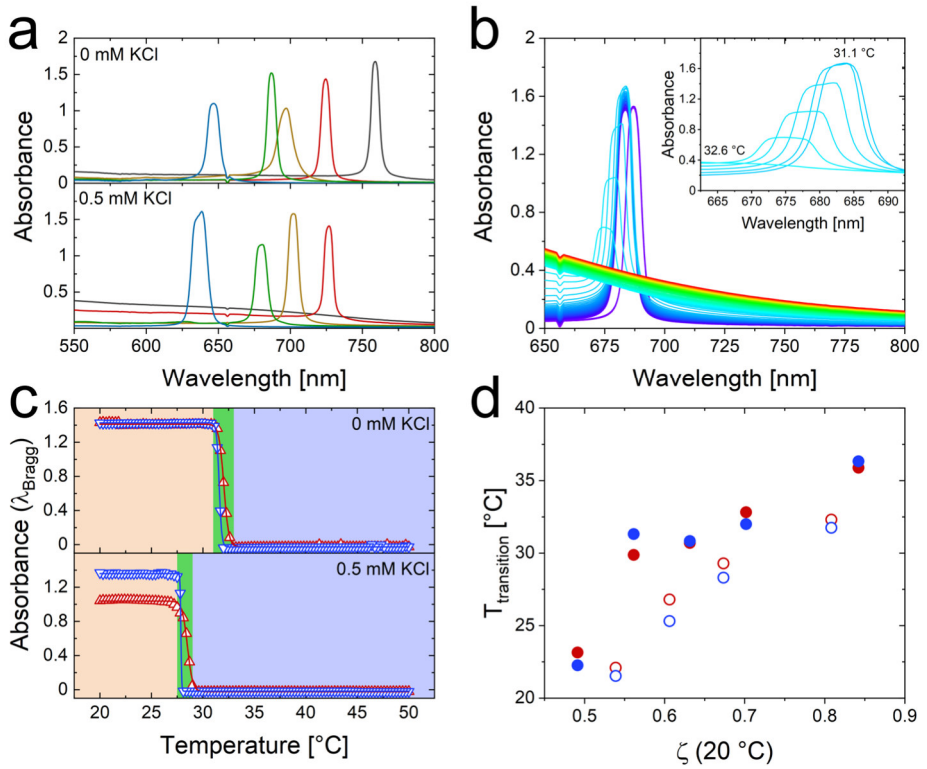

Figure 6.5. Results from temperature-dependent Vis-NIR absorbance spectroscopy. (**a**) Absorbance spectra of CS microgels with ζ of 0.49 (grey), 0.56 (red), 0.63 (orange), 0.70 (green) and 0.84 (blue) in absence of salt (top) and under charge-screened conditions (bottom) recorded at 20 °C. ζ was calculated based on the R_h in the charge-screened state. (**b**) Temperature-dependent Vis-NIR absorbance spectra of a CS microgel dispersion (ζ = 0.70) in absence of salt. Here the colors correspond to an increase in temperature from blue to red. The inset shows a selected temperature range of the spectra with focus on the spectral region of the Bragg peak. (**c**) Background corrected absorbance of the Bragg peak as a function of temperature for the samples with ζ = 0.70 CS microgel dispersion in the charged- (top) and charge-screened state (bottom). Red triangles correspond to the heating- and blue triangles to a cooling cycle. The green area indicates the transition region between 31 and 33 °C or 27.5 and 29 °C depending on the absence or presence of salt. (**d**) Transition temperatures for crystal melting (red) and recrystallization (blue) in dependence of ζ for the respective CS microgel dispersions. Filled circles correspond to the unscreened and empty circles correspond to the charge-screened state.

In **Figure 6.5d** we compare the transition temperatures obtained from heating/cooling cycles in the absence/presence of salt. For details on the determination of the transition temperatures we refer to our previous work.[131] The respective temperature dependent spectra and plots of the Bragg peak absorbance as function of temperature are given in the supporting information, **Figure S6.13** and **S6.14.** The transition temperatures are plotted as a function of the generalized volume fraction of the samples at 20°C (ζ(20 °C)). For an increase in ζ, the transition temperatures increase as well. This is expected as the transition volume fraction of a higher concentrated sample is reached at higher temperatures due to the increased number of CS microgels. The Transition temperatures for samples in the unscreened state (filled symbols) are generally higher compared to the charge-screened state (empty symbols). Generalized volume fractions and the respective R_h's at 20 and 40 °C are listed in **Table S6.10** in the Supporting Information. Since we know the respective CS microgel size (R_h, see **Figure 6.1a**) at the respective transition temperature we can use the particle number concentration N to calculate the critical volume fraction for the phase transition, $\zeta_{\mathrm{transition}}$:

$$\zeta_{\mathrm{transition}} = N\frac{4}{3}\pi R_{\mathrm{h}}(T_{\mathrm{transition}})^3 \tag{6.1}$$

Figure S6.16 shows $\zeta_{\mathrm{transition}}$ as function of the generalized volume fraction at 20 °C (ζ(20 °C)) resulting in an average $\zeta_{\mathrm{transition}}$ of 0.43 ± 0.03 in absence of salt and 0.54 ± 0.02 under charge-screened conditions. The addition of salt that is expected to screen charges in the outer periphery of the CS microgels obviously leads to a reduction of the effective interaction radius of the microgels. This consequently shifts the critical volume fraction of the phase transition to higher values. In comparison to the transition volume fraction of hard spheres (ϕ = 0.49), the CS microgels crystallize at lower volume fractions in the absence of salt. With screened charges, this volume fraction is drastically increased and above the value for hard spheres. This is again attributed to the reduction of the effective interaction radius of the microgels. Interestingly, melting and freezing volume fraction of pNIPAM based microgels in literature are reported to be about 0.56 to 0.61.[36, 222] This is close to the transition volume fraction we found for the CS microgels in the charge-screened state. The microgels investigated in these studies possess a comparably low crosslinker content and the softness of the particles might influence the phase behavior.[124]

In addition, the volume fractions were determined by viscometry, where we rely on number concentration. Therefore, phase borders might slightly shift. The differences between the reported melting and freezing volume fraction and the transition volume fraction found for the CS microgels in the unscreened state may be also related to a more complex ion cloud. A zeta potential of -25 mV was determined for the pure silica core, indicating a pronounced presence of charges. With the recent findings about the size of the ion cloud of microgels from Zhou et al.[217], we cannot exclude an influence of the charges attached to the core on the ion cloud of the microgel shell. Therefore, the difference between the reported freezing volume fractions and the transition volume fraction of the CS microgels in the unscreened state might be related to the dimensions of the ion cloud of the CS microgels. In order to investigate the influence of the core on the ion cloud additional complex experiments utilizing SANS are needed.

6.4.5 Temperature-Dependent Phase Diagram in Dependence of Charge-Screening

Figure 6.6 shows the temperature-dependent phase diagrams in absence (**a**) and presence of salt (**b**). These diagrams were constructed from screening CS microgels over a broad range of concentrations in small steps by using temperature-dependent absorbance spectroscopy. Note that a second batch of CS microgels had to be used for this study. More information can be found in the Experimental Section and the Supporting Information. Absorbance spectra of the respective CS2 microgel dispersions at a temperature of 20 °C are shown in **Figure S6.17**. For temperature ranges where Bragg peaks were detected a crystalline (solid) state was assigned. This phase is colored in light brown in **Figure 6.6**. In contrast a fluid-like phase was assigned when Bragg peaks were missing (light blue areas). The transition region is colored in green and was determined from the respective temperature onsets of melting/recrystallization from respective heating/cooling cycles. This procedure is in agreement with our recently published work.[131] More information can also be found in the Supporting Information. Generally, the phase diagrams reflect the swelling curves of the CS microgels (see **Figure 6.1a**). The crystalline regime is small at low values of ζ and extends over increasing temperature ranges with increasing ζ. The crystalline regime is shifted to higher values of ζ when salt (0.5 mM KCl) is added as already discussed in the context of **Figure 6.5d**. In presence of salt, we also find an overcrowded or jammed phase[123] at very high ζ extending to temperatures reaching the VPTT of the microgels. The solid black lines correspond to the average volume fractions of 0.39 ± 0.07 at c_{KCl} = 0 mM and 0.52 ± 0.03 at c_{KCl} = 0.5 mM where the phase transitions were observed (see **Figure S6.18** in the Supporting Information). Although the two batches of CS microgels used in this work have slightly different core and shell dimensions, we want to highlight, that the average values for $\zeta_{transition}$ are nearly the same for the two batches. This highlights the reproducibility of the synthesis and also the reliability of the analysis by temperature-dependent absorbance spectroscopy. Slight variations between the phase behavior of the two batches when comparing individual samples are most likely attributed to variations in sample preparation rather than differences between the microgels. In **Figure 6.6a** (absence of salt) the transition region (green) fluctuates significantly between samples of different concentrations and sometimes extends over a few °C.

In contrast, in **Figure 6.6b** (presence of salt), the transition region shows a smooth evolution with increasing ζ with much smaller temperature ranges. Importantly, in presence of salt the phase boundary between fluid and solid state and the calculated transition temperatures based on the average $\zeta_{transition}$ (black line) overlap nicely.

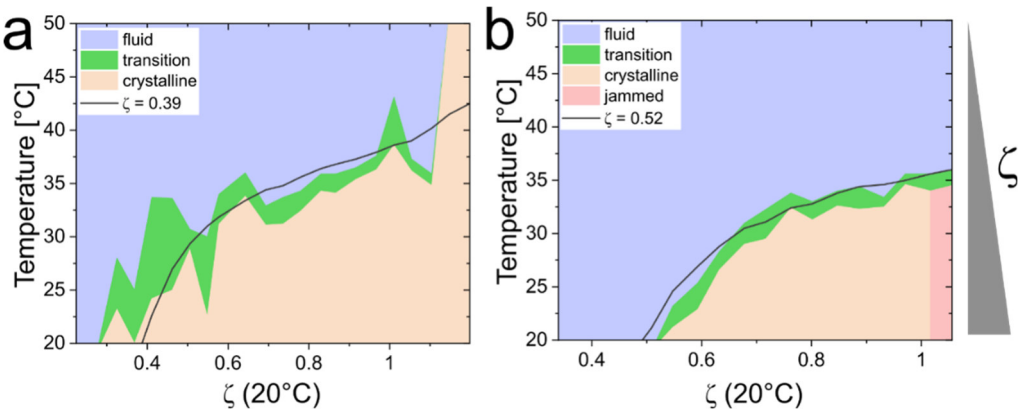

Figure 6.6. Temperature-dependent phase diagrams of CS2 microgels in the charge-unscreened (**a**) and screened state (**b**). The abscissa corresponds to the generalized volume fraction ζ of the investigated samples at 20 °C. The blue area corresponds to the fluid regime and the crystalline regime is indicated in light brown. Between both regimes we find the transition area marked in green. For the area colored in light red in (**b**) no Bragg peaks could be found and we attribute this to an overcrowded (jammed) state. The solid black line indicates the expected transition temperature based on the respective average $\zeta_{transition}$.

The presented phase diagrams set the ground for more detailed studies on phase transitions in dense packings of soft and deformable microgels with temperature-dependent small-angle scattering. It is also shown that electrostatic interactions can have a pronounced influence on the phase behavior of even weakly charged colloidal systems.

6.5 Conclusion

We used slightly charged core-shell microgels to study the phase behavior of soft colloids in the charged and charge-screened state. The addition of 0.5 mM KCl to dispersions of the microgels resulted in a significant reduction of the electrophoretic mobility along with very minor changes in the hydrodynamic dimensions. Importantly, the colloidal stability was maintained even at temperatures well above the VPTT. This allowed for a direct comparison of the phase behavior in presence/absence of salt over a broad range of concentrations and temperatures. Complementary small-angle neutron and X-ray scattering data were used to study the form factor of the microgels in the dilute state. Dense samples were studied by synchrotron-small-angle X-ray scattering revealing crystalline samples with extraordinary long-range order at 20 °C for sufficiently high packing fractions. Here, the addition of salt induced a shift in the phase boundary between the fluid and crystalline phases towards higher volume fractions. In agreement with recent literature the osmotic deswelling of the microgels was not affected by the presence of salt.[194, 204, 217] Samples with the exact same particle number concentrations were investigated in the collapsed state, above the volume phase transition temperature and exhibit pronounced fluid structure factors. The screening of charges in the outer-periphery of the microgels was found to have a direct impact on the structure factors. Here, structure factor analysis with a model utilizing a Yukawa potential indicates a decrease in the effective interaction radius of the core-shell microgels. Similar trends with respect to charge-screening were found in temperature-dependent absorbance spectroscopy, where the transition-temperature for the melting and recrystallization processes decreased in the presence of salt.

We present for the first-time temperature-dependent phase diagrams directly comparing the charged and charge-screened conditions. When 0.5 mM KCl is present, the crystalline phase is shifted to higher volume fractions while the temperature ranges of the phase transition region become much smaller as in the salt-free case. Furthermore, the phase boundary between fluid and solid phase overlaps much better with the transition curve corresponding to the calculated transition temperatures based on average critical volume fractions of the phase transitions when salt is present.

To the best of our knowledge temperature-dependent phase diagrams of slightly charged microgels under charged and charge-screened conditions have not yet been presented in literature. Our work sets the ground for future studies on phase transitions in dense systems of soft colloids, for example using temperature-dependent synchrotron-SAXS. Precise knowledge of the transition regions is of utmost importance for designing future temperature-dependent experiments. Furthermore, our results suggest that studies on the phase behavior of slightly charged microgels are ideally performed under charge-screened conditions, i.e., in presence of low concentrations of salt that do not hamper the colloidal stability above the VPTT. In this case, we believe it will be of particular interest to study samples at high concentrations where we propose the jammed state. Quenching of samples with temperature jumps of different magnitudes might allow phase transitions from fluid to jammed or even from crystalline to jammed states and vice versa.

Conflicts of Interest

There are no conflicts of interest to declare.

Acknowledgements

The authors acknowledge the German Research Foundation (DFG) and the state of NRW for funding the cryo-TEM (INST 208/749-1 FUGG) and Marius Otten from Heinrich-Heine-University Düsseldorf for his assistance with the operation and image recording. The authors thank the Center for Structural Studies (CSS) that is funded by the DFG (Grant numbers 417919780 and INST 208/761-1 FUGG) for access to the SAXS instrument. A. S. thanks the DFG for financial support of project A3 (Project No. 191948804) within the SFB 985 – Functional Microgels and Microgel Systems. The authors acknowledge Déborah Feller for her assistance with the operation of the static light scattering setup. T. L. Wigger performed the data reduction from 2D detector images to enable the Williamson-Hall analysis. The authors thank the Institut Laue-Langevin for allocation of SANS beamtime on D11 (DOI: 10.5291/ILL-DATA.9-11-2027). A. V. Petrunin, T. Höfken, and P. Mota-Santiago helped with the SAXS measurements. The SAXS measurements were performed on the CoSAXS beamline at the MAX IV laboratory (Lund, Sweden) under the proposals 20200777 and 20220526. The Research conducted at MAX IV, a Swedish national user facility, is supported by the Swedish Research council under contract 2018-07152, the Swedish Governmental Agency for Innovation Systems under contract 2018-04969, and Formas under contract 2019-02496. This work benefited from the use of the SasView application, originally developed under NSF award DMR-0520547. SasView contains code developed with funding from the European Union's Horizon 2020 research and innovation program under the SINE2020 project, grant agreement No 654000. Data of this work were discussed and parts of this paper have been written at the Kavli Institute for Theoretical Physics (KITP), Santa Barbara (USA) during the "Nanoparticle Assemblies: A New Form of Matter with Classical Structure and Quantum Function" programme. This research was supported in part by the National Science Foundation under Grant No. NSF PHY-1748958.

6.6 Supporting Information

Transmission Electron Microscopy (TEM)

In order to verify the core-shell (CS) nature of our microgels we performed TEM. As seen in **Figure S6.1a-b,** the microgels possess single cores encapsulated into a rather homogeneous polymer shell, possessing a weaker contrast compared to the core. The fraction of core-less microgels is below 1% and therefore negligible. From these and additional TEM images we determined average core radii of 18 ± 2 nm. The size distribution of the SiO_2 cores is illustrated in **Figure S6.1c**.

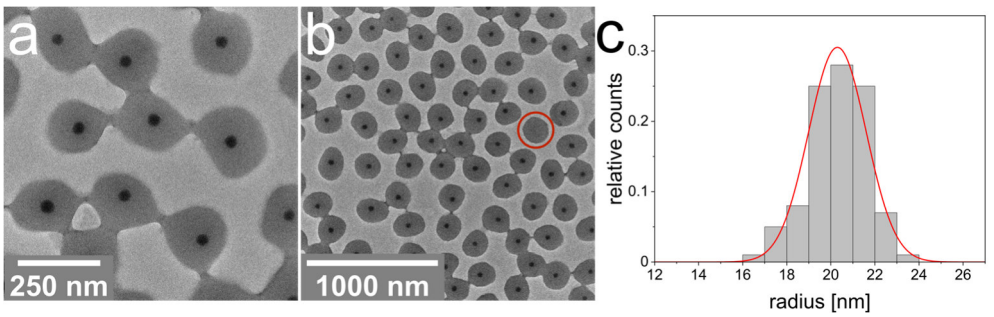

Figure S6.1. Brightfield TEM images of CS1 (**a**, **b**) at different magnifications. (**c**) Shows the respective size distribution of the SiO_2 cores. TEM images and the respective size distribution are adapted from our previous work.[131]

Zeta Potential

Temperature-dependent zeta potential of the CS microgels is shown in **Figure S6.2**. The zeta potential was calculated based on the Smoluchowski approximation. As expected, the temperature dependent evolution of the zeta potential is the same as for the electrophoretic mobility. A negative zeta-potential corresponds to a negative charge while the respective value corresponds to the magnitude of the charges. At low temperatures, the unscreened CS microgels exhibit a zeta potential of -17 mV which decreases after passing a temperature of 35 °C, resulting in a final potential of -28 mV at 50 °C. Due to the negative charge of the initiator, we exhibit a decrease of the negative zeta potential which represents an increase in charge of the microgel. The increase in charge density on the particle is attributed to the thermoresponsive properties of the microgel. Here, an increase in temperature results in a deswelling of the microgel which is accompanied by a reduction of its surface area and therefore an increase in charge density.

When the CS microgels are dispersed in 0.5 mM KCl-solution the magnitude of the zeta potential is decreased to -3 mV at a temperature of 20 °C. This indicates that the ions effectively screen the charges of the microgel at low temperature. For an increase in temperature, we can see the same trend compared to the microgels in in the unscreened state, resulting in a zeta potential of -18 mV at 50 °C.

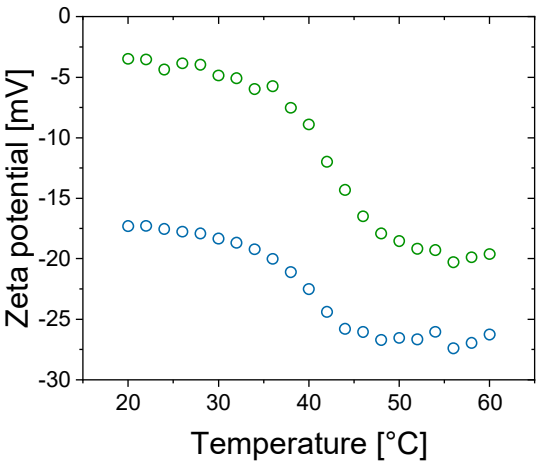

Figure S6.2. Temperature dependent zeta potential of CS microgels in absence (blue) and presence of KCl (green).

Form Factor Modeling and Fitting

We performed small-angle X-ray scattering SAXS and small-angle neutron scattering SANS on dilute and concentrated CS microgel in aqueous dispersion. The scattering data was radially averaged to extract the scattering intensity *I*, as function of the scattering vector *q*.

$$|\vec{q}| = q = \frac{4\pi}{\lambda} sin\frac{\theta}{2} \quad \text{(S6.1)}$$

Here, the wavelength of the respective X-ray or neutron beam is given by λ and the scattering angle is given by θ.

The scattering intensity for the respective *q*-range can be described by the following equation:

$$I(q) = N{V_{\mathrm{particle}}}^2 \Delta SLD^2 P(q) S(q) + I_{\mathrm{B}} \quad \text{(S6.2)}$$

Here, *N* is the particle number density, V_{particle} is the volume of the scattering object and *ΔSLD* is the difference in scattering length density (SLD) between the scattering object and the solvent. With the form factor *P*(*q*) of the scattering object and the structure factor S(*q*). In order to describe additional background contributions I_{B} is added.

For dilute dispersions, the structure factor contributions become neglectable as $S(q) \approx 1$.

In order to describe the scattering intensity *I*(*q*) of the CS microgels we made use of core-shell model:

$$I(q) = \frac{scale}{V_{\mathrm{particle}}}\left[3V_{core}SLD_{\mathrm{core}}k(qR_{\mathrm{core}}) + 3V_{particle}SLD_{\mathrm{shell}}k\left(qR_{\mathrm{particle}}\right) - 3V_{core}SLD_{\mathrm{shell}}k(qR_{\mathrm{core}}) - 3V_{\mathrm{particle}}SLD_{\mathrm{solvent}}k\left(qR_{\mathrm{particle}}\right)\right]^2 + I_{\mathrm{B}} \quad \text{(S6.3)}$$

with

$$k(qR) = \frac{\sin(qR) - qR\cos(qR)}{(qR)^3}$$

Here, *scale* corresponds to a scaling factor (representing the volume fraction if measured in absolute units), *V* is the volume of the respective scattering object and R_{core} and R_{particle} are attributed to the total radii of the core and the particle. Here, R_{particle} is the defined by the sum of thickness of the shell $\Delta t_{\mathrm{shell}}$ and R_{core}. As the core and the solvent possess a homogeneous structure, we kept the *SLD* constant for both materials. *k*(*qR*) corresponds to the form factor oscillations of a spherical scattering object.

In the swollen state (20 °C), the *SLD* of the microgel shell is described with an exponential decay in the *SLD* profile of the shell to ascribe for the gradient in crosslinker density (core-exponential-shell model).[206]

For the CS microgels in their collapsed state (45 °C) the shell is described with a homogeneous shell and therefore, the *SLD* of the shell is kept constant (core-homogeneous-shell model).

More details to the fitting procedure and the applied core-shell models are given in the Supporting Information of our previous work on the same CS microgels.[131]

In order to fit the high q (q > 0.3 nm^{-1}) SANS data, recorded from CS microgels in their swollen state (20 °C), a Lorentzian function (Ornstein-Zernike contribution) was added to describe internal fluctuations of the polymer network.

$$I(q) = \frac{I_0}{1+q^2{\xi_{OZ}}^2} \tag{S6.4}$$

Here, I_o is the forward scattering and ξ_{OZ} corresponds to the correlation length.

The scattering intensity of the silica cores without polymer shell is described with a simple polydisperse sphere model.

$$I(q) = \frac{scale}{V_{\text{particle}}}\left[3V(R)\Delta SLD\,\frac{\sin(qR)-qR\cos(qR)}{(qR)^3}\right]^2 + I_{\text{B}} \tag{S6.5}$$

In order to take the polydispersity of the particles into account, we applied a gaussian distribution on the radius and therefore the volume of the scattering object in the form factor model used to fit the scattering profiles. Here, $\langle R\rangle$ is the average particle radius and σ_{poly} corresponds to the relative size polydispersity.

$$D\left(R,\langle R\rangle,\sigma_{\text{poly}}\right) = \frac{1}{\sqrt{2\pi{\sigma_{\text{poly}}}^2}}exp\left(-\frac{(R-\langle R\rangle)^2}{2{\sigma_{\text{poly}}}^2}\right) \tag{S6.6}$$

The form factor fitting was performed with the SasView[197] software and the respective parameters are listed in **Tables S6.1** and **S6.2**. For details about the fitting procedure of the SAXS data we refer to our previous work.[131] The fitting process of the SANS/SLS data is explained in the respective section of the SI.

Table S6.1. Parameters applied to fit the SAXS and merged SANS/SLS profiles of the dilute CS microgels in aqueous dispersion in absence of salt. Parameters for SAXS are adapted from our previous work.[131]

Parameters	[1]SAXS (20°C)	[2]SANS/SLS (20°C)	[3]SANS/SLS (45°C)
scale	0.029	0.03	0.006
IB [a. u.]	0.2	0.057	0.061
I_0 [a. u.]	-	0.12	-
ξ_{OZ} [nm]	-	3.2	-
R_{core} [nm]	18	18	18
Δt_{shell} [nm]	120	120	70
SLD_{core} [10^{-6} Å^{-2}]	17.75	3.3	3.3
$SLD_{shell,\ in}$ [10^{-6} Å^{-2}]	9.89	5.0	3.4
$SLD_{shell,\ out}$ [10^{-6} Å^{-2}]	9.43	6.4	3.4
$SLD_{solvent}$ [10^{-6} Å^{-2}]	9.43	6.4	6.4
σ_{core}	0.1	0.1	0.1
σ_{shell}	0.1	0.09	0.08
A	2.2	2.4	-

[1]Core-exponential-shell model

[2]Core-exponential-shell model + Ornstein-Zernike contribution

[3]Core-homogeneous-shell model

Table S6.2. Parameters applied to fit the SAXS and merged SANS/SLS profiles of the dilute CS microgels in aqueous dispersion and screened charges.

Parameters	[1]SAXS (20°C)	[2]SANS/SLS (20°C)	[3]SANS/SLS (45°C)
scale	0.029	0.027	0.005
IB [a. u.]	0.2	0.057	0.061
I_0 [a. u.]	-	0.13	-
ξ_{OZ} [nm]	-	3.2	-
R_{core} [nm]	18	18	18
Δt_{shell} [nm]	120	118	71
SLD_{core} [10^{-6} Å^{-2}]	17.75	3.3	3.3
$SLD_{shell,\ in}$ [10^{-6} Å^{-2}]	9.89	5.0	3.3
$SLD_{shell,\ out}$ [10^{-6} Å^{-2}]	9.43	6.4	3.3
$SLD_{solvent}$ [10^{-6} Å^{-2}]	9.43	6.4	6.4
σ_{core}	0.1	0.1	0.1
σ_{shell}	0.1	0.08	0.08
A	2.2	2.3	-

[1]Core-exponential-shell model

[2]Core-exponential-shell model + Ornstein-Zernike contribution

[3]Core-homogeneous-shell model

The volumes of the core and shell in combination with the respective contrast situations in SANS and SAXS based on the difference in SLDs are, are listed in **Table S6.3.** In addition, the interplay between contrast and volume of the scattering of core and shell, based on **Equation S6.2,** is listed in the following table. This reveals a dominating contribution of the shell (PNIPAM) to the scattering profile in both contrast situations. The difference is significant in SAXS and SANS but much more expressed for SANS, where the contribution of the core can be nearly neglected. For SAXS the core contribution is still pronounced and visible in the respective SAXS profiles.

Table S6.3. Influence of the respective SAS contrast Situation and CS microgel dimensions on the scattering properties.

Method	Material	$V_{core/shell}$ [m^3]	ΔSLD [10^{-6} $Å^{-2}$]	$V^2 \cdot \Delta SLD^2$ [10^{12} m^2]
SAXS	SiO_2	2.44E-20	8.32	0.041
	PNIPAM	1.10E-17	0.46	25.530
SANS	SiO_2	2.44E-20	3.1	0.006
	PNIPAM	1.10E-17	1.6	308.860

Figure S6.3 shows the SAXS profile of a dilute dispersion of CS microgels in their collapsed state, recorded at a temperature of 40 °C. We applied a core-homogenous-shell model on the scattering profile in order to fit the from factor of the CS microgel. The fit is presented as solid red line and is in good agreement with the recorded data. In **Table S6.4** we show the respective parameters of the fit which are comparable with our results from SANS. For more details we refer to our previous work.[131]

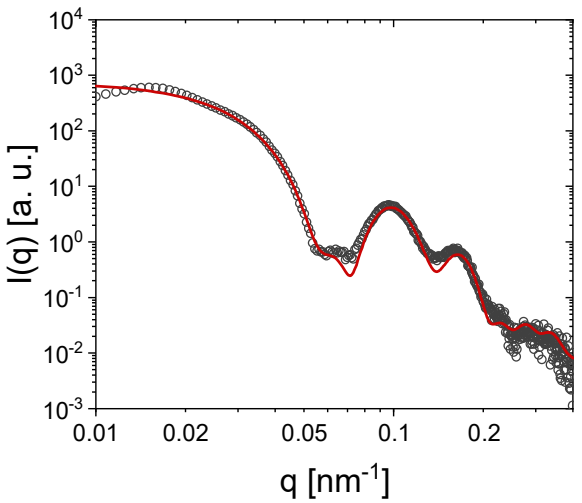

Figure S6.3. SAXS profile of CS microgels with generalized volume fraction ζ (20 °C) = 0.09 recorded at 40 °C. The solid red line indicates the form factor fit based on a core-homogeneous-shell model. Adapted from our previous work.[131]

Table S6.4. Parameters of the core-homogeneous-shell model applied to fit the form factor in the SAXS profile of the dilute CS microgels in aqueous dispersion. Adapted from our previous work.[131]

Parameters	SAXS (40°C)
scale	2.733
IB [a. u.]	0.003
R_{core} [nm]	18
Δt_{shell} [nm]	72
SLD_{core} [10^{-6} Å^{-2}]	17.75
$SLD_{shell,\ in}$ [10^{-6} Å^{-2}]	10.3
$SLD_{shell,\ out}$ [10^{-6} Å^{-2}]	10.3
$SLD_{solvent}$ [10^{-6} Å^{-2}]	9.43
σ_{core}	0.1
σ_{shell}	0.08

Small-Angle Neutron and Static Light Scattering

The recorded SANS profiles were merged with the respective SLS profiles and are shown in **Figure S6.4a**. Blue symbols correspond to CS-microgel dispersions recorded in absence of salt while the green ones were recorded in the charge-screened state. Scattering profiles were recorded at temperatures of 20 °C and 45 °C and the dotted, vertical line indicates the boundary between the merged SLS and SANS section of the scattering profile. The form factor fit which is shown by the solid red line is obtained from form factor analysis of the total scattering profile, including the SLS section. In order to take into account the smearing in SANS, the error in *q* was included in the fitting procedure. Due to the very low error in *q* of the merged SLS data, a very small error of 10^{-4} nm^{-1} was assigned to the respective data points to enable from factor analysis in SasView. A core-exponential-shell model and a core-homogeneous-shell model were used to describe the scattering properties of the CS microgels in the swollen (20 °C) and the collapsed (45 °C) state. In the fitting process known parameters like the *SLD*s of the solvent, core and the radius of the core were set to a fixed value and kept constant. The other parameters were approximated, within physically reasonable values to describe the respective scattering profile. Then all non-fixed parameters of the core-shell model were fitted simultaneously.

For the data recorded at 20 °C, the *SLD* of the shell needed to be limited to a value of $5 \cdot 10^{-6}$ Å^{-2}, because otherwise the fit did not sufficiently describe the low q-range of the scattering profile. In case of the scattering profiles recorded at 45 °C, the procedure was comparable, but *scale* was fixed at a value calculated based on the value of *scale* at 20 °C and the radii of the CS microgels at 20 °C and 45 °C. Here, the SLD of the shell was not limited to any borders.

For the screened and unscreened state, the form factor analysis yielded similar results at both temperatures, as presented in **Table S6.1** and **S6.2.** For all profiles we find distinct form factor oscillations which are well described by the respective fits and are primarily related to the PNIPAM shell of the CS microgel. For both temperatures we barley detect form factor oscillations correspond to the SiO_2 core.

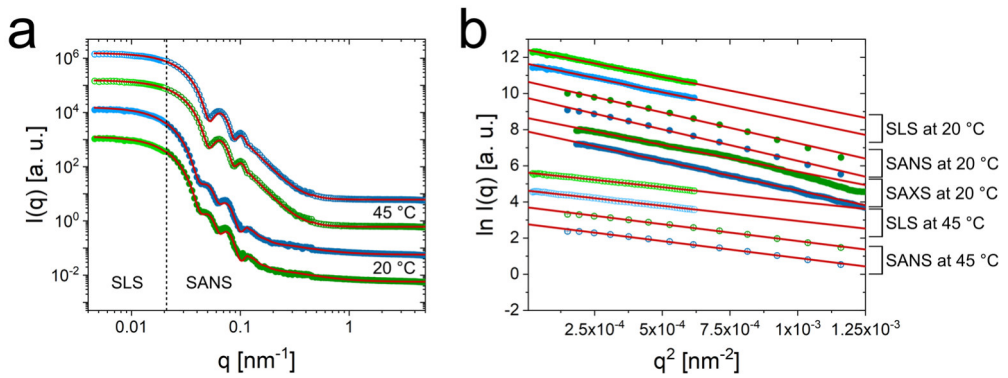

Figure S6.4. Scattering profiles referring to CS microgels measured in the absence of salt (blue) and the presence of 0.5 mM KCl (green) (**a**) Full *q*-range SANS scattering profiles at 20°C (full symbols) and 45°C (open symbols) with merged scattering profiles from SLS. The solid red lines correspond to the respective form factor fits (core-exponential-shell model for the profiles recorded at 20 °C and core-homogeneous-shell model at 45 °C). (**b**) Guinier plots in the *q*-range related to the scattering of the shell for SLS, SANS and SAXS. Plots are shifted on the y-axis for the sake of clarity.

In addition to the form factor analysis, we performed Guinier-analysis on the plateau like section of the scattering profiles related to the scattering of the CS microgels shell. The Guinier plots are shown in **Figure S6.4b** including the linear fits applied on the data points. We find a sufficient agreement between the fits and the respective data points and the results from the Guinier-analysis are presented in **Table S6.5**.

The linearized Guinier equation is shown below:

$$\ln\big(I(q)\big) = \ln(I_0) - \frac{q^2 {R_G}^2}{3} \tag{S6.7}$$

With q, the scattering vector, I_0 being the scattering intensity at infinity small q and the radius of gyration R_g. We extracted radii of gyration between 95 and 102 nm from the scattering profiles recorded at 20°C and radii of gyration between 70 and 75 nm at 45°C. In general, R_g extracted from samples in presence of KCl is slightly smaller than without the addition of salt. The radii of gyration obtained from different scattering techniques are in good agreement with each other and proof the reliability of the results over a broad range of contrast situations.

Table S6.5. Results from Guinier-analysis.

Method	C_{KCl} [mM]	Temperature [°C]	Slope [nm^2]	R_g [nm]
SAXS	0	20	-3272 ± 6	99.1 ± 0.2
SAXS	0.5	20	-2969 ± 15	94.4 ± 0.5
SANS	0	20	-3483 ± 61	102.2 ± 1.8
SANS	0.5	20	-3405 ± 78	101.1 ± 2.3
SANS	0	45	-1869 ± 34	74.9 ± 1.4
SANS	0.5	45	-1863 ± 29	74.8 ± 1.2
SLS	0	20	-3148 ± 23	97.2 ± 0.7
SLS	0.5	20	-3008 ± 16	95.0 ± 0.5
SLS	0	45	-1680 ± 7	71.0 ± 0.3
SLS	0.5	45	-1610 ± 8	69.5 ± 0.3

Characterization of Core-Shell Microgel 2 (CS2)

In terms of recording a temperature dependent phase diagram of the CS microgels in dense packing a second batch of CS microgels (CS2) was synthesized. The synthesis was performed similar to the one of the CS microgels used in this and our previous work[131], but upscaled to yield a higher mass of particles. 7500 mg *N*-isopropylacrylamide (NIPAM, TCI, >98%) and 1535 mg *N*,*N'*-methylenebis(acrylamide) (BIS, Sigma-Aldrich, 99%) were dissolved in 1500 mL of ultra pure water (18.2 MΩcm). 300 mg of 3-(trimethoxysilyl)propyl methacrylate (MPS, Sigma Aldrich, 98%) functionalized SiO_2 particles[114] were added to the solution, which was flushed with argon for 2 h at a temperature of 70 °C. The reaction was initiated with 75 mg potassium persulfate (PPS, Sigma-Aldrich, 99,0%) dissolved in 2 ml water and stopped after 4 h. All chemicals were used as received without further purification.

The core-shell nature of the microgels is shown in the TEM images of CS2 in **Figure S6.5a** and **b**. Only a minor fraction of particles below 1% does not possess a SiO_2 core. One example is indicated by a red circle in **Figure S6.5b**. The size distribution of the cores, based on TEM image analysis, is shown in **Figure S6.5c** resulting in an average R_{TEM} = 20 ± 1 nm. **Figure S6.5d** shows the R_h of CS2 as function of temperature in absence (red) and presence of salt (orange). Hydrodynamic radii of CS1 and CS2 at 20 °C and 40 °C are given in **Tables S6.10** and **S6.11**. Compared to CS1 in terms of R_h (147 nm and 149 nm at 20 °C), core size (18 nm and 20 nm) and the nominal crosslinker ratio (15% for both), the CS2 microgels are an ideal system to perform additional experiments with, while maintaining a direct comparability between the two microgel systems. Even in terms of their electrophoretic mobility, the CS2 microgels show nearly the same mobilities in dependence of temperature and charge screening as shown in **Figure S6.5e**.

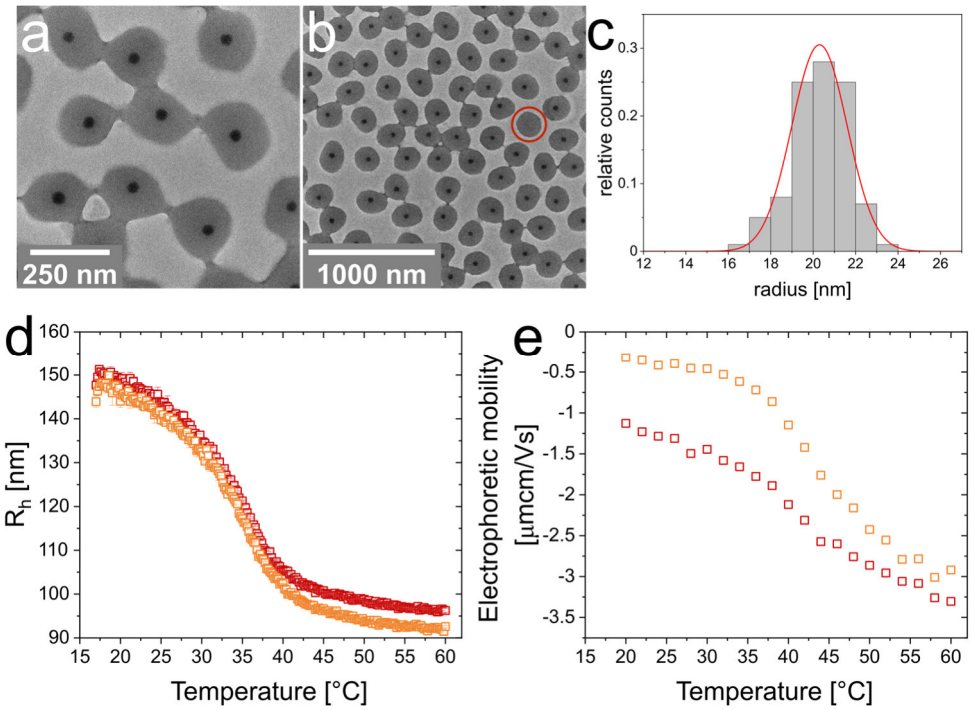

Figure S6.5. Characterization of CS2. (**a**, **b**) TEM images at different magnifications. The red circle indicates a single microgel without a core. (**c**) Size distribution of the SiO_2 cores from TEM image analysis. (**d**) R_h of CS2 as function of temperature in absence of salt (red squares) and in the charge-screened state (orange squares). (**e**) Electrophoretic mobility as function of temperature. Same color coding as in (**d**).

Extraction of Number Concentration for CS2

We extracted the relation between particle number concentration *N* and the mass content of the CS microgel dispersion, based on the scattering intensity of the SiO_2 cores in SAXS at infinitely small *q* (I_0), according to our previous works.[81, 131] We recorded the scattering profiles of three dispersions of CS2 microgels with mass contents of 10 wt% and performed form factor analysis on the scattering data. Here, we focused on the *q*-regime where the scattering of the core dominates the SAXS profile and applied a simple hard sphere model fit, resulting in R_{SAXS} of 20 ± 2 nm. The scattering profiles and respective form factor fits are shown in **Figure S6.6a**. Parameters applied to fit the scattering profiles are listed in **Table S6.6**. For the extraction of I_0 we performed a Guinier analysis on the plateau-like regime of the scattering profile in the low *q* regime (**Figure S6.6b**).

The scattering in the respective *q*-range already exhibits contributions of the shell and is not solely obtained from the SiO_2 core. Therefore, we also performed the Guinier-analysis on the form factor fits (**Figure S6.6c**). With this approach, we verify that the scattering of the shell does not influence our final results. Nevertheless, the data obtained from both approaches is listed in **Table S6.7** and **S6.8**.

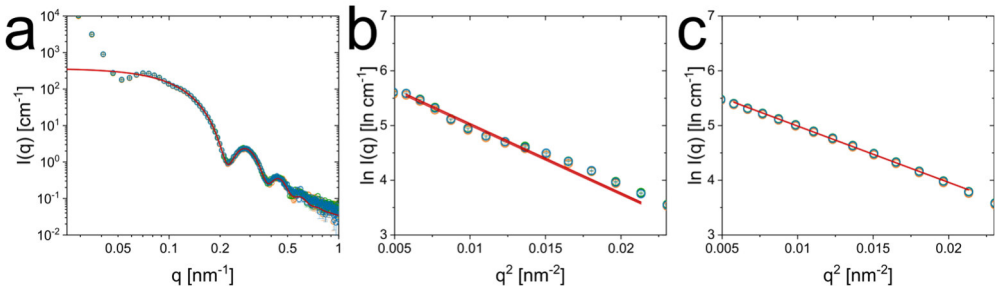

Figure S6.6. Extraction of the particle number concentration *N*. (**a**) Scattering profiles of three 10 wt% CS microgel dispersions. The solid red lines correspond to form factor fits describing the scattering of the SiO_2 core (**Equation S6.5**). Guinier plots of the scattering data (**b**) and the respective form factor fits (**c**). The solid red lines indicate the linear fits applied to the data.

Table S6.6. Fit parameters obtained from the form factor fits (polydisperse sphere model). The Errors of the parameters are smaller by two orders of magnitudes compared to the obtained valuers and therefore not listed.

	I	II	III
scale	0.00145	0.00150	0.00149
I_B [cm^{-1}]	0.03	0.03	0.03
SLD (SiO_2) [10^{-6} $Å^{-2}$]	17.8	17.8	17.8
SLD (H_2O) [10^{-6} $Å^{-2}$]	9.5	9.5	9.5
R [nm]	20	20	20
σ_{poly}	0.08	0.08	0.08

Table S6.7. Results from Guinier analysis of the SAXS data.

	I	II	III
I_0 [cm^{-1}]	528 ± 24	546 ± 26	543 ± 26
R_G [nm]	19.5 ± 0.4	19.5 ± 0.4	19.5 ± 0.4

Table S6.8. Results from the linear fits applied on the Guinier plots of the form factor fits.

	I	II	III
I_0 [cm^{-1}]	404 ± 6	413 ± 6	410 ± 6
R_G [nm]	17.6 ± 0.1	17.6 ± 0.1	17.6 ± 0.1

Similar to our previous work, we yield a lower I_0 from the Guinier analysis of the form factor fits compared to the analysis performed on the scattering data. In addition, the R_g extracted from the form factor fits is closer to the expected value for R_g according to $R_g = \sqrt{\frac{3}{5}}\, R_{P(q)}$ = 15.5 nm. In order to avoid the scattering of the shell, influencing the determination of the particle number concentration N, we used the results from the Guinier analysis of the form factor fits for further calculations.

The particle number concentration N can be calculated by the following equation:

$$N = \frac{I_0\, N_A\, \rho^2}{m\, M_w\, \Delta SLD^2} \tag{S6.8}$$

Here, N_A is Avogadro's number, ρ is the density of the silica cores, the mass of a single scattering object, m, M_w being the molecular weight, of the scattering object, and ΔSLD related to the difference in scattering length density between the solvent and the scattering object. We find an average particle number concentration N of $5.21 \cdot 10^{12}$ wt%$^{-1}$mL^{-1} for the CS2 microgels (**Table S6.9**), this is nearly the same relation as for CS1 ($N = 5.27 \cdot 10^{12}$ wt%$^{-1}$mL^{-1}).[131]

Table S6.9. Number concentrations extracted from the scattering intensity of CS2 microgel dispersions (10wt%).

	I	II	III	$\bar{N}$	SD
N ($I(q)$) [10^{13} 1/mL]	6.73	6.96	6.92	6.87	0.10
N ($P(q)$) [10^{13} 1/mL]	5.15	5.26	5.22	5.21	0.05

Generalized volume fractions (ζ) in presence and absence of salt at temperatures of 20 °C and 40 °C for the CS1 and CS2 microgels are given in **Tables S6.10** and **S6.11**. Here, ζ is calculated based on particle number concentrations N and the respective R_h.

Table S6.10. R_h and the respective ζ for CS microgels at 20 °C and 40 °C.

T = 20 °C c_{KCl} **= 0 mM**	**T = 20 °C** c_{KCl} **= 0.5 mM**	**T = 40 °C** c_{KCl} **= 0 mM**	**T = 40 °C** c_{KCl} **= 0.5 mM**
147 nm	145 nm	103 nm	101 nm
0.42	0.40	0.14	0.14
0.56	0.54	0.19	0.18
0.70	0.67	0.24	0.23
0.84	0.81	0.29	0.27

Table S6.11. R_h and the respective selected ζ for CS2 microgels at 20 °C and 40 °C in absence of salt and in the charge-screened state.

T = 20 °C c_{KCl} **= 0 mM**	**T = 20 °C** c_{KCl} **= 0.5 mM**	**T = 40 °C** c_{KCl} **= 0 mM**	**T = 40 °C** c_{KCl} **= 0.5 mM**
149 nm	144 nm	106 nm	102 nm
0.43	0.39	0.16	0.14
0.58	0.52	0.21	0.19
0.72	0.65	0.26	0.23
0.87	0.78	0.31	0.28

Scattering Pattern in the Fluid Phase at 40 °C

SAXS patterns of CS microgel dispersions with generalized volume fractions ζ (20 °C) of 0.42, 0.56, 0.70 and 0.84 were recorded at a temperature of 40 °C. The increase in temperature leads to a reduction in ζ and therefore the scattering patterns no longer exhibit Bragg peaks but a distinct fluid structure factor. This is presented in **Figure S6.7**, where all CS microgel dispersions feature an isotropic scattering pattern over a broad range of ζ between 0.14 and 0.29. Compared to the scattering patterns recorded in the absence of salt (top row), the structure factors are much broader and less intense in the charge-screened state (bottom row). This is a first indicator that the addition of salt decreases the effective range of inter particle interactions at the probed temperature.

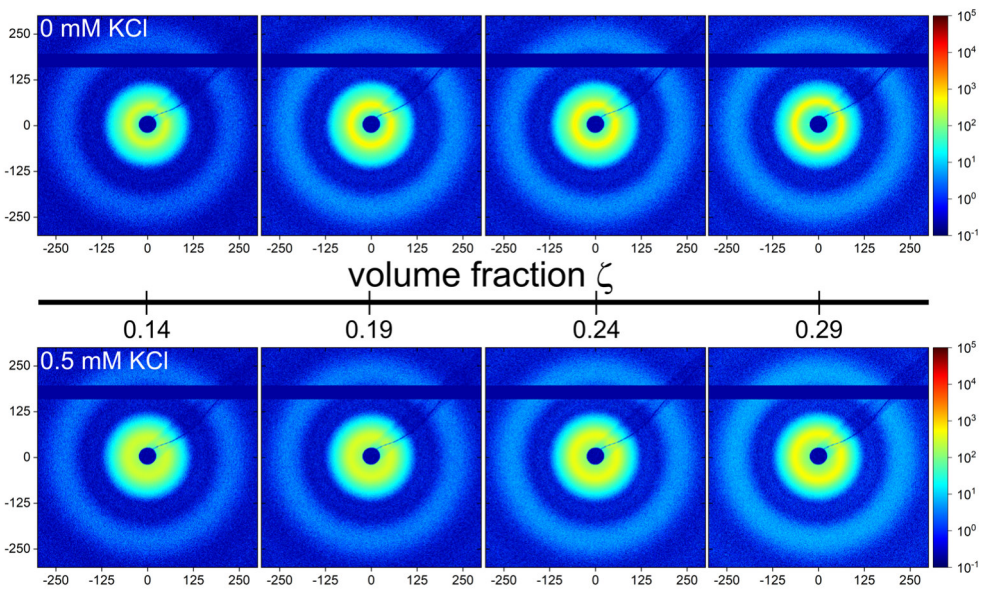

Figure S6.7. SAXS pattern of CS microgels in absence of salt (top) and in the charge-screened state (bottom) with increasing generalized volume fraction ζ (T = 40 °C). ζ is calculated based on number concentration N and the hydrodynamic radius at 40 °C measured in the absence of KCl.

Form Factor Modeling on CS Microgels in Dense Packings at 20 °C

Due to the presence of distinct form factor oscillations in the SAXS profiles of the CS microgels in dense packings, we were able to model form factors describing the scattering of the shell, even when S(q) ≠ 1. The modeled form factors are presented in **Figure 6.3a** in the main manuscript and the respective parameters are listed in **Table S6.12** and **Table S6.13**. For CS microgel dispersions with similar number concentrations, the same parameters could be applied on the scattering profiles recorded from samples in absence and presence of salt.

Table S6.12. Parameters used for the form factor modeling (core-exponential-shell model) of the CS microgel dispersions in the concentrated regime in absence of salt. ζ is calculated based on number concentration N and the hydrodynamic radius at 20 °C in the unscreened state. Adapted from our previous work.[131]

Parameters	ζ (20 °C) = 0.42	ζ (20 °C) = 0.56	ζ (20 °C) = 0.70	ζ (20 °C) = 0.84
scale	0.28	0.34	0.36	0.39
IB [a. u.]	0.2	0.2	0.2	0.2
R_{core} [nm]	18	18	18	18
Δt_{shell} [nm]	120	116	109	98
SLD_{core} [10^{-6} Å^{-2}]	17.75	17.75	17.75	17.75
$SLD_{shell,\ in}$ [10^{-6} Å^{-2}]	9.89	9.89	9.89	9.89
$SLD_{shell,\ out}$ [10^{-6} Å^{-2}]	9.43	9.43	9.43	9.43
$SLD_{solvent}$ [10^{-6} Å^{-2}]	9.43	9.43	9.43	9.43
σ_{core}	0.1	0.1	0.1	0.1
σ_{shell}	0.08	0.08	0.08	0.08
A	2.2	2.6	3.5	4.9

Table S6.13. Parameters used for the form factor modeling (core-exponential-shell model) of the CS microgel dispersions in the concentrated regime in presence of salt. ζ is calculated based on number concentration N and the hydrodynamic radius at 20 °C in the unscreened state.

Parameters	ζ (20 °C) = 0.42	ζ (20 °C) = 0.56	ζ (20 °C) = 0.70	ζ (20 °C) = 0.84
scale	0.28	0.34	0.36	0.39
IB [a. u.]	0.2	0.2	0.2	0.2
R_{core} [nm]	18	18	18	18
Δt_{shell} [nm]	120	116	109	98
SLD_{core} [10^{-6} Å^{-2}]	17.75	17.75	17.75	17.75
$SLD_{shell,\ in}$ [10^{-6} Å^{-2}]	9.89	9.89	9.89	9.89
$SLD_{shell,\ out}$ [10^{-6} Å^{-2}]	9.43	9.43	9.43	9.43
$SLD_{solvent}$ [10^{-6} Å^{-2}]	9.43	9.43	9.43	9.43
σ_{core}	0.1	0.1	0.1	0.1
σ_{shell}	0.08	0.08	0.08	0.08
A	2.2	2.6	3.5	4.9

Lattice Constant Extraction

Since the crystal structure of the colloidal crystals was determined to be a hexagonally closed packed (hcp) structure, we are able to relate the Bragg peaks to the respective miller indices.[131] This enables us to extract the lattice constant *a*, based on the linear dependency between the Bragg peak position q_{hkl} and the lattice spacing, as shown in **Figure S6.8**. The linear dependency is also shown in **Equation S6.9** and enables us to extract the lattice constant.

$$q_{hkl} = \frac{2\pi}{a}\left(\frac{4}{3}(h^2 + hk + k^2) + \frac{3}{8}l^2\right)^{\frac{1}{2}} \quad \text{(S6.9)}$$

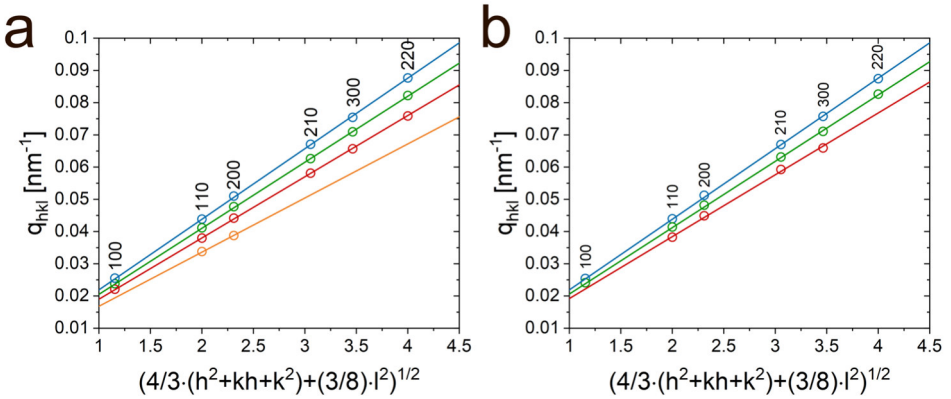

Figure S6.8. Extraction of the lattice constant *a* in absence (**a**) and presence of KCl (**b**). Position of the Bragg peak q_{hkl} as function of $\left(\frac{4}{3}(h^2+hk+k^2)+\frac{3}{8}l^2\right)^{\frac{1}{2}}$. Selected Bragg peaks recorded from CS microgel dispersions with ζ = 0.42 (orange circles), 0.56 (red circles), 0.7 (green circles) and 0.84 (blue circles). The straight, solid lines indicate the linear fits applied to the data. ζ is calculated based on number concentration N and the hydrodynamic radius at 20 °C in the unscreened state. Figure S6a is adapted from our previous work.[131]

Over a broad range of ζ, independent on the concentration of KCl we see a perfect linear relationship between the position of the Bragg peaks and the respective lattice spacings. For the CS microgel dispersion with ζ = 0.42 in the unscreened and ζ = 0.56 in the charge-screened state only a reduced number of Bragg peaks was used for the extraction of the lattice constant. This is due to weak intensity or interference of the Bragg peak with a structure factor maximum related a fluid-like contribution to the scattering profile. The extracted lattice constants and respective slopes of the fits are presented in **Table S6.14**. Here the addition of KCl to the CS microgel dispersion has no noticeable influence on the lattice constants of the colloidal crystals. It rather increases the volume fraction at which the system is able to form stable colloidal crystals.

Table S6.14. Slopes and respective lattice constants *a* extracted from linear fits. ζ is calculated based on number concentration *N* and the hydrodynamic radius at 20 °C in the unscreened state. Data recorded from samples in absence of salt is adapted from our previous work.[131]

ζ (20 °C) / c_{KCl} [mM]	Slope [nm^{-1}]	*a* [nm]
0.42 / 0 mM	0.0168	374
0.42 / 0.5 mM	-	-
0.56 / 0 mM	0.0190	331
0.56 / 0.5 mM	0.0192	327
0.70 / 0 mM	0.0205	306
0.70 / 0.5 mM	0.0206	305
0.84 / 0 mM	0.0219	287
0.84 / 0.5 mM	0.0219	287

Williamson-Hall Analysis

In order to extract the size of the coherently scattering domains of the prepared colloidal crystals, we performed Williamson-Hall analysis on the diffraction pattern. Here, we determined the width of the Bragg peaks in radial and azimuthal orientation as function of the scattering vector *q* as presented in **Figure S6.9**. From the slope of the linear fit applied on the data we could extract the strain of colloidal crystals $g_{rad/azi}$ and the size of the coherently scattering domains $L_{rad/azi}$ based on the respective intercept.

$$w_{rad/azi}{}^2(q) = \left(\frac{2\pi}{L_{rad/azi}}\right)^2 + g_{rad/azi}\, q^2 \qquad \text{(S6.10)}$$

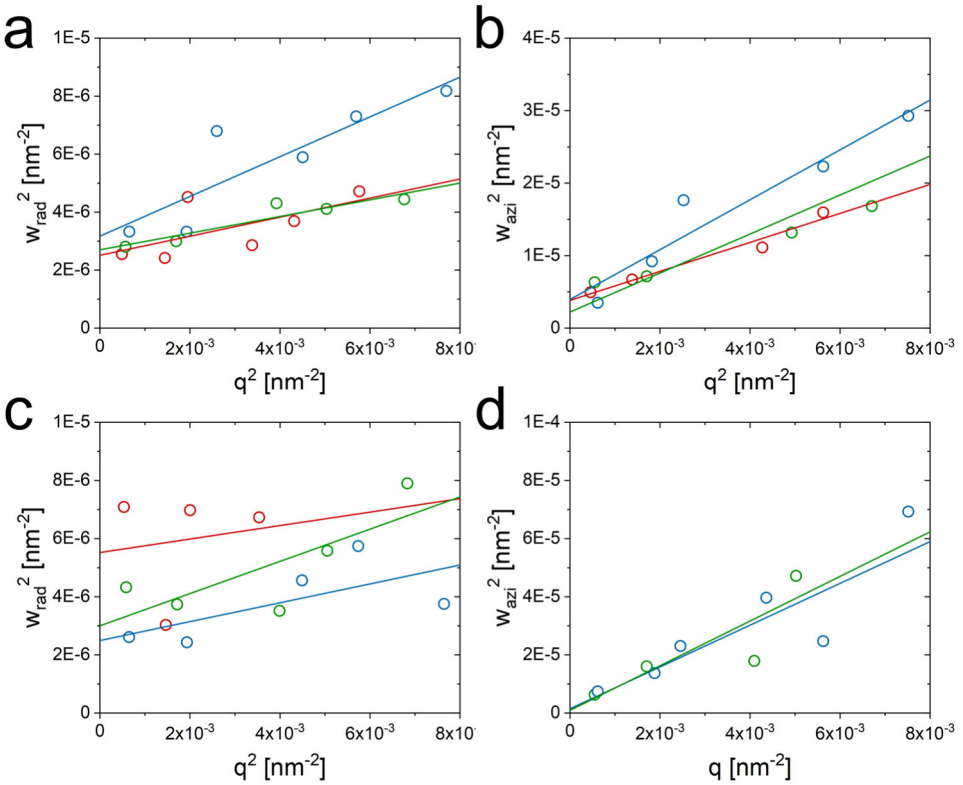

Figure S6.9. Williamson-Hall analysis. The square of the FWHM of the Bragg peaks in radial and azimuthal orientation as function of q^2. Data obtained from ζ = 0.56 CS microgel dispersions is shown in red, green corresponds to 0.70 and blue to 0.84 respectively unscreened (**a**, **b**) and charge-screened state (**c**, **d**). The straight lines represent the linear fits applied to the data. ζ is calculated based on number concentration N and the hydrodynamic radius at 20 °C in the unscreened state. Data from samples in the unscreened state is adapted from our previous work.[131]

The small slopes extracted from the Williamson-Hall analysis indicate only weak strains in our colloidal crystals and the intercepts used to calculate the size of the coherently scattering domains are listed in **Table S6.10** and **Table S6.11**.

Table S6.15. Parameters from linear Fits in Williamson-Hall analysis for CS microgels in absence of salt. Adapted our previous work.[131]

ζ (20 °C)	Intercept (rad.) [nm^{-2}]	Slope (rad.)	Intercept (azi.) [nm^{-2}]	slope (azi.)
0.56	2.5E-6	3.3E-4	3.8E-6	2.0E-3
0.70	2.7E-6	2.9E-4	2.2E-6	2.7E-3
0.84	3.2E-6	6.9E-4	3.9E-6	3.4E-3

Table S6.16. Parameters from linear Fits in Williamson-Hall analysis for CS microgels in the charge-screened state. *ζ* is calculated based on number concentration *N* and the hydrodynamic radius at 20 °C in the unscreened state.

ζ (20 °C)	Intercept (rad.) [nm^{-2}]	Slope (rad.)	Intercept (azi.) [nm^{-2}]	slope (azi.)
0.56	5.5E-6	2.3E-4	-	-
0.70	3.0E-6	5.5E-4	1.5E-6	7.2E-3
0.84	2.5E-6	3.2E-4	9.2E-7	3.2E-4

Figure S6.10 shows the radial and azimuthal coherently scattering domain sizes in dependence of *ζ* and charge screening extracted from the Williamson-Hall analysis. We found domain sizes between 2 and 4 µm. Azimuthal domain sizes in presence of salt possess large error bares in combination with exceptional large domain sizes, which indicates that the Williamson-Hall analysis might be not applicable on the respective scattering patterns.

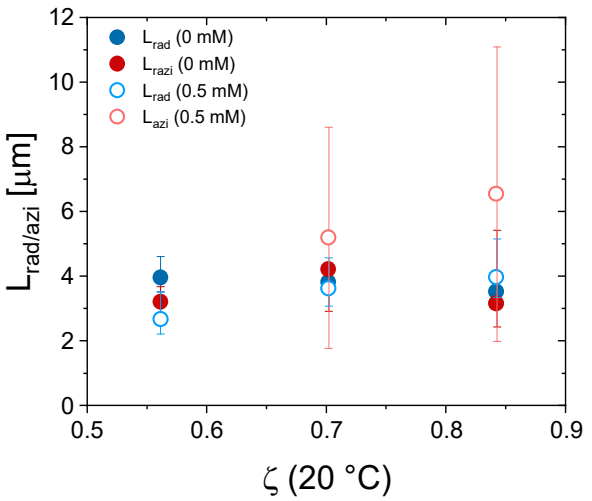

Figure S6.10. Radial and azimuthal coherently scattering domain sizes. Data from samples in the unscreened state is adapted from our previous work.[131]

CS Microgels in the Fluid Phase at 40 °C

SAXS profiles recorded from CS microgel dispersions at temperatures of 40 °C exhibit distinct structure factors in the probed range of volume fractions. At the given temperature, the CS microgels are in their collapsed state and the effective charge density is increased (**Figure 6.1a**). **Figure S6.11a**, **c** and **e** show the recorded structure factors fitted with the PY-model[184] (**a**), the Hayter-Penfold rescaled mean spherical approximation model (HP-RMSA)[220] (**c**) and a hard-core one-Yukawa potential rescaled mean spherical approximation model (1Y-RMSA)[151, 152, 218] (**e**). All applied models can describe the data sufficiently well. For the PY-fits (**Figure S6.11b, Table S6.17**) an increase in ζ results in an expected increase of the volume fraction (PY/circles) but also in a decrease of the hard sphere radius (R_{HS}/squares). This trend can be found independent on the presence of salt. On the example of the samples at ζ(20 °C) = 0.70, the results of the structure factor analysis can be compared quantitatively. In the unscreened state (blue symbols) a volume fraction (PY) of 0.43 and R_{HS} of 133 nm are found, changing to a volume fraction (PY) of 0.28 and R_{HS} = 116 nm when salt is added to the dispersion (green symbols). These differences can be found for all probed samples and indicate that the increase of the dispersions ionic strength might decrease the effective interaction radius of the CS microgels.

As the PY-model does not ascribe for the influence of electrostatic repulsion, the extracted effective radii and volume fraction do not correspond to exact physical quantities. Therefore, we applied two additional models to fit the structure factors which ascribe for electrostatic interactions. The HP-RMSA model accounts for the ionic strength of the dispersion and yields an effective number of charges. **Figure S6.11d** shows the number of effective charges (Z_{eff}) in absence of salt (blue) and under charge-screened conditions (green) and the respective fit parameters are listed in **Tables S6.18** and **S6.19**. The number of charges and effective radii are similar for both states and the decrease in the amplitude of the structure factor for samples with similar ζ(20 °C) can solely described by the increase in ionic strength due to the addition of salt. Here, we want to note that it is known from literature that the HP-RMSA model can overestimate the number of effective charges and the extracted Z_{eff} of around 400 might be higher than the real Z_{eff}.[152]

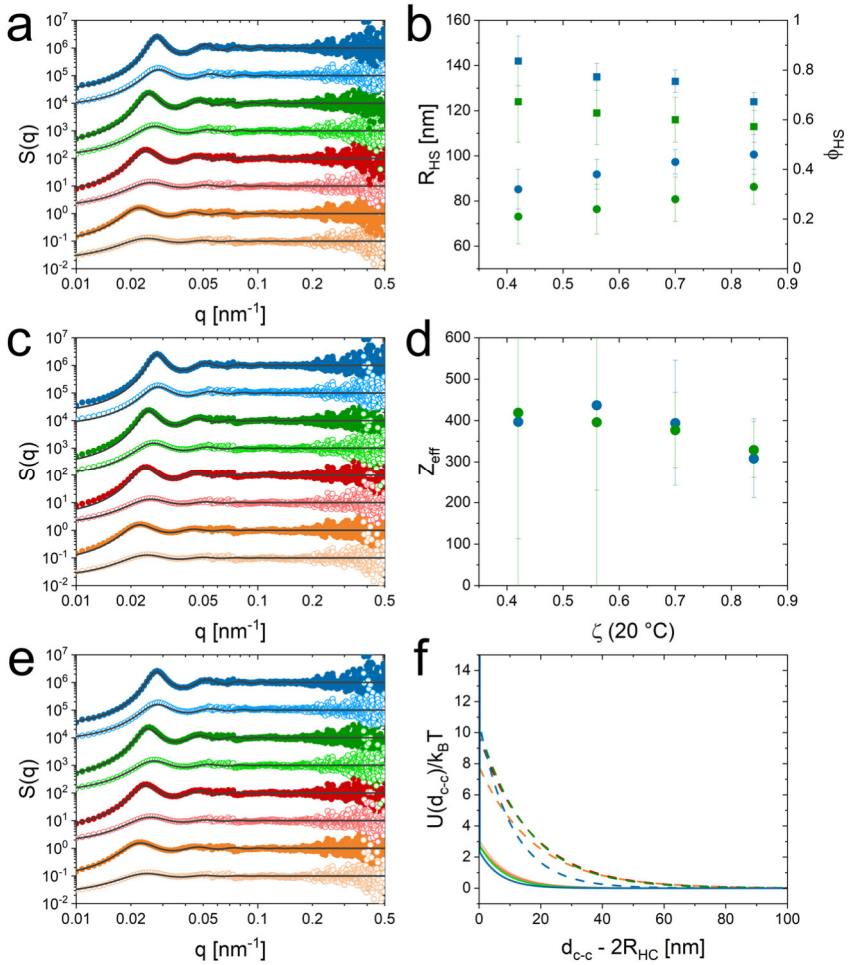

Figure S6.11. Structure factors from CS microgel dispersions at a temperature of 40 °C with ζ (20 °C) of 0.42 (orange), 0.56 (red), 0.70 (green) and 0.84 (blue). The darker color corresponds to the CS microgels in absence of salt and the lighter color corresponds to the CS microgels in the charge-screened state. Applied structure factor models are the PY-model[184] (**a**), the Hayter-Penfold rescaled mean spherical approximation (HP-RMSA) model[220] (**b**) and a hard-core one-Yukawa potential rescaled mean spherical approximation model (1Y-RMSA) (**c**).[151, 152, 218] The effective hard sphere radius (R_{HS}, squares) and the volume fraction (ϕ, circles) extracted from the PY-model structure factor fits (**b**). The effective number of charges (Z_{eff}) based on the HP-RMSA fits (**d**). Blue symbols in **b** and **d** correspond to the CS microgels in absence of salt and green symbols to the charge-screened state. (**f**) The one-Yukawa potentials corresponding to the respective structure factor fits. Dashed lines correspond to the samples in absence of salt while the solid lines correspond to the CS microgels in the charge-screened state. The color scheme is the same as for the structure factors.

Figure S6.11f shows the repulsive Yukawa potentials extracted from the hard-core 1Y-RMSA model structure factor fits as function of the center-to-center distance ($d_{c\text{-}c}$) subtracted by the hard-core radius (R_{HC}). The respective parameters are listed in **Tables S6.20** and **S6.21**. The one-Yukawa potential is a simplification of the two-Yukawa potential (**Eq. S6.11**),[151] where the potential strength *K* of the second term (*K2*) is made infinitely small and the inverse attraction or repulsion range (λ) of both terms is kept the same. As we only focus on the repulsive contribution to the potential, we will describe λ as inverse repulsive range. With R_{HC} corresponding to the effective hard-core radius of the particles in this model and $d_{c\text{-}c}$ being the center-to-center distance. The potential solely ascribes for a repulsive interaction. Here, the size of R_{HC} is about 110 nm and therefore slightly larger than the hydrodynamic radius of the CS microgels (R_h (40 °C) = 103 nm). We suppose that this difference is attributed to the dimensions of the ion cloud of the CS microgels.

$$\frac{U(d_{c-c})}{k_B T} = \infty \qquad if\ d_{c-c} \leq 2R_{HC}$$

$$= -2R_{HC}K1\frac{\exp\left(-\lambda 1(d_{c-c}-2R_{HC})\right)}{d_{c-c}} + 2R_{HC}K2\frac{\exp\left(-\lambda 2(d_{c-c}-2R_{HC})\right)}{d_{c-c}} \qquad if\ d_{c-c} > 2R_{HC} \tag{S6.11}$$

The extracted potentials from the CS microgels in absence of salt (dashed lines) are very pronounced and express a certain long-range repulsion. The potentials increase at lower $d_{c\text{-}c}$ - R_{HC} and tend towards infinity when $d_{c\text{-}c}$ - R_{HC} approaches zero. For the CS microgels with ζ (20 °C) = 0.84 (blue) the potential is slightly decreased. We attribute this to the increase in the number of counterions in the dispersion due to the high concentration of microgels and the successive increase in charge screening. The extracted potentials for the microgels in the charge-screened state are shown as solid lines and exhibit a weaker repulsion at short distances of around 10 nm. All potentials express a very similar progression which is nearly independent of the CS microgel concentration. The influence of charge screening is clearly shown by the respective potentials as the potential strength is significantly higher in the unscreened state. This is also reflected by the *K1* values extracted from the structure factor analysis with the 1Y-RMSA model.

Nevertheless, the performed fits also indicate that the range of repulsion for the CS microgels is increased by 6.5 ± 0.5 nm when charges are screened. This is quite counterintuitive as the range of repulsion was expected to decrease when charges are screened. Due to the potential strength being significantly decreased in the charge screened state, the influence of the repulsion range on the potentials is found to be rather small. Nevertheless, the influence of charge screening is still described by the potentials yielded from the 1Y-RMSA structure factor fits with a significant reduction of the interaction potential when charges are screened.

Table S6.17. Parameters from the PY structure factor fits applied on the extracted structure factors from the CS microgels in their collapsed state at 40 °C. ζ (20 °C) is calculated based on number concentration N and the hydrodynamic radius at 20°C in the unscreened state. Data from samples in the unscreened state is adapted from our previous work.[131]

ζ (20 °C) / c_{KCl} [mM]	R_{HS} [nm]	ϕ_{PY}	S(q = 0)
0.42 / 0	142 ± 11	0.32 ± 0.08	0.08
0.42 / 0.5	124 ± 18	0.21 ± 0.11	0.2
0.56 / 0	135 ± 6	0.38 ± 0.06	0.05
0.56 / 0.5	119 ± 14	0.24 ± 0.10	0.15
0.70 / 0	133 ± 5	0.43 ± 0.05	0.03
0.70 / 0.5	116 ± 10	0.28 ± 0.09	0.1
0.84 / 0	124 ± 4	0.46 ± 0.08	0.023
0.84 / 0.5	113 ± 7	0.33 ± 0.07	0.07

Table S6.18. Parameters from the HP-RMSA[220] structure factor fits applied on the extracted structure factors from the CS microgels in their collapsed state at 40 °C in absence of salt. The effective radius is $R_{eff\ (HP)}$ and the volume fraction in the HP-model is $\phi_{HP.}$ ε_r corresponds to the relative permittivity.

Parameters	ζ **(20 °C) =** 0.42	ζ **(20 °C) =** 0.56	ζ **(20 °C) =** 0.70	ζ **(20 °C) =** 0.84
$R_{eff\ (HP)}$ [nm]	105	106	109	105
Φ_{HP}	0.14	0.19	0.24	0.3
Z_{eff}	397 ± 284	437 ± 207	394 ± 152	308 ± 96
T [K]	313	313	313	313
Ionic strength [mM]	0.1	0.1	0.1	0.1
ε_r	73	73	73	73

Table S6.19. Parameters from the HP-RMSA[220] structure factor fits applied on the extracted structure factors from the CS microgels in their collapsed state at 40 °C in the charge-screened state. The effective radius is $R_{eff\ (HP)}$ and the volume fraction in the HP-model is ϕ_{HP}. ε_r corresponds to the relative permittivity.

Parameters	**ζ (20 °C) =** 0.42	**ζ (20 °C) =** 0.56	**ζ (20 °C) =** 0.70	**ζ (20 °C) =** 0.84
$R_{eff\ (HP)}$ [nm]	110	107	108	106
Φ_{HP}	0.15	0.17	0.23	0.28
Z_{eff}	419 ± 436	396 ± 761	377 ± 91	329 ± 68
T [K]	313	313	313	313
Ionic strength [mM]	0.5	0.5	0.5	0.5
ε_r	73	73	73	73

Table S6.20. Parameters from the 1Y-RMSA[151, 218] structure factor fits applied on the extracted structure factors from the CS microgels in their collapsed state at 40 °C in the unscreened state. The hard-core radius is R_{HC} and the volume fraction in the 1Y-model is ϕ_{1Y}. *K1* and *λ1* corresponds to the potential strength and the inverse repulsion range.

Parameters	**ζ (20 °C) =** 0.42	**ζ (20 °C) =** 0.56	**ζ (20 °C) =** 0.70	**ζ (20 °C) =** 0.84
R_{HC} [nm]	111	110	112	107
Φ_{1Y}	0.14	0.19	0.24	0.29
K1	-7.8	-9.8	-10.3	-10.7
λ1 [1/nm]	0.16	0.15	0.14	0.1

Table S6.21. Parameters from the 1Y-RMSA[151, 218] structure factor fits applied on the extracted structure factors from the CS microgels in their collapsed state at 40 °C in the charge-screened state. The hard-core radius is R_{HC} and the volume fraction in the 1Y-model is ϕ_{1Y}. *K1* and *λ1* corresponds to the potential strength and the inverse repulsion range.

Parameters	**ζ (20 °C) =** 0.42	**ζ (20 °C) =** 0.56	**ζ (20 °C) =** 0.70	**ζ (20 °C) =** 0.84
R_{HC} [nm]	110	110	110	109
Φ_{1Y}	0.14	0.19	0.24	0.29
K1	-3.1	-2.8	-2.8	-2.4
λ1 [1/nm]	0.08	0.08	0.07	0.06

Absorbance Spectroscopy of CS microgels in Dense Packings

In **Figure S6.12** we want to compare the Vis-NIR absorbance spectra recorded from CS microgels in dense packing used for the SAXS experiments and for temperature dependent absorbance spectroscopy. Nearly all spectra show narrow Bragg peaks indicating the presence of crystalline structures. The samples at ζ (20 °C) = 0.42 (orange) in **Figure S6.12a** and ζ = 0.49 in the charge-screened state (grey) in **Figure S6.12b** show no Bragg peaks. In general, for higher volume fractions the Bragg peaks shift towards lower wavelength. This reflects the decrease in the lattice constant *a* of the colloidal crystals presented in **Table S6.22** and **S6.23**.

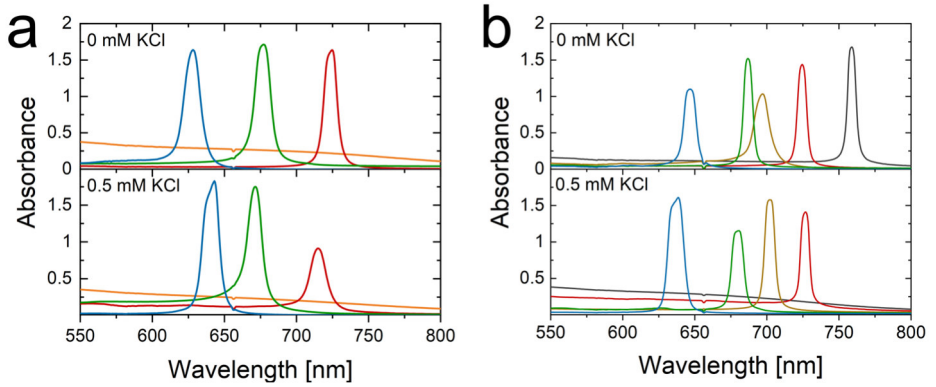

Figure S6.12. Vis-NIR absorbance spectra of CS microgels in dense packing in absence and presence of salt after thermal treatment. The dispersions exhibit generalized volume fractions ζ (20 °C) of 0.42 (orange), 0.49 (grey), 0.56 (red), 0.63 (dark orange), 0.70 (green) and 0.84 (blue). Spectra were recorded at a temperature of 20 °C. (**a**) CS microgel dispersions used for SAXS experiments and (**b**) for temperature dependent absorbance spectroscopy. ζ (20 °C) is calculated based on number concentration *N* and the hydrodynamic radius at 20 °C in the unscreened state. Data from samples prepared without the addition of salt presented in (**a**) is adapted from our previous work.[131]

For all CS microgel dispersions possessing the same ζ, we find similar Bragg peak positions. Only for the ζ being 0.84 (**Figure S6.9a**) we find a larger deviation of 20 nm between Peak positions. In terms of the lattice constant this translates to a deviation of 3% and we ascribe this to an imperfect formation of the crystalline structures in the respective probed volume. Bragg peak positions and the respective lattice constants *a* are given in **Table S6.22** (**Figure S6.12a**) and **Table S6.23** (**Figure S6.12b**).

Table S6.22. Bragg peak position and respective lattice constants for the hcp crystal structure obtained from the absorbance spectra of the CS microgel samples used for SAXS experiments. ζ (20 °C) is calculated based on number concentration *N* and the hydrodynamic radius at 20 °C in the unscreened state. Data recorded in absence of salt is adapted from our previous work.[131]

ζ (20 °C)	c_{KCl} [mM]	Bragg peak [nm]	Lattice constant *a* [nm]
0.42	0	-	-
0.42	0.5	-	-
0.56	0	724	329
0.56	0.5	715	325
0.70	0	676	308
0.70	0.5	671	305
0.84	0	628	286
0.84	0.5	641	292

Table S23. Bragg peak position and respective lattice constants for the hcp crystal structure of obtained from the absorbance spectra of the CS microgel samples used for temperature dependent absorbance spectroscopy. ζ (20 °C) is calculated based on number concentration *N* and the hydrodynamic radius at 20 °C in the unscreened state.

ζ (20 °C)	c_{KCl} [mM]	Bragg peak [nm]	Lattice constant *a* [nm]
0.49	0	759	346
0.49	0.5	-	-
0.56	0	724	330
0.56	0.5	726	331
0.63	0	696	317
0.63	0.5	702	320
0.70	0	687	313
0.70	0.5	680	310
0.84	0	647	295
0.84	0.5	637	290

Phase Transitions Followed by Temperature-Dependent Spectroscopy

Phase transitions between crystalline and fluid structures in CS microgels at dense packings are followed by the temperature dependent absorbance of the Bragg peaks. Here, we recoded Vis-NIR absorbance spectra between 20 °C and 50 °C in 0.3 °C steps with equilibration times of 720 s. The samples were prepared in absence and presence of KCl. For an increase in temperature, a decrease in the Bragg peak intensity followed by a complete disappearance can be monitored for all samples. The same trend in reverse can be found for the cooling process where the Bragg peak reappears and increases in intensity. Here we want to note that the presence of a Bragg peak is a clear indicator for the presence of crystalline structures in the probed volume but does not generally exclude the co-existence of a fluid subphase. Nevertheless, fluid subphases can be neglected for higher volume fractions as their presence is not indicated by SAXS for $\zeta > 0.56$. **Figure S6.13** and **Figure S6.14** show the temperature dependent absorbance spectra as well as the background corrected absorbance of the Bragg peaks as function of temperature. The green area indicates the respective temperature range, where the CS microgels undergo the transition between the crystalline- and fluid state. In general, we can detect some minor changes of the Bragg peak position and intensity before and after the temperature dependent measurements. We associate this to small changes in the unit cell dimensions and long-range order of the colloidal crystals in the probed sample volume.

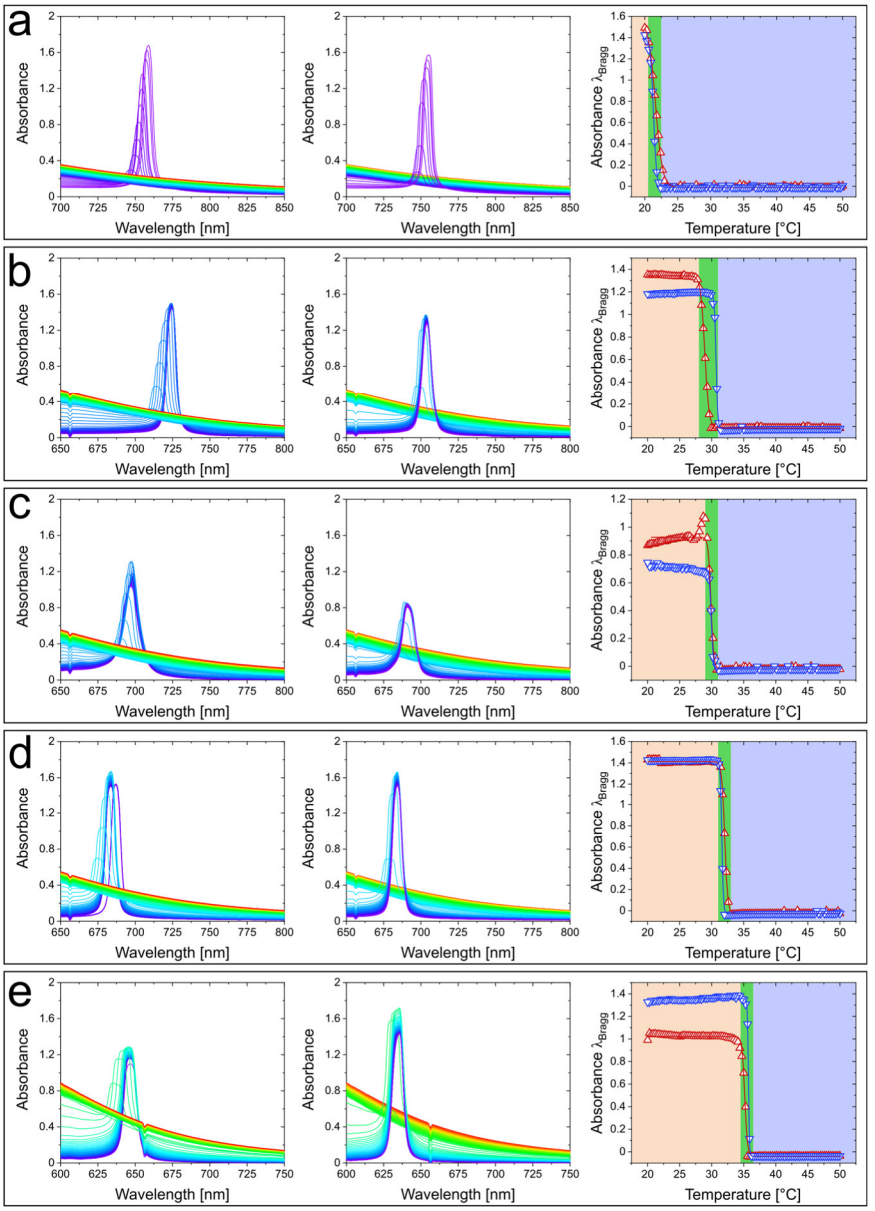

Figure S6.13. Temperature dependent Vis-NIR absorbance spectra of the CS microgel dispersions for the heating and cooling process as well as the background corrected absorbance of the Bragg peak as function of temperature. The color transition from blue to red indicates the change in temperature and the red and blue triangles correspond to the heating and cooling process. Here, the solid red and blue lines are sigmoidal fits indicating the course of the transition of the Bragg peak absorbance. Spectra were recorded of CS microgel dispersions with ζ (20 °C) of (**a**) 0.49, (**b**) 0.56, (**c**) 0.63, (**d**) 0.70 and (**e**) 0.84 in the absence of salt.

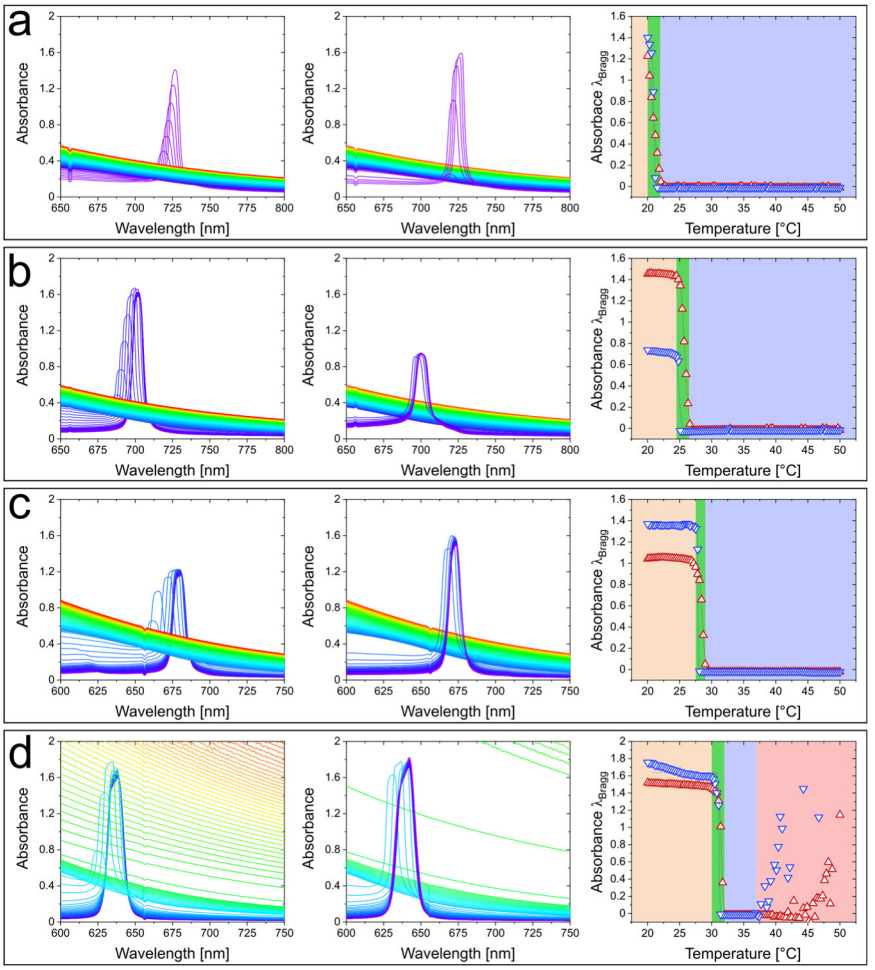

Figure S6.14. Temperature dependent Vis-NIR absorbance spectra of the CS microgel dispersions for the heating and cooling process as well as the background corrected absorbance of the Bragg peak as function of temperature. The color transition from blue to red indicates the change in temperature and the red and blue triangles correspond to the heating and cooling process. Here, the solid red and blue lines are sigmoidal fits indicating the course of the transition of the Bragg peak absorbance. Spectra were recorded of CS microgel dispersions with ζ (20 °C) of (**a**) 0.56, (**b**) 0.63 (**c**) 0.70 and (**d**) 0.84 in the charge-screened state. ζ (20 °C) is calculated based on number concentration *N* and the hydrodynamic radius at 20°C for the unscreened state.

The general temperature dependent behavior of the CS microgel dispersions prepared in absence and presence of salt is very similar. When reaching a specific temperature, the Bragg peak intensity decreases until the Bragg peak disappeared. The process is reversible when the temperature is decreased again. In comparison to the unscreened state, dispersions in the charge-screened state exhibit a shift of the transition temperature towards lower temperatures. The Vis-NIR absorbance spectra in **Figure S6.14d**, correspond to ζ (20 °C) = 0.84 in the charge-screened state exhibit a strong increase in absorbance after the phase transition, indicated in red. This behavior was not observed for any other sample, and we conclude that the presence of KCl in combination with the volume fraction enabled aggregation of the CS microgels above a certain temperature. The aggregation of the microgels would lead to larger scattering objects followed by an increase in light scattering of the sample. In absorbance spectroscopy an increase in the scattering contribution of the sample would lead to an increase in absorbance as less light being able to pass through the sample. This can be seen in **Figure S6.15** where the absorbance at the wavelength of 700 nm is presented as function of temperature. The absorbance increases above a temperature of 36 °C for the heating and cooling procedure until it reaches the instrumental limitations around a value of 3.5.

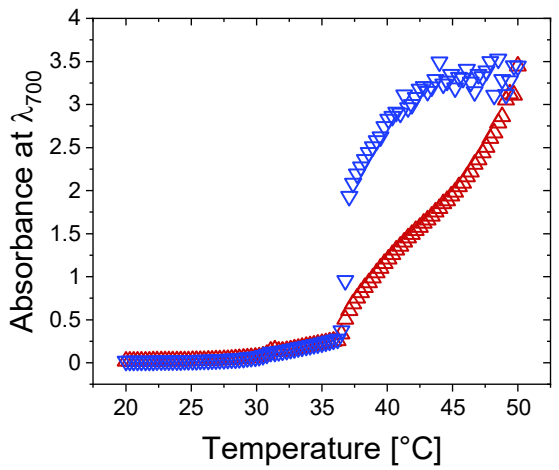

Figure S6.15. Temperature dependent absorbance at the wavelength of 700 nm for ζ (20 °C) = 0.84 CS microgel dispersion in the charge-screened state. Red corresponds to the heating and blue to the cooling process.

Temperature dependent Vis-NIR spectroscopy enables the determination of the phase transition temperature between the crystalline- and fluid state of the CS microgel dispersions, in dependence of ζ (20 °C). From temperature dependent DLS we know R_h at these transition temperatures and are able to calculate the respective volume of the CS microgels. In combination with particle number concentration N, extracted from the scattering intensity of the SiO_2 cores, we can calculate the generalized volume fraction ($\zeta_{transition}$) for the transition process. $\zeta_{transition}$ in absence (full circles) and presence (open circles) of salt as function of ζ (20 °C) is shown in **Figure S6.16a.** The heating and cooling processes are indicated by red and blue symbols. It is clearly shown that the screening of charges increases $\zeta_{transition}$ from a value of 0.43 ± 0.03 (c_{KCl} = 0 mM) to 0.54 ± 0.02 (c_{KCl} = 0.5 mM). The shift of $\zeta_{transition}$ is attributed to a reduction of the effective electrostatic interaction radius between the CS microgels, due to screened charges in the presence of additional ions. This is in good agreement with the results from the structure factor analysis (SAXS) of the CS microgels in the fluid state at 40 °C. Based on the following equation, under the assumption that the CS microgels crystallize similar to hard spheres, at a volume fraction of 0.494[120], we were able to calculate an effective hard sphere radius of the microgels:

$$R_{\text{hard sphere}} = \frac{\left(\frac{\zeta_{\text{transition}} R_{\text{h,transition}}{}^{-3}}{0.494}\right)^{-\frac{1}{3}}}{R_{\text{h,transition}}} R_{\text{h,20 °C}} \qquad \text{(S6.12)}$$

The effective hard sphere radius is $R_{hard\ sphere}$ and $R_{h,\ transition}$ corresponds to the hydrodynamic radius at the transition temperature. The calculated effective hard sphere radii are shown in **Figure S6.16b**. Similar to $\zeta_{transition}$ we detect a distinct influence of the charge screening, as the effective hard sphere radius deceases from 154 for the unscreened state to 143 nm in the screened state. An influence of ζ (20 °C) on $\zeta_{transition}$ and the effective hard sphere radius was not found. This might be attributed to the fact, that the here performed calculations are based on R_h(T) and potential osmotic deswelling or changes of the ionic strength of the dispersion due to an increase in microgel concentration could not be addressed.

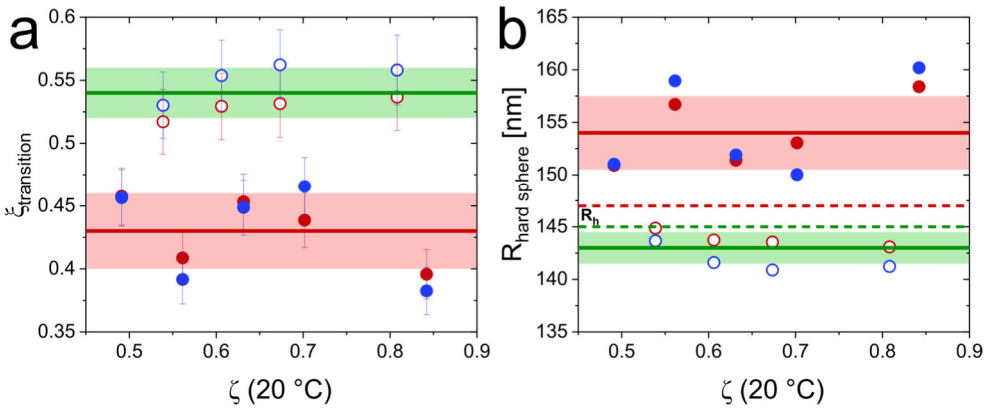

Figure S6.16. Transition volume fraction and corresponding hard sphere mapping. Full circles correspond to dispersions in absence of salt and empty circle correspond to samples in the charge-screened state. The melting and recrystallization process are indicated by the red and blue color of the symbols. (**a**) Generalized volume fraction $\zeta_{transition}$ of the CS microgel dispersions regarding the transition between fluid and crystalline regime in dependence of ζ (20 °C). The straight lines indicate the average $\zeta_{transition}$, red for the absence of salt and green for the charge-screened state. The colored area displays the respective standard deviation. (**b**) Hard sphere radius of the CS microgels as function of ζ (20 °C). Assuming that the CS microgels would actually crystallize similar to hard spheres at a volume fraction of 0.494. The straight lines indicate the average hard sphere radius, red for the absence of salt and green for the charge-screened state. The colored area displays the standard deviation and the dashed lines correspond to the respective R_h's at 20 °C.

Vis-NIR Absorbance Spectroscopy for the Preparation of the Phase Diagrams

Absorbance spectra of the CS2 microgel dispersions before (a) and after annealing (b) are shown in **Figure S6.17.** In accordance to our previous work,[131] the annealing procedure increased the intensity and decreased the width of the Bragg peaks. For more details we refer to the respective Supporting Information. After the annealing procedure, the spectra express similar trends compared to the spectra recorded from the CS1 system (**Figure 6.5a**). Here, Bragg peaks were detected from samples with ζ(20 °C) of 0.32 in the unscreened state. This is a much lower volume fraction than expected, based on the results from the CS1 microgel system. When charges are screened, a ζ(20 °C) of 0.51 is needed for the CS2 microgel dispersions to exhibit Bragg peaks, which is in good agreement with the previous results for the CS1 microgels. We performed temperature dependent Vis-NIR spectroscopy on samples in a range of ζ from 0.32 to 1.20 for CS microgels in the absence of salt and from 0.55 to 1.06 under charge-screened conditions. Here, the 1.20 and 1.06 CS2 microgel dispersions in the unscreened and screened state, respectively, possess the same particle number concentration N. The reason for the difference in ζ(20 °C) is the slightly smaller R_h recorded under charge-screened conditions, which was used to calculate ζ. A comparison of selected values of ζ and the respective R_h's at 20 and 40 °C in absence and presence of KCl is given in **Table S6.11**.

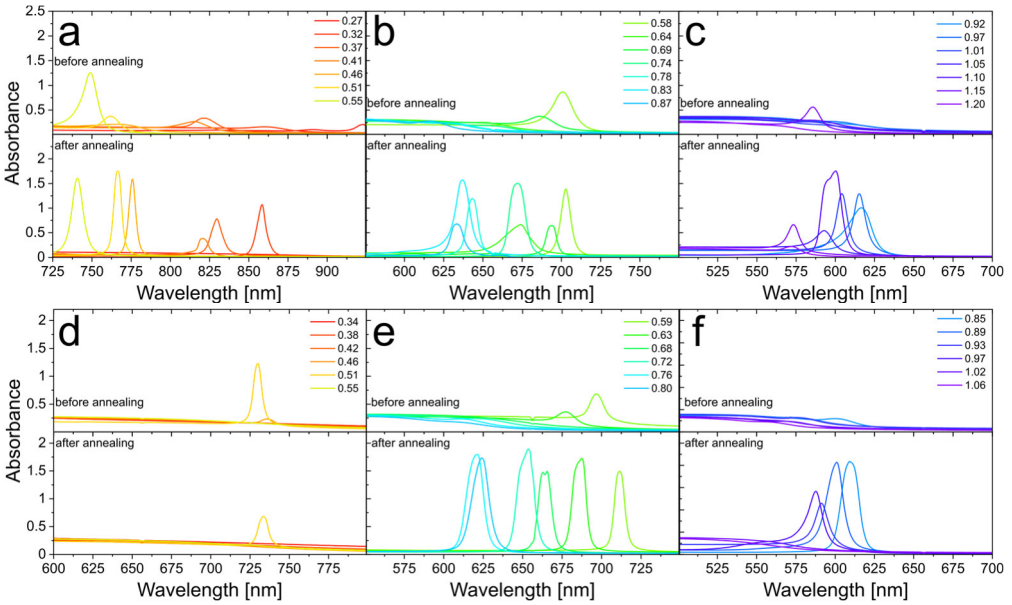

Figure S6.17. Vis-NIR absorbance spectra of CS2 microgels before and after the annealing process over a broad range of generalized volume fractions ζ, for c_{KCl} = 0 mM (top, **a**, **b**, **c**) and c_{KCl} = 0.5 mM (bottom, **d**, **e**, **f**) recorded at a temperature of 20 °C.

Temperature dependent Vis-NIR spectroscopy was performed on samples shown in **Figure S6.17**. The transition temperatures between the fluid and crystalline state were extracted similar to the CS1 microgels (**Figures S6.13** and **S6.14**) and are shown in **Figure S6.18a** and **S6.18b**. As expected, the transition temperature increases for higher ζ and the addition of KCl to the microgel dispersion lowers the transition temperature for the respective ζ compared to the CS microgels in the unscreened state.

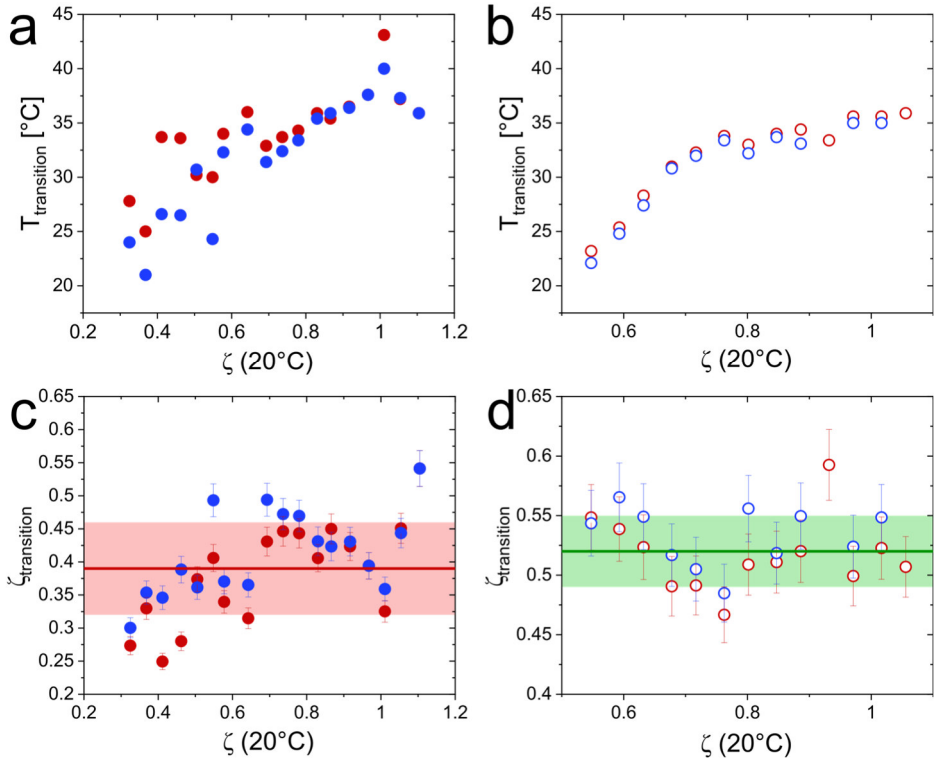

Figure S6.18. Transition temperature between the fluid and crystalline state for CS2 microgel dispersions in absence of salt (**a**) and in the charged-screened state (**b**). The temperature is given in dependence of the generalized volume fraction ζ, extracted from temperature dependent Vis-NIR absorbance spectra. $\zeta_{transition}$ as function of ζ(20 °C) in absence of salt (**c**) and in the charged-screened state (**d**). The sloid lines indicate the average $\zeta_{transition}$ and the colored area corresponds to the respective standard deviation. Red symbols refer to the heating and blue symbols to the cooling process.

Based on the transition temperature, the respective R_h and particle number concentration N, we can calculate $\zeta_{transition}$ for the CS2 system at in absence of salt and in the charge-screened state shown in **Figure S18c** and **S18d**. The average $\zeta_{transition}$, indicated by the solid line, is 0.39 ± 0.07 for the unscreened state and 0.52 ± 0.03 in presence of salt. The transition volume fractions extracted from temperature dependent Vis-NIR absorbance spectroscopy on CS2 microgel dispersions yield nearly the same results compared to the CS1 microgel system (c_{KCl} = 0 mM: 0.43 ± 0.03; c_{KCl} = 0.5 mM: 0.54 ± 0.02). Comparing two very similar but different batches of CS microgels and yielding nearly the same average $\zeta_{transition}$ underlines the reliability of the applied method.

7. Conclusion and Perspectives

Microgels are often discussed as model system for soft colloids.[8-10, 107] This thesis shows that this model system can be supplemented by the incorporation of a small inorganic core into the microgel. With core dimensions less than 15 % of the total size of the core-shell microgel, the core makes up below 1% of the volume of the particle and therefore a contribution of the core to interparticle interactions becomes rather neglectable for the here presented systems. Therefore, the core-shell microgels are expected to behave like standard microgels, but express additional features. Gold and silica were used as core materials, in combination with a thermoresponsive poly-*N*-isopropylacrylamide (PNIPAM) hydrogel shell. In this thesis, the phase behavior of these core-shell microgels was investigated with scattering techniques, primarily small-angle X-ray scattering (SAXS). These methods provide access to structural information as well as insights into particle sizes and morphologies. In the analysis of scattering data, recorded from microgels in dense packings, it is a common obstacle to separate the structure factor contributions from the scattering profile, due to superimposition of the form and structure factor oscillations. This is further complicated as it is known that the form factor of microgels in dense packings can undergo alterations as a result of deswelling, deformation or interpenetration processes, attributed to their softness.

In order to face these challenges, such core-shell microgels are promising systems, especially for the investigation with small-angle X-ray scattering (SAXS), due to different contrasts of the core and shell. The contribution of a small gold core featuring a very high contrast, dominates the SAXS profile recorded from a dispersion of core-shell microgels significantly as the form factor oscillations of the rather small microgel shell are only weakly pronounced. This simplifies the extraction of the structure factor, as a less pronounced form factor contribution of the polymer shell expresses less interferences with the structure factor. Therefore, information about interparticle distances and respective spatial correlation between the microgels become accessible. Regarding the analysis of potential structures exhibited by the dispersion of microgels, the main goal was the formation of crystalline structures through spontaneous self-assembly. For this, samples of microgels in dense packings and sufficiently large volume fractions were prepared. The resulting crystalline structures show pronounced structure factors which makes them an adequate challenge for a structure factor extraction.

An additional benefit from core-shell microgels with core materials of a known density and therefore a defined contrast, is that the ratio between particle number concentration and mass content of the microgels becomes accessible via the scattering intensity of the cores in SAXS. The lack of knowledge about particle number concentration is one of the crucial obstacles in many experiments, which complicates the comparability between theoretically and experimentally obtained insights into such systems. Due to the thermoresponsive properties of core-shell microgels, size and volume fraction become a function of temperature, allowing for *in situ* control over these parameters during experiments. The combination of known particle number concentration and the hydrodynamic radii, determined from temperature-dependent dynamic light scattering, facilitate a precise mapping of the generalized volume fraction of the core-shell microgels over a broad range of concentrations and temperatures.

The larger shell size of the silica core-shell microgel (R_{core} = 18 nm, R_h = 147 nm (20 °C)), in comparison to the gold core-shell system (R_{core} = 6.5 nm, R_h = 105 nm (20 °C)), provided a more pronounced form factor contribution of the shell to the SAXS profile. Meanwhile, the access to particle number concentrations was maintaining due to the presence of the core. It is notable that the form factor oscillations related to the core and shell in the SAXS profiles do not significantly interfere due to the differences in size between core and shell. Thus, the first form factor minima of the core and shell are separated by about one magnitude in q. In contrast to the gold core-shell system, the microgels possessing silica cores allow for detailed form factor analysis, including the soft polymer shell, even in dense packings. This was enabled by the small width of the Bragg peaks recorded for crystalline samples of the microgels. The form factor analysis revealed that the core-shell microgels exhibit osmotic deswelling as response towards the dense packing. The deswelling even occurred before direct interparticle contact, which has not been reported for such systems.[74, 80] Scattering patterns recorded from the concentrated dispersions of microgels exhibited multiple diffraction orders of narrow and distinct Bragg peaks, related to high spatial correlation in the arrangement of microgels and domain sizes of several micrometers. This allowed for a precise determination of the crystal structure which is hcp, by simulations of the scattering patterns and a detailed assignment of the Bragg peaks to the corresponding miller indices.

The high spatial correlation and domain size of the crystalline structures was attributed to a refined thermal annealing protocol with slow heating and cooling rates. At high temperatures, the core-shell microgels decrease in radius and thus volume fraction while the slow cooling rate allows the microgels to self-assemble into crystalline structures in a very controlled manner while the particles slowly increase in size.

With lattice constants slightly below the wavelength of visible light, the crystalline structures formed by the core-shell microgels in dense packings also exhibit photonic properties, manifesting as single and narrow Bragg peaks in optical spectroscopy. The detected Bragg peak can be used as tracker to follow the phase transition between the crystalline and fluid state. Thus, the phase behavior of crystalline dispersions of core-shell microgels was investigated by temperature-dependent absorbance spectroscopy and allowed for a determination of the minimum volume fraction, necessary for the microgels to self-assemble into crystalline structures. The result of the minimal volume fraction (unscreened state) being between 0.39 and 0.45 was lower than the known value for a system of hard spheres (0.49) and the freezing volume fraction of common microgels (0.56-0.59).[36, 222] In addition to absorbance spectroscopy, SAXS was conducted at elevated temperatures to prove the transition of the former crystalline dispersions into a completely fluid phase. Here, structure factor analysis indicated the presence of a pronounced electrostatic contribution to the effective interaction radius of the core-shell microgels, which might also be the reason for the formation of crystalline structures at relatively low volume fractions.

By screening the charges of the microgels through the addition of the monovalent and inert salt potassium chloride, electrostatic contributions could be reduced, revealing a significant influence on the phase behavior of the investigated microgels. The morphology and size of the core-shell microgels in the dilute state was investigated by SAXS, SANS, DLS and SLS. Here, no significant influence of the presence of salt on the microgels could be found. In the concentrated state, the influence of charge screening on the phase behavior of the microgels was investigated by SAXS and temperature-dependent absorbance spectroscopy. This revealed an increase in the volume fraction needed for the core-shell microgels to self-assemble into crystalline structures to a value of around 0.52. Dispersions of core-shell microgels featuring crystalline structures in presence of salt possessed similar spatial correlation and domain sizes compared to the samples prepared in absence of salt, exhibiting multiple diffraction orders of narrow Bragg peaks in SAXS.

Therefore, the screening of charges did not prevent the system from successful crystallization but increased the volume fraction needed for the self-assembly process. This thesis also features experimentally recorded temperature-dependent phase diagrams of core-shell microgels as function of the generalized volume fraction. The phase diagrams are based on the temperature-dependent evolution of the Bragg peaks in absorbance spectroscopy and show the influence of screened charges on the phase behavior of the microgels. Here, the temperatures at which the dispersions of densely packed core-shell microgels undergo the transition from the crystalline into the fluid phase are significantly decreased. In addition, the increased volume fraction needed for the crystallization of the system indicated a reduction in the effective interaction radius of the microgels. This is further supported by the structure factor analysis performed on SAXS profiles recorded from core-shell microgels in the fluid state at elevated temperatures. Here, screening of charges also indicated a reduction in the effective interaction radius. In conclusion, the impact of electrostatic interactions on the phase behavior of weakly charged microgels, could be shown in these phase diagrams which feature the generalized volume fraction as quantity to describe particle concentrations. This might set the ground for potential theoretical works, simulating soft colloids in dense packings, based on experimentally recorded data.

For future works, it would be of great interest to perform additional temperature-dependent synchrotron SAXS experiments to investigate the phase behavior of the core-shell microgels in more detail. Especially screening the transition regime in small temperature steps with synchrotron SAXS would enable an even more detailed analysis of the phase transition process. This would also provide access to information about the particle morphology and size in the respective packing and temperature regimes. In addition, performing quenching experiments on the microgels in dense packings could give access to a glassy phase, which was not observed in the presented phase diagrams. This is attributed to the annealing process, in which microgels always pass a section in volume fraction exhibiting crystalline structures before reaching the potential glass phase known from the hard sphere phase diagram.[120] These phases could be accessed by rapid cooling of heated suspensions of core-shell microgels.

Here, the system quickly passes the phase boundary between the fluid and solid phase (glass, crystal or jammed) as the volume fraction of the microgels increases drastically in response to the change in temperature on a relatively short time scale. With fast acquisition times in the range of milliseconds, synchrotron SAXS is an excellent method to provide detailed structural information, combined with great statistics and great time resolution.

The investigated microgels are generally considered as only weakly charged or even as neutral microgels, as ionic functionalities are only incorporated by the radical initiator. Despite this, the microgels still feature a pronounced electrostatic contribution in their interactions, which influences their phase behavior. Therefore, screening potential charges is of particular importance, even for weakly charged systems when it comes to the investigation of soft-soft particle interactions.

Recent works on microgels show that the softness of microgels is also influencing their assembly process.[80, 124] Core-shell microgels, similar to the presented systems could be used to get further insights into this topic. A variation in the crosslinker density, influences the softness of the microgels and SAXS could be used to study this in dense packings.

As the core provides access to the particle number concentration, such core-shell particles are perfectly suitable for all kinds of experiments where this quantity needs to be known. In addition, the core can act as tracer for the microgel, not only in SAXS, but also in electron microscopy techniques, for example in low contrast environments when the microgels are incorporated into other structures like a macrogel matrix.

The here presented class of core-shell microgels is clearly a versatile model system to study the behavior of soft colloids, with special advances in low contrast environments and therefore perfectly suitable to investigate microgels in crowded environments.

References

1 Rutherford, E., LXXIX. The scattering of α and β particles by matter and the structure of the atom. *The London, Edinburgh, and Dublin Philosophical Magazine and Journal of Science* **1911,** *21* (125), 669-688.

2 Bragg, W. H.; Bragg, W. L., The reflection of X-rays by crystals. *Proceedings of the Royal Society of London. Series A, Containing Papers of a Mathematical and Physical Character* **1913,** *88* (605), 428-438.

3 Pich, A. Z.; Adler, H. J. P., Composite aqueous microgels: an overview of recent advances in synthesis, characterization and application. *Polym Int* **2007,** *56* (3), 291-307.

4 Fernández-Barbero, A.; Suárez, I. J.; Sierra-Martín, B.; Fernández-Nieves, A.; de las Nieves, F. J.; Marquez, M.; Rubio-Retama, J.; López-Cabarcos, E., Gels and microgels for nanotechnological applications. *Advances in Colloid and Interface Science* **2009,** *147-48*, 88-108.

5 Karg, M.; Hellweg, T., New "smart" poly(NIPAM) microgels and nanoparticle microgel hybrids: Properties and advances in characterisation. *Curr Opin Colloid In* **2009,** *14* (6), 438-450.

6 Saunders, B. R.; Laajam, N.; Daly, E.; Teow, S.; Hu, X. H.; Stepto, R., Microgels: From responsive polymer colloids to biomaterials. *Advances in Colloid and Interface Science* **2009,** *147-48*, 251-262.

7 Pelton, R., Temperature-sensitive aqueous microgels. *Advances in Colloid and Interface Science* **2000,** *85* (1), 1-33.

8 Karg, M.; Pich, A.; Hellweg, T.; Hoare, T.; Lyon, L. A.; Crassous, J. J.; Suzuki, D.; Gumerov, R. A.; Schneider, S.; Potemkin, I. I.; Richtering, W., Nanogels and Microgels: From Model Colloids to Applications, Recent Developments, and Future Trends. *Langmuir* **2019,** *35* (19), 6231-6255.

9 Stieger, M.; Pedersen, J. S.; Lindner, P.; Richtering, W., Are thermoresponsive microgels model systems for concentrated colloidal suspensions? A rheology and small-angle neutron scattering study. *Langmuir* **2004,** *20* (17), 7283-7292.

10 Antonietti, M.; Bremser, W.; Schmidt, M., Microgels - Model Polymers for the Cross-Linked State. *Macromolecules* **1990,** *23* (16), 3796-3805.

11 Scheffold, F., Pathways and challenges towards a complete characterization of microgels. *Nature Communications* **2020,** *11* (1), 4315.

12 Iyer, A. S.; Lyon, L. A., Self-Healing Colloidal Crystals. *Angewandte Chemie-International Edition* **2009,** *48* (25), 4562-4566.

13 Roger, K.; Crassous, J. M. J., How the interplay of molecular and colloidal scales controls drying of microgel dispersions. *Proceedings of the National Academy of Sciences of the United States of America* **2021,** *118* (46), e2105530118.

14 Scotti, A.; Bochenek, S.; Brugnoni, M.; Fernandez-Rodriguez, M. A.; Schulte, M. F.; Houston, J. E.; Gelissen, A. P. H.; Potemkin, II; Isa, L.; Richtering, W., Exploring the colloid-to-polymer transition for ultra-low crosslinked microgels from three to two dimensions. *Nature Communications* **2019,** *10*, 1418.

15 Brugger, B.; Rosen, B. A.; Richtering, W., Microgels as Stimuli-Responsive Stabilizers for Emulsions. *Langmuir* **2008,** *24* (21), 12202-12208.

16 Plamper, F. A.; Richtering, W., Functional Microgels and Microgel Systems. *Accounts Chem Res* **2017,** *50* (2), 131-140.

17 Atkin, R.; Bradley, M.; Vincent, B., Core-shell particles having silica cores and pH-responsive poly(vinylpyridine) shells. *Soft Matter* **2005,** *1* (2), 160-165.

18 Pich, A.; Tessier, A.; Boyko, V.; Lu, Y.; Adler, H. J. P., Synthesis and characterization of poly(vinylcaprolactam)-based microgels exhibiting temperature and pH-sensitive properties. *Macromolecules* **2006,** *39* (22), 7701-7707.

19 Dalmont, H.; Pinprayoon, O.; Saunders, B. R., Study of pH-Responsive microgels containing methacrylic acid: Effects of particle composition and added calcium. *Langmuir* **2008,** *24* (6), 2834-2840.

20 Duracher, D.; Elaïssari, A.; Pichot, C., Characterization of cross-linked poly(N-isopropylmethacrylamide) microgel latexes. *Colloid and Polymer Science* **1999,** *277* (10), 905-913.

21 Petrunin, A. V.; Schmidt, M. M.; Schweins, R.; Houston, J. E.; Scotti, A., Self-Healing of Charged Microgels in Neutral and Charged Environments. *Langmuir* **2023,** *39* (22), 7530-7538.

22 Debord, J. D.; Lyon, L. A., Thermoresponsive photonic crystals. *Journal of Physical Chemistry B* **2000,** *104* (27), 6327-6331.

23 Hertle, Y.; Hellweg, T., Thermoresponsive copolymer microgels. *J Mater Chem B* **2013,** *1* (43), 5874-5885.

24 Pelton, R. H.; Chibante, P., Preparation of aqueous lattices with n-isopropylacrylamide. *Colloids and Surfaces* **1986,** *20* (3), 247-256.

25 Wu, X.; Pelton, R. H.; Hamielec, A. E.; Woods, D. R.; McPhee, W., The kinetics of poly(n-isopropylacrylamide) microgel latex formation. *Colloid and Polymer Science* **1994,** *272* (4), 467-477.

26 Duracher, D.; ElaÏssari, A.; Pichot, C., Preparation of poly(N-isopropylmethacrylamide) latexes kinetic studies and characterization. *Journal of Polymer Science Part a-Polymer Chemistry* **1999,** *37* (12), 1823-1837.

27 Senff, H.; Richtering, W., Influence of cross-link density on rheological properties of temperature-sensitive microgel suspensions. *Colloid and Polymer Science* **2000,** *278* (9), 830-840.

28 Heskins, M.; Guillet, J. E., Solution Properties of Poly(N-isopropylacrylamide). *Journal of Macromolecular Science: Part A - Chemistry* **1968,** *2* (8), 1441-1455.

29 Boon, N.; Schurtenberger, P., Swelling of micro-hydrogels with a crosslinker gradient. *Physical Chemistry Chemical Physics* **2017,** *19* (35), 23740-23746.

30 Stieger, M.; Richtering, W.; Pedersen, J. S.; Lindner, P., Small-angle neutron scattering study of structural changes in temperature sensitive microgel colloids. *Journal of Chemical Physics* **2004,** *120* (13), 6197-6206.

31 Cors, M.; Wiehemeier, L.; Hertle, Y.; Feoktystov, A.; Cousin, F.; Hellweg, T.; Oberdisse, J., Determination of Internal Density Profiles of Smart Acrylamide-Based Microgels by Small-Angle Neutron Scattering: A Multishell Reverse Monte Carlo Approach. *Langmuir* **2018,** *34* (50), 15403-15415.

32 Ponomareva, E.; Tadgell, B.; Hildebrandt, M.; Krüsmann, M.; Prévost, S.; Mulvaney, P.; Karg, M., The fuzzy sphere morphology is responsible for the increase in light scattering during the shrinkage of thermoresponsive microgels. *Soft Matter* **2022,** *18* (4), 807-825.

33 Scheffold, F.; Díaz-Leyva, P.; Reufer, M.; Ben Braham, N.; Lynch, I.; Harden, J. L., Brushlike Interactions between Thermoresponsive Microgel Particles. *Physical Review Letters* **2010,** *104* (12), 128304.

34 Mohanty, P. S.; Paloli, D.; Crassous, J. J.; Zaccarelli, E.; Schurtenberger, P., Effective interactions between soft-repulsive colloids: Experiments, theory, and simulations. *Journal of Chemical Physics* **2014,** *140* (9), 094901.

35 Bergman, M. J.; Gnan, N.; Obiols-Rabasa, M.; Meijer, J. M.; Rovigatti, L.; Zaccarelli, E.; Schurtenberger, P., A new look at effective interactions between microgel particles. *Nature Communications* **2018,** *9*, 5039.

36 Senff, H.; Richtering, W., Temperature sensitive microgel suspensions: Colloidal phase behavior and rheology of soft spheres. *Journal of Chemical Physics* **1999,** *111* (4), 1705-1711.

37 Paul, T. J.; Rubel, S.; Hildebrandt, M.; Strzelczyk, A. K.; Spormann, C.; Lindhorst, T. K.; Schmidt, S., Thermosensitive Display of Carbohydrate Ligands on Microgels for Switchable Binding of Proteins and Bacteria. *Acs Appl Mater Inter* **2019,** *11* (30), 26674-26683.

38 Zou, Z.; Gau, E.; El-Awaad, I.; Jakob, F.; Pich, A.; Schwaneberg, U., Selective Functionalization of Microgels with Enzymes by Sortagging. *Bioconjugate Chem* **2019,** *30* (11), 2859-2869.

39 Wilms, D.; Müller, J.; Urach, A.; Schröer, F.; Schmidt, S., Specific Binding of Ligand-Functionalized Thermoresponsive Microgels: Effect of Architecture, Ligand Density, and Hydrophobicity. *Biomacromolecules* **2022,** *23* (9), 3899-3908.

40 Saha, P.; Santi, M.; Frenken, M.; Palanisamy, A. R.; Ganguly, R.; Singha, N. K.; Pich, A., Dual-Temperature-Responsive Microgels from a Zwitterionic Functional Graft Copolymer with Superior Protein Repelling Property. *Acs Macro Lett* **2020,** *9* (6), 895-901.

41 Vlassopoulos, D.; Cloitre, M., Tunable rheology of dense soft deformable colloids. *Curr Opin Colloid In* **2014,** *19* (6), 561-574.
42 Andablo-Reyes, E.; Yerani, D.; Fu, M.; Liamas, E.; Connell, S.; Torres, O.; Sarkar, A., Microgels as viscosity modifiers influence lubrication performance of continuum. *Soft Matter* **2019,** *15* (47), 9614-9624.
43 Debord, J. D.; Eustis, S.; Debord, S. B.; Lofye, M. T.; Lyon, L. A., Color-tunable colloidal crystals from soft hydrogel nanoparticles. *Adv Mater* **2002,** *14* (9), 658-662.
44 Isapour, G.; Lattuada, M., Bioinspired Stimuli-Responsive Color-Changing Systems. *Adv Mater* **2018,** *30* (19), 1707069.
45 Zhang, B.; Cheng, Y.; Wang, H.; Ye, B. F.; Shang, L. R.; Zhao, Y. J.; Gu, Z. Z., Multifunctional inverse opal particles for drug delivery and monitoring. *Nanoscale* **2015,** *7* (24), 10590-10594.
46 Highley, C. B.; Song, K. H.; Daly, A. C.; Burdick, J. A., Jammed Microgel Inks for 3D Printing Applications. *Adv Sci* **2019,** *6* (1), 1801076.
47 Karg, M.; Hellweg, T.; Mulvaney, P., Self-Assembly of Tunable Nanocrystal Superlattices Using Poly-(NIPAM) Spacers. *Advanced Functional Materials* **2011,** *21* (24), 4668-4676.
48 Karg, M.; Jaber, S.; Hellweg, T.; Mulvaney, P., Surface Plasmon Spectroscopy of Gold-Poly-N-isopropylacrylamide Core-Shell Particles. *Langmuir* **2011,** *27* (2), 820-827.
49 Fitzgerald, J. P. S.; Karg, M., Plasmon resonance coupling phenomena in self-assembled colloidal monolayers. *Phys Status Solidi A* **2017,** *214* (8), 1600947.
50 Sindram, J.; Volk, K.; Mulvaney, P.; Karg, M., Silver Nanoparticle Gradient Arrays: Fluorescence Enhancement of Organic Dyes. *Langmuir* **2019,** *35* (26), 8776-8783.
51 Mei, Y.; Lu, Y.; Polzer, F.; Ballauff, M.; Drechsler, M., Catalytic activity of palladium nanoparticles encapsulated in spherical polyelectrolyte brushes and core-shell microgels. *Chem Mater* **2007,** *19* (5), 1062-1069.
52 Lu, Y.; Proch, S.; Schrinner, M.; Drechsler, M.; Kempe, R.; Ballauff, M., Thermosensitive core-shell microgel as a "nanoreactor" for catalytic active metal nanoparticles. *J Mater Chem* **2009,** *19* (23), 3955-3961.
53 Welsch, N.; Wittemann, A.; Ballauff, M., Enhanced Activity of Enzymes Immobilized in Thermoresponsive Core-Shell Microgels. *Journal of Physical Chemistry B* **2009,** *113* (49), 16039-16045.
54 Welsch, N.; Ballauff, M.; Lu, Y., Microgels as Nanoreactors: Applications in Catalysis. *Adv Polym Sci* **2010,** *234*, 129-163.
55 Camerin, F.; Gnan, N.; Ruiz-Franco, J.; Ninarello, A.; Rovigatti, L.; Zaccarelli, E., Microgels at Interfaces Behave as 2D Elastic Particles Featuring Reentrant Dynamics. *Phys Rev X* **2020,** *10* (3), 031012.
56 Geisel, K.; Richtering, W.; Isa, L., Highly ordered 2D microgel arrays: compression versus self-assembly. *Soft Matter* **2014,** *10* (40), 7968-7976.
57 Bochenek, S.; Scotti, A.; Ogieglo, W.; Fernández-Rodríguez, M. A.; Schulte, M. F.; Gumerov, R. A.; Bushuev, N. V.; Potemkin, I. I.; Wessling, M.; Isa, L.; Richtering, W., Effect of the 3D Swelling of Microgels on Their 2D Phase Behavior at the Liquid-Liquid Interface. *Langmuir* **2019,** *35* (51), 16780-16792.
58 Rey, M.; Hou, X. A.; Tang, J. S. J.; Vogel, N., Interfacial arrangement and phase transitions of PNiPAm microgels with different crosslinking densities. *Soft Matter* **2017,** *13* (46), 8717-8727.
59 Rauh, A.; Rey, M.; Barbera, L.; Zanini, M.; Karg, M.; Isa, L., Compression of hard core-soft shell nanoparticles at liquid-liquid interfaces: influence of the shell thickness. *Soft Matter* **2017,** *13* (1), 158-169.
60 Rey, M.; Fernández-Rodríguez, M. A.; Steinacher, M.; Scheidegger, L.; Geisel, K.; Richtering, W.; Squires, T. M.; Isa, L., Isostructural solid-solid phase transition in monolayers of soft core-shell particles at fluid interfaces: structure and mechanics. *Soft Matter* **2016,** *12* (15), 3545-3557.
61 Kuk, K.; Abgarjan, V.; Gregel, L.; Zhou, Y. C.; Fadanelli, V. C.; Buttinoni, I.; Karg, M., Compression of colloidal monolayers at liquid interfaces: in situ vs. ex situ investigation. *Soft Matter* **2023,** *19* (2), 175-188.
62 Grillo, F.; Fernandez-Rodriguez, M. A.; Antonopoulou, M. N.; Gerber, D.; Isa, L., Self-templating assembly of soft microparticles into complex tessellations. *Nature* **2020,** *582* (7811), 219.

63 Volk, K.; Honold, T.; Feller, D.; Karg, M., Surface Lattice Resonances in Self-Templated Plasmonic Honeycomb and Moire Lattices. *Adv Mater Interfaces* **2021,** *8* (13), 2100317.

64 Feller, D.; Karg, M., Fluid interface-assisted assembly of soft microgels: recent developments for structures beyond hexagonal packing. *Soft Matter* **2022,** *18* (34), 6301-6312.

65 Debord, S. B.; Lyon, L. A., Influence of particle volume fraction on packing in responsive hydrogel colloidal crystals. *Journal of Physical Chemistry B* **2003,** *107* (13), 2927-2932.

66 Hellweg, T.; Dewhurst, C. D.; Brückner, E.; Kratz, K.; Eimer, W., Colloidal crystals made of poly(N-isopropylacrylamide) microgel particles. *Colloid and Polymer Science* **2000,** *278* (10), 972-978.

67 Hellweg, T.; Dewhurst, C. D.; Eimer, W.; Kratz, K., PNIPAM-co-polystyrene core-shell microgels: Structure, swelling behavior, and crystallization. *Langmuir* **2004,** *20* (11), 4330-4335.

68 Bocanegra-Flores, J.; Haro-Pérez, C.; Reyes-Contreras, D.; Rojas-Ochoa, L. F., Crystallization kinetics of charged PNIPAM microgels dispersions at low volume fractions. *Frontiers in Physics* **2022,** *10*, 988903.

69 Gasser, U.; Lietor-Santos, J. J.; Scotti, A.; Bunk, O.; Menzel, A.; Fernandez-Nieves, A., Transient formation of bcc crystals in suspensions of poly(N-isopropylacrylamide)-based microgels. *Physical Review E* **2013,** *88* (5), 052308.

70 Scotti, A.; Houston, J. E.; Brugnoni, M.; Schmidt, M. M.; Schulte, M. F.; Bochenek, S.; Schweins, R.; Feoktystov, A.; Radulescu, A.; Richtering, W., Phase behavior of ultrasoft spheres show stable bcc lattices. *Physical Review E* **2020,** *102* (5), 052602.

71 Brijitta, J.; Tata, B. V. R.; Joshi, R. G.; Kaliyappan, T., Random hcp and fcc structures in thermoresponsive microgel crystals. *Journal of Chemical Physics* **2009,** *131* (7), 074904.

72 Lyon, L. A.; Debord, J. D.; Debord, S. B.; Jones, C. D.; McGrath, J. G.; Serpe, M. J., Microgel colloidal crystals. *Journal of Physical Chemistry B* **2004,** *108* (50), 19099-19108.

73 Rauh, A.; Carl, N.; Schweins, R.; Karg, M., Role of Absorbing Nanocrystal Cores in Soft Photonic Crystals: A Spectroscopy and SANS Study. *Langmuir* **2018,** *34* (3), 854-867.

74 Scotti, A.; Denton, A. R.; Brugnoni, M.; Houston, J. E.; Schweins, R.; Potemkin, II; Richtering, W., Deswelling of Microgels in Crowded Suspensions Depends on Cross-Link Density and Architecture. *Macromolecules* **2019,** *52* (11), 3995-4007.

75 Scotti, A.; Denton, A. R.; Brugnoni, M.; Schweins, R.; Richtering, W., Absence of crystals in the phase behavior of hollow microgels. *Physical Review E* **2021,** *103* (2), 022612.

76 Conley, G. M.; Aebischer, P.; Nöjd, S.; Schurtenberger, P.; Scheffold, F., Jamming and overpacking fuzzy microgels: Deformation, interpenetration, and compression. *Sci Adv* **2017,** *3* (10), e1700969.

77 Nöjd, S.; Mohanty, P. S.; Bagheri, P.; Yethiraj, A.; Schurtenberger, P., Electric field driven self-assembly of ionic microgels. *Soft Matter* **2013,** *9* (38), 9199-9207.

78 Mohanty, P. S.; Nöjd, S.; van Gruijthuijsen, K.; Crassous, J. J.; Obiols-Rabasa, M.; Schweins, R.; Stradner, A.; Schurtenberger, P., Interpenetration of polymeric microgels at ultrahigh densities. *Scientific Reports* **2017,** *7*, 1487.

79 Nöjd, S.; Holmqvist, P.; Boon, N.; Obiols-Rabasa, M.; Mohanty, P. S.; Schweins, R.; Schurtenberger, P., Deswelling behaviour of ionic microgel particles from low to ultra-high densities. *Soft Matter* **2018,** *14* (20), 4150-4159.

80 Scotti, A., Characterization of the volume fraction of soft deformable microgels by means of small-angle neutron scattering with contrast variation. *Soft Matter* **2021,** *17* (22), 5548-5559.

81 Hildebrandt, M.; Lazarev, S.; Pérez, J.; Vartanyants, I. A.; Meijer, J. M.; Karg, M., SAXS Investigation of Core-Shell Microgels with High Scattering Contrast Cores: Access to Structure Factor and Volume Fraction. *Macromolecules* **2022,** *55* (7), 2959-2969.

82 Lapkin, D.; Mukharamova, N.; Assalauova, D.; Dubinina, S.; Stellhorn, J.; Westermeier, F.; Lazarev, S.; Sprung, M.; Karg, M.; Vartanyants, I. A.; Meijer, J. M., In situ characterization of crystallization and melting of soft, thermoresponsive microgels by small-angle X-ray scattering. *Soft Matter* **2022,** *18* (8), 1591-1602.

83 Bergman, M. J.; Pedersen, J. S.; Schurtenberger, P.; Boon, N., Controlling the morphology of microgels by ionic stimuli. *Soft Matter* **2020,** *16* (11), 2786-2794.

84 Baker, W. O., Microgel, a New Macromolecule - Relation to Sol and Gel as Structural Elements of Synthetic Rubber. *Ind Eng Chem* **1949,** *41* (3), 511-520.

85 Lyon, L. A.; Serpe, M. J., *Hydrogel Micro and Nanoparticles*. Wiley-VCH Verlag GmbH & Co. KGaA: 2012.
86 Daly, E.; Saunders, B. R., Temperature-dependent electrophoretic mobility and hydrodynamic radius measurements of poly(N-isopropylacrylamide) microgel particles: structural insights. *Physical Chemistry Chemical Physics* **2000,** *2* (14), 3187-3193.
87 Hoare, T.; Pelton, R., Functional group distributions in carboxylic acid containing poly(N-isopropylacrylamide) microgels. *Langmuir* **2004,** *20* (6), 2123-2133.
88 Karg, M.; Pastoriza-Santos, I.; Rodriguez-González, B.; von Klitzing, R.; Wellert, S.; Hellweg, T., Temperature, pH, and ionic strength induced changes of the swelling behavior of PNIPAM-poly(allylacetic acid) copolymer microgels. *Langmuir* **2008,** *24* (12), 6300-6306.
89 Utashiro, Y.; Takiguchi, M.; Satoh, M., Zeta potential of PNIPAM microgel particles dispersed in water-effects of charged radical initiators vs. OH- ion adsorption. *Colloid and Polymer Science* **2017,** *295* (1), 45-52.
90 Volk, K.; Deißenbeck, F.; Mandal, S.; Löwen, H.; Karg, M., Moiré and honeycomb lattices through self-assembly of hard-core/soft-shell microgels: experiment and simulation. *Physical Chemistry Chemical Physics* **2019,** *21* (35), 19153-19162.
91 Gnan, N.; Rovigatti, L.; Bergman, M.; Zaccarelli, E., In Silico Synthesis of Microgel Particles. *Macromolecules* **2017,** *50* (21), 8777-8786.
92 Atkins, P. W.; Paula, J.; Keeler, J. J., *Physikalische Chemie*. 6 ed.; Wiley-VCH: 2022; p 1232.
93 Kawaguchi, T.; Kojima, Y.; Osa, M.; Yoshizaki, T., Cloud points in aqueous poly(N-isopropylacrylamide) solutions. *Polym J* **2008,** *40* (5), 455-459.
94 Ise, T.; Nagaoka, K.; Osa, M.; Yoshizaki, T., Cloud points in aqueous solutions of poly(N-isopropylacrylamide) synthesized by aqueous redox polymerization. *Polym J* **2011,** *43* (2), 164-170.
95 Kawaguchi, H., On Going to a New Era of Microgel Exhibiting Volume Phase Transition. *Gels* **2020,** *6* (3), 26.
96 Pelton, R., Poly(N-isopropylacrylamide) (PNIPAM) is never hydrophobic. *Journal of Colloid and Interface Science* **2010,** *348* (2), 673-674.
97 Wedel, B.; Zeiser, M.; Hellweg, T., Non NIPAM Based Smart Microgels: Systematic Variation of the Volume Phase Transition Temperature by Copolymerization. *Z Phys Chem* **2012,** *226* (7-8), 737-748.
98 Cors, M.; Wiehemeier, L.; Oberdisse, J.; Hellweg, T., Deuteration-Induced Volume Phase Transition Temperature Shift of PNIPMAM Microgels. *Polymers* **2019,** *11* (4), 620.
99 Flory, P. J., *Principles of polymer chemistry*. Cornell university press: 1953.
100 Flory, P. J.; Rehner, J., Jr., Statistical Mechanics of Cross-Linked Polymer Networks I. Rubberlike Elasticity. *The Journal of Chemical Physics* **1943,** *11* (11), 512-520.
101 Godbole, R. V.; Khabaz, F.; Khare, R.; Hedden, R. C., Swelling of Random Copolymer Networks in Pure and Mixed Solvents: Multi-Component Flory-Rehner Theory. *Journal of Physical Chemistry B* **2017,** *121* (33), 7963-7977.
102 Friesen, S.; Kakorin, S.; Hellweg, T., Modified Flory-Rehner Theory Describes Thermotropic Swelling Transition of Smart Copolymer Microgels. *Polymers* **2022,** *14* (10), 1999.
103 Saunders, B. R., On the structure of poly(N-isopropylacrylamide) microgel particles. *Langmuir* **2004,** *20* (10), 3925-3932.
104 Wiehemeier, L.; Cors, M.; Wrede, O.; Oberdisse, J.; Hellweg, T.; Kottke, T., Swelling behaviour of core-shell microgels in H2O, analysed by temperature-dependent FTIR spectroscopy. *Physical Chemistry Chemical Physics* **2019,** *21* (2), 572-580.
105 Brändel, T.; Dirksen, M.; Hellweg, T., Tuning the Swelling Properties of Smart Multiresponsive Core-Shell Microgels by Copolymerization. *Polymers* **2019,** *11* (8), 1269.
106 Cors, M.; Wrede, O.; Genix, A. C.; Anselmetti, D.; Oberdisse, J.; Hellweg, T., Core-Shell Microgel-Based Surface Coatings with Linear Thermoresponse. *Langmuir* **2017,** *33* (27), 6804-6811.
107 Siebenbürger, M.; Fuchs, M.; Ballauff, M., Core-shell microgels as model colloids for rheological studies (vol 8, pg 4014, 2012). *Soft Matter* **2012,** *8* (48), 12133-12133.

108 Laurenti, M.; Guardia, P.; Contreras-Cáceres, R.; Pérez-Juste, J.; Fernandez-Barbero, A.; Lopez-Cabarcos, E.; Rubio-Retama, J., Synthesis of Thermosensitive Microgels with a Tunable Magnetic Core. *Langmuir* **2011,** *27* (17), 10484-10491.

109 Magnozzi, M.; Brasse, Y.; Konig, T. A. F.; Bisio, F.; Bittrich, E.; Fery, A.; Canepa, M., Plasmonics of Au/Polymer Core/Shell Nanocomposites for Thermoresponsive Hybrid Metasurfaces. *Acs Appl Nano Mater* **2020,** *3* (2), 1674-1682.

110 Karg, M., Multifunctional inorganic/organic hybrid microgels. *Colloid and Polymer Science* **2012,** *290* (8), 673-688.

111 Carl, N.; Sindram, J.; Gallei, M.; Egelhaaf, S. U.; Karg, M., From normal diffusion to superdiffusion: Photothermal heating of plasmonic core-shell microgels. *Physical Review E* **2019,** *100* (5), 052605.

112 Stöber, W.; Fink, A.; Bohn, E., Controlled Growth of Monodisperse Silica Spheres in Micron Size Range. *Journal of Colloid and Interface Science* **1968,** *26* (1), 62.

113 Bogush, G. H.; Tracy, M. A.; Zukoski, C. F., Preparation of Monodisperse Silica Particles - Control of Size and Mass Fraction. *J Non-Cryst Solids* **1988,** *104* (1), 95-106.

114 Hartlen, K. D.; Athanasopoulos, A. P. T.; Kitaev, V., Facile preparation of highly monodisperse small silica spheres (15 to > 200 nm) suitable for colloidal templating and formation of ordered arrays. *Langmuir* **2008,** *24* (5), 1714-1720.

115 Dubbert, J.; Honold, T.; Pedersen, J. S.; Radulescu, A.; Drechsler, M.; Karg, M.; Richtering, W., How Hollow Are Thermoresponsive Hollow Nanogels? *Macromolecules* **2014,** *47* (24), 8700-8708.

116 Dubbert, J.; Nothdurft, K.; Karg, M.; Richtering, W., Core-Shell-Shell and Hollow Double-Shell Microgels with Advanced Temperature Responsiveness. *Macromol Rapid Comm* **2015,** *36* (2), 159-164.

117 Geisel, K.; Rudov, A. A.; Potemkin, I. I.; Richtering, W., Hollow and Core-Shell Microgels at Oil-Water Interfaces: Spreading of Soft Particles Reduces the Compressibility of the Monolayer. *Langmuir* **2015,** *31* (48), 13145-13154.

118 Scotti, A.; Brugnoni, M.; Rudov, A. A.; Houston, J. E.; Potemkin, II; Richtering, W., Hollow microgels squeezed in overcrowded environments. *Journal of Chemical Physics* **2018,** *148* (17), 174903.

119 Rauh, A.; Honold, T.; Karg, M., Seeded precipitation polymerization for the synthesis of gold-hydrogel core-shell particles: the role of surface functionalization and seed concentration. *Colloid and Polymer Science* **2016,** *294* (1), 37-47.

120 Pusey, P. N.; Van Megen, W., Phase-Behavior of Concentrated Suspensions of Nearly Hard Colloidal Spheres. *Nature* **1986,** *320* (6060), 340-342.

121 Rey, M.; Fernandez-Rodriguez, M. A.; Karg, M.; Isa, L.; Vogel, N., Poly-N-isopropylacrylamide Nanogels and Microgels at Fluid Interfaces. *Accounts Chem Res* **2020,** *53* (2), 414-424.

122 Gottwald, D.; Likos, C. N.; Kahl, G.; Löwen, H., Phase behavior of ionic microgels. *Physical Review Letters* **2004,** *92* (6), 068301.

123 Sierra-Martin, B.; Fernandez-Nieves, A., Phase and non-equilibrium behaviour of microgel suspensions as a function of particle stiffness. *Soft Matter* **2012,** *8* (15), 4141-4150.

124 Scotti, A.; Schulte, M. F.; Lopez, C. G.; Crassous, J. J.; Bochenek, S.; Richtering, W., How Softness Matters in Soft Nanogels and Nanogel Assemblies. *Chemical Reviews* **2022,** *122* (13), 11675–11700.

125 Scotti, A.; Pelaez-Fernandez, M.; Gasser, U.; Fernandez-Nieves, A., Osmotic pressure of suspensions comprised of charged microgels. *Physical Review E* **2021,** *103* (1), 012609.

126 Borrega, R.; Cloitre, M.; Betremieux, I.; Ernst, B.; Leibler, L., Concentration dependence of the low-shear viscosity of polyelectrolyte micro-networks: From hard spheres to soft microgels. *Europhys Lett* **1999,** *47* (6), 729-735.

127 Pelaez-Fernandez, M.; Souslov, A.; Lyon, L. A.; Goldbart, P. M.; Fernandez-Nieves, A., Impact of Single-Particle Compressibility on the Fluid-Solid Phase Transition for Ionic Microgel Suspensions. *Physical Review Letters* **2015,** *114* (9), 098303.

128 de Aguiar, I. B.; van de Laar, T.; Meireles, M.; Bouchoux, A.; Sprakel, J.; Schroën, K., Deswelling and deformation of microgels in concentrated packings. *Scientific Reports* **2017,** *7*, 10223.

129 Höfken, T.; Strauch, C.; Schneider, S.; Scotti, A., Changes in the Form Factor and Size Distribution of Nanogels in Crowded Environments. *Nano Lett* **2022,** *22* (6), 2412-2418.
130 Brändel, T.; Sabadasch, V.; Hannappel, Y.; Hellweg, T., Improved Smart Microgel Carriers for Catalytic Silver Nanoparticles. *Acs Omega* **2019,** *4* (3), 4636-4649.
131 Hildebrandt, M.; Pham Thuy, D.; Kippenberger, J.; Wigger, T. L.; Houston, J. E.; Scotti, A.; Karg, M., Fluid-solid transitions in photonic crystals of soft, thermoresponsive microgels. *Soft Matter* **2023,** *19* (37), 7122.
132 Huffman, D. R.; Bohren, C. F., *Absorption and Scattering of Light by Small Particles* **1998**.
133 Schärtl, W., *Light Scattering from Polymer Solutions and Nanoparticle Dispersions*. Springer Berlin: Heidelberg, 2007.
134 Guinier, A.; Fournet, G., *Small-Angle Scattering of X-Rays*. John Wiley and Sons. Inc: New York, 1955.
135 Hamley, I. W., *Small-Angle Scattering*. 1 ed.; John Wiley & Sons Ltd: 2021.
136 Dulle, M.; Jaber, S.; Rosenfeldt, S.; Radulescu, A.; Förster, S.; Mulvaney, P.; Karg, M., Plasmonic gold-poly(N-isopropylacrylamide) core-shell colloids with homogeneous density profiles: a small angle scattering study. *Physical Chemistry Chemical Physics* **2015,** *17* (2), 1354-1367.
137 Hendel, T.; Wuithschick, M.; Kettemann, F.; Birnbaum, A.; Rademann, K.; Polte, J., In Situ Determination of Colloidal Gold Concentrations with UV-Vis Spectroscopy: Limitations and Perspectives. *Anal Chem* **2014,** *86* (22), 11115-11124.
138 Ballauff, M., SAXS and SANS studies of polymer colloids. *Curr Opin Colloid In* **2001,** *6* (2), 132-139.
139 Hashimoto, T.; Tanaka, H.; Koizumi, S.; Kurosaki, K.; Ohmae, M.; Kobayashi, S., Chemical reaction at specific sites and reaction-induced self-assembly as observed by in situ and real time SANS: Enzymatic polymerization to synthetic cellulose. *Biomacromolecules* **2006,** *7* (9), 2479-2482.
140 Nayuk, R.; Zacher, D.; Schweins, R.; Wiktor, C.; Fischer, R. A.; van Tendeloo, G.; Huber, K., Modulated Formation of MOF-5 Nanoparticles-A SANS Analysis. *J Phys Chem C* **2012,** *116* (10), 6127-6135.
141 ILL https://www.ill.eu/users/instruments/instruments-list/d11/description/instrument-layout (accessed 04.05.2023).
142 DESY https://photon-science.desy.de/facilities/petra_iii/beamlines/p62_saxsmat/experimental_station/index_eng.html (accessed 04.05.2023).
143 Allen, A. J.; Zhang, F.; Kline, R. J.; Guthrie, W. F.; Ilavsky, J., Small-angle scattering standards and absolute intensity calibration. *Acta Crystallogr A* **2017,** *73*, C1443-C1443.
144 Jin, L.; Jarand, C. W.; Brader, M. L.; Reed, W. F., Angle-dependent effects in DLS measurements of polydisperse particles. *Meas Sci Technol* **2022,** *33* (4), 045202.
145 Urban, C.; Schurtenberger, P., Characterization of turbid colloidal suspensions using light scattering techniques combined with cross-correlation methods. *Journal of Colloid and Interface Science* **1998,** *207* (1), 150-158.
146 Franzen, A. http://www.gwoptics.org/ComponentLibrary/ (accessed 26.04.2023).
147 Koppel, D. E., Analysis of Macromolecular Polydispersity in Intensity Correlation Spectroscopy - Method of Cumulants. *Journal of Chemical Physics* **1972,** *57* (11), 4814.
148 Frisken, B. J., Revisiting the method of cumulants for the analysis of dynamic light-scattering data. *Appl Optics* **2001,** *40* (24), 4087-4091.
149 Provencher, S. W., A Constrained Regularization Method for Inverting Data Represented by Linear Algebraic or Integral-Equations. *Comput Phys Commun* **1982,** *27* (3), 213-227.
150 Prahl, S. https://omlc.org/calc/mie_calc.html (accessed 14.03.2023).
151 Liu, Y.; Chen, W. R.; Chen, S. H., Cluster formation in two-Yukawa fluids. *Journal of Chemical Physics* **2005,** *122* (4).
152 Heinen, M.; Holmqvist, P.; Banchio, A. J.; Nagele, G., Pair structure of the hard-sphere Yukawa fluid: An improved analytic method versus simulations, Rogers-Young scheme, and experiment. *Journal of Chemical Physics* **2011,** *134* (4).
153 Berndt, I.; Richtering, W., Doubly temperature sensitive core-shell microgels. *Macromolecules* **2003,** *36* (23), 8780-8785.

154 Dupin, D.; Fujii, S.; Armes, S. P.; Reeve, P.; Baxter, S. M., Efficient synthesis of sterically stabilized pH-responsive microgels of controllable particle diameter by emulsion polymerization. *Langmuir* **2006,** *22* (7), 3381-3387.
155 Garcia, A.; Marquez, M.; Cai, T.; Rosario, R.; Hu, Z. B.; Gust, D.; Hayes, M.; Vail, S. A.; Park, C. D., Photo-, thermally, and pH-responsive microgels. *Langmuir* **2007,** *23* (1), 224-229.
156 Hoare, T.; Pelton, R., Functionalized microgel swelling: Comparing theory and experiment. *Journal of Physical Chemistry B* **2007,** *111* (41), 11895-11906.
157 Huang, G.; Hu, Z. B., Phase behavior and stabilization of microgel arrays. *Macromolecules* **2007,** *40* (10), 3749-3756.
158 Schütter, S.; Roller, J.; Kick, A.; Meijer, J. M.; Zumbusch, A., Real-space imaging of translational and rotational dynamics of hard spheres from the fluid to the crystal. *Soft Matter* **2017,** *13* (44), 8240-8249.
159 Lazarev, S.; Besedin, I.; Zozulya, A. V.; Meijer, J. M.; Dzhigaev, D.; Gorobtsov, O. Y.; Kurta, R. P.; Rose, M.; Shabalin, A. G.; Sulyanova, E. A.; Zaluzhnyy, I. A.; Menushenkov, A. P.; Sprung, M.; Petukhov, A. V.; Vartanyants, I. A., Ptychographic X-Ray Imaging of Colloidal Crystals. *Small* **2018,** *14* (3), 1702575.
160 Singh, C. R.; Honold, T.; Gujar, T. P.; Retsch, M.; Fery, A.; Karg, M.; Thelakkat, M., The role of colloidal plasmonic nanostructures in organic solar cells. *Physical Chemistry Chemical Physics* **2016,** *18* (33), 23155-23163.
161 Ponomareva, E.; Volk, K.; Mulvaney, P.; Karg, M., Surface Lattice Resonances in Self-Assembled Gold Nanoparticle Arrays: Impact of Lattice Period, Structural Disorder, and Refractive Index on Resonance Quality. *Langmuir* **2020,** *36* (45), 13601-13612.
162 Murray, W. A.; Barnes, W. L., Plasmonic materials. *Adv Mater* **2007,** *19* (22), 3771-3782.
163 Honold, T.; Volk, K.; Rauh, A.; Fitzgerald, J. P. S.; Karg, M., Tunable plasmonic surfaces via colloid assembly. *J Mater Chem C* **2015,** *3* (43), 11449-11457.
164 Volk, K.; Fitzgerald, J. P. S.; Retsch, M.; Karg, M., Time-Controlled Colloidal Superstructures: Long-Range Plasmon Resonance Coupling in Particle Monolayers. *Adv Mater* **2015,** *27* (45), 7332.
165 Volk, K.; Fitzgerald, J. P. S.; Ruckdeschel, P.; Retsch, M.; König, T. A. F.; Karg, M., Reversible Tuning of Visible Wavelength Surface Lattice Resonances in Self-Assembled Hybrid Monolayers. *Adv Opt Mater* **2017,** *5* (9), 1600971.
166 Volk, K.; Fitzgerald, J. P. S.; Karg, M., In-Plane Surface Lattice and Higher Order Resonances in Self Assembled Plasmonic Monolayers: From Substrate-Supported to Free-Standing Thin Films. *Acs Appl Mater Inter* **2019,** *11* (17), 16096-16106.
167 Donev, A.; Stillinger, F. H.; Chaikin, P. M.; Torquato, S., Unusually dense crystal packings of ellipsoids. *Physical Review Letters* **2004,** *92* (25), 255506.
168 Schneider, C. A.; Rasband, W. S.; Eliceiri, K. W., NIH Image to ImageJ: 25 years of image analysis. *Nature Methods* **2012,** *9* (7), 671-675.
169 Girardot, R.; Viguier, G.; Pérez, J.; Ounsy, M. In *FOXTROT: A JAVA-based application to reduce and analyze SAXS and WAXS piles of 2D data at synchrotron SOLEIL*.
170 Bressler, I.; Kohlbrecher, J.; Thünemann, A. F., SASfit: a tool for small-angle scattering data analysis using a library of analytical expressions. *Journal of Applied Crystallography* **2015,** *48*, 1587-1598.
171 Förster, S.; Apostol, L.; Bras, W., Scatter: software for the analysis of nano- and mesoscale small-angle scattering. *Journal of Applied Crystallography* **2010,** *43*, 639-646.
172 Meng, Z. Y.; Cho, J. K.; Debord, S.; Breedveld, V.; Lyon, L. A., Crystallization behavior of soft, attractive microgels. *Journal of Physical Chemistry B* **2007,** *111* (25), 6992-6997.
173 Lu, Y.; Drechsler, M., Charge-Induced Self-Assembly of 2-Dimensional Thermosensitive Microgel Particle Patterns. *Langmuir* **2009,** *25* (22), 13100-13105.
174 NCNR https://www.ncnr.nist.gov/resources/activation/ (accessed 2022-17-03).
175 Fernández-Barbero, A.; Fernández-Nieves, A.; Grillo, I.; López-Cabarcos, E., Structural modifications in the swelling of inhomogeneous microgels by light and neutron scattering. *Physical Review E* **2002,** *66* (5), 051803.
176 Pan, G. S.; Tse, A. S.; Kesavamoorthy, R.; Asher, S. A., Synthesis of highly fluorinated monodisperse colloids for low refractive index crystalline colloidal arrays. *Journal of the American Chemical Society* **1998,** *120* (26), 6518-6524.

177 Zhang, J. H.; Sun, Z. Q.; Yang, B., Self-assembly of photonic crystals from polymer colloids. *Curr Opin Colloid In* **2009,** *14* (2), 103-114.

178 Petukhov, A. V.; Dolbnya, I. P.; Aarts, D. G. A. L.; Vroege, G. J.; Lekkerkerker, H. N. W., Bragg rods and multiple x-ray scattering in random-stacking colloidal crystals. *Physical Review Letters* **2003,** *90* (2), 028304.

179 Förster, S.; Timmann, A.; Schellbach, C.; Frömsdorf, A.; Kornowski, A.; Weller, H.; Roth, S. V.; Lindner, P., Order causes secondary Bragg peaks in soft materials. *Nat Mater* **2007,** *6* (11), 888-893.

180 Hilhorst, J.; Abramova, V. V.; Sinitskii, A.; Sapoletova, N. A.; Napolskii, K. S.; Eliseev, A. A.; Byelov, D. V.; Grigoryeva, N. A.; Vasilieva, A. V.; Bouwman, W. G.; Kvashnina, K.; Snigirev, A.; Grigoriev, S. V.; Petukhov, A. V., Double Stacking Faults in Convectively Assembled Crystals of Colloidal Spheres. *Langmuir* **2009,** *25* (17), 10408-10412.

181 Meijer, J. M.; Shabalin, A.; Dronyak, R.; Yefanov, O. M.; Singer, A.; Kurta, R. P.; Lorenz, U.; Gorobstov, O.; Dzhigaev, D.; Gulden, J.; Byelov, D. V.; Zozulya, A. V.; Sprung, M.; Vartanyants, I. A.; Petukhov, A. V., Double hexagonal close-packed structure revealed in a single colloidal crystal grain by Bragg rod analysis. *Journal of Applied Crystallography* **2014,** *47*, 1199-1204.

182 Tang, S. J.; Hu, Z. B.; Zhou, B.; Cheng, Z. D.; Wu, J. Z.; Marquez, M., Melting kinetics of thermally responsive microgel crystals. *Macromolecules* **2007,** *40* (26), 9544-9548.

183 Karthickeyan, D.; Joshi, R. G.; Tata, B. V. R., FCC-HCP coexistence in dense thermo-responsive microgel crystals. *Journal of Chemical Physics* **2017,** *146* (22), 224503.

184 Percus, J. K.; Yevick, G. J., Analysis of Classical Statistical Mechanics by Means of Collective Coordinates. *Phys Rev* **1958,** *110* (1), 1-13.

185 Destribats, M.; Lapeyre, V.; Wolfs, M.; Sellier, E.; Leal-Calderon, F.; Ravaine, V.; Schmitt, V., Soft microgels as Pickering emulsion stabilisers: role of particle deformability. *Soft Matter* **2011,** *7* (17), 7689-7698.

186 Berndt, I.; Pedersen, J. S.; Richtering, W., Structure of multiresponsive "intelligent" core-shell microgels. *Journal of the American Chemical Society* **2005,** *127* (26), 9372-9373.

187 Karg, M.; Prévost, S.; Brandt, A.; Wallacher, D.; von Klitzing, R.; Hellweg, T., Poly-NIPAM Microgels with Different Cross-Linker Densities. In *Progress in Colloid and Polymer Science*, Springer International Publishing Switzerland, 2013; Vol. 140, pp 63-76.

188 Heskins, M.; Guillet, J. E., Solution Properties of Poly(N-isopropylacrylamide). *J. Macromol. Sci., Part A: Pure Appl. Chem.* **1968,** *2*, 1441-1455.

189 Halperin, A.; Kroger, M.; Winnik, F. M., Poly(N-isopropylacrylamide) Phase Diagrams: Fifty Years of Research. *Angewandte Chemie-International Edition* **2015,** *54* (51), 15342-15367.

190 Hellweg, T., Towards Large-Scale Photonic Crystals with Tuneable Bandgaps. *Angewandte Chemie-International Edition* **2009,** *48* (37), 6777-6778.

191 Fernández-Rodríguez, M. A.; Elnathan, R.; Ditcovski, R.; Grillo, F.; Conley, G. M.; Timpu, F.; Rauh, A.; Geisel, K.; Ellenbogen, T.; Grange, R.; Scheffold, F.; Karg, M.; Richtering, W.; Voelcker, N. H.; Isa, L., Tunable 2D binary colloidal alloys for soft nanotemplating. *Nanoscale* **2018,** *10* (47), 22189-22195.

192 Alsayed, A. M.; Islam, M. F.; Zhang, J.; Collings, P. J.; Yodh, A. G., Premelting at defects within bulk colloidal crystals. *Science* **2005,** *309* (5738), 1207-1210.

193 Immink, J. N.; Bergman, M. J.; Maris, J. J. E.; Stenhammar, J.; Schurtenberger, P., Crystal-to-Crystal Transitions in Binary Mixtures of Soft Colloids. *Acs Nano* **2020,** *14* (11), 14861-14868.

194 Scotti, A.; Gasser, U.; Herman, E. S.; Pelaez-Fernandez, M.; Han, J.; Menzel, A.; Lyon, L. A.; Fernandez-Nieves, A., The role of ions in the self-healing behavior of soft particle suspensions. *Proceedings of the National Academy of Sciences of the United States of America* **2016,** *113* (20), 5576-5581.

195 Pellet, C.; Cloitre, M., The glass and jamming transitions of soft polyelectrolyte microgel suspensions. *Soft Matter* **2016,** *12* (16), 3710-3720.

196 Batchelor, G. K., Effect of brownian-motion on bulk stress in a suspension of spherical-particles. *Journal of Fluid Mechanics* **1977,** *83* (NOV), 97-117.

197 SasView. http://www.sasview.org/.

198 Tadgell, B.; Ponomareva, E.; Karg, M.; Mulvaney, P., Temperature-Jump Spectroscopy of Gold-Poly(N-isopropylacrylamide) Core-Shell Microgels. *J Phys Chem C* **2022,** *126* (8), 4118-4131.
199 Eckert, T.; Richtering, W., Thermodynamic and hydrodynamic interaction in concentrated microgel suspensions: Hard or soft sphere behavior? *Journal of Chemical Physics* **2008,** *129* (12), 124902.
200 Gasser, U.; Fernandez-Nieves, A., Crystal structure of highly concentrated, ionic microgel suspensions studied by small-angle x-ray scattering. *Physical Review E* **2010,** *81* (5), 052401.
201 Meijer, J. M.; de Villeneuve, V. W. A.; Petukhov, A. V., In-plane stacking disorder in polydisperse hard sphere crystals. *Langmuir* **2007,** *23* (7), 3554-3560.
202 Sanchez-Burgos, I.; Sanz, E.; Vega, C.; Espinosa, J. R., Fcc vs. hcp competition in colloidal hard-sphere nucleation: on their relative stability, interfacial free energy and nucleation rate. *Physical Chemistry Chemical Physics* **2021,** *23* (35), 19611-19626.
203 Sulyanova, E. A.; Shabalin, A.; Zozulya, A. V.; Meijer, J. M.; Dzhigaev, D.; Gorobtsov, O.; Kurta, R. P.; Lazarev, S.; Lorenz, U.; Singer, A.; Yefanov, O.; Zaluzhnyy, I.; Besedin, I.; Sprung, M.; Petukhov, A. V.; Vartanyants, I. A., Structural Evolution of Colloidal Crystal Films in the Process of Melting Revealed by Bragg Peak Analysis. *Langmuir* **2015,** *31* (19), 5274-5283.
204 Gasser, U.; Scotti, A.; Fernandez-Nieves, A., Spontaneous deswelling of microgels controlled by counterion clouds. *Physical Review E* **2019,** *99* (4), 042602.
205 Polte, J.; Ahner, T. T.; Delissen, F.; Sokolov, S.; Emmerling, F.; Thünemann, A. F.; Kraehnert, R., Mechanism of Gold Nanoparticle Formation in the Classical Citrate Synthesis Method Derived from Coupled In Situ XANES and SAXS Evaluation. *Journal of the American Chemical Society* **2010,** *132* (4), 1296-1301.
206 Feigin, L. A.; Svergun, D. I., *Structure Analysis by Small-Angle X-ray and Neutron Scattering*. Springer New York, NY: 1987.
207 Stieger, M.; Richtering, W.; Pedersen, J. S.; Lindner, P., Small-angle neutron scattering study of structural changes in temperature sensitive microgel colloids. *The Journal of Chemical Physics* **2004,** *120* (13), 6197-6206.
208 Berndt, I.; Pedersen, J. S.; Lindner, P.; Richtering, W., Influence of shell thickness and cross-link density on the structure of temperature-sensitive - Poly-N-isopropylacrylamide-poly-N-isopropylmethacrylamide core-shell microgels investigated by small-angle neutron scattering. *Langmuir* **2006,** *22* (1), 459-468.
209 Schindelin, J.; Arganda-Carreras, I.; Frise, E.; Kaynig, V.; Longair, M.; Pietzsch, T.; Preibisch, S.; Rueden, C.; Saalfeld, S.; Schmid, B.; Tinevez, J. Y.; White, D. J.; Hartenstein, V.; Eliceiri, K.; Tomancak, P.; Cardona, A., Fiji: an open-source platform for biological-image analysis. *Nature Methods* **2012,** *9* (7), 676-682.
210 Aguirre, C. I.; Reguera, E.; Stein, A., Tunable Colors in Opals and Inverse Opal Photonic Crystals. *Advanced Functional Materials* **2010,** *20* (16), 2565-2578.
211 Kotlarchyk, M.; Chen, S. H., Analysis of small-angle neutron-scattering spectra from polydisperse interacting colloids. *Journal of Chemical Physics* **1983,** *79* (5), 2461-2469.
212 Wedel, B.; Hertle, Y.; Wrede, O.; Bookhold, J.; Hellweg, T., Smart Homopolymer Microgels: Influence of the Monomer Structure on the Particle Properties. *Polymers* **2016,** *8* (4), 162.
213 Shaulli, X.; Rivas-Barbosa, R.; Bergman, M. J.; Zhang, C.; Gnan, N.; Scheffold, F.; Zaccarelli, E., Probing Temperature Responsivity of Microgels and Its Interplay with a Solid Surface by Super-Resolution Microscopy and Numerical Simulations. *Acs Nano* **2023,** *17* (3), 2067-2078.
214 Lopez, C. G.; Richtering, W., Does Flory-Rehner theory quantitatively describe the swelling of thermoresponsive microgels? *Soft Matter* **2017,** *13* (44), 8271-8280.
215 Wu, J. Z.; Zhou, B.; Hu, Z. B., Phase behavior of thermally responsive microgel colloids. *Physical Review Letters* **2003,** *90* (4), 048304.
216 Ruiz-Franco, J.; Rivas-Barbosa, R.; Lara-Peña, M. A.; Villanueva-Valencia, J. R.; Licea-Claverie, A.; Zaccarelli, E.; Laurati, M., Concentration and temperature dependent interactions and state diagram of dispersions of copolymer microgels. *Soft Matter* **2023,** *19* (20), 3614-3628.

217 Zhou, B. Y.; Gasser, U.; Fernandez-Nieves, A., Measuring the counterion cloud of soft microgels using SANS with contrast variation. *Nature Communications* **2023,** *14* (1).
218 Kohlbrecher, J.; Bressler, I., Updates in SASfit for fitting analytical expressions and numerical models to small-angle scattering patterns. *Journal of Applied Crystallography* **2022,** *55*, 1677-1688.
219 Holmqvist, P.; Mohanty, P. S.; Nägele, G.; Schurtenberger, P.; Heinen, M., Structure and Dynamics of Loosely Cross-Linked Ionic Microgel Dispersions in the Fluid Regime (vol 109, 048302, 2012). *Physical Review Letters* **2016,** *117* (17), 179901.
220 Hayter, J. B.; Penfold, J., An Analytic Structure Factor for Macroion Solutions. *Mol Phys* **1981,** *42* (1), 109-118.
221 Tadgell, B.; Ponomareva, E.; Karg, M.; Mulvaney, P., Scattering of Visible Light by Au-PNIPAM Core-Shell Microgels. *J Phys Chem C* **2022,** *126* (36), 15336-15347.
222 Scotti, A.; Gasser, U.; Herman, E. S.; Han, J.; Menzel, A.; Lyon, L. A.; Fernandez-Nieves, A., Phase behavior of binary and polydisperse suspensions of compressible microgels controlled by selective particle deswelling. *Physical Review E* **2017,** *96* (3), 032609